ALMA MATER STUDIORUM
UNIVERSITÀ DI BOLOGNA

DOTTORATO DI RICERCA IN

MECCANICA E SCIENZE AVANZATE DELL'INGEGNERIA

Ciclo 36

Settore Concorsuale: 09/A2 - MECCANICA APPLICATA ALLE MACCHINE

Settore Scientifico Disciplinare: ING-IND/13 - MECCANICA APPLICATA ALLE MACCHINE

A FAST CABLE-DRIVEN PARALLEL ROBOT FOR VISION-ASSISTED PICK-AND-PLACE OPERATIONS

Presentata da: Luca Guagliumi

Coordinatore Dottorato	**Supervisore**
Lorenzo Donati	Marco Carricato

Esame finale anno 2024

ALMA MATER STUDIORUM - UNIVERSITÀ DI BOLOGNA

A FAST CABLE-DRIVEN PARALLEL ROBOT FOR VISION-ASSISTED PICK-AND-PLACE OPERATIONS

A dissertation submitted in partial fulfillment
of the requirements for the degree of Doctor of Philosophy
in Mechanics and Advanced Engineering Sciences

Luca Guagliumi

Bologna, Italy,
September 18, 2024

Abstract

Pick-and-place operations are widely performed by robots in industrial packaging machines to move products between two planar surfaces (e.g., conveyor belts). However, more complex tasks also exist, like the so-called *3D-picking* or *bin-picking*, which requires the robot to take products from a pile (usually contained in a box) to reposition them in the place area. This operation is often performed by robots with a serial architecture, which is characterized by high dexterity but limited dynamics.

Marchesini Group S.p.a. proposed the development of a bin-picking cell for feeding an automated packaging machine with lightweight products taken from a pile with a productivity equal to 100pieces/min. The aim of this thesis is to develop the manipulator to be used in the aforementioned bin-picking cell.

Based on the constraints related to the coexistence of the robot with the vision system and the fast movements that the manipulator must perform to satisfy the required productivity, an overconstrained Cable-Driven Parallel Robot (CDPR) is proposed. The small footprint of the manipulator in the pick-up area facilitates the task of the vision system, and its parallel architecture in an overconstrained configuration guarantees high dynamic capabilities. The proposed CDPR has a configuration with 8 cables and 6 degrees of freedom, and it is called *CORHDA*: *Cable-driven Overconstrained Robot for Highly Dynamical Applications*.

The kinematic and dynamic models used to describe the manipulator are taken from the literature, whereas the conceptual and mechanical design of the robot prototype is carried out based on an example application.

For an overconstrained CDPR to operate effectively, it is necessary to guarantee that all the cables remain taut through forces bounded between given thresholds. The literature analyzes this problem well, but currently available control techniques involve force sensors. This thesis suggests a new approach based on modifying a previously developed hybrid control strategy without directly measuring cable forces (HC-*e* controller). The controller is introduced from a conceptual point of view, and then it is implemented on the IPAnema 3 Mini CDPR. On this robot, the HC-*e* controller is assessed for slow movements and compared to other control methods. It gives optimal results compared to a pure inverse kinematic controller (which does not use force sensors) and similar results to those obtained with other controllers based on force sensors. The HC-*e* controller is then implemented on the CORHDA. The outcomes are still good, demonstrating its applicability even for the high dynamics required by fast bin-picking tasks.

The performance of the CORHDA prototype is evaluated in terms of force tracking, positioning accuracy, and dynamic capabilities. In particular, movements up to 8.8m/s and 255m/s^2 of velocity and acceleration prove to be feasible, with cables always remaining taut. The robot is not yet sufficiently accurate for executing the bin-picking task, but it is highly repeatable. Accordingly, it is assumed that a future calibration of the robot geometric parameters will increase its positioning precision.

Contents

Chapter 1

Introduction

In automatic machines for packaging, it is often necessary to move products from one place (e.g., a conveyor belt) to another (e.g., a filling station). This operation, called "pick-and-place," is widely executed by robots in completely automated lines. When high productivity is required, the pick-and-place tasks assigned to the manipulator are simple since the products are treated before they arrive in the robot pick-up area, so they are already spread on a planar conveyor belt [1,2]. In this case, a 2D vision system recognizes the product position and rotation about the gravity axis, and it gives this information to the manipulator, which brings the object to its new location by performing a 3D translation of the end-effector (EE) and, optionally, a rotation about the vertical axis [3,4] (Fig. 1.1(a)). The drawback of this method is the necessity of rearranging products before the robot pick-up area, which leads to adding complex and bulky parts to the automatic packaging line [5].

For this reason, it may be desirable to execute the pick-and-place operation by directly taking products from a pile (usually contained in a box). This operation, called *3D-picking* or *bin-picking*, is more complex than the previous one because products could have any orientation and position in a pile, and both the task of the vision system and the robot become harder. In particular, the vision system must recognize the position in three dimensions (not only in the plane) and the complete orientation of the product. At the same time, the robot movement must involve all six Degrees of Freedom (DOFs) to guarantee the rearrangement of the product in the correct position and orientation in the place area. These factors usually determine the usage of robotic serial arms to perform *bin-picking* [6–8]. However, these devices allow productivity between $30 \div 40 pieces/min$, which is very low for the packaging industry (Fig. 1.1(b)).

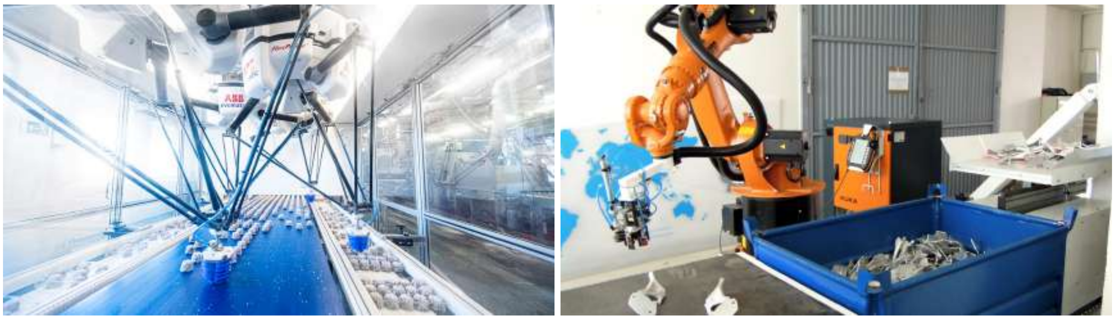
(a) (b)

Figure 1.1: A classical 2D pick-and-place operation (a) and a bin-picking one (b).

This work is based on an issue proposed by Marchesini Group S.p.a., which aims to design a robot to execute highly dynamical *3D-picking* applications. In particular, the target is to feed an automatic packaging machine by picking lightweight products from a pile with productivity equal to $100 pieces/min$.

1.1 The bin-picking task

During the design of a bin-picking cell, all the elements involved in the process must be considered by taking into account their interaction: the robot, the vision system, and the gripper [9]. Even if it will not be analyzed in this work, the vision system is a crucial part of the cell. Systems for object identification have been widely used in the industrial field for decades, and an interesting comparative study on object recognition algorithms for robot vision in 2D and 3D environments was already presented in 1986 [10]. Even many years later, the main problems connected to the robot vision remain the same, due to the following requirements:

- speed of acquiring and analyzing an image;
- accuracy in determining the positions and orientations of the objects;
- the flexibility of the vision system to work with different objects.

It is difficult to guarantee good flexibility with a cost-effective robot vision system, especially for 3D object recognition. However, flexibility is not the main requirement for the application at hand (i.e., feeding of an automatic packaging machine): once the object treated by the machine is defined, it is always the same until a format change is scheduled. On the contrary, both the speed of the image acquisition and processing and the accuracy of these procedures are fundamental to guarantee the reliable functioning of the bin-picking cell by satisfying the real-time requirements of the robot task. Many studies have been conducted in the last years on this topic [11–15], and this point is even more critical for integrating a bin-picking cell in the packaging industry environment. It is common for computer-vision algorithms to work with a 3D model of the treated object to create a database that will be used during the object identification [14, 16–19]. The object recognition task becomes more complex when the products are partially occluded [20, 21] or when they are wrapped with plastic (or similar materials) which make them bodies with non-Lambertian reflectance [22].

Problems not directly related to the vision system are also involved in the bin-picking task. Even if an object is correctly detected, it is crucial to find the best grasping strategy to take it [23–25] and to choose the appropriate gripper for the execution of the task [24, 26–31]. These issues become even more demanding when different objects are treated during the same bin-picking operation [32]. Finally, when the robot gripper has taken the object, it is not straightforward to compute a suitable trajectory to move it since the motion law executed by the manipulator must take into account the gripper, the grasping strategy, other bodies eventually present in the workspace and the overall architecture of the robot [33, 34].

1.2 Choice of the robot architecture

The crucial aspect to be considered in the choice of the robot architecture is the high dynamics required. In particular, by considering a productivity equal to $100 pieces/min$, the time for the execution of every cycle (i.e., a complete pick-and-place including the return to the pick-up area) is equal to $0.6s$. This short time available brings to the following constraints.

- If we assumed to mount the vision system on the EE [7,8], we would have to stop the robot to acquire the image of the pick-up area at every cycle by reducing the time for the movement of the manipulator, which is already very short. This is impossible, so the vision system must be mounted on a fixed point of the robot frame above the pick-up area. The image acquisition must be executed when the robot EE is in the operation area but when the robot itself does not occlude the view of the vision system. Then, the image processing for the object identification task must be executed during the robot movement.
- The robot must have a parallel architecture to perform the required motion dynamics [35–37]. Parallel manipulators have higher intrinsic stiffness than robots with a serial architecture. This allows them to be lighter than their serial counterparts by still reaching high performances in terms of precision. This is due to the geometry of parallel manipulators since they are made of several kinematic chains (the "legs" of the robot) composed of links and joints that connect the EE to the fixed base. In contrast, serial robots comprise one open kinematic chain between the fixed base and the EE 1.2. For this reason, parallel robots [3,4] are widely used for highly dynamical movements due to the lower inertia forces that arise from their lighter links (compared to the ones of serial robots). This makes them particularly suitable for the packaging industry, where very fast motions are required.

Using a parallel manipulator in a bin-picking cell with a fixed vision system on the frame introduces a new problem: the view of the products pile can be partially occluded by the robot legs, making it impossible to detect the objects correctly. To overcome this problem, in the project developed in this Thesis we decided to use a Cable-Driven Parallel Robot (CDPR), namely a parallel manipulator in which wires replace

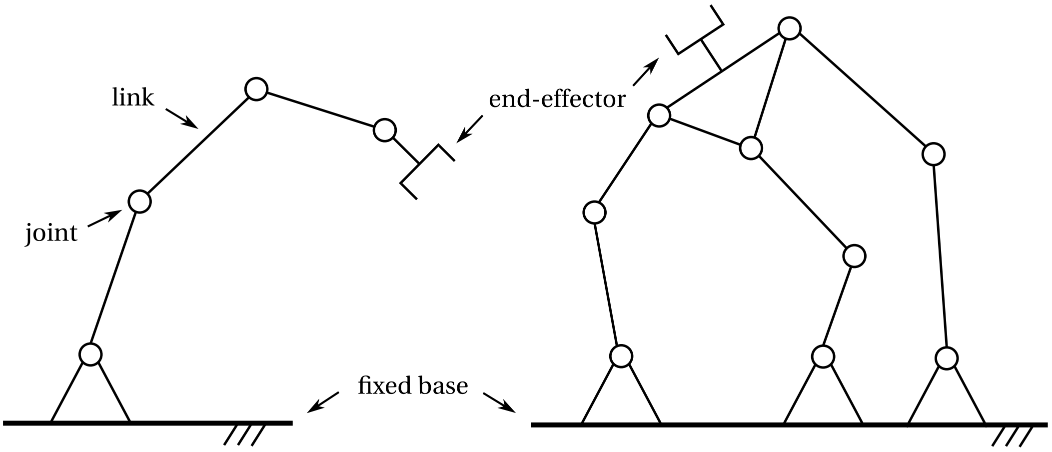

Figure 1.2: Scheme of robots with serial (left) and parallel (right) architecture [38].

the rigid links of the legs [39]. Using cables gives CDPRs a bigger workspace and lower moving masses than other robots; moreover, it is easy to design manipulators with simple reconfigurability. Another advantage is the mechanical simplicity of the robot actuation system, which usually consists of a drum connected to a motor (eventually through a gear) on which the cable is coiled, thus forming a winch. For the application at hand, the main advantage of using cables is that they can guarantee a small footprint in the pick-up area, minimizing the occlusion of the vision system on the product pile.

1.3 CDPR classification

CDPRs were introduced in the '80 [41, 42], and in the last decades, they have been studied in many fields of application, even if many open issues about their functioning still exist [43]. CDPRs with different aims can have different characteristics and be classified according to several criteria. The most common classification is the one introduced by Ming and Higuchi in [44]. Considering a generic robot with an EE capable of n DOFs and actuated through m cables, the *degree of redundancy* is defined as $r = m - n$. From here, one can divide the CDPRs into three categories:

- incompletely restrained CDPRs, with $m \leq n$ ($r \leq 0$);
- completely restrained CDPRs, with $m = n + 1$ ($r = 1$);
- redundantly restrained CDPRs, with $m > n + 1$ ($r > 1$).

However, this classification may be misleading, and it must be modified to make it consistent with the classical mechanics theory [38]. Both completely restrained and redundantly restrained CDPRs are overconstrained mechanisms since their inverse dynamic problem admits infinite solutions. At the same time, robots with the same number of cables and DOFs in which all the wires are taut are defined as incompletely restrained, even if the pose of their EE is totally defined by the kinematic constraints imposed by the cables.

(a) (b)

Figure 1.3: Schemes of a suspended underactuated CDPR (a) and an overconstrained not suspended CDPR (b) [40].

A new classification based on the number of instantaneously taut cables was introduced in [45] to overcome these discrepancies:

- overconstrained CDPRs, when $m > n$ ($r > 0$) and all cables are taut;
- fully-constrained CDPRs, when $m = n$ ($r = 0$) and all cables are taut;
- underconstrained CDPRs, when $m < n$ ($r < 0$) or $m \geq n$ ($r \geq 0$), but the taut cables are less than n.

This classification allows one to consider the situation in which not all the cables are taut, but this is not the working condition for which a generic robot is commonly designed. For this reason, by neglecting the situation in which only some cables are taut, the main advantage of underconstrained CDPRs with $m < n$ cables is that they need fewer motors than other classes of CDPRs to execute a task. However, the main disadvantage of this robot class is that the inverse kinematic and static problems are not decoupled, so they must be solved together. Indeed, only some of the DOFs of the robot EE can be controlled and the feasibility of a planned motion also depends on the external wrench applied to the EE.

Another classification of CDPRs considers the position of the cable attachment points on the frame. If all these points are above the workspace of the manipulator, the robot is in a *suspended* configuration (or *crane* configuration). This classification is completely independent of the previous one, so every kind of CDPR previously defined can be suspended. However, it is common for suspended CDPRs to be underactuated or fully-constrained. This is because, in the suspended configuration, there is always the action of the gravity force that acts on the EE to help to keep the cables taut. However, for applications in which other external wrenches arise on the platform, it is necessary to guarantee that cable tensioning is not only due to the gravity action. This is why overconstrained CDPRs (with at least one redundant cable) in a non-suspended configuration are commonly chosen for tasks that require the execution of fast movements or interaction with the environment. Indeed, controlling cables that arrive on the EE from different directions spread in the space makes it possible to counterbalance a wide range of external wrenches that can arise on the platform 1.3.

From the previous considerations, an overconstrained CDPR in a non-suspended configuration will be necessary to execute the bin-picking task since highly dynamic movements and capability of interaction with the products are required. The robot will be called *CORHDA*: *Cable-driven Overconstrained Robot for Highly Dynamical Applications*. The name of the manipulator identifies the robot architecture and it reflects the most important constraint that was taken into account during its design: the capability of executing fast movements such that it will be possible to satisfy the productivity required for the fast bin-picking task.

1.4 CDPR applications

One of the most important industrial applications of CDPRs is in the field of moving cameras [51]. Different companies produce robots with the same aim of filming sports events (e.g., football matches) or music venues. Examples are the SkyCam [52, 53], the SpiderCam [46] (Fig. 1.4(a)), and the CableCam [54]. All these cameras are suspended

(a) The SpiderCam [46] (b) A Portable CDPR for rescue operations [47]

(c) The FAST CDPR [48]

(d) The CoGiRo CDPR [49] (e) The NeReBot CDPR [50]

Figure 1.4: Suspended CDPRs for different applications.

underconstrained CDPRs, usually mounted on stadiums, and can provide aerial perspectives of the event they are filming. Using an overconstrained CDPR with cables coming from the ground would be impossible for this kind of application. The same is for CDPRs studied for rescue operations [47, 55] which should be portable and modular (Fig. 1.4(b)): they must be reconfigured by simply moving their winches, which are installed in unstructured environments. Another interesting application of a suspended CDPR is in Guizhou province, in China, where a fully-constrained robot was designed to realize a radio telescope [48, 56] (Fig. 1.4(c)). More common is finding suspended CDPRs (underconstrained or fully-constrained) for load-lifting applications: one of the first was the Nist Spider [57], a robotic fully-constrained crane; a more recent example is an underconstrained CDPR for boat lifting in open-sea operations [58]. The advantage of using a cable robot instead of a simple crane is the better control of the carried load. However, for the manipulation of heavy payloads, also overconstrained CDPRs (still in a suspended configuration) have been developed [49] (Fig. 1.4(d)).

For rehabilitation tasks, CDPRs are widely used, but the choice of the robot architecture can be different based on its specific tasks. However, also for a predefined task, the choice may not be trivial [63]. Examples of CDPRs used for rehabilitation can be found in [50, 64, 65] (suspended robot with three cables) (Fig. 1.4(e)), [66, 67] (spatial overconstrained CDPR), and [68] (planar overconstrained robot).

(a) The Hephaestus CDPR [59]

(b) A CDPR for warehousing operations [60]

(c) The Kite Robot for window cleaning [61]

(d) The CableRobot simulator [62]

Figure 1.5: Overconstrained non-suspended CDPRs for different applications.

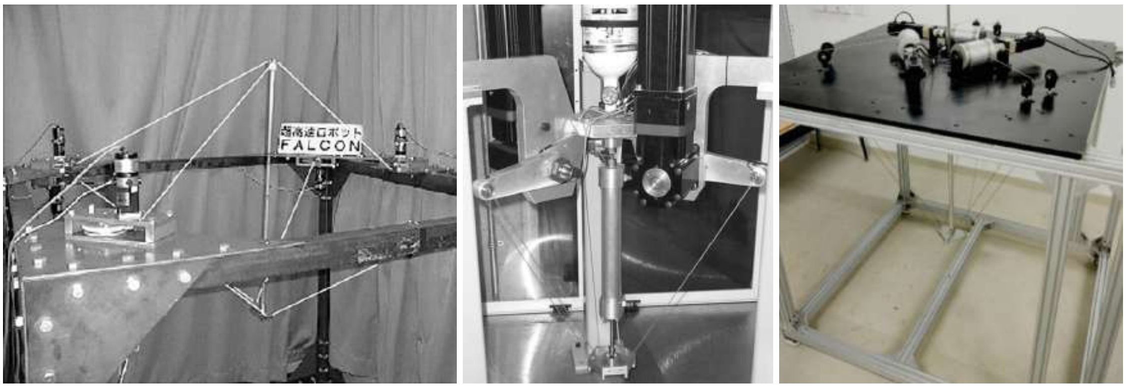

(a) The FALCON-7 CDPR [78, 79] (b) The DeltaBot CDPR [81] (c) The T-Bot CDPR [82, 83]

Figure 1.6: CDPRs developed for fast object manipulation tasks.

As mentioned in Section 1.3, using non-suspended overconstrained CDPRs for tasks requiring interaction with the environment is common. This happens for the construction of buildings [69] or operations on their facades [59, 70, 71] (Fig. 1.5(a)). Similar Robots are also designed for the execution of warehousing operations [60, 72–74] (Fig. 1.5(b)) or for window cleaning [75]. For this last task, the robot movements are in two dimensions, so also planar CDPRs actuated with four cables have been proposed in the literature [76] and by companies [61] (Fig. 1.5(c)). For the same reason, in [77], a planar overconstrained robot is designed to perform laser engraving. Another interesting use of an overconstrained CDPR is the one shown in [62], where the large workspace and high stiffness of a manipulator with eight cables are exploited for the realization of a simulator developed for studies in the field of human perception research and virtual reality (Fig. 1.5(d)).

Finally, overconstrained CDPRs for executing fast object manipulation have also been proposed. One of the most famous prototypes is the FALCON-7 [78, 79], which is actuated by seven cables (Fig. 1.6(a)). Instead, the WARP manipulator is actuated by eight cables and was designed without pulleys to solve the friction problems of the FALCON-7. However, the workspace of the WARP is too small, while the one of the FALCON-7 is not symmetric. For this reason, it is common to design robots with eight cables having attachment points on the frame approximately on the vertices of a parallelepiped [80]. Other robots were designed with fewer cables and in a suspended configuration for classical pick-and-place operations. An example is the DeltaBot introduced in [81] (Fig. 1.6(b)). These robot cables are taut through a central element pushing the EE. The same concept was applied in [82, 83] to develop the T-Bot(Fig. 1.6(c)). These robots have a shape that resembles the Delta robots [3], and they show excellent performances in the execution of classical pick-and-place tasks. However, they are unsuitable for a bin-picking operation since they are incapable of rotational movements (and the central pushing element may hinder the vision-system visibility).

1.5 Thesis Goals and Outline

This thesis aims to develop an overconstrained CDPR capable of executing fast 3D-picking operations by cooperating with a vision system in a bin-picking cell. This kind of architecture is justified by the need for a small footprint of the manipulator on the pick-up area (to facilitate the task of the vision system), together with the advantages of parallel robots for executing movements with high dynamics. The main objective is to develop the robot from a conceptual point of view by defining its main characteristics in terms of kinematics, mechanical design, and control strategies by taking into account its future application. The final result is to validate the concept by realizing and testing the first robot prototype, called *CORHDA*: *Cable-driven Overconstrained Robot for Highly Dynamical Applications*.

Chapter 2 describes the CORHDA kinematic and dynamic models, as well as the model describing the cable elastic behavior. Since the robot has an overconstrained architecture, an algorithm is presented to compute the optimal cable-force distribution for a generic end-effector pose.

Chapter 3 introduces the controller developed to govern the end-effector pose and cable tensions. This is the main innovative contribution of the thesis, since the controller is based on the idea of applying a hybrid position-force control strategy without using any force sensor. The controller is first implemented and evaluated on the IPAnema 3 Mini CDPR of the Fraunhofer Institute for Manufacturing Engineering and Automation (IPA) in Stuttgart and then applied to the CORHDA

Chapter 4 presents the conceptual design of the CORHDA prototype, by taking into account the constraints imposed by the bin-picking task and the control strategy introduced in Chapter 3. The mechanical design of the robot is described, including its actuators, the end-effector, and the other elements in the kinematic chains.

Chapter 5 reports the experimental validation of the controller on the IPAnema 3 Mini and the CORHDA. The CORHDA-prototype performance in terms of pose precision and repeatability, as well as in cable-force tracking, paves the way for its future practical use.

Chapter 6 draws conclusions and describes future developments

Chapter 2

Modeling

This chapter aims to introduce the mathematical models used to describe the behavior of the robot CORHDA. For the aim of this work, the cables are considered massless, so straight linear segments can represent them, and their elasticity will be considered.

As explained in Chapter 1, to perform the bin-picking operation, an overconstrained CDPR is necessary. Moreover, the EE must be capable of moving in all the six DOFs of the spatial Euclidean motion group $SE(3)$. In practice, the manipulator is made by a rigid body (the EE) moved in the space by $m \geq 7$ cables. Using only seven wires reduces the number of motors, but in this way, the workspace of the manipulator is not symmetric [79]. For this reason, a design with eight cables will be developed. However, this chapter treats the mathematical modeling of overconstrained CDPRs as generally as possible.

2.1 Kinematic model

The pose of a rigid body is defined by six coordinates in $SE(3)$: three distances to identify its position and three angles to represent its orientation. A reference system fixed with the robot frame is necessary to define these coordinates ($O - xyz$). In the following, we will refer to this reference system by simply calling it FRS (*Fixed Reference System*). Similarly, we can define another reference system connected to the EE ($O' - x'y'z'$) and refer to it as MRS (*Mobile Reference System*). The motion of the EE is defined as the movement of the MRS with reference to the FRS. The position of the EE is described by the vector $\mathbf{p}$ that points from O to O' in the FRS. The orientation of the EE is defined through Euler angles, i.e., three successive rotations about axes of the FRS, respectively ϵ_x, ϵ_y, and ϵ_z, which are collected in the array $\boldsymbol{\epsilon} = [\epsilon_x, \epsilon_y, \epsilon_z]^T$ [84]. The Euler angles allow the computation of the rotation matrix $\mathbf{R} = \mathbf{R}(\boldsymbol{\epsilon})$. This matrix transforms the coordinates of a position vector from the MRS to the FRS. In this work, a prime is used to distinguish the vectors expressed in the coordinates of the MRS from those in the coordinates of the FRS.

The finite kinematics involves only the position and orientation of the EE, while for the differential kinematics, it is necessary to also consider the time derivatives of the position ($\dot{\mathbf{p}}$, $\ddot{\mathbf{p}}$) and orientation ($\dot{\boldsymbol{\epsilon}}$, $\ddot{\boldsymbol{\epsilon}}$) of the EE. In particular, from the rate of change of Euler angles, one can compute the angular velocity ($\boldsymbol{\omega}$) and acceleration ($\dot{\boldsymbol{\omega}}$) of the EE.

$$\boldsymbol{\omega} = \mathbf{H}(\boldsymbol{\epsilon})\dot{\boldsymbol{\epsilon}} = \begin{bmatrix} 1 & 0 & \sin(\epsilon_y) \\ 0 & \cos(\epsilon_x) & -\sin(\epsilon_x)\cos(\epsilon_y) \\ 0 & \sin(\epsilon_x) & \cos(\epsilon_x)\cos(\epsilon_y) \end{bmatrix} \dot{\boldsymbol{\epsilon}} \tag{2.1}$$

$$\dot{\boldsymbol{\omega}} = \mathbf{H}(\boldsymbol{\epsilon})\ddot{\boldsymbol{\epsilon}} + \dot{\mathbf{H}}(\boldsymbol{\epsilon},\dot{\boldsymbol{\epsilon}})\dot{\boldsymbol{\epsilon}} \tag{2.2}$$

2.1.1 Finite kinematics

For a robot with m cables, by considering the generic wire $i = 1\dots m$, the cable exit point from the robot frame is A_i (*proximal* anchor point), while the attachment point on the EE is B_i (*distal* anchor point). The vector representing the position of A_i in FRS is $\mathbf{a}_i$, while the vector representing the position of B_i in MRS is $\mathbf{b}'_i$ (its projection in FRS is $\mathbf{b}_i$).

The simplest kinematic model of a CDPR is based on the assumption that both $\mathbf{a}_i$ and $\mathbf{b}'_i$ do not change in time, i.e., all the distal and proximal anchor points are fixed. In many practical cases, this is true for the distal anchor points but not for the proximal anchor points. In fact, it is common to mount swivel pulleys on the robot frame to guide the cable toward the EE. This is done to avoid the cables slipping on fixed surfaces, which can cause their wear and damage. In this case, the presence of pulleys must be considered in the kinematic model. Since the swivel axis is tangent to the pulley in $A_{0,i}$, the vector $\mathbf{a}_{0,i}$ is constant during the movement of the EE (Figure 2.1). The proximal anchor point A_i is where the cable leaves the pulley in a direction tangent to it. The vector from the center of the swivel pulley $A_{C,i}$ to A_i is $\mathbf{a}_{t,i}$, whereas the vecor from $A_{0,i}$ to $A_{C,i}$ is $\mathbf{a}_{C,i}$. Both $\mathbf{a}_{t,i}$ and $\mathbf{a}_{C,i}$ change during the EE motion, but their magnitude is constant and equal to the pulley radius (r_i).

From these considerations, one can obtain the closure equation for the i-th cable:

$$\boldsymbol{\rho}_i = \mathbf{a}_{0,i} + \mathbf{a}_{C,i} + \mathbf{a}_{t,i} - \mathbf{R}\mathbf{b}'_i - \mathbf{p} \tag{2.3}$$

where $\boldsymbol{\rho}_i$ is the vector representing the i-th wire. Following the procedure described in [40,85], it is possible to find $\mathbf{a}_{t,i}$ and $\mathbf{a}_{C,i}$ in coordinates of a reference system connected to the swivel pulley, whose unit vectors corresponding to x, y, and z axes are $\mathbf{i}_{p,i}$, $\mathbf{j}_{p,i}$,

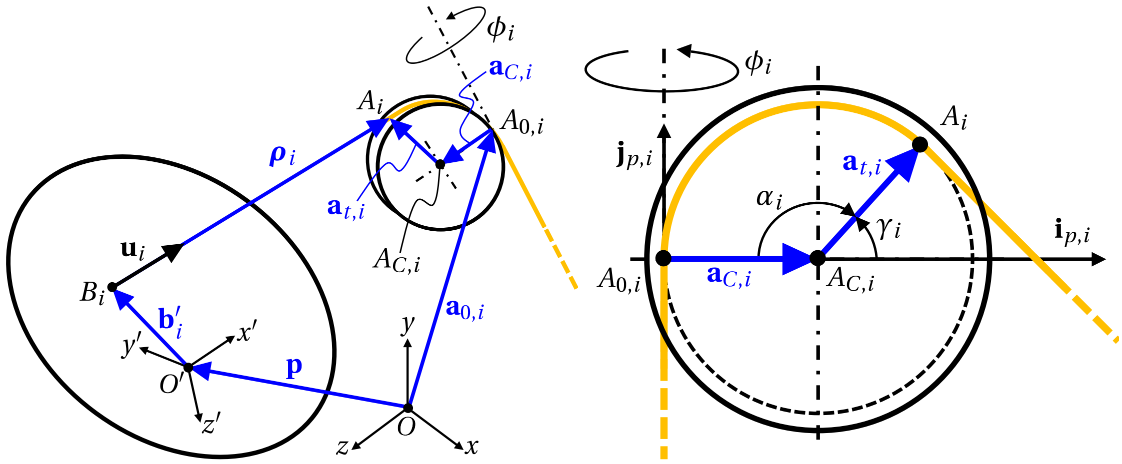

(a) (b)

Figure 2.1: Swivel-pulley kinematics.

and $\mathbf{k}_{p,i}$:

$$\begin{aligned} \mathbf{a}_{C,i} &= r_i \mathbf{i}_{p,i} \\ \mathbf{a}_{t,i} &= r_i \left[\cos(\gamma_i)\mathbf{i}_{p,i} + \sin(\gamma_i)\mathbf{j}_{p,i}\right] \end{aligned} \tag{2.4}$$

Where the angle γ_i is the supplementary to the wrapping angle α_i. The simplified cable vector is the one that does not consider the swivel pulley, i.e., it points to $A_{0,i}$:

$$\boldsymbol{\rho}_{0,i} = \mathbf{a}_{0,i} - \mathbf{p} - \mathbf{R}\mathbf{b}'_i \tag{2.5}$$

By introducing (2.4) and (2.5) in (2.3), the closure equation becomes:

$$\boldsymbol{\rho}_i = \boldsymbol{\rho}_{0,i} + r_i \mathbf{i}_{p,i} + r_i \left[\cos(\gamma_i)\mathbf{i}_{p,i} + \sin(\gamma_i)\mathbf{j}_{p,i}\right] \tag{2.6}$$

One can compute the magnitude of the cable vector $\boldsymbol{\rho}_i$ by using the expression of the unit vector $\mathbf{u}_i$ that represents the wire direction. $\mathbf{u}_i$ is found through the help of Figure 2.2:

$$\mathbf{u}_i = -\sin(\gamma_i)\mathbf{i}_{p,i} + \cos(\gamma_i)\mathbf{j}_{p,i} \tag{2.7}$$

By taking the scalar product of Eqs. (2.6), and (2.7), one obtains the following:

$$||\boldsymbol{\rho}_i|| = \boldsymbol{\rho}_{0,i} \cdot \left[-\sin(\gamma_i)\mathbf{i}_{p,i} + \cos(\gamma_i)\mathbf{j}_{p,i}\right] - r_i \sin(\gamma_i) \tag{2.8}$$

The value of γ_i is computed with the procedure described in [40, 85]. First, the scalar product of both sides of Eq. (2.6) with a unit vector directed as $\mathbf{a}_{t,i}$ is taken. Since the cable is tangent to the pulley in A_i, $\boldsymbol{\rho}_i$ is perpendicular to $\mathbf{a}_{t,i}$, thus obtaining the following result:

$$\boldsymbol{\rho}_{0,i} \cdot \left[\cos(\gamma_i)\mathbf{i}_{p,i} + \sin(\gamma_i)\mathbf{j}_{p,i}\right] + r_i \cos(\gamma_i) + r_i = 0 \tag{2.9}$$

By collecting the sine and cosine of γ_i, the equation becomes:

$$\cos(\gamma_i)\left(\boldsymbol{\rho}_{0,i} \cdot \mathbf{i}_{p,i} + r_i\right) + \sin(\gamma_i)\left(\boldsymbol{\rho}_{0,i} \cdot \mathbf{j}_{p,i}\right) + r_i = 0 \tag{2.10}$$

$\sin(\gamma_i)$ and $\cos(\gamma_i)$ can be expressed as functions of $t_i = \tan(\gamma_i/2)$:

$$\sin(\gamma_i) = \frac{2t_i}{1+t_i^2} \qquad \cos(\gamma_i) = \frac{1-t_i^2}{1+t_i^2} \tag{2.11}$$

By using the parametric formulation (2.11) of $\sin(\gamma_i)$ and $\cos(\gamma_i)$ in Eq. (2.10), we have:

$$(1-t_i^2)\left(\boldsymbol{\rho}_{0,i} \cdot \mathbf{i}_{p,i} + r_i\right) + 2t_i\left(\boldsymbol{\rho}_{0,i} \cdot \mathbf{j}_{p,i}\right) + r_i(1+t_i^2) = 0 \tag{2.12}$$

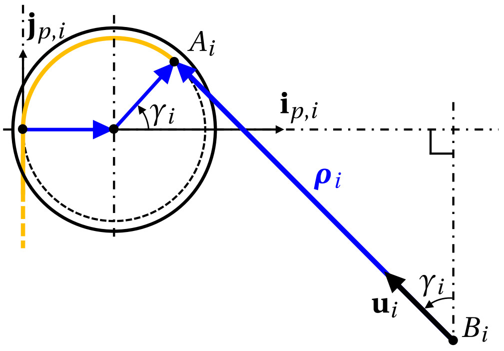

Figure 2.2: Swivel pulley plane.

By simply rearranging the terms, the following second-order equation in t_i is obtained:

$$t_i^2 - 2t_i \frac{\boldsymbol{\rho}_{0,i} \cdot \mathbf{j}_{p,i}}{\boldsymbol{\rho}_{0,i} \cdot \mathbf{i}_{p,i}} - \frac{2r_i}{\boldsymbol{\rho}_{0,i} \cdot \mathbf{i}_{p,i}} - 1 = 0 \tag{2.13}$$

Based on the instructions given in [40, 85], only one of the two solutions of Eq. (2.13) is acceptable, thus the value of γ_i can be directly computed:

$$\gamma_i = 2 \text{ atan} \left[\frac{\boldsymbol{\rho}_{0,i} \cdot \mathbf{j}_{p,i}}{\boldsymbol{\rho}_{0,i} \cdot \mathbf{i}_{p,i}} + \sqrt{\left(\frac{\boldsymbol{\rho}_{0,i} \cdot \mathbf{j}_{p,i}}{\boldsymbol{\rho}_{0,i} \cdot \mathbf{i}_{p,i}} \right)^2 + 1 + \frac{2r_i}{\boldsymbol{\rho}_{0,i} \cdot \mathbf{i}_{p,i}}} \right] \tag{2.14}$$

By substituting Eqs. (2.5) and (2.14) in Eq. (2.6) and recalling that $\alpha_i = \pi - \gamma_i$, one can express the geometrical constraint imposed by the i-th cable connected to the EE as a function of the EE pose and swivel pulley radius:

$$\boldsymbol{\rho}_i \cdot \boldsymbol{\rho}_i - (l_i - r_i \alpha_i)^2 = 0 \tag{2.15}$$

where l_i is the overall cable length, including both the rectilinear part (i.e., $||\boldsymbol{\rho}_i||$) and the arc of the swivel pulley between $A_{0,i}$ and A_i (i.e., angle α_i).

2.1.2 Differential kinematics

This paragraph introduces the kinematic equations describing the relations between the EE velocity and acceleration ($\mathbf{v}$, $\dot{\mathbf{v}}$) and the cable elongation velocities and accelerations ($\dot{\mathbf{l}}$, $\ddot{\mathbf{l}}$) for a CDPR with swivel pulleys. The EE velocity is represented in matrix notation by the vector $\mathbf{v} = [\dot{\mathbf{p}}^T \ \boldsymbol{\omega}^T]^T$, while the array containing the cable elongation velocities is $\dot{\mathbf{l}} = [\dot{l}_1 \ \dots \ \dot{l}_m]^T$.

The differential kinematics of a CDPR can be obtained by computing the derivatives of the closure equations (2.15) with respect to the time. Before doing it, for the kinematic model of a CDPR with swivel pulleys, it is necessary to define the differential kinematics of the swivel pulleys.

2.1.2.1 Differential kinematics of the swivel pulley

For the i-th generic swivel pulley, one can define a reference system whose unit vectors corresponding to x, y, and z axes are $\mathbf{i}_{fp,i}$, $\mathbf{j}_{fp,i}$, and $\mathbf{k}_{fp,i}$. This coordinates system indicates how the pulley is mounted with reference to the frame: the mounting orientation of the pulley is defined through the rotation matrix $\mathbf{R}_{pul,i}$. The only difference between the fixed reference system of the pulley and the mobile one (with unit vectors $\mathbf{i}_{p,i}$, $\mathbf{j}_{p,i}$, and $\mathbf{k}_{p,i}$), is the rotation around the swivel axis (i.e., angle ϕ_i) that changes during the EE motion. With reference to Figure 2.3, for a generic pose of the EE, the unit vectors of the mobile system of the swivel pulley can be expressed in coordinates of the fixed one as follows:

$$\begin{aligned} \mathbf{i}_{p,i} &= \cos(\phi_i)\mathbf{i}_{fp,i} - \sin(\phi_i)\mathbf{k}_{fp,i} \\ \mathbf{j}_{p,i} &= \mathbf{j}_{fp,i} \\ \mathbf{k}_{p,i} &= \sin(\phi_i)\mathbf{i}_{fp,i} + \cos(\phi_i)\mathbf{k}_{fp,i} \end{aligned} \tag{2.16}$$

The time derivatives of these unit vectors are:

$$\begin{aligned} \dot{\mathbf{i}}_{p,i} &= -\sin(\phi_i)\dot{\phi}_i\mathbf{i}_{fp,i} - \cos(\phi_i)\dot{\phi}_i\mathbf{k}_{fp,i} = -\dot{\phi}_i\mathbf{k}_{p,i} \\ \dot{\mathbf{j}}_{p,i} &= 0 \\ \dot{\mathbf{k}}_{p,i} &= \cos(\phi_i)\dot{\phi}_i\mathbf{i}_{fp,i} - \sin(\phi_i)\dot{\phi}_i\mathbf{k}_{fp,i} = \dot{\phi}_i\mathbf{i}_{p,i} \end{aligned} \tag{2.17}$$

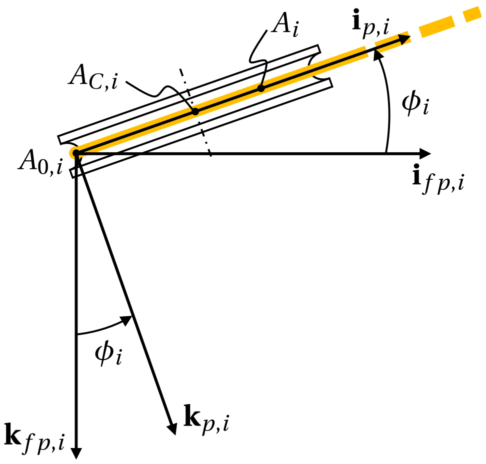

Figure 2.3: Top view of the swivel pulley.

To completely define the swivel pulley differential kinematics, we will also compute the rate of change of the swivel angle ϕ_i and the supplementary to the wrapping angle γ_i.

Since $\boldsymbol{\rho}_{0,i}$, and $\boldsymbol{\rho}_i$ are in the pulley plane, they are both perpendicular to $\mathbf{k}_{p,i}$, thus:

$$\boldsymbol{\rho}_{0,i} \cdot \mathbf{k}_{p,i} = 0 \qquad\qquad \boldsymbol{\rho}_i \cdot \mathbf{k}_{p,i} = 0 \tag{2.18}$$

By taking the time derivative of the scalar product between $\boldsymbol{\rho}_{0,i}$ and $\mathbf{k}_{p,i}$, the following equation is obtained:

$$\dot{\boldsymbol{\rho}}_{0,i} \cdot \mathbf{k}_{p,i} + \boldsymbol{\rho}_{0,i} \cdot \dot{\mathbf{k}}_{p,i} = 0 \tag{2.19}$$

By introducing Eq.(2.17) and the time derivative of Eq. (2.5) in Eq. (2.19) and rearranging the result, the time derivative of the swivel angle is obtained as:

$$\dot{\phi}_i = \frac{\mathbf{k}_{p,i} \cdot (\dot{\mathbf{p}} + \dot{\mathbf{b}}_i)}{\mathbf{i}_{p,i} \cdot \boldsymbol{\rho}_{0,i}} \tag{2.20}$$

The rate of change of the supplementary to the wrapping angle γ_i (see Figure 2.1(b)) is computed by taking the time derivative of Eq. (2.10):

$$\begin{aligned}-\sin(\gamma_i)\dot{\gamma}_i \left(\boldsymbol{\rho}_{0,i} \cdot \mathbf{i}_{p,i} + r_i\right) + \cos(\gamma_i) \left(\dot{\boldsymbol{\rho}}_{0,i} \cdot \mathbf{i}_{p,i} + \boldsymbol{\rho}_{0,i} \cdot \dot{\mathbf{i}}_{p,i}\right) + \\ + \cos(\gamma_i)\dot{\gamma}_i \left(\boldsymbol{\rho}_{0,i} \cdot \mathbf{j}_{p,i}\right) + \sin(\gamma_i) \left(\dot{\boldsymbol{\rho}}_{0,i} \cdot \mathbf{j}_{p,i}\right) = 0\end{aligned} \tag{2.21}$$

By using the expression of $\dot{\mathbf{i}}_{p,i}$ shown in (2.17) and collecting $\dot{\gamma}_i$, yields:

$$\begin{aligned}\dot{\gamma}_i \left\{-r_i \sin(\gamma_i) + \boldsymbol{\rho}_{0,i} \cdot \left[-\sin(\gamma_i)\mathbf{i}_{p,i} + \cos(\gamma_i)\mathbf{j}_{p,i}\right]\right\} + \\ + \dot{\boldsymbol{\rho}}_{0,i} \cdot \left[\cos(\gamma_i)\mathbf{i}_{p,i} + \sin(\gamma_i)\mathbf{j}_{p,i}\right] = 0\end{aligned} \tag{2.22}$$

If (2.8) is introduced in (2.22) one obtains:

$$\dot{\gamma}_i ||\boldsymbol{\rho}_i|| + \dot{\boldsymbol{\rho}}_{0,i} \cdot \left[\cos(\gamma_i)\mathbf{i}_{p,i} + \sin(\gamma_i)\mathbf{j}_{p,i}\right] = 0 \tag{2.23}$$

Finally, remembering the definition of $\boldsymbol{\rho}_{0,i}$ in Eq. (2.5), the time derivative of the supplementary to the wrapping angle is:

$$\dot{\gamma}_i = \frac{\left[\cos(\gamma_i)\mathbf{i}_{p,i} + \sin(\gamma_i)\mathbf{j}_{p,i}\right] \cdot (\dot{\mathbf{p}} + \dot{\mathbf{b}}_i)}{||\boldsymbol{\rho}_i||} \tag{2.24}$$

2.1.2.2 Velocity closure equations

Once the differential kinematics of the swivel pulleys is defined, the velocity closure equations of the CDPR are derived by taking the time derivative of Eq. (2.15). Before doing it, it is helpful to compute the rate of change of the vector representing the cable $\boldsymbol{\rho}_i$ from Eq. (2.6) by taking advantage of the definition of $\boldsymbol{\rho}_{0,i}$ in Eq. (2.5) and the results in Eq. (2.17):

$$\dot{\boldsymbol{\rho}}_i = -\dot{\mathbf{p}} - \dot{\mathbf{b}}_i - r_i\dot{\phi}_i\left[1+\cos(\gamma_i)\right]\mathbf{k}_{p,i} - r_i\dot{\gamma}_i\left[\sin(\gamma_i)\mathbf{i}_{p,i} - \cos(\gamma_i)\mathbf{j}_{p,i}\right] \tag{2.25}$$

Where the derivative $\dot{\mathbf{b}}_i$ of the vector representing the position of the distal anchor point in FRS is a function of the angular velocity of the EE [84]:

$$\dot{\mathbf{b}}_i = \dot{\mathbf{R}}\mathbf{b}'_i = \boldsymbol{\omega}\times\mathbf{R}\mathbf{b}'_i = \boldsymbol{\omega}\times\mathbf{b}_i \tag{2.26}$$

Once the previous preliminary computations are explained, it is possible to compute the time derivative of Eq. (2.15):

$$2\boldsymbol{\rho}_i\cdot\dot{\boldsymbol{\rho}}_i - 2(l_i - r_i\alpha_i)(\dot{l}_i - r_i\dot{\alpha}_i) = 0 \tag{2.27}$$

By substituting Eq. (2.25) in Eq. (2.27), one obtains:

$$\begin{aligned}-\boldsymbol{\rho}_i\cdot\dot{\mathbf{p}} - \boldsymbol{\rho}_i\cdot\dot{\mathbf{b}}_i - r_i\dot{\phi}_i\left[1+\cos(\gamma_i)\right]\boldsymbol{\rho}_i\cdot\mathbf{k}_{p,i} + r_i\dot{\gamma}_i\boldsymbol{\rho}_i\cdot\left[-\sin(\gamma_i)\mathbf{i}_{p,i} + \cos(\gamma_i)\mathbf{j}_{p,i}\right] + \\ -(l_i - r_i\alpha_i)(\dot{l}_i - r_i\dot{\alpha}_i) = 0\end{aligned} \tag{2.28}$$

Introducing Eqs. (2.18) and (2.7) in (2.28) yields:

$$-\boldsymbol{\rho}_i\cdot\dot{\mathbf{p}} - \boldsymbol{\rho}_i\cdot\dot{\mathbf{b}}_i + r_i\dot{\gamma}_i\boldsymbol{\rho}_i\cdot\mathbf{u}_i - (l_i - r_i\alpha_i)(\dot{l}_i - r_i\dot{\alpha}_i) = 0 \tag{2.29}$$

Since $\gamma_i = \pi - \alpha_i$, then $\dot{\gamma}_i = -\dot{\alpha}_i$. Moreover, $\boldsymbol{\rho}_i\cdot\mathbf{u}_i = ||\boldsymbol{\rho}_i|| = l_i - r_i\alpha_i$, so Eq. (2.29) is simplified as:

$$-\boldsymbol{\rho}_i\cdot\dot{\mathbf{p}} - \boldsymbol{\rho}_i\cdot\dot{\mathbf{b}}_i - (l_i - r_i\alpha_i)\dot{l}_i = 0 \tag{2.30}$$

By introducing (2.26) in (2.30) and exploiting the properties of vector and scalar product, one finally obtains:

$$-\boldsymbol{\rho}_i\cdot\dot{\mathbf{p}} + \boldsymbol{\rho}_i\times\mathbf{b}_i\cdot\boldsymbol{\omega} - (l_i - r_i\alpha_i)\dot{l}_i = 0 \tag{2.31}$$

By using a matrix notation, and remembering that $\mathbf{v} = [\dot{\mathbf{p}}^T\ \boldsymbol{\omega}^T]^T$, we have:

$$-\begin{bmatrix}\boldsymbol{\rho}_i^T & -(\boldsymbol{\rho}_i\times\mathbf{b}_i)^T\end{bmatrix}\mathbf{v} = (l_i - r_i\alpha_i) \tag{2.32}$$

Since $\boldsymbol{\rho}_i = (l_i - r_i\alpha_i)\mathbf{u}_i$, the term $(l_i - r_i\alpha_i)$ cancels out on both sides of Eq. (2.32), so that:

$$-\begin{bmatrix}\mathbf{u}_i^T & (\mathbf{b}_i\times\mathbf{u}_i)^T\end{bmatrix}\mathbf{v} = \dot{l}_i \tag{2.33}$$

By considering all cables $i = 1,\dots,m$, the kinematic Jacobian of the robot $\mathbf{J}_k$ can be used to find the final formulation of the velocity closure equations:

$$-\mathbf{J}_k\mathbf{v} = \dot{\mathbf{l}} \quad \text{with} \quad \mathbf{J}_k = \begin{bmatrix}\mathbf{u}_1^T & (\mathbf{b}_1\times\mathbf{u}_1)^T \\ \vdots & \vdots \\ \mathbf{u}_m^T & (\mathbf{b}_m\times\mathbf{u}_m)^T\end{bmatrix} \tag{2.34}$$

If the pose of the EE is known (i.e. the kinematic Jacobian of the robot $\mathbf{J}_k$ is completely defined), from Eq. (2.34), one can compute the cable elongation velocities (i.e. $\dot{\mathbf{l}}$) by knowing the EE velocity $\mathbf{v}$ or vice-versa.

2.1.2.3 Acceleration closure equations

The acceleration kinematics of a CDPR is described by the time derivative of Eq. (2.34):

$$-\dot{\mathbf{J}}_k \mathbf{v} - \mathbf{J}_k \dot{\mathbf{v}} = \ddot{\mathbf{l}} \tag{2.35}$$

where the i-th row of the time derivative $\dot{\mathbf{J}}_k$ is:

$$\dot{\mathbf{J}}_{k,i} = \begin{bmatrix} \dot{\mathbf{u}}_i^T & (\dot{\mathbf{b}}_i \times \mathbf{u}_i + \mathbf{b}_i \times \dot{\mathbf{u}}_i)^T \end{bmatrix} \tag{2.36}$$

The only unknown term in Eq. (2.36) is $\dot{\mathbf{u}}_i$, that can be found differentiating the equation representing the vector $\boldsymbol{\rho}_i$ as a function of the unit vector $\mathbf{u}_i$:

$$\dot{\boldsymbol{\rho}}_i = \frac{d}{dt}\left[(l_i - r_i\alpha_i)\mathbf{u}_i\right] = (\dot{l}_i - r_i\dot{\alpha}_i)\mathbf{u}_i + (l_i - r_i\alpha_i)\dot{\mathbf{u}}_i$$

which leads to:

$$\dot{\mathbf{u}}_i = \frac{\dot{\boldsymbol{\rho}}_i - (\dot{l}_i - r_i\dot{\alpha}_i)\mathbf{u}_i}{l_i - r_i\alpha_i} \tag{2.37}$$

where the time derivative of the wrapping angle is simply equal to $\dot{\alpha}_i = -\dot{\gamma}_i$, $\dot{\gamma}_i$ can be found by Eq. (2.24) and $\dot{\boldsymbol{\rho}}_i$ is provided by Eq. (2.25). Both $\dot{\gamma}_i$ and $\dot{\boldsymbol{\rho}}_i$ are completely defined if the swivel pulley kinematics is solved.

If the pose and the velocity of the EE are known (i.e. $\mathbf{J}_k$, $\dot{\mathbf{J}}_k$, and $\mathbf{v}$ are completely defined), from the acceleration closure equations in Eq. (2.35), one can compute the cable elongation accelerations (i.e. $\ddot{\mathbf{l}}$) by knowing the EE acceleration $\mathbf{a}$ or vice-versa.

2.2 Dynamic model

The dynamic model of a CDPR is developed by studying the equilibrium of the EE under the effect of the cable forces, the inertia wrench, and a generic external wrench $\mathbf{w}_E = [\mathbf{f}_E^T \ \boldsymbol{\tau}_E^T]^T$. $\mathbf{f}_E$ is the sum of the external forces acting on the EE and applied in its center of mass G, while $\boldsymbol{\tau}_E$ is the resultant external moment applied on the EE about G. If the center of MRS O' is chosen for the computation of the rotational equilibrium of the EE, the resultant moment about O' due to the external wrenches is $\boldsymbol{\tau}_E + \mathbf{d} \times \mathbf{f}_E$, where $\mathbf{d}$ is the vector connecting G with O' (see Figure 2.4).

The mass properties of the EE are represented by its mass m and its inertia matrix $\mathbf{I}'_G$ with reference to G and projected on MRS. Given a generic orientation $\mathbf{R}$ of the EE, the inertia matrix of the EE projected on FRS is $\mathbf{I}_G = \mathbf{R}\mathbf{I}'_G\mathbf{R}^T$. Knowing that the position vector of the center of mass of the EE is $\mathbf{p}_G$ (and thus the acceleration of G is $\ddot{\mathbf{p}}_G$), the inertia force acting on the EE is $-m\ddot{\mathbf{p}}_G$, while the inertia torque about G is $-\mathbf{I}_G\dot{\boldsymbol{\omega}} - \boldsymbol{\omega} \times \mathbf{I}_G\boldsymbol{\omega}$. Accordingly, the inertia moment about O' is $-\mathbf{I}_G\dot{\boldsymbol{\omega}} - \boldsymbol{\omega} \times \mathbf{I}_G\boldsymbol{\omega} - m\mathbf{d} \times \ddot{\mathbf{p}}_G$.

The D'Alambert equations that describe the dynamic equilibrium of the EE are the following:

$$\begin{cases} m\ddot{\mathbf{p}}_G - \mathbf{f}_E - \mathbf{f}_C = \mathbf{0} \\ \mathbf{I}_G\dot{\boldsymbol{\omega}} + \boldsymbol{\omega} \times \mathbf{I}_G\boldsymbol{\omega} + m\mathbf{d} \times \ddot{\mathbf{p}}_G - (\boldsymbol{\tau}_E + \mathbf{d} \times \mathbf{f}_E) - \boldsymbol{\tau}'_C = \mathbf{0} \end{cases} \tag{2.38}$$

where $\mathbf{f}_C$ is the sum of the cable forces, and $\boldsymbol{\tau}'_C$ is the sum of the moments produced by the cable forces about O'. The first equation represents the translational equilibrium of the EE, while the second one represents the rotational equilibrium about O' of the EE. The acceleration of G can be rewritten as a function of the acceleration of O':

$$\ddot{\mathbf{p}}_G = \ddot{\mathbf{p}} + \dot{\boldsymbol{\omega}} \times \mathbf{d} + \boldsymbol{\omega} \times (\boldsymbol{\omega} \times \mathbf{d}) \tag{2.39}$$

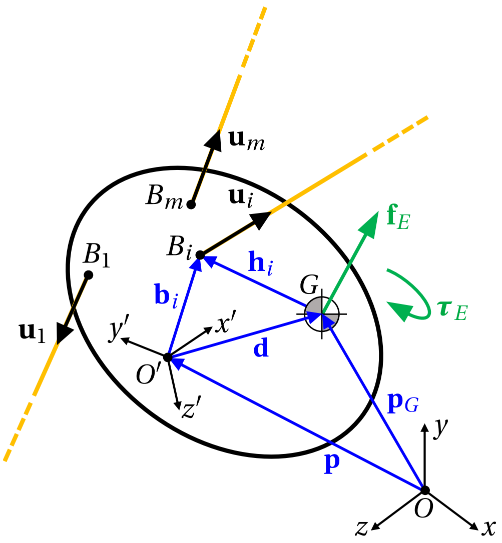

Figure 2.4: Scheme of the EE as a free rigid body.

By introducing Eq (2.39) in Eq. (2.38), and using the properties of the vector product the equilibrium equations can be written as:

$$\begin{cases} m\ddot{\mathbf{p}} - m\mathbf{d} \times \dot{\boldsymbol{\omega}} - m\boldsymbol{\omega} \times (\mathbf{d} \times \boldsymbol{\omega}) - \mathbf{f}_E - \mathbf{f}_C = \mathbf{0} \\ \mathbf{I}_G\dot{\boldsymbol{\omega}} - m\mathbf{d} \times (\mathbf{d} \times \dot{\boldsymbol{\omega}}) + m\mathbf{d} \times \ddot{\mathbf{p}} + \boldsymbol{\omega} \times [\mathbf{I}_G\boldsymbol{\omega} - m\mathbf{d} \times (\mathbf{d} \times \boldsymbol{\omega})] + \\ \qquad - (\boldsymbol{\tau}_E + \mathbf{d} \times \mathbf{f}_E) - \boldsymbol{\tau}_C = \mathbf{0} \end{cases} \tag{2.40}$$

or, by expressing the inertia matrix about G as a function of the inertia matrix about O' ($\mathbf{I}_G = \mathbf{I}_{O'} + m\tilde{\mathbf{d}}\tilde{\mathbf{d}}$), as:

$$\begin{cases} m\ddot{\mathbf{p}} - m\tilde{\mathbf{d}}\dot{\boldsymbol{\omega}} - m\tilde{\boldsymbol{\omega}}\tilde{\mathbf{d}}\boldsymbol{\omega} - \mathbf{f}_E - \mathbf{f}_C = \mathbf{0} \\ \mathbf{I}_{O'}\dot{\boldsymbol{\omega}} + m\tilde{\mathbf{d}}\ddot{\mathbf{p}} + \tilde{\boldsymbol{\omega}}\mathbf{I}_{O'}\boldsymbol{\omega} - \left(\boldsymbol{\tau}_E + \tilde{\mathbf{d}}\mathbf{f}_E\right) - \boldsymbol{\tau}_C = \mathbf{0} \end{cases} \tag{2.41}$$

where $(\tilde{\cdot})$ represents the matrix notation for the vector product [84]. The generic i-th cable force has magnitude f_i and is directed along $\mathbf{u}_i$, so that the sum of the cable forces is $\mathbf{f}_C = \sum_{i=1}^{m} f_i\mathbf{u}_i$, while the resultant moment of the cable forces about O' is $\boldsymbol{\tau}_C = \sum_{i=1}^{m} f_i\tilde{\mathbf{b}}_i\mathbf{u}_i$. By using a matrix notation Eq. (2.41) can be thus written as:

$$\begin{bmatrix} m\mathbf{I}_3 & -m\tilde{\mathbf{d}} \\ m\tilde{\mathbf{d}} & \mathbf{I}_{O'} \end{bmatrix} \begin{bmatrix} \ddot{\mathbf{p}} \\ \dot{\boldsymbol{\omega}} \end{bmatrix} + \begin{bmatrix} \mathbf{0}_3 & -m\tilde{\boldsymbol{\omega}}\tilde{\mathbf{d}} \\ \mathbf{0}_3 & \tilde{\boldsymbol{\omega}}\mathbf{I}_{O'} \end{bmatrix} \begin{bmatrix} \dot{\mathbf{p}} \\ \boldsymbol{\omega} \end{bmatrix} - \begin{bmatrix} \mathbf{f}_E \\ \boldsymbol{\tau}_E + \tilde{\mathbf{d}}\mathbf{f}_E \end{bmatrix} - \begin{bmatrix} \mathbf{u}_1 & \dots & \mathbf{u}_m \\ \tilde{\mathbf{b}}_1\mathbf{u}_1 & \dots & \tilde{\mathbf{b}}_m\mathbf{u}_m \end{bmatrix} \mathbf{f} = \mathbf{0} \tag{2.42}$$

where $\mathbf{f} = [f_1 \dots f_m]^T$ is the array containing the cable tensions, $\mathbf{I}_3$ is the 3×3 identity matrix, and $\mathbf{0}_3$ is the 3×3 null matrix. Finally, by remembering the expression of the kinematic jacobian in Eq. (2.34) and using a compact notation for all involved matrices, the equation representing the dynamic equilibrium of the EE about O' becomes:

$$\mathbf{M}'\dot{\mathbf{v}} + \mathbf{C}'\mathbf{v} - \mathbf{w}'_E - \mathbf{J}_k^T\mathbf{f} = \mathbf{0} \tag{2.43}$$

where:

$$\mathbf{M}' = \begin{bmatrix} m\mathbf{I}_3 & -m\tilde{\mathbf{d}} \\ m\tilde{\mathbf{d}} & \mathbf{I}_{O'} \end{bmatrix}, \; \mathbf{C}' = \begin{bmatrix} \mathbf{0}_3 & -m\tilde{\boldsymbol{\omega}}\tilde{\mathbf{d}} \\ \mathbf{0}_3 & \tilde{\boldsymbol{\omega}}\mathbf{I}_{O'} \end{bmatrix}$$
$$\mathbf{w}'_E = \begin{bmatrix} \mathbf{f}_E \\ \boldsymbol{\tau}_E + \tilde{\mathbf{d}}\mathbf{f}_E \end{bmatrix}, \qquad \mathbf{J}_k = \begin{bmatrix} \mathbf{u}_1^T & (\mathbf{b}_1 \times \mathbf{u}_1)^T \\ \vdots & \vdots \\ \mathbf{u}_m^T & (\mathbf{b}_m \times \mathbf{u}_m)^T \end{bmatrix} \tag{2.44}$$

If the center of mass G is chosen as the reference point for the computation of the moments, Eq. (2.38) is simplified as:

$$\begin{cases} m\ddot{\mathbf{p}}_G - \mathbf{f}_E - \mathbf{f}_C = \mathbf{0} \\ \mathbf{I}_G\dot{\boldsymbol{\omega}} + \boldsymbol{\omega} \times \mathbf{I}_G\boldsymbol{\omega} - \boldsymbol{\tau}_E - \boldsymbol{\tau}_C = \mathbf{0} \end{cases} \tag{2.45}$$

where $\boldsymbol{\tau}_C = \sum_{i=1}^{m} f_i \tilde{\mathbf{h}}_i \mathbf{u}_i$. It follows that Eq. (2.42) is modified as:

$$\begin{bmatrix} m\mathbf{I}_3 & \mathbf{0}_3 \\ \mathbf{0}_3 & \mathbf{I}_G \end{bmatrix} \begin{bmatrix} \ddot{\mathbf{p}}_G \\ \dot{\boldsymbol{\omega}} \end{bmatrix} + \begin{bmatrix} \mathbf{0}_3 & \mathbf{0}_3 \\ \mathbf{0}_3 & \tilde{\boldsymbol{\omega}}\mathbf{I}_G \end{bmatrix} \begin{bmatrix} \dot{\mathbf{p}}_G \\ \boldsymbol{\omega} \end{bmatrix} - \begin{bmatrix} \mathbf{f}_E \\ \boldsymbol{\tau}_E \end{bmatrix} - \begin{bmatrix} \mathbf{u}_1 & \dots & \mathbf{u}_m \\ \tilde{\mathbf{h}}_1\mathbf{u}_1 & \dots & \tilde{\mathbf{h}}_m\mathbf{u}_m \end{bmatrix} \mathbf{f} = \mathbf{0} \tag{2.46}$$

Here, for the generic i-th cable, $\mathbf{h}_i$ is the vector connecting the distal point B_i to the center of gravity G (see Figure 2.4). Finally, the equation representing the dynamic equilibrium of the EE about G is:

$$\mathbf{M}\dot{\mathbf{v}} + \mathbf{C}\mathbf{v} - \mathbf{w}_E - \mathbf{J}_g^T\mathbf{f} = \mathbf{0} \tag{2.47}$$

where:

$$\begin{aligned} \mathbf{M} &= \begin{bmatrix} m\mathbf{I}_3 & \mathbf{0}_3 \\ \mathbf{0}_3 & \mathbf{I}_G \end{bmatrix}, \quad \mathbf{C} = \begin{bmatrix} \mathbf{0}_3 & \mathbf{0}_3 \\ \mathbf{0}_3 & \tilde{\boldsymbol{\omega}}\mathbf{I}_G \end{bmatrix} \\ \mathbf{w}_E &= \begin{bmatrix} \mathbf{f}_E \\ \boldsymbol{\tau}_E \end{bmatrix}, \qquad \mathbf{J}_g = \begin{bmatrix} \mathbf{u}_1^T & (\mathbf{h}_1 \times \mathbf{u}_1)^T \\ \vdots & \vdots \\ \mathbf{u}_m^T & (\mathbf{h}_m \times \mathbf{u}_m)^T \end{bmatrix} \end{aligned} \tag{2.48}$$

Notice that if $O' \equiv G$, it follows that $\mathbf{I}_{O'} = \mathbf{I}_G$, $\ddot{\mathbf{p}} = \ddot{\mathbf{p}}_G$, $\dot{\mathbf{p}} = \dot{\mathbf{p}}_G$, $\mathbf{d} = \mathbf{0}$, and $\mathbf{b}_i = \mathbf{h}_i \forall i = 1, \dots, m$, so Eq. (2.43) is simplified in Eq. (2.47).

Regardless of whether Eq. (2.43) or (2.47) is used to model the dynamics of a CDPR, it is always possible to obtain the following formulation for the description of the equilibrium of the EE:

$$\mathbf{A}\mathbf{f} + \mathbf{w}_T = \mathbf{0} \tag{2.49}$$

where $\mathbf{A}$ is called *structure matrix*, and $\mathbf{w}_T$ is the total external wrench acting on the EE which represents all the forces and torques that act on the EE except the ones exerted by the cables.

2.3 Force distribution computation

The dynamic equilibrium of the EE in $SE(3)$ is always described by six equations since the structure matrix $\mathbf{A}$ in Eq. (2.49) has dimensions $6 \times m$. The inverse kinetostatic problem consists in solving Eq. (2.49) to find the cable tensions (i.e., $\mathbf{f}$). Notice that, when solving an inverse dynamic problem, the total wrench acting on the robot platform ($\mathbf{w}_T$) is known since the external forces and torques applied to the EE must be known, as well as its trajectory that allows to compute its inertial wrench. Even the structure matrix can be easily computed by knowing the pose of the EE.

In the case of an overconstrained CDPR, the system of equations (2.49) is undetermined since it has more unknowns (m) than equations (6). Remembering that r is the number of redundant cables (in the case of a manipulator moving in all the 6 DOFs of $SE(3)$, $r = m - 6$), this system generally has ∞^r solutions. Since cables can only exert positive forces, all solutions involving negative tensions must be discarded. In many practical cases, it is desirable to maintain cable forces higher than a lower limit f_{min} greater than zero to prevent cables from becoming slack and lower than a maximum value f_{max} to avoid cable damage. Imposing these limits is insufficient to guarantee a unique solution to the problem; on the contrary, the constraints could make the system unsolvable. For this reason, it is necessary to implement an algorithm to choose the correct *Force Distribution* (FD) among all the possible sets of cable tensions (if the problem admits a solution).

The problem of finding the correct FD within the range of forces defined by f_{min} and f_{max} is not straightforward, and many authors have introduced different approaches to solve it. In [86], the cable-tension computation problem is analyzed for cases in which the redundancy is $r = 1$, or $r > 1$. The authors present a simple algorithm for the former case, while they use interval analysis and gradient-based optimizers for the latter. Interval analysis provides guaranteed solutions but is computationally demanding and unsuitable for real-time applications. Gradient-based methods can be applied even in real-time. However, their iterative nature cannot always guarantee finding a solution in a strict number of iterations (i.e., in a cycle time). In the same period, an iterative approach based on the Dykstra method was introduced in [87]; it is interesting to notice that in this study, the redundant limbs of the investigated robots are not extra cables but cylinders that apply forces on the EE. The Dykstra method is also applied in [88]; here, when there is no unique solution that satisfies both the constraints (the statics of the manipulator and the force limits), the algorithm allows one to find two different solutions, each one satisfying only one constraint. This method could be helpful during the design of a new CDPR. An analytic approach is applied in [89] to reduce the computational effort of iterative methods. At the same time, in [90], the authors set up a linear programming optimization problem instead of a quadratic one. A linear programming problem is also solved in [91], but here the objective function differs from the previous ones because the algorithm aims to find the set of tensions that maximize the robot stiffness in a specific direction. The main drawback of using a linear programming approach is that there is no mathematical proof that the problem solution is continuous, and the continuity of cable tensions is mandatory during the robot operation. On the contrary, the authors in [92] solve a quadratic programming problem to obtain exact values of the cable tensions when the EE is inside the wrench feasible workspace (see Section 2.5) and approximate solutions when the EE is outside (a situation possible in haptic applications).

In most works in which the real-time capabilities of the algorithms are the main requirement, iterative approaches are discarded. In [93], a barycentric approach is developed, but the algorithm becomes computationally expensive for a high redundancy. To overcome this problem, the authors in [94] introduce a closed-form method for robots with an arbitrary redundancy; this technique was improved first in [95] and then in [96] by combining it with the puncture method to obtain a fast solution, but also capable of minimizing the cable tensions. With a similar aim, [97] introduces a method to compute the minimum 2-norm non-negative wire tension vector by modifying the solution obtained with the Moore-Penrose generalized inverse of the Jacobian matrix. The same method was extended in [98] by using interval arithmetic to compute the cable tensions when there are uncertainties in the robot parameters. The minimum 2-norm solution of the cable tension array is also obtained with the technique proposed in [99], where cable sagging is also considered. Other recent methods introduced to obtain fast results are based on a geometric approach [100–103]. Gouttefarde et al. [100] introduced one of the most used techniques. This method is suitable only for robots with a redundancy $r = 2$ because their set of feasible cable tensions is a 2-D convex polygon. First, the algorithm finds the vertices of this polygon (if a solution to the problem exists for the analyzed EE pose). Then, the cable tensions are computed by choosing between different solutions (minimum 2-norm, minimum 1-norm, centroid, weighted barycenter).

Since the design chosen for the robot CORHDA exploits eight cables to move the EE in all the six DOFs of $SE(3)$, the algorithm shown in [100] will be used for the FD computation in the following. The main reason behind this choice is the possibility to execute the FD computation in real-time due to the fastness of the algorithm. The solution obtained with this method for the cable tension array has the following form:

$$\mathbf{f} = \mathbf{A}^{+}\mathbf{w}_T + \mathbf{N}\boldsymbol{\lambda} \tag{2.50}$$

where $\mathbf{A}^{+}$ is the Moore-Penrose pseudoinverse of the structure matrix, $\mathbf{N}$ is the $m \times 2$ nullspace matrix of $\mathbf{A}$, and $\boldsymbol{\lambda} = [\lambda_1 \lambda_2]^T$ is a vector representing a generic point in the 2-D nullspace of the structure matrix. The solution in Eq. (2.50) is obtained as the sum of a particular solution $\mathbf{f}_p = \mathbf{A}^{+}\mathbf{w}_T$ and a homogeneous solution $\mathbf{f}_h = \mathbf{N}\boldsymbol{\lambda}$. The particular solution is the minimum 2-norm solution of the cable tension array that does not consider the constraints on the minimum and maximum values of the wire forces. This means that the components of $\mathbf{f}_p$ can be greater than f_{max}, lower than f_{min}, or even negative, which is not a physical solution since cables can only provide positive tensions on the EE. The homogeneous solution is added to modify the particular solution to obtain a force vector that satisfies the imposed constraints. In fact, for the definition of $\mathbf{N} = \text{null}(\mathbf{A})$, $\mathbf{A}\mathbf{N}\boldsymbol{\lambda} = \mathbf{0}$, which means that substituting the solution (2.50) in Eq. (2.49) leads to $\mathbf{A}\mathbf{f}_p + \mathbf{w}_T = \mathbf{0}$. Therefore, the homogeneous solution does not affect the equilibrium on the EE.

The set of feasible FD is a 2-D convex polytope Λ obtained by the intersection of the 2-D space of the solution to Eq. (2.49) Σ, and the m-dimensional hypercube of feasible cable tensions Ω:

$$\begin{aligned} \Lambda &= \Sigma \cap \Omega \\ \Sigma &= \{\mathbf{f} \mid \mathbf{A}\mathbf{f} + \mathbf{w}_T = \mathbf{0}\} \\ \Omega &= \{\mathbf{f} \mid \mathbf{f}_{min} \le \mathbf{f} \le \mathbf{f}_{max}\} \end{aligned} \tag{2.51}$$

Here, $\mathbf{f}_{min}$, $\mathbf{f}_{max}$ are arrays in $\mathbb{R}^m$ in which every element is equal to f_{min} and f_{max}, respectively. The solution (2.50) can be seen as a function of $\boldsymbol{\lambda}$, since $\mathbf{N}$ can be easily computed from $\mathbf{A}$, that is known once the inverse kinematic problem is solved: $\mathbf{f} = \mathscr{F}(\boldsymbol{\lambda})$. Given a certain subset Ψ of the domain of $\mathscr{F}$, the *image* of Ψ through $\mathscr{F}$ is a subset Φ of the codomain of $\mathscr{F}$. Similarly, the *preimage* of Φ through $\mathscr{F}$ is a subset Ψ of the domain of $\mathscr{F}$ that, through $\mathscr{F}$, maps Φ (see Figure 2.5). In the case of $\mathbf{f} = \mathscr{F}(\boldsymbol{\lambda})$, the preimage of Λ through $\mathscr{F}$ is the following:

$$\mathscr{F}^{-1}(\Lambda) = \{\boldsymbol{\lambda} \in \mathbb{R}^2 \mid \mathbf{f}_{min} \le \mathbf{f}_p + \mathbf{N}\boldsymbol{\lambda} \le \mathbf{f}_{max}\} \tag{2.52}$$

Since Λ is a convex polytope, its preimage through $\mathscr{F}$ is a convex polytope. Moreover, $\mathscr{F}^{-1}(\Lambda)$ belongs to $\mathbb{R}^2$, so it is a convex polygon called *feasible polygon*. In practice, the feasible polygon is obtained by the intersection between the following $2m$ inequalities (one for the f_{min} constraint and one for the f_{max} constraint for each cable).

$$\mathbf{f}_{min} - \mathbf{f}_p \le \mathbf{N}\boldsymbol{\lambda} \le \mathbf{f}_{max} - \mathbf{f}_p \tag{2.53}$$

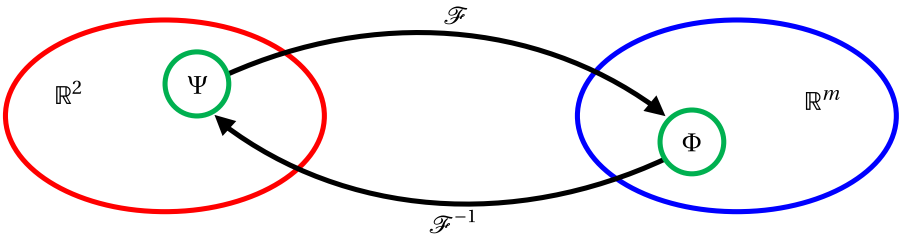

Figure 2.5: Image and preimage of function $\mathscr{F}$.

Every inequality represents a half-plane in $\mathbb{R}^2$. The algorithm shown in [100] aims to find the vertices of the feasible polygon without computing all the intersections among the $2m$ lines obtained by setting the inequalities to equalities.

If the feasible polygon exists, once its vertices are computed, the homogeneous solution $\mathbf{f}_h$ is found by choosing the correct $\boldsymbol{\lambda} \in \mathscr{F}^{-1}(\Lambda)$ with a specific criterion. In particular, the minimum 2-norm solution of the cable tension array was chosen in such a way as to minimize the power required to the motors and to obtain a set of forces that is continuous during a trajectory of the EE. This solution is found by solving the following quadratic program:

$$\begin{cases} \min_{\boldsymbol{\lambda}} \; ||\boldsymbol{\lambda}||^2 \\ \mathbf{f}_{min} - \mathbf{f}_p \;\leq\; \mathbf{N}\boldsymbol{\lambda} \;\leq\; \mathbf{f}_{max} - \mathbf{f}_p \end{cases} \tag{2.54}$$

2.4 Cables elastic model

One of the issues related to using wires instead of rigid links is that cables are flexible elements subjected to elongation. In some applications where forces are low, the cable elongation can be negligible, or it is not considered for simplicity since it is not straightforward to correctly estimate it. Many authors use Irvine's catenary model to represent the wires behavior when the cable masses are considered [104–107]. This is the case with large-scale robots like the FAST [105] or the CoGiRo [106], where no fast motions are required in general, and, for this reason, even steel ropes can be used. In smaller robots requiring faster movements, it is common to use fiber ropes (e.g., Dyneema ones) that guarantee a high payload-to-mass ratio with respect to steel wires. In this way, the small rope mass does not influence the system dynamics, and its effect can be neglected in the cable model: the wire is treated as a straight line subjected to a linear elongation [39, 108, 109]. In this case, the elastic model of the rope is equal to that of a spring in which the elastic coefficient depends on the cable length:

$$F = k'(l)\Delta l = \frac{k}{l}\Delta l = k\epsilon \tag{2.55}$$

with $\epsilon = \Delta l / l$.

A simple linear model like the one in Eq. (2.55) could be insufficient to represent the elastic behavior of fiber ropes. For this reason, in [110], the elastic coefficient is supposed to be a function of the force applied to the cable. In contrast, other authors introduced different functions to represent the elastic behavior of these wires. In [78, 79], a polynomial with degree three in the cable elongation is used, while in [111], a fourth-order polynomial or an exponential function are introduced. In [112], a different approach is exploited since a mass-spring-damper system is used to represent the cable in such a way as to model (through the damper) the friction effects due to the slipping of the fibers with each other.

The behavior of braided fiber ropes is not easily represented with simple, time-independent functions. In [113], the hysteresis of cables is also considered by the model, a phenomenon already analyzed in [114] with a black-box approach. It is particularly interesting the behavior of the cable during the first load cycle, which can be seen in the results in [113]: when a virgin cable is stretched, a residual elongation is visible even after the unloading. Similar effects are also shown in specific studies on braided ropes [115,116], as seen in Figure 2.6. The reason could be related to the nature of the braided ropes, obtained by braided strands that leave empty areas in the wire section. For these kinds of cables, it is possible to define a fill factor that represents the percentage of the section of the rope that is actually "filled" with material [117]. During the first loading cycle, the strands of the rope may rearrange themselves by filling large parts of the empty areas (i.e., the fill factor increases), and this causes, in practice, an elongation of the cable that is not an elastic effect but a geometrical one due to volume conservation. From a practical point of view, pre-stretching cables before doing the tests to estimate their elastic model and before their use in a CDPR is desirable.

For a more realistic cable modeling, wear should also be taken into account. Indeed, even if a correct model that represents the elastic behavior of the cable is estimated, it is not guaranteed that the parameters of the model remain unchanged in time due to the wear caused by the cable slipping on pulleys or other mechanical parts of the robot [107].

For the aim of this work, a simple linear elastic model like the one shown in (2.55) is considered acceptable. This is because not considering the cable elasticity produces errors, but using a wire model that is too complex is a problem from a computation point of view since the model must be implemented in real-time for the computation of the correct cable length. During one cycle time (commonly equal to $1ms$), many operations must be done, not only related to the resolution of the manipulator kinematics. For this reason, it is desirable to maintain the computations as simple as possible. The choice of a linear elastic model is a good compromise between the increase of computational complexity due to considering wires elasticity and the necessity of having a robot model that is accurate enough for the execution of the predefined task.

Finally, we must mention that not only problems related to the most suitable model

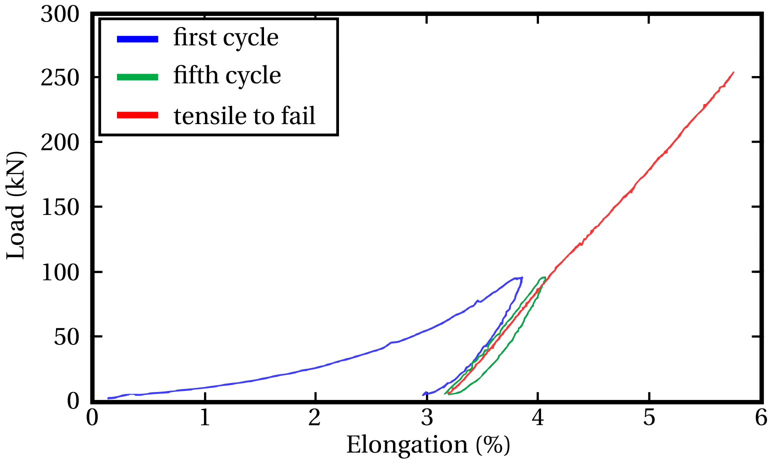

Figure 2.6: Results shown in [115] for the loading cycle tests executed on a braided fiber rope.

of the cable force-elongation characteristic arise on CDPRs; the behavior of the wires on the drums may also be a problem, both because assessing the elongation of the wound cable is very difficult and because the ovalization of the rope can change the theoretical transmission ratio between the motor and the cable by producing errors in the EE positioning [118].

2.5 Workspace

The workspace is one of a robot essential properties, and it is the first aspect to consider in choosing a manipulator for the execution of a given task. In practice, it is the set of poses that the EE can reach by satisfying some performance constraints. Considering the most general case of a robot moving in $SE(3)$, it is possible to define different subsets of the six-dimensional workspace. In the following, only some are listed; for a complete treatment of this topic, see [119]. P is the reference point on the EE, i.e., the point used to define its position.

- *Constant Orientation Workspace* or *Translation Workspace*: set of all possible positions that can be reached by P with a given (constant) orientation.
- *Orientation Workspace* or *Rotational Workspace*: set of all possible orientations that can be reached by the EE while P is in a given (constant) position.
- *Maximal Workspace* or *Reachable Workspace*: set of all possible positions that can be reached by P with at least one orientation of the EE.
- *Total Orientation Workspace*: set of all possible positions that can be reached by P with all possible orientations of the EE belonging to a given set.

If we are not interested in the wrench that the EE must generate in a given pose, this pose belongs to a specific definition of the workspace if the geometry of the manipulator (i.e., the legs) allows to reach it. However, it is not guaranteed that if a pose is reachable from a geometric point of view, it belongs to the robot workspace since it is not sure that the EE in that pose may be in equilibrium. This condition is often verified for standard parallel manipulators actuated by rigid links that can exert tensile and compressive forces and react to bending. On the contrary, the wires of a CDPR can generate only tensile forces on the EE, and it is easy to verify that in certain poses that could be reachable from a geometric point of view, this leads to requiring too small (or even negative) or too high tensions on some cables to satisfy the equilibrium of the EE. For this reason, the concept of *Wrench Closure Workspace* [120] was introduced for CDPRs. This is the set of poses where the EE can be balanced by cable forces higher than zero (i.e., the cables do not become slack). However, since in practical applications a lower limit $f_{min} > 0$ and a higher limit f_{max} are defined for the cable tensions, the *Wrench Feasible Workspace* [121] was defined as the set of poses in which the EE can be balanced by cable tensions such that $f_{min} \leq f_i \leq f_{max} \ \forall \ i = 1, \ldots, m$.

Moreover, it is necessary to verify the non-interference of cables to confirm if a pose belongs to the robot actual workspace. This problem is significant for overconstrained CDPRs that have many cables (even coming from the bottom of the workspace). The regions of the constant orientation workspace where interference of cables with each other or with the EE occur are identified in [122]. In [123], the interference of cables with external bodies within the robot workspace is also considered for three different definitions of workspace (constant orientation, orientation, and total orientation). Some authors studied the problem of cable interference for developing CDPRs with movable proximal points, as in [124], where an algorithm capable of working in real-time on a CDPR is introduced to compute the movement to command to the proximal anchor points for preventing cable intersection.

Generally, cable interference is studied by supposing cables as straight lines. In this way, the distance between two wires, j, and k, can be easily computed with a geometrical procedure, and it is called d_{jk}. By adding the non-interference constraint among cables to the conditions that must be satisfied by the points of the workspace, one can define the *Total Orientation Wrench Feasible Workspace* ($\mathscr{W}_{\mathscr{T}\mathscr{O}}$) as the set of positions $\mathbf{p}$ in which the following two conditions are verified for all the orientations belonging to a given set $\mathscr{R}_{\mathscr{O}}$:

$$\mathbf{A}(\mathbf{p},\mathbf{R})\mathbf{f}+\mathbf{w}_T=\mathbf{0} \quad \text{with} \quad f_{min}<f_i<f_{max} \quad \text{for} \quad i=1\dots m \quad \forall\ \mathbf{R}\in\mathscr{R}_{\mathscr{O}} \tag{2.56}$$

$$d_{jk}>d_c \quad \text{for} \quad j=1\dots m\setminus\{k\} \quad , \quad k=1\dots m\setminus\{j\} \tag{2.57}$$

where d_c is the cable diameter.

Chapter 3

Robot Control

This chapter describes the controller developed for the robot CORHDA. The proposed scheme is based on the hybrid position-force control in the joint space introduced in [125, 126], but its implementation is innovative since it does not require the force sensors commonly used in CDPRs. This work was initially developed on the IPAnema 3 Mini, one of the robots of the Ipanema family [127] developed at the Fraunhofer Institute for Manufacturing Engineering and Automation (IPA) in Stuttgart. The robot is shown in Figure 3.1. The picture is taken from [128], where more information about the manipulator can be found. After the first implementation on the IPAnema 3 Mini, the controller was applied to the CORHDA.

3.1 Hybrid position-force control in joint space

To correctly control the pose of the EE of a CDPR, it is necessary to ensure that all cables do not become slack; otherwise, the EE could lose some DOFs, and/or the positioning of the platform could be not precise since the kinematic model described in Section 2.1

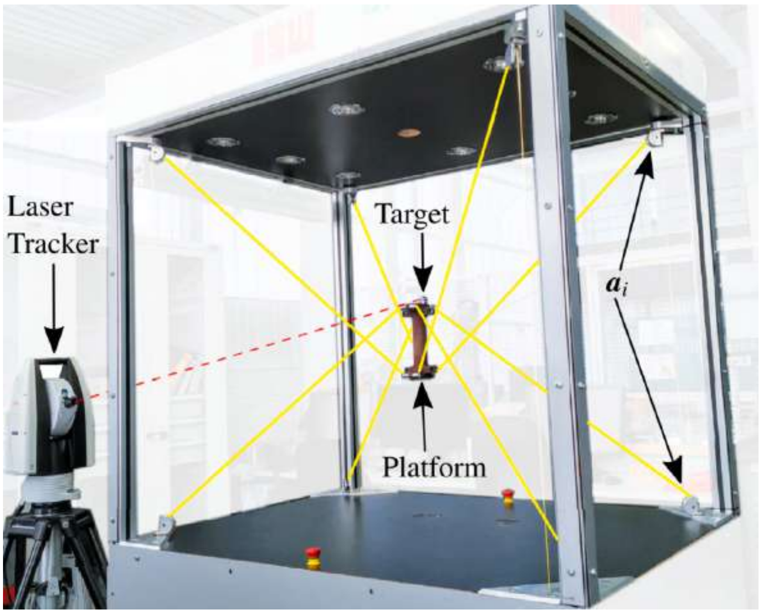

Figure 3.1: IPAnema 3 Mini, with the laser tracker used to measure the position of the EE [128].

considers the cables as straight lines. The necessity of having the wires tensed is why a minimum force $f_{min} > 0$ is imposed as a constraint on all cable tensions to compute the desired FD, as explained in Section 2.3.

Suppose that a pure inverse kinematic controller is implemented in the robot. In that case, it is impossible to guarantee that the cable forces are the ones of the desired FD. If the elastic model of the wires is not considered, the geometric cable lengths (output of the inverse kinematics) do not correlate with the desired forces (output of the FD algorithm). In contrast, if the elastic model of the wires is taken into account from the desired cable lengths and forces, one can compute the theoretical rope elongation that needs to be used to correct the geometric length. If everything is perfect in the model of the robot, by simply correcting the geometric lengths with the theoretical elongations, one can obtain the prescribed FD. However, this is an ideal situation that will not be achievable in practice since it is impossible to have a perfect model of the wire elasticity (see Section 2.4). For this reason, it is necessary to implement a control algorithm in the robot, which also aims to control the cable forces correctly, not only their lengths.

Once the FD is computed, the forces must be converted into motor inputs, such as torques [129, 130], velocities [131], or positions [103]. In general, to be sure to apply the computed tensions, the theoretical motor inputs must be modified by using the real cable-force values read by suitable load cells with a particular method, like a feedback linearization controller [132]. When the EE should apply a specific wrench during contact with an external object, Refs. [133, 134] apply a hybrid position-force control strategy in Cartesian space. In [133], the authors divide the EE DOFs into force and position controlled. The same concept can be used in the joint space to develop a different hybrid position-force control. We will refer to this method as Hybrid Control (HC). This concept was introduced in [125, 126]: the idea is to control n cables of the robot in position to obtain a specific pose of the platform and to perform a force control on the r redundant cables to get the correct FD in the whole system. The nomenclature is the same as that used in Section 1.3. Mattioni et al. in [135–137] developed the HC by introducing the FD sensitivity index that allows one to choose the r cables to force control among the overall m wires. This work aims to extend the research about the HC by applying it without force sensors. To do so, it is necessary to build a friction model of the kinematic chain of each robot winch in such a way as to obtain a reliable correlation between the value of torque given by a motor and the effective force produced at the cable attachment point on the EE. Especially when many pulleys are involved between the motor and the platform, the friction effects cannot be negligible [138–142].

Using a controller that does not exploit force sensors is helpful for simplifying the robot kinematic chain [142]. The most common strategies for mounting load cells into a CDPR require integration with [39]:

- the platform (Figure 3.2(a));
- the winch (Figure 3.2(b));
- the pulley mechanism (Figure 3.2(c)).

Using platform-integrated force sensors [141, 143] is convenient since, in this way, the measured force is the real one acting on the wire without any friction effect. Also, adding any mechanical element to the kinematic chain of one cable, besides the sensor, is unnecessary. However, in this way, the load cell inertias can affect the EE dy-

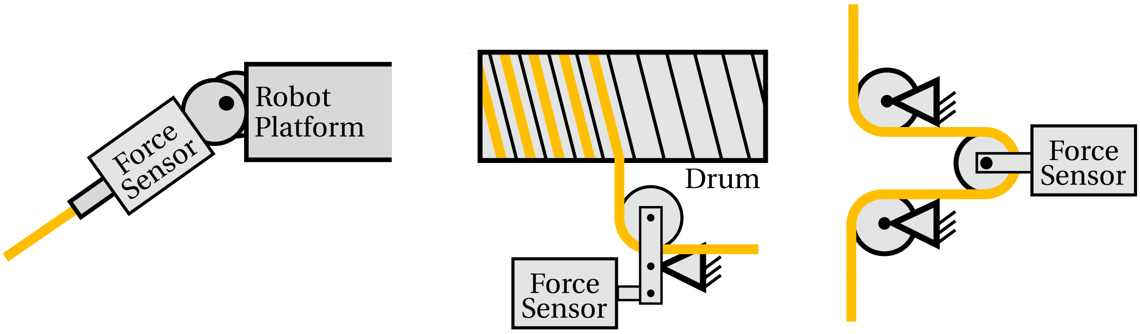

(a) Platform integration (b) Winch integration (c) Pulley mechanism integration

Figure 3.2: Strategies for force sensors integration [39].

namics if their mass is not negligible. Moreover, it is necessary to transmit the output signals of the sensors from the EE to the fixed frame.

Using winch-integrated force sensors is helpful because it allows one to have compact hardware that is easy to install and reconfigure. However, it is necessary to have an element in the kinematic chain that is movable with the exit point of the cable from the drum. In some cases, a spooling helper is used [127], while in others, a winch with a translatory drum is developed [77, 144, 145].

Finally, another frequently used technique is to mount the force sensors on specially designed pulley mechanisms [70, 139]. In this way, the load cells can be easily added to a previously developed kinematic chain without modifying the mechanical parts of the EE or the winches. Moreover, the data are directly available on the robot frame and can be easily used in the controller if necessary. However, this strategy requires using more pulleys in the robot kinematic chain, producing higher friction and wear of the wires, especially when subjected to double-bending windings.

For the robot CORHDA, it is impossible to use winch-integrated force sensors since they would require adding moving parts (i.e., moving masses) in the kinematic chain. The movement of these masses during the robot operation would increase the inertial torque acting on the motor shaft due to the high accelerations necessary to satisfy the required productivity. This would lead to bigger motors. The platform-integrated load cells are also not desirable to avoid additional connections to the EE for transmitting the output data of the force sensors to the robot frame and to keep the EE mass as small as possible. Finally, to reduce the friction in the kinematic chain and the cable wear in such a way as to obtain a robot that can be reliable for long-term functioning, the number of pulleys should be minimized, thus making the use of pulleys for mounting load cells undesirable. For these reasons, a control strategy that does not exploit force sensors was preferred in the following. Load cells were mounted on the cable attachment points to the EE of the CORHDA only during some tests in order to validate the effectiveness of the proposed control scheme. The platform integration of the force sensors was deemed the only possible to avoid the effect of friction in force measurements and to avoid modifications in the robot kinematic chain.

3.2 Friction model

To control cable forces without using any force sensor, the main problem is to find the correlation between the torque τ_i applied by the motor and the actual force f_i applied on the EE, namely:

$$\tau_i = f_i r_D + \tau_F(f_i, v_i) + \tau_{In}(a_i) \tag{3.1}$$

where r_D is the drum radius, τ_{In} is the inertial torque produced by the moving parts of the winch (motor shaft, drum, ...), τ_F is the torque generated by friction phenomena between the motor and the cable attachment point on the EE, and v_i and a_i are the cable velocity and acceleration, respectively. In both the IPAnema 3 Mini and the CORHDA robot, no gearboxes are used, so the drums are directly connected to the motor shafts. This means that the friction torque τ_F is generated only by the motor, the drum, and the pulleys. It is necessary to model this term to properly control some robot cables in force.

3.2.1 IPAnema 3 Mini

Figure 3.3 shows a scheme of one cable kinematic chain of the IPAnema 3 Mini, representing the mechanical parts that generate the friction torque τ_F, including the location of the force sensor (a Futek LRM200 JR S-Beam load cell with a maximum load capacity equal to 25 lb). Since the sensor is mounted on the third pulley, a friction force f_F makes the force measurement different from the real one acting on the EE due to the friction between the third pulley and the cable attachment point. In general, τ_F and f_F depend on both the cable force and velocity. The geometric and inertia properties of the mechanical parts of the winch are known, as well as the desired force f_i (found by the FD algorithm). The motion law of the motor is computed through the robot inverse kinematics, which provides v_i and a_i. The motor motion law allows one to compute the inertial torque τ_{In}. Accordingly, the only unknown term in Eq. (3.1) is τ_F. To determine this quantity, it is necessary to build a friction model by means of experimental tests.

An experimental study was conducted on the kinematic chain of one winch (Figure 3.3) by detaching the cable from the EE. Different weights were attached to the cable and moved up and down, with trajectories reaching several values of steady-state constant velocity. Every mass in Table 3.1 is accelerated to every constant velocity shown in Table 3.2. The masses generate a set of cable forces that approximately cover the tension interval defined for the robot operation, from $f_{min} = 5$ N to $f_{max} = 35$ N. The lower and higher constant velocities reached are $v_L = 0.25$ m/min and $v_H = 6$ m/min.

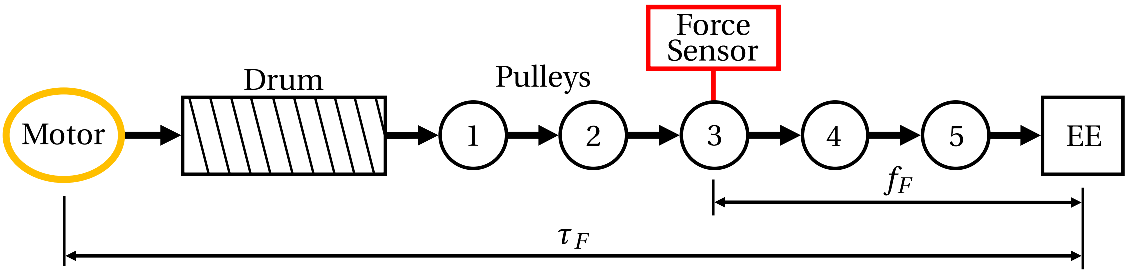

Figure 3.3: Scheme of the IPAnema 3 Mini kinematic chain and the areas in which the friction torque τ_F and force f_F are modeled.

Table 3.1: Weights used to estimate the friction model of the IPAnema 3 Mini. Every mass is accelerated to every constant velocity shown in Table 3.2.

m (kg)	0.28	0.51	0.90	1.39	2.68	3.19

Table 3.2: Velocities used to estimate the friction model of the IPAnema 3 Mini.

v (m/min)	0.25	0.50	1.00	2.00	3.00	4.00	5.00	6.00

A scheme of the winch kinematic chain during the experiments is shown in Figure 3.4. Pulley 1 guides the cable arriving from the drum; pulleys 2, 3, and 4 are used to add the force sensor in the kinematic chain; pulley 5 guides the wire to the EE. During the constant-velocity portion of the motion, the term τ_{In} in Eq. (3.1) is zero, and $f_i = mg$, where m is the mass of the weight attached to the cable, and g is the gravitational acceleration. The torque measured by the motor is saved, and its mean value is computed during different movements with the same constant velocity in the same direction. In this way, two different torques were obtained for each velocity (in magnitude) and force of the cable, one for the movement in the positive direction and one for the movement in the negative direction. By inserting these torques in Eq. (3.1) as τ_i, one can find the value of τ_F corresponding to a given velocity and cable tension for each motion direction. The distinction between the different movement directions is necessary since the results obtained with the experimental tests show different frictions in the two cases. The constant velocity used to build the friction model is the one commanded to the motor without the necessity of measuring the real velocity with an external sensor. This is acceptable since the velocity set for the motor will be used as an input of the final friction model in the control scheme.

During the tests for the estimation of the friction model parameters, the cable routing in the first four pulleys is the same as in the working robot, so the friction that arises in this part of the kinematic chain is the same during the tests and during the robot operation. The same can be said for the drum and motor friction effects. However, this is not strictly true for friction effects in the last pulley of the kinematic chain. During testing, in fact, the wrapping angle is always equal to 180° (see Figure 3.4). In contrast,

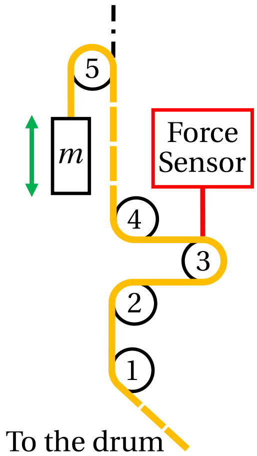

Figure 3.4: Scheme of the IPAnema 3 Mini cable routing during the tests executed to estimate the friction model parameters in the cable actuation chain.

during operation, this angle varies with the trajectory of the EE. Its value is always between 90° and 180° for the higher pulleys of the robot and between 0° and 90° for the lower ones. The approximation adopted for estimating friction parameters is, thus, better suited for the higher pulleys than the lower ones. This is due to the fact that, in all the tested trajectories, the force-controlled cables (namely, the ones in which the friction model is applied) are the higher ones. The scheme shown in Figure 3.4 allows one to execute friction tests by only detaching the i-th cable from the EE without touching any other part of the robot. This means that friction tests can easily be executed whenever necessary (e.g., if some mechanical parts change or the friction parameters change in time due to wear of some components). This is the main advantage of the simplified friction model introduced in this section; its suitability will be assessed by the experiments reported in Section 5.1.

By analyzing the set of points obtained in the tests, we chose a model for estimating the friction torque that is linear in the force and parabolic in the velocity, namely,

$$\tau_F(f,v) = c_1 v + c_2 v^2 + c_3 f + c_4 \tag{3.2}$$

The function shape at the right-hand side of Eq. (3.2) is chosen as the best fit for the registered data. The shape is the same for the positive and negative motion directions, but the coefficients c_i found through a best-fitting procedure differ. Since our experiments provide data to estimate dynamic friction only starting from the minimum velocity v_L (the tests conducted with smaller velocities showed little repeatability and, thus, were considered unreliable), it is necessary to model the friction torque for velocities in the interval $[-v_L; v_L]$. This was achieved by using a polynomial $p(f,v)$ with degree four in v for every force value, i.e., the polynomial coefficients are functions of f, and they are recomputed for every input force value. In this way, the complete model of the friction torque is

$$\tau_F(f,v) = \begin{cases} c_{1n} v + c_{2n} v^2 + c_{3n} f + c_{4n} & v \in [-v_H; -v_L[\\ p(f,v) = b_0 + \sum_{j=1}^{4} b_j(f) v^j & v \in [-v_L; v_L] \\ c_{1p} v + c_{2p} v^2 + c_{3p} f + c_{4p} & v \in \;]v_L; v_H] \end{cases} \tag{3.3}$$

The degree of $p(f,v)$ allows one to impose five conditions for the computation of coefficients $b_j(f)$:

- $p(f,0) = 0$; this condition is necessary to represent the behavior of the dynamic friction that is zero at rest (static friction is not modeled);
- continuity of the polynomial at the borders: $p(f,-v_L) = \tau_F(f,-v_L) = \tau_{vn}$ and $p(f,v_L) = \tau_F(f,v_L) = \tau_{vp}$;
- continuity of the derivative of the polynomial at the borders: $\frac{\partial p(f,-v_L)}{\partial v} = \frac{\partial \tau_F(f,-v_L)}{\partial v} = \partial \tau_{vn}$, and $\frac{\partial p(f,v_L)}{\partial v} = \frac{\partial \tau_F(f,v_L)}{\partial v} = \partial \tau_{vp}$.

The resulting coefficients are:

$$
\begin{aligned}
b_0 &= 0 \\
b_1 &= -\frac{3(\tau_{vn} - \tau_{vp}) + v_L(\partial\tau_{vn} + \partial\tau_{vp})}{4v_L} \\
b_2 &= \frac{4(\tau_{vn} + \tau_{vp}) + v_L(\partial\tau_{vn} - \partial\tau_{vp})}{4v_L^2} \\
b_3 &= \frac{\tau_{vn} - \tau_{vp} + v_L(\partial\tau_{vn} + \partial\tau_{vp})}{4v_L^3} \\
b_4 &= -\frac{2(\tau_{vn} + \tau_{vp}) + v_L(\partial\tau_{vn} - \partial\tau_{vp})}{4v_L^4}
\end{aligned}
\tag{3.4}
$$

The coefficients obtained for the friction torque model are listed in the first two rows of Table 3.3. These data are obtained by applying the Matlab function `lsqnonlin` with a step tolerance and a function tolerance both equal to 10^{-6}. The `lsqnonlin` function implements a nonlinear least squares solver for curve-fitting problems, and it is used to find the coefficients c_{in} and c_{ip} on the right-hand side of Eq. (3.3) that minimize the 2-norm of the error vector between the friction torques computed with the model in Eq. (3.3), and the torques recorded during the friction tests. Figure 3.5 represents the friction torque model described in Eq. (3.3) with the coefficients listed in Table 3.3. The black points are the results provided by the experimental tests. The model gives a good estimation of the physical phenomenon since the coefficient of determination [146] is higher than 0.9 (if $R^2 = 1$, the function exactly interpolates the input data). Interestingly, the maximum value of the predicted friction torque is 0.15 Nm, which is approximately 22% of the nominal motor torque (equal to 0.69 Nm). This suggests the importance of the friction model introduced in this section.

Experimental tests were carried out to develop a customized friction model for each winch of the robot, but the results obtained on the control of the overall robot do not show an appreciable improvement in performance compared to the use of the same friction model for all winches (as long as all the winches and the kinematic chains between the drums and the attachment points on the EE are the same). For this reason, the same friction model developed on one winch was applied to the winches.

During the tests executed for developing the friction torque model, the data recorded by the load cell mounted in the kinematic chain (Figure 3.3) were saved. These data allow us to derive a model for the friction force f_F mentioned at the beginning of this

Table 3.3: Coefficients of the torque and force dynamic friction model for the IPAnema 3 Mini. To use these coefficients in Eq. (3.3), the input force f must be given in newtons, and the input velocity must be given in meters per minute, as in Figure 3.5. R^2 is the coefficient of determination of the model.

		$i = 1$	$i = 2$	$i = 3$	$i = 4$	R^2
τ_F (Nm)	c_{ip}	$-3.64 \cdot 10^{-3}$	$-5.85 \cdot 10^{-6}$	$-4.66 \cdot 10^{-4}$	$-2.45 \cdot 10^{-2}$	0.949
	c_{in}	$-5.97 \cdot 10^{-3}$	$-2.31 \cdot 10^{-4}$	$3.10 \cdot 10^{-3}$	$2.52 \cdot 10^{-2}$	0.995
f_F (N)	c_{ip}	$-1.73 \cdot 10^{-1}$	$1.62 \cdot 10^{-2}$	$-2.51 \cdot 10^{-2}$	$2.93 \cdot 10^{-1}$	0.920
	c_{in}	$-1.60 \cdot 10^{-1}$	$-1.40 \cdot 10^{-2}$	$1.25 \cdot 10^{-1}$	$1.81 \cdot 10^{-1}$	0.986

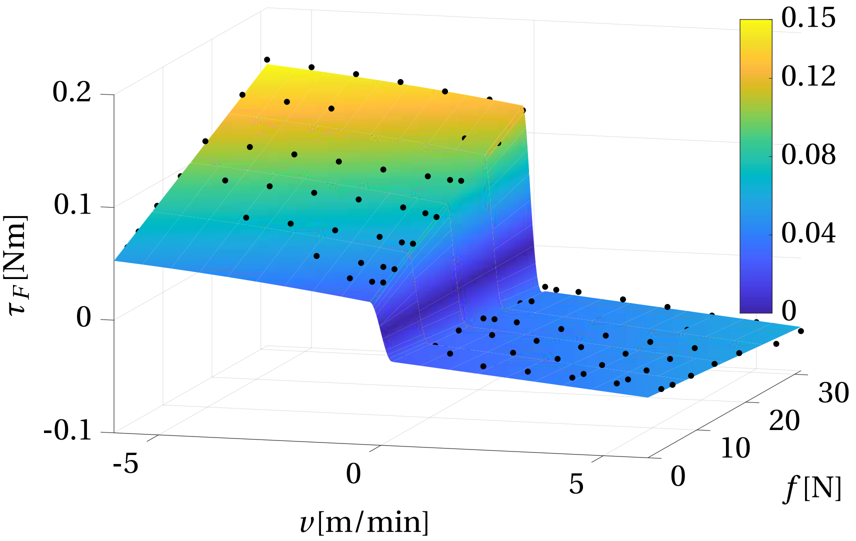

Figure 3.5: Friction torque model described in Eq. (3.3) and with the coefficients listed in Table 3.3.

section. This model is analogous to that in Eq. (3.3), with f_F replacing τ_F and distinct coefficients c_i (third and fourth rows of Table 3.3):

$$f_F(f,v)=\begin{cases} c_{1n}v+c_{2n}v^2+c_{3n}f+c_{4n} & v\in[-v_H;-v_L[\\ b_0+\sum_{j=1}^{4}b_j(f)v^j & v\in[-v_L;v_L] \\ c_{1p}v+c_{2p}v^2+c_{3p}f+c_{4p} & v\in\ ]v_L;v_H] \end{cases} \tag{3.5}$$

Using a friction model to correct the force measured by the load cells is necessary to accurately estimate the actual force acting on the cable attachment point [139]. The measured forces are not used for the new control algorithms described in Section 3.4, but they are exploited during the validation experiments described in Section 5.1.

3.2.2 CORHDA

The procedure used to estimate the friction model of the CORHDA is broadly the same as the one already described for the IPAnema 3 Mini. The kinematic chain of the CORHDA (Figure 3.6) is simpler than the one of the IPAnema 3 Mini. Moreover, the HC will be tested on this manipulator during fast motions. These aspects led to some modifications that were necessary in the development of the friction model of the kinematic chain.

The force sensors were mounted on the CORHDA only to verify the effectiveness of the control approach presented in this thesis. In particular, on every wire, a CALT DYMH-103 inline load cell with a maximum load capacity equal to 100kg is mounted on the cable attachment point to the EE, so the force measured by the sensor is the real one acting on the EE, i.e., $f_F=0$. This means that measuring the friction force during the friction tests is unnecessary. For this reason, the simple cable routing of the CORHDA adopted in the friction tests, shown in Figure 3.7, does not involve any force sensor. As already done for the IPAnema 3 Mini, the influence of the change of the wrapping angle of the cable on the swivel pulley is neglected; the only assumption is to consider a wrapping angle between 90^o and 180^o (including these values). Moreover, the tests are executed only on one winch, and the resulting model is applied to

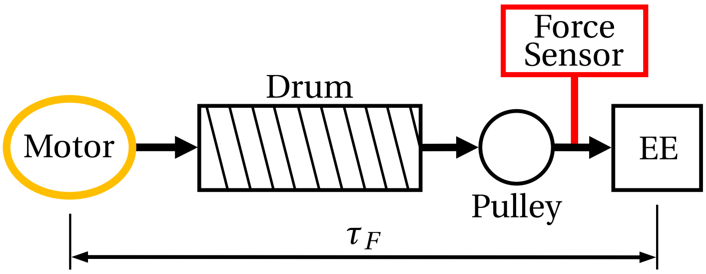

Figure 3.6: Scheme of the CORHDA kinematic chain showing the area in which the friction torque τ_F is modeled.

all the winches of the robot by neglecting the differences in friction on different cables, drums, and pulleys. This assumption is considered valid based on the previous experience on the IPAnema 3 Mini, where the friction in the kinematic chain was relatively higher than the one in the CORHDA.

As seen in Section 3.2.1, to estimate the friction model, some weights were attached at the end of the cable of one winch (Figure 3.7), and they were moved up and down to reach different constant velocities in different tests. In particular, every mass in Table 3.4 is tested for all the different constant velocities listed in Table 3.5. However, for the CORHDA, it is necessary to model the friction torque for higher values of forces (i.e., masses) and velocities with respect to the maximum ones shown in Table 3.5 since the controller will be applied when the robot executes bin-picking tasks with high dynamics. In particular, the force limits defined for the CORHDA are $f_{min} = 20$ N, $f_{max} = 350$ N, and cable velocities up to 12 m/s are approximately needed to satisfy the productivity required to execute the bin-picking task described in Chapter 1 (i.e., $100 pieces/min$).

The tests estimating the friction-model parameters were not directly performed on the CORHDA but on a test bench, which uses a winch and a swivel pulley mounted according to the cable routing scheme in Figure 3.7. The layout of the test bench was designed according to the dimensions of the CORHDA frame: this means that the mounting height of the pulley is limited by the maximum mounting height of the pulleys in the CORHDA. This arrangement is due to the necessity of reproducing the tests for the friction-torque estimation on the robot by simply detaching one cable from the EE (as in the case of the IPAnema 3 Mini). This way, it is easier to execute friction tests several times to make new estimations of the friction model if some parts of the kinematic chain change or if the friction parameters change over time due to the wear of the mechanical parts. However, in this case, the maximum displacement that can be executed during the friction tests is bounded by the dimensions of the robot frame and by the

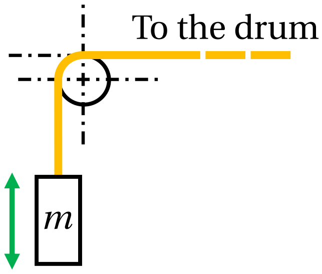

Figure 3.7: Scheme of the CORHDA cable routing during the tests executed to estimate the friction model parameters in the cable actuation chain.

Table 3.4: Weights used to estimate the friction model of the CORHDA. Every mass is accelerated to every constant velocity shown in Table 3.5

m (kg)	1.04	2.66	4.58	7.58	10.50	12.5	15.90

Table 3.5: Velocities used to estimate the friction model of the CORHDA.

v (m/s)	0.05	0.10	0.20	0.30	0.40	0.50	1.00	2.00

mounting positions of the winches. For this reason, it is necessary to execute movements with high accelerations to reach high velocities. However, the limitations on the maximum torque of the winch motor and the risk of triggering unwanted mass oscillations make it impossible to achieve the necessary accelerations to cover the complete velocity interval in which friction should be modeled. Accordingly, only tests related to the masses and velocities listed in Tables 3.4 and 3.5 could be performed, but these are insufficient to estimate the complete friction model for all cable forces and velocities reached during the bin-picking task for which the robot is developed. For this reason, another set of tests was executed on the CORHDA. In this case, higher values of constant velocities are reached without any mass attached to the cable: all the wire is coiled on the drum, which is moved with different trajectories to reach values of constant velocity between 0.05 m/s and 15 m/s (expressed as cable equivalent velocity). This way, the internal friction of the winch is measured without considering the effect of the cable force on it, namely with a value of m equal to 0. Finally, the lower and higher velocities for which the friction model is defined for the CORHDA are $v_L = 0.05$ m/s and $v_H = 15$ m/s.

To avoid the aforementioned problems, one could think of executing the friction tests on a different test bench that is not limited by the robot dimensions. Even in this case, some issues would still arise. In fact, to reach high velocities with limited accelerations by moving masses attached to a cable in the gravity direction requires mounting the pulley in the configuration shown in Figure 3.7 at several meters above the ground. Figure 3.8 shows the trajectory necessary to reach a constant velocity equal to 12m/s for 1s with maximum acceleration and deceleration equal to 10m/s^2. The yellow area with a duration of 1s represents the part of the motion law for which the constant velocity is maintained, and it is the part of the trajectory that must be analyzed to save motor-torque measurements. To execute such a motion law, the test-bench pulley should be mounted at a height higher than 30m, which is clearly impractical. The maximum displacement in Figure 3.8 also corresponds to the amount of cable that must be coiled on the drum to execute the trajectory at hand with the winch. It is impossible with the CORHDA winches to coil this quantity of wire, so a different drum (associated with a different friction model) should be used. These considerations justify the testing strategy described in the previous paragraph to estimate the friction-model parameters.

Since the set of friction tests executed does not cover all the intervals of possible cable forces and velocities, the friction model for high forces and velocities is only extrapolated based on the acquired data. The expression of the friction torque is assumed to be the same already introduced for the IPAnema 3 Mini, i.e., the one shown in Eq. (3.3) with coefficients b_i in Eq. (3.4). The friction coefficients in Eq. (3.3) are computed with a best-fit procedure by applying the Matlab function `lsqnonlin` with a step toler-

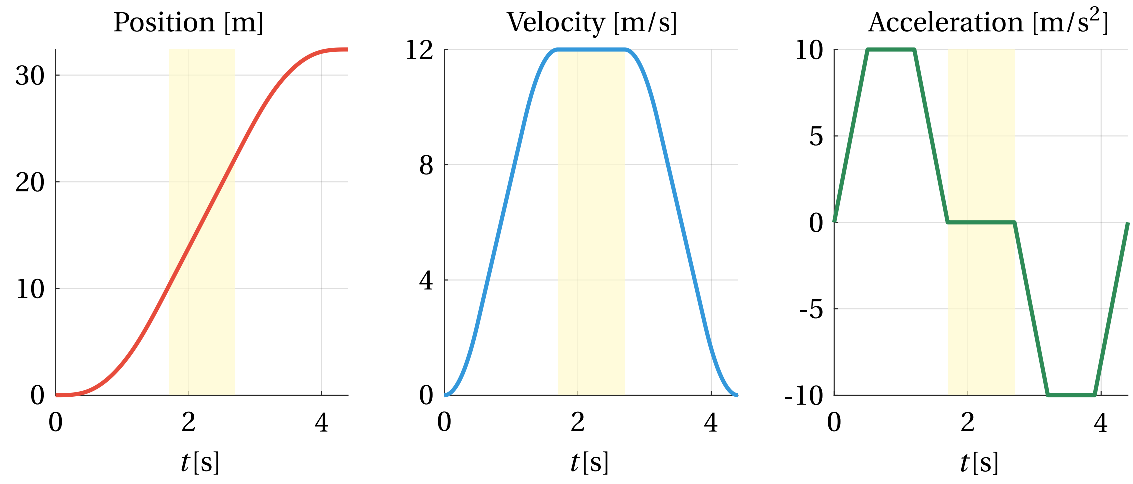

Figure 3.8: Trapezoid acceleration motion law to reach a constant velocity of 12m/s for 1s with a maximum acceleration equal to 10m/s^2.

ance and a function tolerance both equal to 10^{-6}. The resulting coefficients are listed in Table 3.6. The friction torque expressed as a function of the desired cable force and velocity when the coefficients in Table 3.6 are used is shown in Figure 3.9.

If we compare the values of the coefficient of determination [146] for the friction model of the CORHDA (Table 3.6) with the ones obtained for the IPAnema 3 Mini (Table 3.3) we notice that the model for the former are less accurate than for the latter (the indices R^2 were closer to 1 for the IPAnema robot). The reason is probably related to the oscillations that arise during the friction tests of the CORHDA, which influence the torque measurements. Building the friction model is generally more challenging when high forces and velocities are involved. However, the results seem accurate enough to justify the positive results that will be obtained in the experimental tests described in Section 5.3. The reason is probably due to the magnitude of the friction torques on the motor shaft in the CORHDA kinematic chain. The maximum friction torque we can observe in Figure 3.9 is approximately equal to 0.32 Nm. Even if this torque is more than doubled with respect to the maximum torque estimated for the IPAnema 3 Mini (Figure 3.5), it corresponds only to 15% of the nominal torque (2.1 Nm) of the motors mounted on the CORHDA. This means that the influence of the friction in the kinematic chain of the CORHDA is smaller than in the kinematic chain of the IPAnema 3 Mini, where the maximum friction torque was 22% of the nominal motor torque. This is consistent with the design choices made during the development of the CORHDA, where there is only one pulley between the motor and the EE (Figure 3.6) to reduce cable wear and friction, whereas, in the IPAnema 3 Mini, there are five pulleys (Figure 3.3).

Table 3.6: Coefficients of the CORHDA friction torque model in Eq. (3.3), where f must be given in newtons, and v must be given in meters per second, as in Figure 3.9. R^2 is the coefficient of determination of the model.

		$\boldsymbol{i=1}$	$\boldsymbol{i=2}$	$\boldsymbol{i=3}$	$\boldsymbol{i=4}$	$\boldsymbol{R^2}$
τ_F (Nm)	c_{ip}	$-1.86\cdot10^{-2}$	$5.14\cdot10^{-4}$	$-3.38\cdot10^{-4}$	$-3.02\cdot10^{-2}$	0.892
	c_{in}	$-1.64\cdot10^{-2}$	$-5.18\cdot10^{-4}$	$3.86\cdot10^{-4}$	$5.55\cdot10^{-2}$	0.79

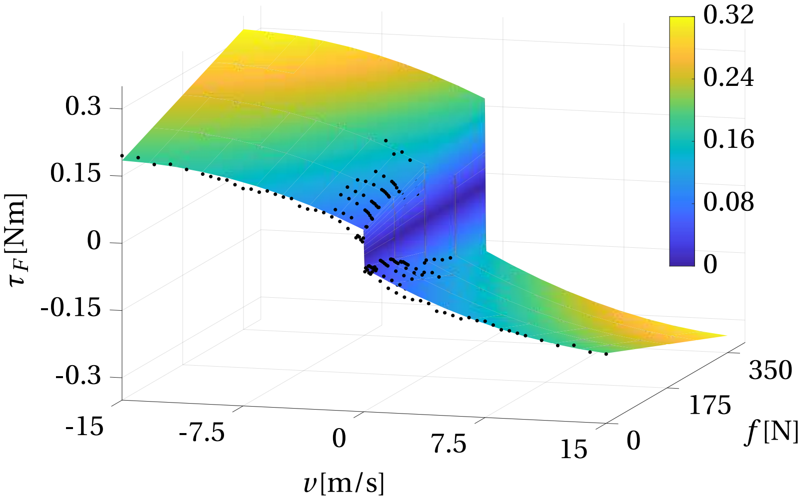

Figure 3.9: Friction torque model described in Eq. (3.3) and with the coefficients listed in Table 3.6.

3.3 Following-error model

As an alternative to using the motor torque in the feedback loop to control the cable forces (see Section 3.4), we propose using the so-called *Following-Error* (FE), which is the difference between the position set for to the motor and the actual one. This is because the torque that the motor measures is usually noisy, and it must be filtered before it can be used in a feedback control loop. Filtering the torque means introducing a delay, which could be a problem for fast movements. The FE has a noisy behavior too, but its oscillations are usually appreciably smaller than the torque ones. Our experiments show that the FE can be used in a feedback loop without any filter.

3.3.1 IPAnema 3 Mini

The IPAnema 3 Mini is equipped with Beckhoff servomotors AM3121-0201 connected to Beckhoff EL7201 terminals, which receive inputs from a Programmable Logic Control (PLC) program developed in TwinCAT 3.1 and running with a cycle time of 1 ms. The motors are velocity controlled (i.e., a velocity command is given to the motor by the PLC program every millisecond), with a PI controller at the drive level ($PI_{velLoop}$). The position feedback loop is closed in the PLC program with a different P controller ($P_{posLoop}$) that was untouched in this work. If the integral part of the velocity control loop of the drive is removed, a pure proportional controller designed only through its gain K_p acts on the motor ($P_{velLoop}$). In this configuration, when an external torque is applied to the motor shaft, the latter moves to a position that allows the motor torque to balance the external one. Due to the proportional nature of the control law, the position reached by the motor is different from the commanded one, so that a FE arises. In practice, the motor behaves as a torsional spring: a FE on the shaft gives a specific torque and vice versa. This behavior was modeled through experimental tests similar to those used to model the friction torque. In this case, the tests were executed in a static way by applying different loads to the cable with different values of K_p. By recording the motor torque τ and the motor FE for every test, a set of FE points (every one corresponding to a given torque and a given K_p) is found, which provides, through

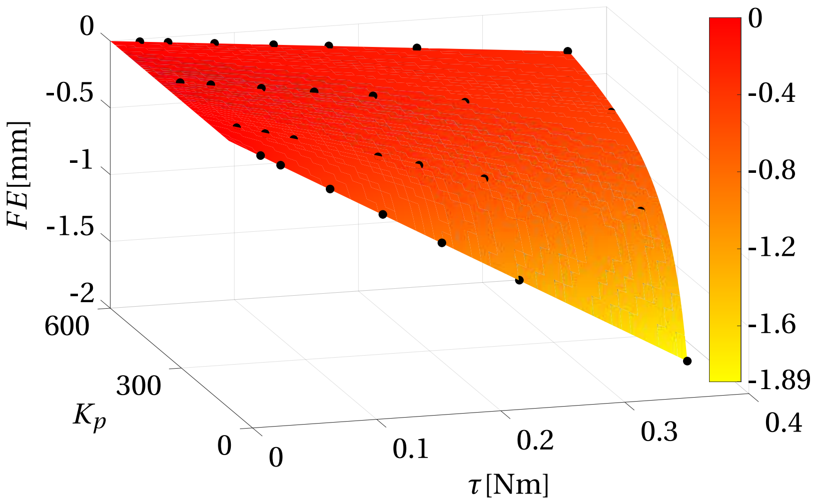

Figure 3.10: FE model described in Eq. (3.6), with $c_f = -0.511$, and $c_v = 8.893 \cdot 10^{-5}$

a best-fit procedure, the coefficient c_f in the static model reported below (Figure 3.10):

$$FE(\tau, K_p) = c_f \frac{\tau}{K_p} \tag{3.6}$$

However, Eq. (3.6) is insufficient to model the FE during a movement. Indeed, while executing the dynamic tests to model the friction torque, the FE was also recorded. Even though the complete PI controller at the drive level was used in those tests, a FE approximately proportional to the cable velocity (and not influenced by the applied force) was observed. The corresponding coefficient c_v was obtained through a best-fit procedure.

To obtain the final model of the FE, the terms depending on the torque and the cable velocity are summed together:

$$FE(\tau, v) = c_f \frac{\tau}{K_p} + c_v v \tag{3.7}$$

In this work, K_p is always equal to 200. This default value was considered appropriate to avoid a too stiff transmission (with a higher K_p) or too compliant (with a smaller K_p).

In the experimental tests, the FE is computed as a difference between the actual cable length and the commanded one. So it is measured in meters, as a length. The values of the coefficients c_f and c_v are found with the same procedure used for the computation of the friction model coefficients, i.e., by using the Matlab function `lsqnonlin` with a step tolerance and a function tolerance both equal to 10^{-6}. Their values are $c_f = -0.511$, and $c_v = 8.893 \cdot 10^{-5}$, with τ expressed in newtons per meter and v in meters per minute. These values lead to a coefficient of determination R^2 of the FE model equal to 0.999. The coefficients c_f and c_v differ by several orders of magnitude, but the value that multiplies τ in Eq. (3.7) is $c_f/K_p = -2.55 \cdot 10^{-3}$. Working with coefficients with this order of magnitude was not a problem since double-precision variables were used in the PLC code.

3.3.2 CORHDA

The CORHDA is equipped with Beckhoff servomotors AX8041-0H21 linked to Beckhoff AX8206-0100 dual-axis modules connected to a Beckhoff AX8640-0000 power supply module. The robot is controlled with a PLC program written in MPS (Marchesini Programming System), the programming language used to develop the control logic of Marchesini Group machines. MPS is a language different from the classical Structured Text commonly used in industrial automation applications, but it acts similarly from a logical point of view. The PLC program of the CORHDA runs with a cycle time of 1 ms.

The main difference between the control strategy developed on the CORHDA, and the one already described for the IPAnema 3 Mini is that the motors of the CORHDA are position-controlled at the drive level. This means that the drive takes a position reference as input, and the internal $P_{posLoop}$ controller of the drive closes the position control loop and, at a higher frequency, the velocity control loop. On the contrary, on the IPAnema 3 Mini, the position control loop was closed in the PLC program (i.e., with a frequency corresponding to the cycle time of the PLC program), and the velocity control loop was closed at the drive level. To replicate the motor behavior as a torsional spring described in Section 3.3.1, the procedure is the same: using a pure proportional controller on the velocity loop is necessary. The fact that the position control loop is directly operated by the drive allows this loop to be closed with higher frequencies that are possible thanks to the better performances of the drive of the CORHDA if compared to the ones of the IPAnema 3 Mini. This means that the reference position commanded to the motors is better tracked, so the part of the FE depending on the velocity in Eq. (3.7) is always negligible (i.e. $c_v \rightarrow 0$), reducing Eq. (3.7) to Eq. (3.6).

Following the experience gained on the IPAnema 3 Mini, the FE model of the CORHDA was developed for the default value $K_p = 0.081$, which is considered appropriate to avoid a transmission that is too stiff (with a higher K_p) or too compliant (with a smaller K_p). In practice, there is a simple linear correlation between the torque on the motor shaft and the FE, which is represented by the following equation:

$$FE(\tau) = c'_f \tau \tag{3.8}$$

The coefficient $c'_f = c_f / K_p$ was found with the data acquired in a set of static tests as the ones described for the IPAnema 3 Mini. The best-fit procedure with the Matlab function `lsqnonlin` gives a coefficient $c'_f = 5144.71$ count/Nm. The coefficient of determination R^2 in this case is equal to 0.99999998. Instead of expressing the FE as an equivalent cable length, here, it was preferred to represent it in motor counts. For every motor shaft revolution, 262144 counts are defined: one count represents the precision of the motor encoder. The FE model of the CORHDA kinematic chain is shown in Figure 3.11.

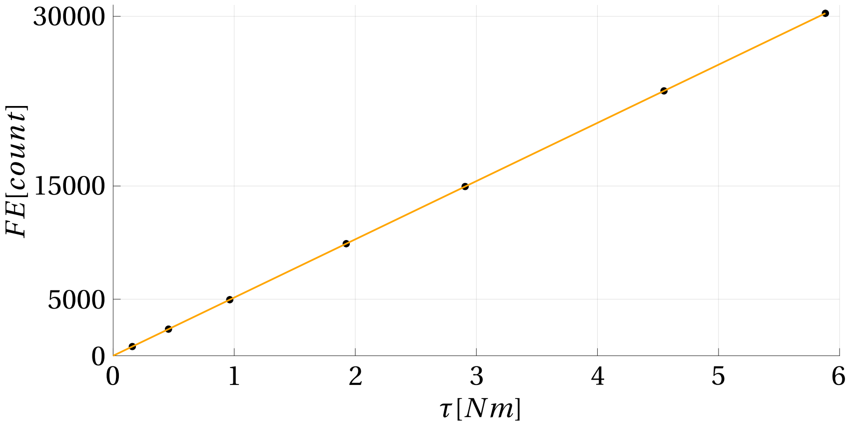

Figure 3.11: FE model described in Eq. (3.8) with $c'_f = 5144.71$ count/Nm

3.4 Hybrid control strategy

3.4.1 IPAnema 3 Mini

For the HC strategy adopted in this thesis, the first step is to choose the pair of cables to be force-controlled for a given pose of the EE or a given trajectory. To achieve this, the FD sensitivity index σ_{ij} introduced in [135–137] is computed for every possible pair of cables i and j of the IPAnema 3 Mini. We choose to force control the pairs of cables $1,2$ and $3,4$ because they guarantee $\sigma_{ij} < 1.5$ N in large parts of the robot static constant-orientation wrench feasible workspace, as shown in Figure 3.12 (for this computation, the EE orientation is always considered to be described by the rotation matrix $\mathbf{R} = \mathbf{I}_3$, where $\mathbf{I}_3$ is the 3×3 identity matrix). Choosing a pair of force-controlled cables with a small σ_{ij} (values of σ_{ij} smaller than 2 N can be considered practically acceptable [137]) helps to minimize the errors in the achieved FD.

Once the force-controlled cables are identified, it is necessary to define the control strategy that acts on these wires to obtain the desired forces. Figure 3.13 shows three schemes in which the subscript "i" refers to the generic i-th cable. All schemes present a high-level PID controller (PID_{HL}) which computes the value Δl to be added to the cable length l_i after a multiplication with a scaling factor h. The locution "high-level" is used to differentiate this controller from the ones that act on the motor at the drive level. The controllers differ in the variables that are given to PID_{HL} as input for the computation of Δl: a force in HC-f (Figure 3.13a), a torque in HC-τ (Figure 3.13b), and a FE in HC-e (Figure 3.13c). For all controllers, l_i is computed (as the cable velocity v_i and acceleration a_i) by the robot inverse kinematics (IK). The force f_i desired in the i-th cable is computed by the FD algorithm. The scaling factor h is always in the interval $[0;1]$, and it is modified only during the activation or deactivation phases of the controller or when changing the pair of cables to be force-controlled, according to the function

$$h = sin^2(\alpha \pm \delta) \tag{3.9}$$

α starts from 0 when the controller is activated, and it is increased at every iteration by δ until it reaches (or exceeds) $\pi/2$. Then, α is held constantly equal to $\pi/2$ ($h = 1$) until the force control is deactivated. When the controller is switched off, δ is subtracted until α reaches (or exceeds) 0. To change the force-controlled cables, it is sufficient to switch on the force control in the new cables and switch it off in the old ones. The shape of the function on the right-hand side of Eq. (3.9) is chosen in order to have a smooth transition of the coefficient h from 0 to 1 during the activation and deactivation of the controller.

The scheme in Figure 3.13(a) (HC-f) is the simplest, and it represents the situation in which force sensors are used. In this case, f_{act} is the force measured by the load cell mounted in the kinematic chain of cable i. The high-level PID controller compares f_{act} with the desired one $f_{set,i}$, which is computed by correcting the output force of the FD algorithm f_i with the friction force f_F estimated through the model in Eq. (3.5). For the computation of f_F, the theoretical values f_i and v_i are used because they yield non-noisy results. Once the cable length l_i is corrected with $h\Delta l$, it is fed to the proportional controller for the position feedback loop ($P_{posLoop}$) in the PLC, which computes a reference velocity to give as input to the PI controller ($PI_{velLoop}$) of the motor (M) drive (velocity control loop). The position-controlled cables do not need the computation of Δl, so in this case, l_i is directly input into $P_{posLoop}$.

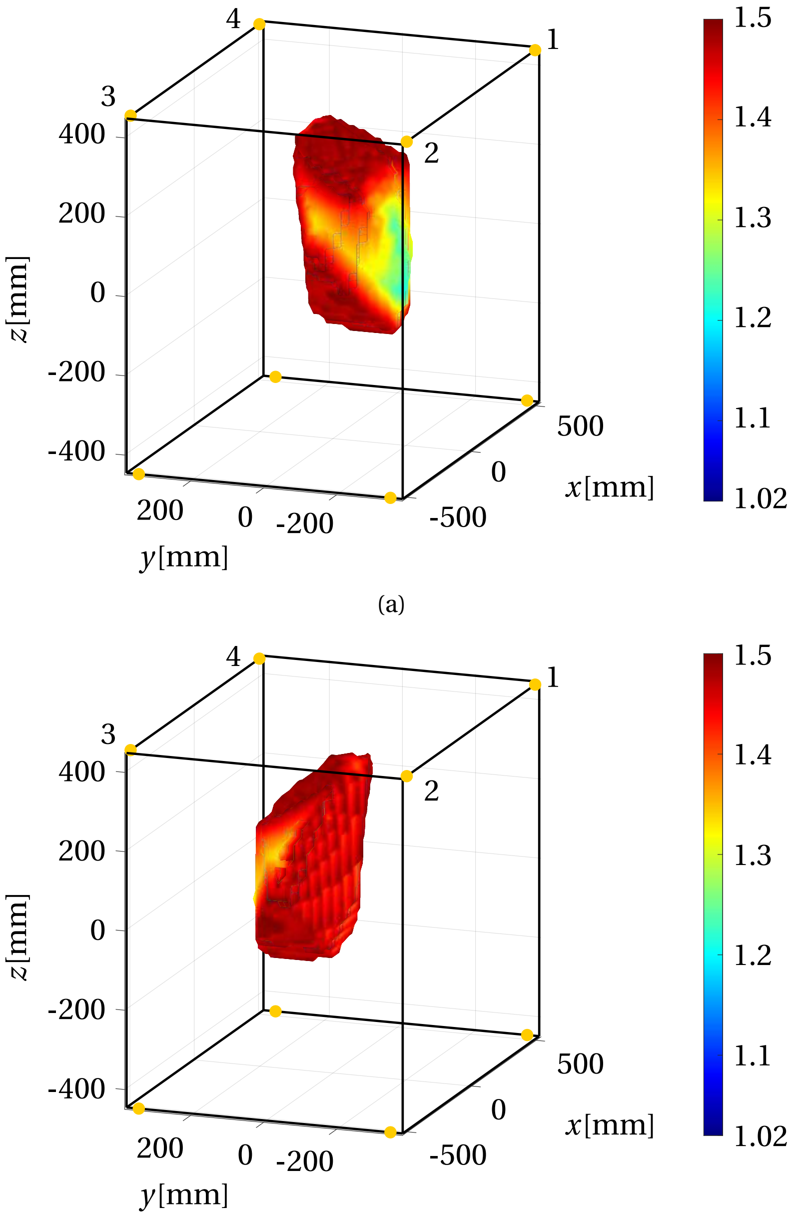

(a)

(b)

Figure 3.12: Workspace of the IPAnema 3 Mini with $\sigma_{ij} < 1.5$ N when the force-controlled cables are 1,2 (a) or 3,4 (b). The yellow dots represent the exit points of the cables from the frame.

The scheme in Figure 3.13(b) (HC-τ) is the first to force-control cable i without using the load cell. Here, the high-level PID controller takes as input the actual torque given by the motor τ_{act} and the torque τ_i that we wish to command to the motor to obtain force f_i in the cable. τ_i is computed using Eq. (3.1), where the friction torque τ_F is estimated by the model in Eq. (3.3). J_D is the inertia of all moving parts connected to the motor shaft.

Finally, the scheme in Figure 3.13(c) (HC-e) allows the i-th cable to be force-controlled using the motor FE. Here, after the computation of torque τ_i, the model in Eq. (3.7) is used to compute the FE that is desired on motor i (FE_{set}) to generate force f_i. This FE is one of the two inputs of the high-level PID controller, while the other is the actual FE measured by the motor (FE_{act}). In this case, a pure proportional controller with a gain

$K_p = 200$ is used at the drive level on the velocity loop ($P_{velLoop}$). Interestingly, in this case, the position-controlled cables that can be switched to be force-controlled during the robot motion must also have a pure proportional controller at the drive level (not to change the drive controller online). This can cause a small error in the length of the position-controlled cables, but in practice this phenomenon does not affect the robot accuracy (see Section 5.1).

The first tests of the HC were executed on a simple test bench with only two cables. One of the two cables is position-controlled, whereas the other is force-controlled by imposing a specific tension. In this configuration, all control schemes shown in Figure 3.13 were tested to tune the controller parameters with a heuristic procedure based on the Ziegler–Nichols method [147]. The transfer function that describes the high-

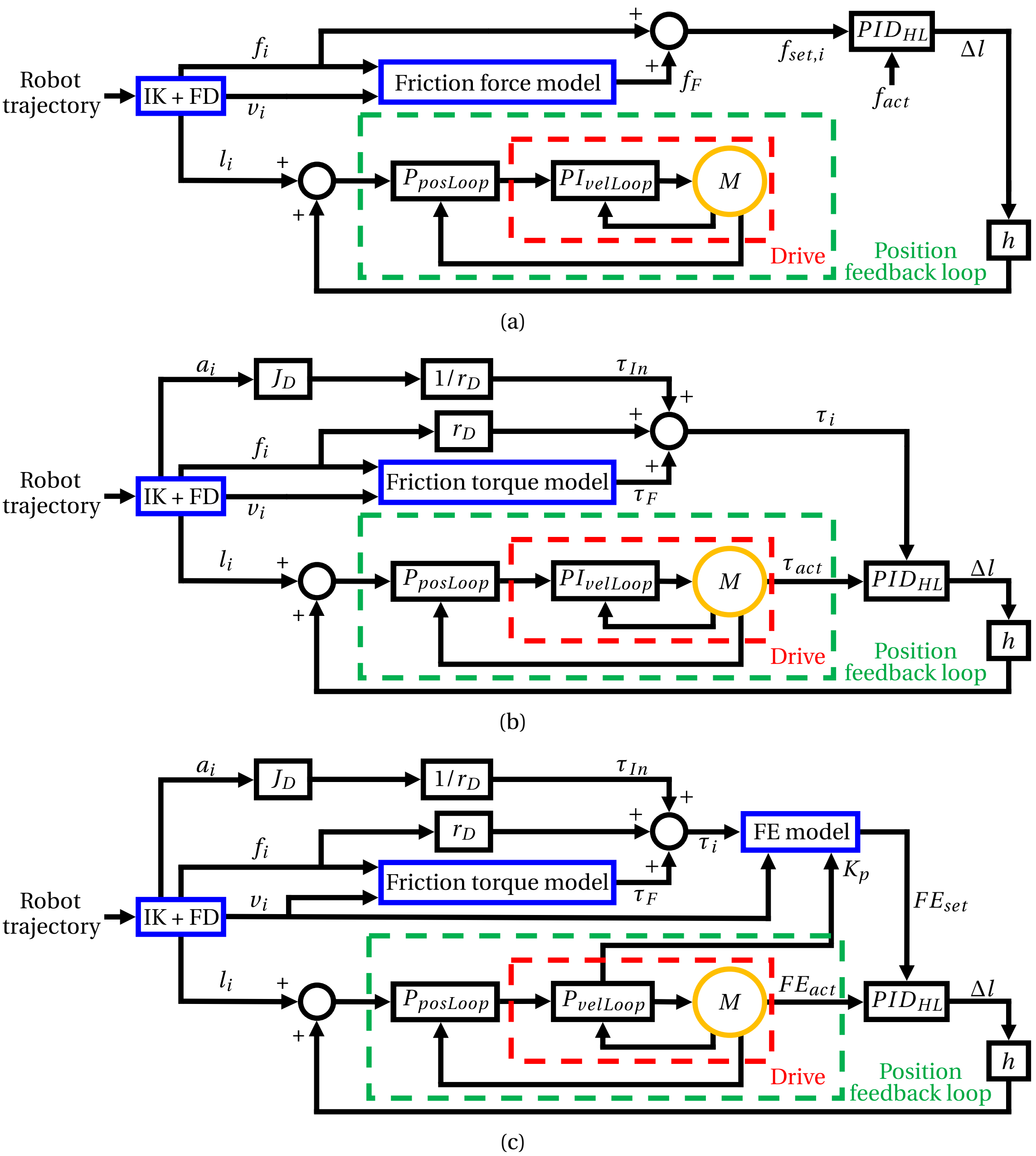

Figure 3.13: Control schemes applied to force-controlled cables by using (a) force sensor feedback, HC-f; (b) motor-torque feedback, HC-τ; and (c) FE feedback, HC-e.

level PID controller in the Laplace domain is

$$G(s) = K_{HL}\left(1 + \frac{1}{T_i s} + \frac{T_v s}{1 + T_d s}\right) \tag{3.10}$$

The parameters to be identified are the proportional gain K_{HL}, the integral action time T_i, the derivative action time T_v, and the damping time T_d. The values found for the three controllers shown in the schemes of Figure 3.13 are listed in Table 3.7. When $T_v = 0$, and thus $T_d = 0$, the derivative part of the controller is switched off and it becomes a PI controller. This happens for the controllers HC-τ and HC-e, because the values of FE and torque given by the motor (even if the torque is smoothed with a filter) are affected by some noise and using noisy inputs in the controller when the derivative part is switched on results in unwanted vibrations on the motor shaft.

3.4.2 CORHDA

As for the IPAnema 3 Mini, the static constant-orientation wrench feasible workspace of the CORHDA is analyzed to find compact areas in which force controlling a single pair of cables i, j guarantees low values of the FD sensitivity index σ_{ij}. Since it would be challenging and expensive in terms of computational time to take into account every possible orientation of the platform, the EE orientation in this phase is always described by the rotation matrix $\mathbf{R} = \mathbf{I}_3$, where $\mathbf{I}_3$ is the 3×3 identity matrix. In this way, it is possible to split the static constant-orientation wrench feasible workspace of the robot into two main areas in which it is convenient to force-control respectively the pair of cables 5,6 and 7,8. The situation is shown in Figure 3.14. Choosing to force control the pair of cables 5,6 and 7,8 guarantees to have a value of $\sigma_{ij} < 2$ when the robot EE is moved in these volumes with an orientation described by $\mathbf{R} = \mathbf{I}_3$. For motions requiring different EE orientations, the value of σ_{ij} could be different for every sampled point of the trajectory, and a different pair of cables could be the best to be force-controlled. As mentioned, it is difficult to consider every possible platform orientation a priori to make a more general characterization of the workspace. For this reason, the pair of force-controlled cables for all the trajectories tested in this thesis was done based on the workspace analysis shown in Figure 3.14.

It is possible to change the strategy for choosing the best pair of wires to be force-controlled to overcome the issue of taking into account the platform orientation in the computation of the FD sensitivity index for the robot workspace characterization. One could choose them for every trajectory tested, but this situation would not be realistically applicable to the final robot. In fact, one cannot know a priori the motion laws that the robot EE will execute since they will depend on the information coming from the vision system of the bin-picking cell. The best option would be to design an

Table 3.7: Parameters of the three different high-level PID controllers shown in Figure 3.13.

Controller	K_{HL}	T_i **(ms)**	T_v **(ms)**	T_d **(ms)**
HC-f	$3.0 \cdot 10^{-4}$	70	15	5
HC-τ	$2.0 \cdot 10^{-2}$	200	0	0
HC-e	$4.5 \cdot 10^{-1}$	7	0	0

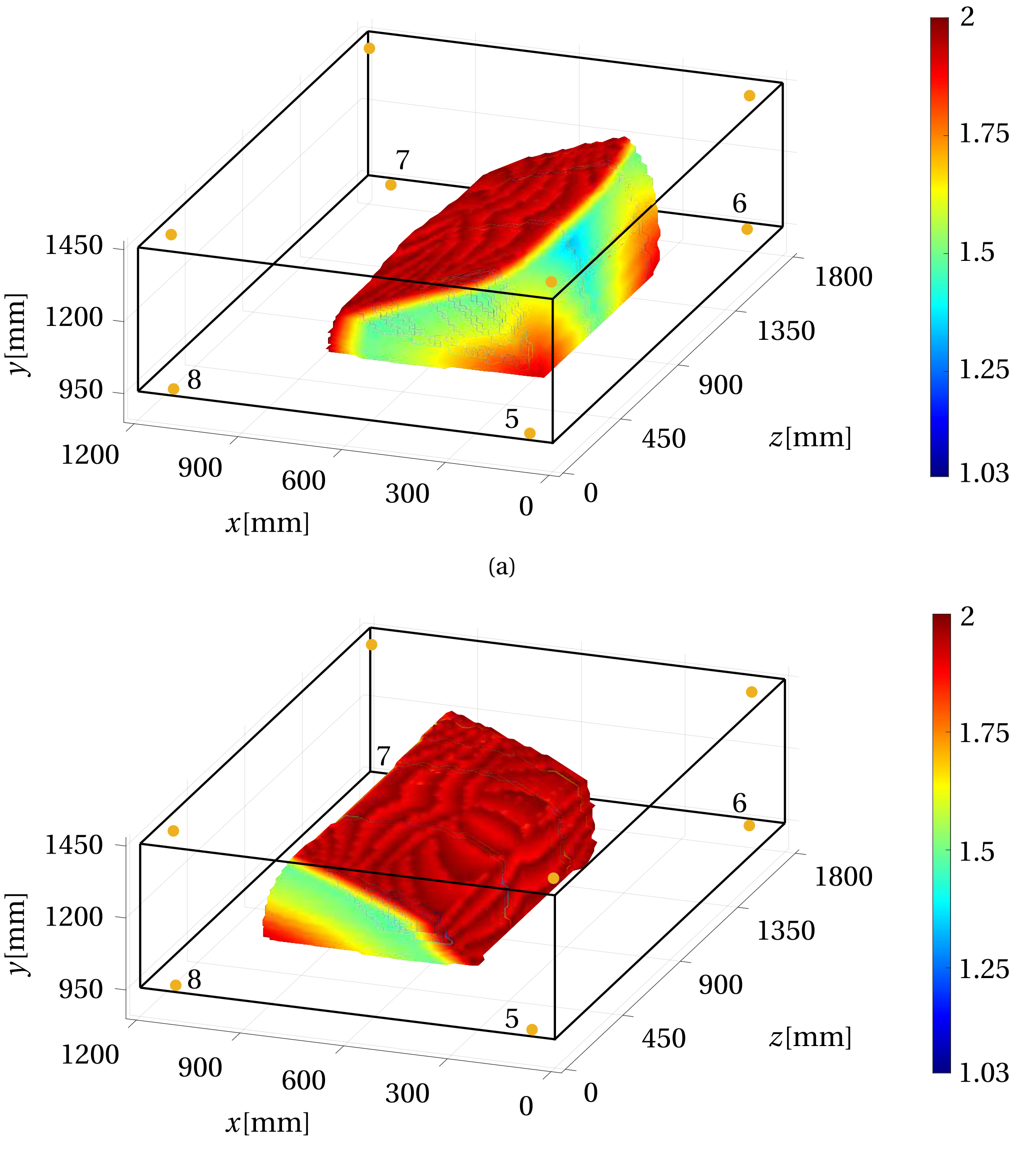

(a)

(b)

Figure 3.14: Workspace of the CORHDA with $\sigma_{ij} < 2$N when the force-controlled cables are 5, 6 (a) or 7, 8 (b). The yellow dots represent the exit points of the cables from the frame.

algorithm to compute the best pair of cables to be force-controlled for every specific movement in real-time. This can be a future research topic that still needs to be analyzed. At the moment, to verify the effectiveness of the state-of-the-art HC strategy on the CORHDA for the execution of the fast bin-picking task, the pair of force-controlled cables must be chosen according to an offline workspace characterization, like the one shown in Figure 3.14.

The control scheme for applying the HC-e controller on the CORHDA is shown in Figure 3.15(a). The scheme is similar to the one applied on the IPAnema 3 Mini in Figure 3.13(c). The main difference regards the inputs to the FE model block since, in this case, the desired FE on the force-controlled cables is only a function of the desired torque on the motor shaft, as expressed by Eq. (3.8). The control scheme highlights that the motors are controlled in position since the $P_{posLoop}$ controller is inside the drive block. Finally, the FE model returns a value (FE_{set}) directly expressed in motor

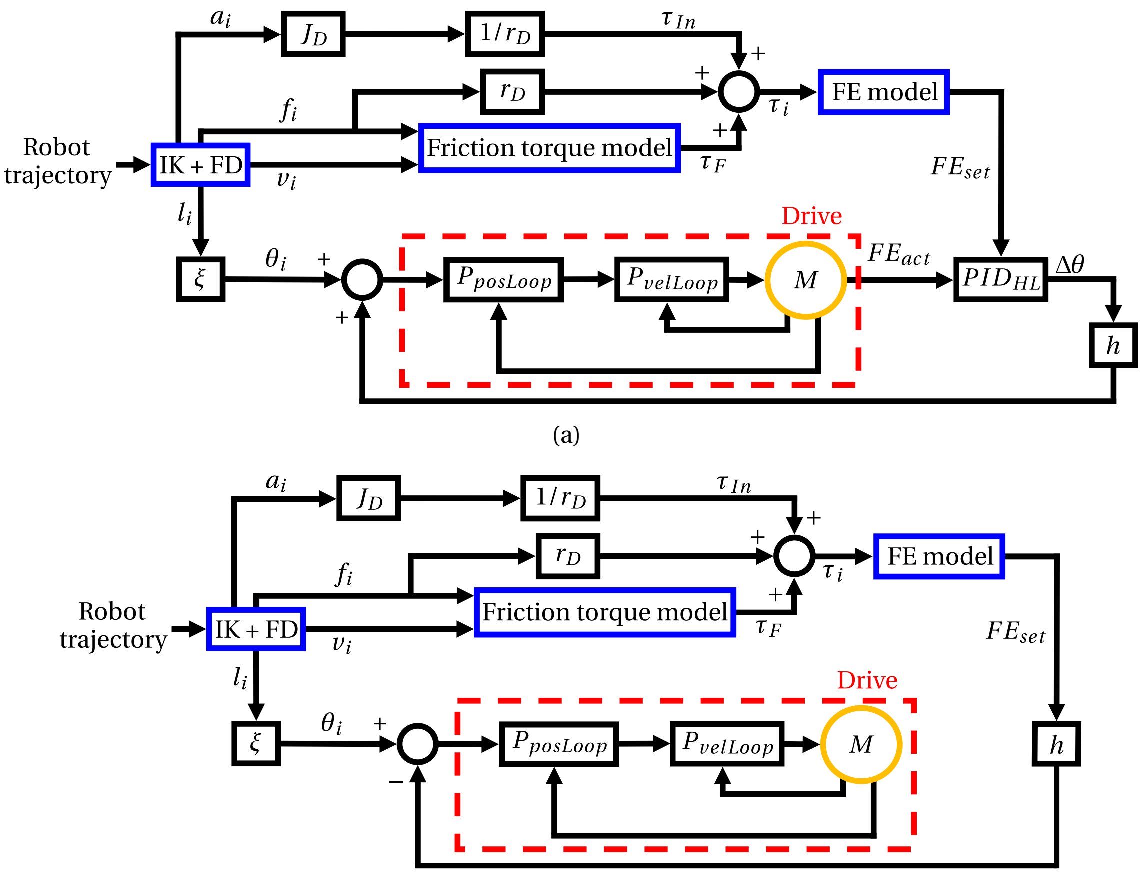

(a)

(b)

Figure 3.15: Control schemes applied to the force-controlled cables (a) and to the length-controlled cables (b) on the CORHDA.

counts. The high-level PID controller works with motor counts in input (also the actual FE coming from the motor (FE_{act}) is expressed in motor counts), and it gives in output a value $\Delta\theta$ in counts. For this reason, it is necessary to introduce the transmission ratio ξ to find the counts to command to the motor (θ_i) from the cable length computed by the robot inverse kinematics.

As done on the IPAnema 3 Mini, all CORHDA winches to be force-controlled must have the same controller at the drive level to be able to change their control in real-time (from force control to position control and vice versa). This is done smoothly through the same scaling factor (3.9) used on the IPAnema 3 Mini.

Using a pure proportional controller in the velocity loop at the drive level also for the position-controlled winches can produce an error in the cable lengths that may affect the robot accuracy. This error was considered negligible in the IPAnema 3 Mini, but this assumption is no longer valid for the CORHDA. The control scheme in Figure 3.15(b) is used to correct the theoretical commands to the position-controlled motors. The same friction model and FE model used on the force-controlled cables are introduced to compute a theoretical FE (FE_{set}) corresponding to the theoretical force acting on the i-th cable (f_i, from the FD algorithm). Since the motors behave as springs when a load is applied on the cable, the motor position (in count) corresponding to the theoretical cable length (θ_i) is modified by the actual force acting on the wire (f_i') by producing a positive FE (FE_{act}). If the force on the wire is exactly the one computed with the FD algorithm ($f_i = f_i'$), then the corresponding positive FE on the motor

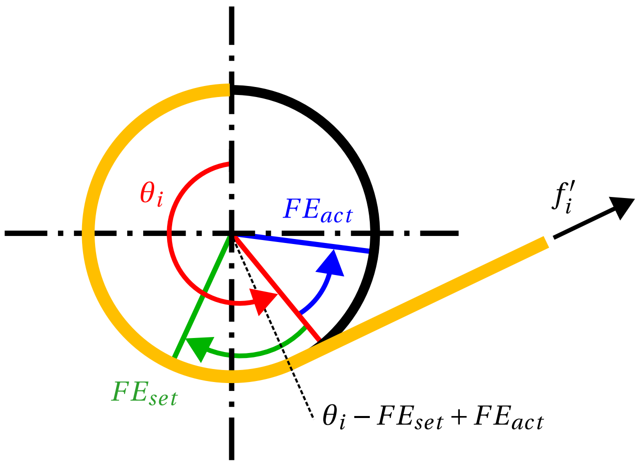

Figure 3.16: Scheme of the correction applied on the position-controlled cables of the CORHDA following the control scheme in Figure 3.15(b).

shaft is $FE_{act} = FE_{set}$. In this condition, FE_{set} is subtracted from the motor theoretical input θ_i, so the position $\theta_i - FE_{set}$ is commanded to the motor. In this way, the motor actual position after the shaft displacement due to the force $f'_i = f_i$ acting on the cable is exactly the theoretical motor input θ_i. If the force acting on the cable is different from the theoretical one (i.e., $f'_i \neq f_i$) or there are errors in the friction or FE model, FE_{act} is different from FE_{set}, and the actual position reached by the motor is $\theta_i - FE_{set} + FE_{act} \neq \theta_i$ producing an error in the pose of the EE. It was observed with static tests that the correction on the motor inputs of the position-controlled cables with FE_{set} allows to maintain errors in the motor actual position less than $1000 counts$ from the desired position θ_i. This value corresponds to a maximum error less than 1.37^o on the motor shaft and 0.48mm on the cable length. The scheme of the correction on the motor shaft is shown in Figure 3.16.

The parameters of the high-level PID, namely PID_{HL} (the ones in Eq. (3.10)) were tuned with the same procedure adopted for the IPAnema 3 Mini: the controller was first applied on a test bench with two cables (see Section 5.2 for more details). In this case, a first estimation of the parameters was done with the Ziegler-Nichols method [147]. As it happened with the IPAnema 3 Mini, the derivative part of the PID triggers unwanted oscillations on the motor shaft, so it is switched off ($T_v = 0$, $T_d = 0$). In this case, the proportional part of the controller is also not used: only low values of K_{HL} (lower than 0.5), corresponding to low controller outputs (dozens of motor counts that are negligible), are applicable in practice since higher gains make the system resonate. Finally, a pure integral controller is chosen on the test bench with two cables, and the integral gain identified was $K_i = K_{HL}/T_i = 200$. This value was tested even on the controller applied on the complete robot, and it seems to be usable for both the tested EEs: the one originally designed for the prototype (we will refer to it as EE-1) and the one developed to allow the load cells to be mounted (we will refer to it as EE-2). More details will be given in Section 4.3.3.

During the first experimental tests executed on the CORHDA with EE-1, it was seen that a more reactive PID controller with respect to the one tuned on the test bench with two cables is needed for highly dynamic motions to reasonably track the FE desired on the force-controlled cables. Some experimental tests were conducted with the overall robot to better tune the PID_{HL} controller. The controller proportional and derivative parts seem useless, and so they are still switched off ($T_v = 0$, $T_d = 0$). Only the integral

Table 3.8: Parameters of the high-level PID controllers for the HC of the CORHDA (Figure 3.15(a)) with the two different EEs.

	K_{HL}	K_{iMin}	K_{iMax}	T_v (ms)	T_d (ms)
EE-1	0	100	500	0	0
EE-2	0	100	200	0	0

gain was increased. Empirically, a gain equal to $K_i = 500$ was found for the EE-1 to build a more reactive PID. However, such a high gain gives problems when the platform is at rest by triggering unwanted vibrations of the EE, making it resonate. For this reason, it was established to change the integral gain based on the EE commanded motion: a minimum (K_{iMin}) and a maximum (K_{iMax}) integral gain are defined. When the EE is at rest, the integral gain is maintained at its minimum value ($K_{iMin} = 200$), and it is increased with a smooth transition to its maximum value ($K_{iMax} = 500$) when a movement is commanded to the robot. The same integral gains with the smooth transition between K_{iMin} and K_{iMax} were tested when the EE-2 was mounted on the robot. In this case, an integral gain of 500 is too high even during the movement of the platform, and it is not applicable. In general, every integral gain higher than 200 gave problems. For this reason, we chose $K_{iMax} = 200$ in this case. An integral gain equal to 200 is considered usable for every motion condition on the robot with the EE-2. However, it is not the best option when the platform is at rest since sometimes it could trigger small vibrations (it means that this value of K_i is nearly the maximum admissible). When the platform is at rest, a lower K_i guarantees a better behavior, so $K_{iMin} = 100$ was chosen for the EE-2.

Following the empirical considerations reported above, the same K_{iMax} cannot be chosen for both EEs. In contrast, a $K_{iMin} = 100$ works well even for the EE-1 at rest. This is because, when the platform is not moving, it is not necessary to have a reactive PID_{HL} since the desired FE is constant: even a very low K_i could work well; the only difference is the time necessary for the actual FE to reach the desired one during the tensioning phase of the cables when the robot is switched on. For this reason, K_{iMin} was unified for the EEs, leading to the integral gains listed in Table 3.8.

The procedure just described to find the gains of the PID_{HL} is empirical. The approach is not based on a mathematical model of the system for different reasons:

- It would require a long time to study an equivalent mathematical model together with the study of the methods applied in the literature to find the best tuning of the controller parameters;

- Even if a more rigorous procedure would have worked well in one case, it does not mean that the found parameters would be suitable in different cases; e.g., the fine-tuning of the parameters on the test bench with two cables could not be appropriate on the robot prototype with EE-1, or a fine-tuning based on the model of the robot with EE-1 could not work well with EE-2;

- Due to the strict time to develop the prototype described in this thesis, it was chosen to give more importance to the controller itself (one of the main novelties introduced with this work) than to the procedure to find its optimal gains.

This thesis aims to develop from a conceptual point of view the first prototype of a

CDPR capable of executing the fast bin-picking task: design, mechanical requirements, kinematics, and control architecture; the development of the complete final robot will be the object of future work. For the final manipulator, it will be helpful to study the best fine-tuning procedure of the PID_{HL} to find the optimal gains of the controller.

Chapter 4

Robot Design

This chapter deals with the design of the CORHDA prototype, developed to prove the feasibility of the bin-picking task described in Chapter 1. The mathematical models introduced in Chapter 2, as well as the HC-e controller presented in Chapter 3, are implemented in the robot software.

4.1 Robot task and conceptual design

A more specific task than the one described for a general bin-picking application in Chapter 1 must be defined to develop the CORHDA prototype. In particular, the maximum dimensions of the robot and the dynamics necessary to satisfy the required productivity must be considered when designing its mechanical parts. For this reason, an exemplary task is introduced in this Section.

First, the frame should be as small as possible, but it must guarantee the required workspace. The pick-up area is defined by two boxes of dimensions 420 × 300mm in the top view, with a height of 100mm, while the placing area is represented by a conveyor belt with a width of 200mm. The bins and the conveyor belt are located at a height of 900mm from the ground (see Figure 4.1). These data were defined by Marchesini Group s.p.a., and they will be considered assigned for the rest of the robot development; the manipulator frame dimensions in the top view are then assumed to be

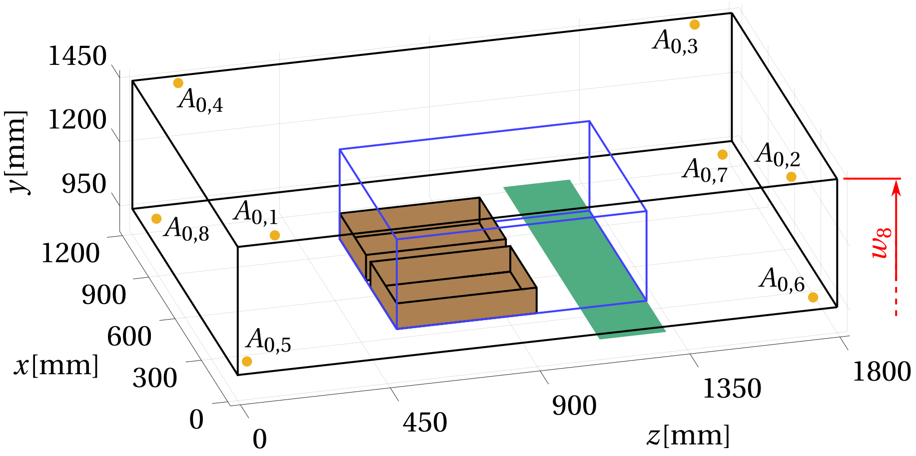

Figure 4.1: Exemplary bin-picking task. The blue lines identify the task workspace. The mounting height of the higher pulleys (w_8) is a free parameter left to the designer's choice.

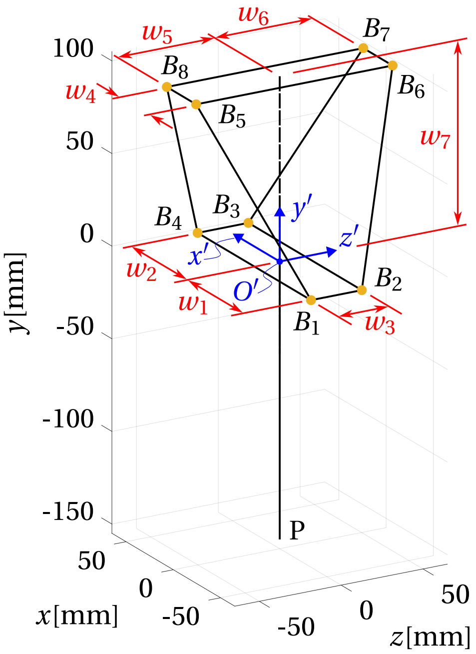

Figure 4.2: Scheme of the EE designed for the CORHDA prototype. The dimensions $w_1, \dots, w_7$ are free parameters that are not constrained by the predefined task.

1800×1200mm. To develop a robot with a symmetric architecture capable of six DOFs, eight cable exit points arranged approximately in the vertices of a parallelepiped must be used. Swivel pulleys mounted on the frame were chosen to reduce cable wear. The bins and the conveyor belt constrain the mounting height of the lower set of pulleys, i.e. the y coordinate of $A_{0,i}$, with $i = 5, 6, 7, 8$ (see Figure 2.1) to $950mm$. The only free parameter in the definition of the robot frame is, thus, the mounting height of the higher pulleys (points $A_{0,i}$ with $i = 1, 2, 3, 4$), i.e., w_8. In the first design of the CORHDA prototype, this dimension is chosen to be 1450mm. However, Section 4.2 will show how w_8 can be optimized, together with the EE geometry. The final locations of points $A_{0,i}$ are decided considering the mechanical dimensions of the swivel pulleys and winches (see Section 4.3) and are listed in Table 4.1.

To allow the robot to grasp products inside the bins, an offset between the cable attachment points and the picking point P is necessary on the EE (i.e., the distance between points P and O' in Figure 4.2). A value between 100mm and 200mm is considered appropriate for a general bin-picking task. Accordingly, an offset dimension equal to 150mm was chosen for the exemplary task described in this section, as shown in Figure 4.2. This scheme also shows the cable arrangement established according to the analysis presented in [148] and the first simulations to verify cables non-intersections. The wires that exit from the higher layer of the proximal anchor points are connected to the lower layer of distal anchor points and vice-versa. This choice is common in many overconstrained CDPRs with 8 cables and 6 DOFs. Besides the previous assumptions, the rest of the EE geometry is defined by the dimensions $w_1, \dots, w_7$, which are free parameters left to the designer's choice. For the first robot prototype, these values (see Table 4.1) were not optimized, but they were simply chosen to allow the CORHDA to cover almost all the so-called *task workspace*, i.e., the volume in which the bins and the central part of the conveyor belt are located. This volume is represented by the blue parallelepiped shown in Figure 4.1. Section 4.2 describes a method to determine the EE geometry: this strategy will be adopted for future developments once the ma-

	x	y	z		x'	y'	z'
$A_{0,1}$	50.0	1450.0	124.5	B_1	−60.0	0.0	−15.5
$A_{0,2}$	50.0	1450.0	1675.5	B_2	−60.0	0.0	15.5
$A_{0,3}$	1150.0	1450.0	1675.5	B_3	60.0	0.0	15.5
$A_{0,4}$	1150.0	1450.0	124.5	B_4	60.0	0.0	−15.5
$A_{0,5}$	84.5	950.0	50.0	B_5	−15.5	100.0	−60.0
$A_{0,6}$	84.5	950.0	1750.0	B_6	−15.5	100.0	60.0
$A_{0,7}$	1115.5	950.0	1750.0	B_7	15.5	100.0	60.0
$A_{0,8}$	1115.5	950.0	50.0	B_8	15.5	100.0	−60.0

Table 4.1: Cable attachment points of the CORHDA on the frame (expressed in coordinates of the FRS $O - xyz$ shown in Figure 2.1(a)) and on the EE (expressed in coordinates of the MRS $O' - x'y'z'$ shown in Figures 2.1(a) and 4.2). All values are expressed in millimeters.

nipulator real task inside the bin-picking cell will be defined.

Figure 4.3 shows an example of a pick-and-place trajectory. It is chosen with a pick-up point in the bin area as distant as possible from the place point (on the conveyor belt) to find one of the most challenging movements. The orientations of the EE do not contribute much to increasing the motion dynamics; for this reason, a constant orientation described by the rotation matrix $\mathbf{R} = \mathbf{I}_3$ is assumed throughout the movement. For working areas like those represented in Figure 4.3, the CORHDA should satisfy the maximum productivity of 100pieces/min, which means that one complete movement cycle (i.e., the back-and-fort motion between the bins and the conveyor belt) must be executed in 0.6s. If only the movement from the bins to the conveyor belt is taken into account, a duration of 0.3s is required. During the pick-and-place cycle, downtime due to the picking and placing of the product should be considered, so a time smaller than 0.3s is available for executing the robot movement from the pick-ap area to the placing one. The path shown in Figure 4.3 is supposed to be traveled with the velocity and acceleration profiles shown in Figure 4.4, which satisfy the required motion duration. This way, a maximum overall velocity and acceleration, respectively, of 8.6m/s and 228m/s^2 are reached by the EE. These values are taken as a benchmark that should

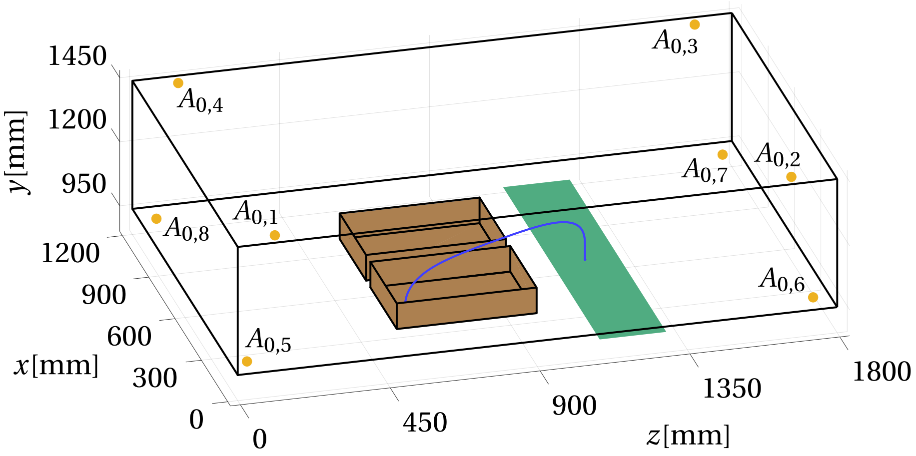

Figure 4.3: Example path of typical pick-and-place task. To define the maximum dynamics that the CORHDA must achieve. This path is executed by the point P of the EE as shown in Figure 4.4.

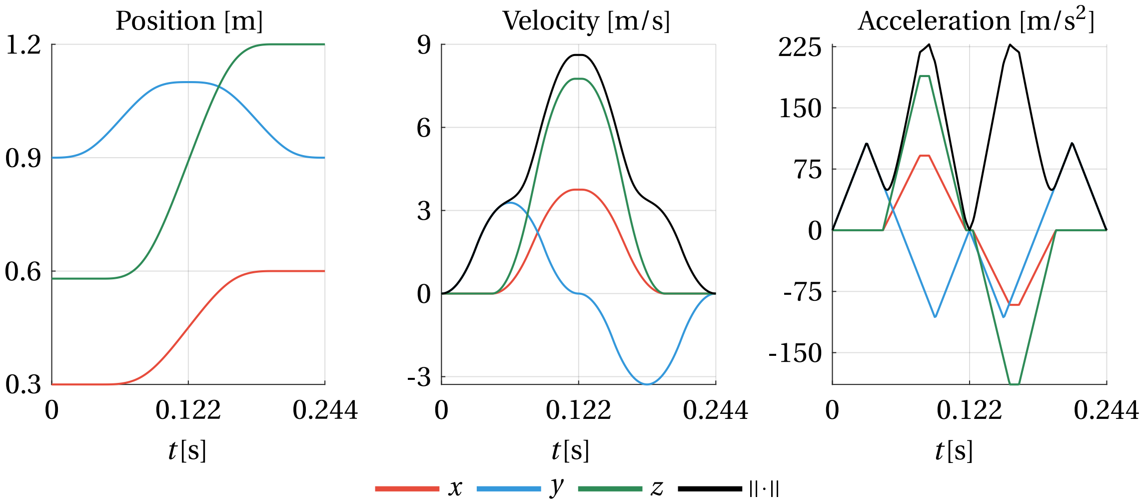

Figure 4.4: Evolution in time of the EE position, velocity, and acceleration during the execution of the path shown in Figure 4.3 for the definition of the maximum CORHDA velocity (8.6m/s) and acceleration (228m/s^2).

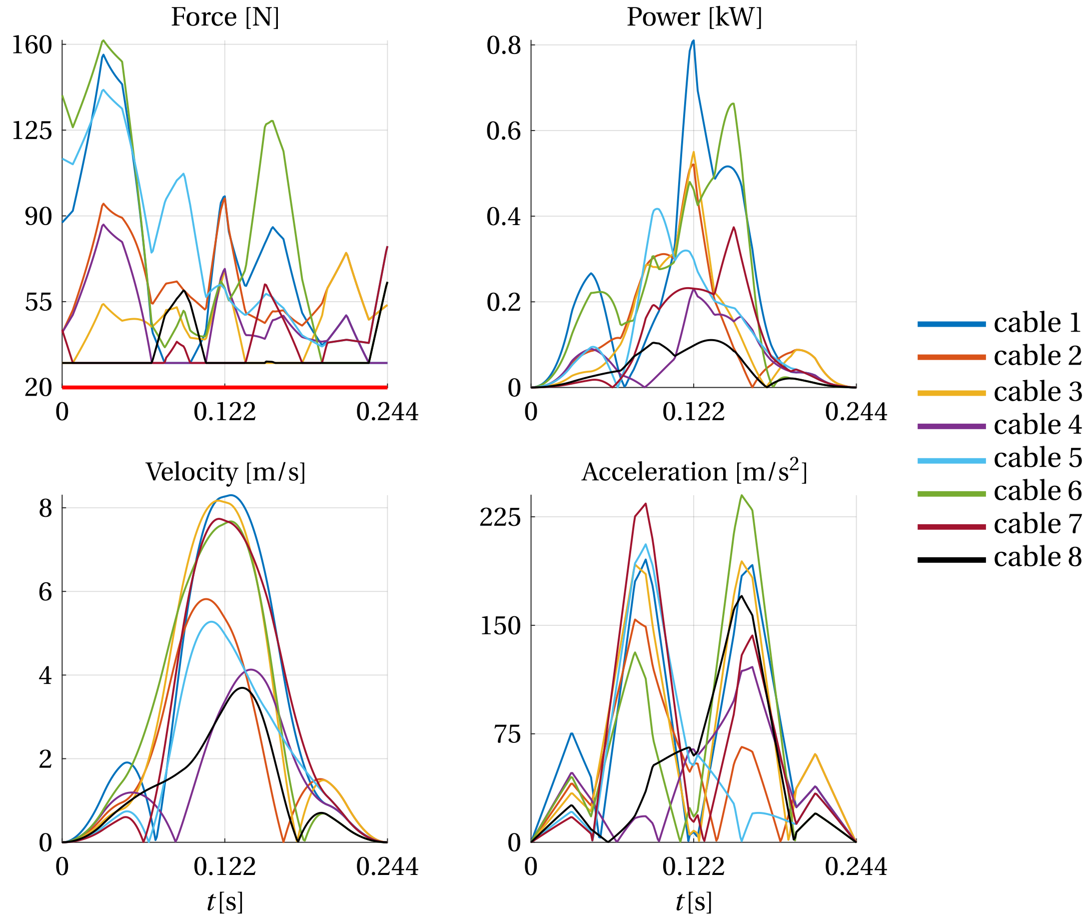

Figure 4.5: Evolution in time of the quantities found with the resolution of the inverse kinetostaic problem of the CORHDA along the trajectory shown in Figures 4.3 and 4.4. These data are considered in the development of the CORHDA mechanical design.

be satisfied by the CORHDA prototype.

The aforementioned trajectory is exploited to define the mechanical design of the manipulator. Based on the robot geometry, the inverse kinematics of the manipulator (see Section 2.1) can be solved along the motion law to find the evolution in time of cable lengths, velocities, and accelerations. Cable velocities and accelerations are shown in Figure 4.5. These data are important for defining the winches mechanical architecture (including the motors). The maximum cable velocity (8.3m/s) determines (together with the transmission ratio between the motor and the cable) the maximum motor speed, while the maximum acceleration is an important factor in the choice of the winch architecture. This parameter can be neglected for applications with low dynamics because the torque generated by the desired cable tension is much higher than the inertial torque of the masses connected to the motor shaft. However, this is not true for the CORHDA, where cable accelerations reach values as high as 234m/s^2.

For solving the manipulator inverse kinetostatics, the method described in Section 2.3, based on the algorithm introduced in [100], is exploited. The FD chosen minimizes the 2-norm of the cable tension array to reduce the power demand on motors (due to the high reachable velocities). The limits defined for cable tensions are those already presented in Section 3.2.2. The higher limit $f_{max} = 350$N is necessary to avoid cable breaking. The lower limit considered for the FD computation is $f'_{min} = 30$N, which is slightly increased compared to that defined in Section 3.2.2, i.e., $f_{min} = 20$N. This is done to take some margin to avoid the real wire forces dropping under the limit due to inevitable small inaccuracies in the force control (see Section 5.3). To compute the FD for a given pose of the EE, it is necessary to know its mass properties. During the design phase of the manipulator, the EE mass was initially defined based on its first CAD model. Along the iterative process of the robot design, this mass was modified until the feasibility of the movement with the final mass was verified. Figure 4.5 shows the cable forces computed with the mass of EE-1 (see Section 4.3). These tensions

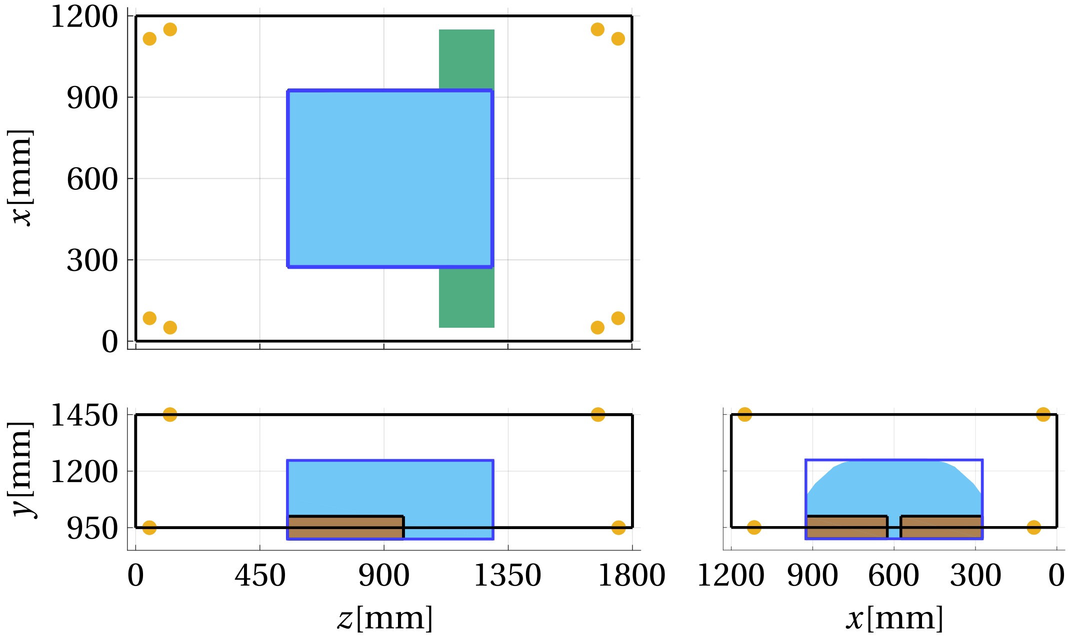

Figure 4.6: Representation (in light blue) of the total orientation wrench feasible workspace volume of the CORHDA inside the task workspace (89.2%), when $\mathscr{R}_{\mathscr{O}} \equiv \mathbf{I}_3$ (pure translational workspace).

(as the velocities) influence the winch design because they must be considered when defining the transmission ratio between the cable and the motor shaft. Figure 4.5 also shows the evolution in time of the power generated on cables (based on the desired force and velocity).

Once the robot geometry and its force limits are known, it is possible to compute the manipulator Total Orientation Wrench Feasible Workspace ($\mathcal{W}_{\mathcal{T}\mathcal{O}}$, see Eq. (2.56)). To give an idea of the robot capabilities, $\mathcal{W}_{\mathcal{T}\mathcal{O}}$ is computed for a fixed orientation of the EE described by the rotation matrix $\mathbf{R} = \mathbf{I}_3$. This is the so-called pure translational workspace of the manipulator. To perform the workspace computation, a discretization method [39] is applied by sampling the task workspace shown in Figure 4.1 with a dense grid of points. The workspace volume is estimated through the number of sampled points that belong to $\mathcal{W}_{\mathcal{T}\mathcal{O}}$ [149,150]. The pure translational workspace of the CORHDA is shown in Figure 4.6, and its volume is 89.2% of the task workspace.

4.2 Optimization of the end-effector geometry

This section introduces a procedure for performing the geometric optimization of the CORHDA EE. The method is general, and it will be applied for defining the EE geometry when a real bin-picking task will be defined (the task analyzed in Section 4.1 is only an example for the development of the first CORHDA prototype).

The positions of the EE distal anchor points are among the main parameters influencing the robot behavior and its workspace [151,152]. The topic of CDPR optimal design was analyzed in the literature for different fields and with different approaches. Some examples refer to:

- warehousing [73,74];
- rehabilitation [63,68];
- construction and maintenance of building facades [71];
- load lifting [49,149];
- classical 3-DOF pick-and-place [83];
- generic CDPRs without a specific task [80,150].

The main goal of designing an efficient EE geometry for the application in the bin-picking task is to maximize the Total Orientation Wrench Feasible Workspace $\mathcal{W}_{\mathcal{T}\mathcal{O}}$ of the manipulator by neglecting the rotation of the EE around the y' direction of the MRS (see Figure 4.2). This is the less important DOF for picking products from a pile: if the pile is approximated with a pyramid, the rotations around x' and z' are necessary to bring the EE in the correct pose to take products from the faces of the pyramid. In practice, the optimization aims to maximize the semi-aperture angle ψ of the cone that the EE can describe in every position of the task workspace (see Figure 4.7). The whole cone is described by varying the angle β from 0^o to 360^o. The platform geometry is completely defined by the dimensions shown in Figure 4.2, which determine the cable attachment points on the EE. These, together with the mounting height of the pulleys at the top of the workspace (see Figure 4.1), form the vector $\mathbf{w} = [w_1\ w_2\ w_3\ w_4\ w_5\ w_6\ w_7\ w_8]$ of the optimization problem unknowns.

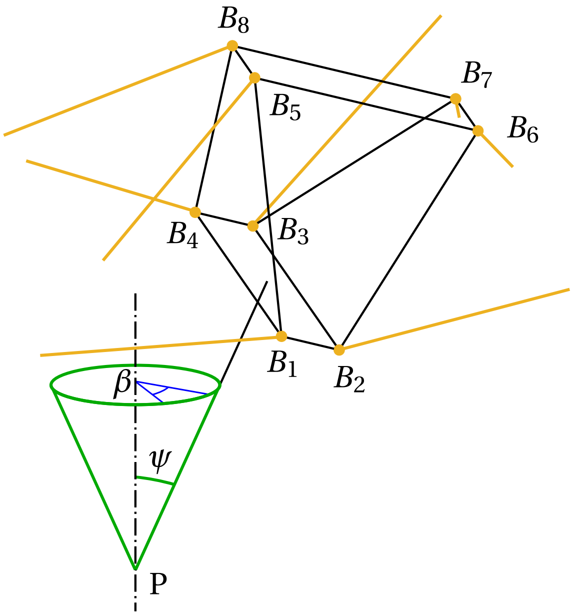

Figure 4.7: Cone described by the EE to define $\mathscr{W}_{\mathscr{T}\mathscr{O}}$.

The fitness function is built with a set of points (P_k with $k = 1,\dots,r$) defined in the task workspace. A weight (c_k) is associated with every point based on the robot task: the most important points (with a higher weight) are those in the pick-up area (i.e., the bins area in Figure 4.1), since here it is more important to have a bigger ψ. The exact numerical values of the weights c_k are empirically designed by running some tests of the optimization problem and by evaluating the workspace of the optimized EE geometries in different cases: they are a free parameter to be chosen by the designer. The fitness function $f(\mathbf{w})$ is computed as follows:

$$f(\mathbf{w}) = \sum_{k=1}^{r} \left(90 - \psi_{max,k}(\mathbf{w})\right) \cdot c_k \tag{4.1}$$

where $\psi_{max,k}$ is an approximate estimation of the maximum semi-aperture angle ψ (in degrees) of the cone that the EE can describe in P_k such that P_k belongs to the robot workspace for every orientation in which $\psi \le \psi_{max,k}$. In practice, Eq. (4.1) represents the weighted sum of angles complementary to the maximum ψ in every point P_k; the complementary value of $\psi_{max,k}$ is used only for simplicity since it is common to deal with fitness functions to be minimized (not to be maximized). To apply Eq. (4.1), the mass and moment of inertia of the platform are estimated for the current set of parameters ($\mathbf{w}$) based on the volume that the current distal EE points enclose. Then, the following operations are executed for every point P_k:

- the EE is placed in P_k;
- if conditions (2.56) and (2.57) are not verified with $\mathbf{R} = \mathbf{I}_3$ (i.e., P_k do not belong to the pure translational workspace of the robot), then $\psi_{max,k} = -90^o$ and $c_k = max_k(c_k)$ are imposed; in this situation, the $k-$th term of the summation in Eq. (4.1) is equal to $180^o \cdot max_k(c_k)$, which is a very high value compared to the terms corresponding to points that belong to the pure translational workspace, even if the point is assigned a small weight; as a matter of fact, it is important to obtain a platform that guarantees to reach all points P_k at least with $\mathbf{R} = \mathbf{I}_3$;

- otherwise, the maximum cone angle reachable by the platform in P_k is approximately estimated by repeating the check on conditions (2.56) and (2.57) for incremental values of ψ; for each ψ, such conditions are verified for sampled values of β from 0^o to 360^o; when one of the two conditions is no longer valid, the iterations stop; $\psi_{max,k}$ is the maximum value of ψ for which conditions (2.56) and (2.57) are valid for all sampled values of β.

To obtain an optimized solution, the fitness function (4.1) is minimized by using a Genetic Algorithm (GA). A GA can work even if the fitness function is highly non-linear and discontinuous, i.e., when gradient-based algorithms fail; GAs were already used for CDPR optimization [63, 73, 80]. In particular, the GA defined in MATLAB through the function `ga` is exploited. Since the GA works by creating an initial random population and then making random changes to some individuals at every new population, the same algorithm was executed many times with the same input parameters. This is because the results of the random choices made by the algorithm produce different sets of optimal parameters (even if all the optimal solutions are similar). Moreover, different input parameters (e.g., different sets of input points and their weights) are tested. The parameters settled on Matlab to manage the GA are the following:

- maximum number of generations (500);
- function tolerance (10^{-3}) and maximum number of stall generations (15), which together define the stopping criteria of the optimization;
- crossover fraction (0.7), which defines the percentage value of individuals created for the next generation by crossover;
- initial population Matrix (Initial Guess in Table 4.2), which defines the first individual for a constrained minimization problem;
- lower and upper bounds (shown in Table 4.2) which constrain the searching area.

The initial guess given in input to the GA is not chosen according to the distal anchor points listed in Table 4.1, otherwise w_3 and w_4 would be too similar to the lower bound defined in Table 4.2, and their value could influence the optimization algorithm.

The optimized parameters ($\mathbf{w}_{opt}$) obtained through the GA are shown in Table 4.2. It is interesting to notice that an asymmetry is introduced in the EE, since $w_5 \neq w_6$. This is due to the nature of the task, which is not symmetric along the z-coordinate because of the presence of the bins (pick-up area). Here, the total orientation of the EE is more important for the correct gripping of the products. For this reason, a higher weight is associated with the points P_k in this area. If the task is different (e.g., different locations of bins or conveyor belt), by simply changing the position and the weights of

	w_1	w_2	w_3	w_4	w_5	w_6	w_7	w_8
Lower bound	45	45	30	30	45	45	60	1150
Upper bound	100	100	150	150	100	100	200	2000
Initial guess	60	60	50	50	60	60	100	1450
$\mathbf{w}_{opt}$	88.3	88.3	31.5	31.5	54.6	70.8	127.8	1640

Table 4.2: Optimized parameters in millimeters.

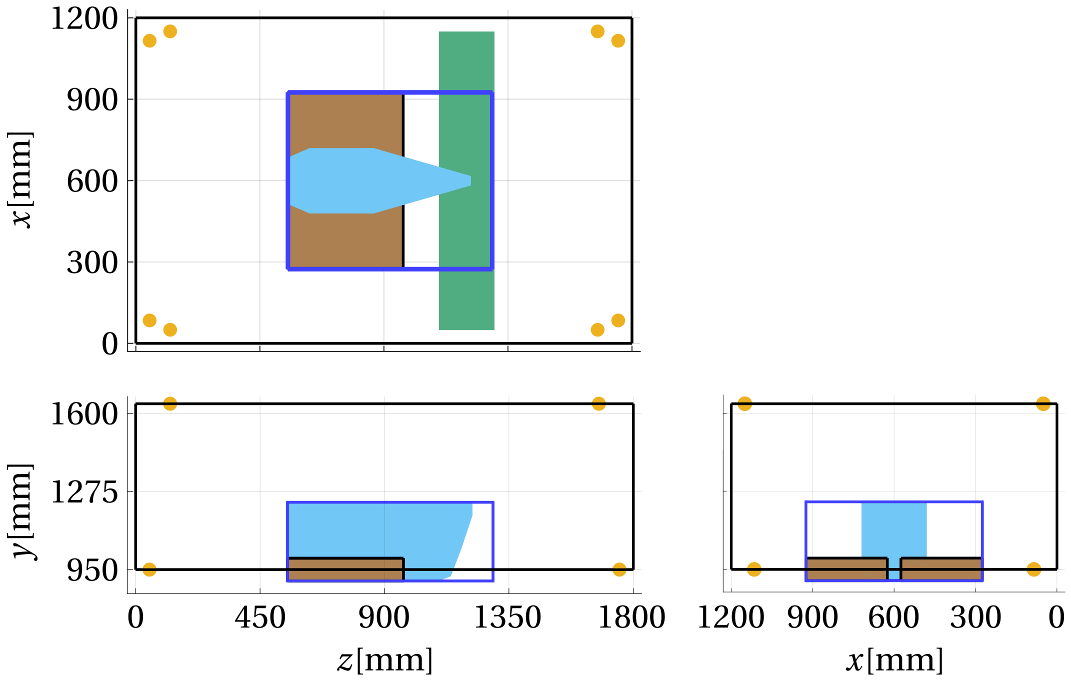

Figure 4.8: Representation of the total orientation wrench feasible workspace volume of the CORHDA for $\psi = 35^o$ in the optimized configuration.

the points given in input to the fitness function, one can obtain another EE geometry with a different symmetry.

The Total Orientation Wrench Feasible Workspace volume is computed for different values of the cone angle ψ. The case $\psi = 0^o$ represents the pure translational workspace. The results are shown in Table 4.3 for the actual EE (see Table 4.1) and the optimized solution. For the new EE geometry, Figure 4.8 shows the robot workspace when $\psi = 35^o$. This volume is asymmetric due to the asymmetry of the new platform. This reflects the robot task and the fitness function designed for it.

Since the optimization aims only to maximize $\mathscr{W}_{\mathcal{T}\mathcal{O}}$, there is no control over the tensions required to maintain the platform in equilibrium. The robot geometry influences its statics, so in many works related to CDPR optimization, one of the main objectives is minimizing the maximum cable tensions. This is important to reduce the motor size. To verify the acceptability of the proposed solution, the same pick-and-place trajectory defined by Figures 4.3 and 4.4 was simulated even with the optimized EE geometry. The evolution in time of the cable forces in this situation is shown in Figure 4.9, where they are compared to those already shown in Figure 4.5 for the actual CORHDA EE. Higher forces are required for the optimized solution, but their increment is small. Finally, the maximum cable-tension average value in the pure translational workspace of the robot is evaluated. This parameter reaches 126.6N for the initial guess solution and 111.4N for the optimized one. These values validate the usability of the optimized platform for executing the task.

ψ Actual EE	0^o 89.2%	10^o 75.3%	20^o 64.9%	30^o 42.6%	35^o 0.0%
$\mathbf{w}_{opt}$	95.5%	87.9%	80.2%	64.5%	22.8%

Table 4.3: Percentage volumes of $\mathscr{W}_{\mathcal{T}\mathcal{O}}$ compared to the task workspace.

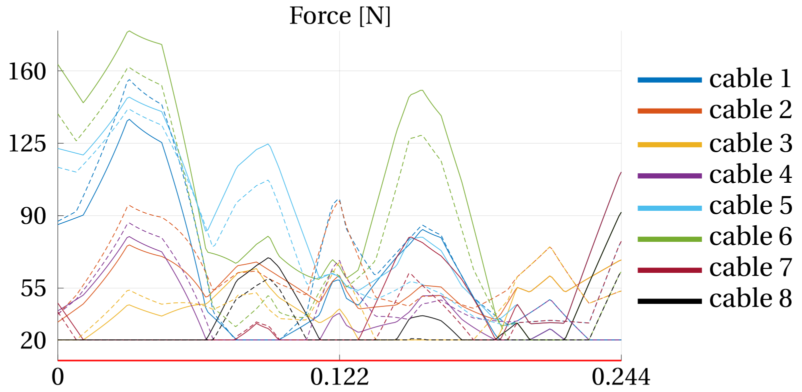

Figure 4.9: Evolution in time of the cable tensions during the trajectory in Figure 4.4 with the optimized EE (solid lines) compared to those computed with the actual EE shown in Figure 4.2 (dashed lines).

4.3 Mechanical design of the robot components

The simulations described in Section 4.1 were the starting point for the mechanical design of the robot components.

4.3.1 Winch design

The actuation system is the first element that must be defined for the robot operation. A complete analysis of this topic is reported in [145].

Initially, linear actuators were considered [66], but they would require a too-long stroke for the cable length that must be uncoiled in the CORHDA winches. To solve this problem, it is possible to mount several pulleys on the linear actuator by using a hoist architecture as shown in [109]. However, this system seems inappropriate in an industrial context since the double bending of the wires increases their wear. The classical solution is to coil the cable on a drum (typically with a helicoidal geometry) connected to a motor. This method is widely used, and it has different implementations. The cable exit point is often fixed, employing mobile elements. For example in [127, 153] a spooling helper is used to guide the cable out of the winch. The spooling helper is an element connected to the drum that moves along the direction of the rotation axis by following the wire exit point, which changes over time. A similar concept is also applied when the movement of the cable exit point is compensated by the motion of the drum itself instead of the spooling helper [77, 144, 145]. To do so, the drum is commonly mounted on a screw with the same pitch as the drum helix. Both these solutions are interesting because they allow easy reconfigurability of the robot by simply moving the winches with fewer constraints than in other cases. For example, if a fixed drum architecture is used, the movement of the wire exit point on the drum forces to mount the first guiding pulley to a certain distance from the winch such that the angle δ in Figure 4.10 is always below a certain limit (approximately 2^o). However, both solutions involving the spooling helper and the translating drum were discarded since, in those cases, the motor has to move many mechanical elements in the kinematic chain. This is a problem for the CORHDA if the wire accelerations are considered. When cable dynamics like those shown in Figure 4.5 are involved during the robot movement, the inertial torque on the motor generated by the moving elements is very high. The more moving elements are connected to the drum, the more motor torque is required. For

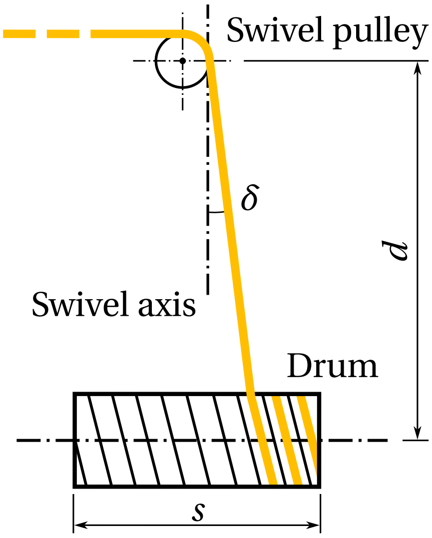

Figure 4.10: Scheme of the winch architecture chosen for the CORHDA prototype. The drum is fixed to minimize the inertia connected to the motor.

this reason, the winch based on a fixed drum configuration like that in Figure 4.10 was chosen for the CORHDA prototype.

It was decided to directly connect the motors to the drums to reduce the friction in the kinematic chain. This is paramount for applying the hybrid control strategy introduced in Chapter 3 for obtaining the desired cable tensions without directly measuring the actual forces in the wires with load cells. Using gears between motors and drums would have made modeling the friction in the kinematic chain more difficult, making the controller unusable. The transmission ratio between the motor and the cable only depends on the drum radius. The simulations introduced in Section 4.1 demonstrated that high cable velocities are required for the execution of the fast movements related to the bin-picking task (see Figure 4.5). A large drum radius is preferable to reach high cable velocities. On the contrary, high cable tensions are easier to obtain with a small drum radius; otherwise, the torque necessary to correctly tense the cables would be too high. Considering the possible motor sizes available from the Beckhoff catalog, the choice was to design a drum with a radius $r_D = 20\text{mm}$ directly connected to the Beckhoff servomotor AX8041-0H21. When connected to a power supply with a nominal voltage of 400V, this motor guarantees nominal and maximum torques, respectively, equal to $\tau_n = 2.1\text{Nm}$ and $\tau_{max} = 9.1\text{Nm}$. Its maximum mechanical speed is $n_{max} = 9000\text{rpm}$, while its nominal power is $P_n = 1.76\text{kW}$. By considering the drum radius, it is possible to compute the corresponding nominal cable force (f_n), maximum cable force (f_{max}), and maximum cable velocity (v_{max}), namely:

$$\begin{aligned} f_n &= \frac{\tau_n}{r_D \cdot 10^{-3}} = 105N \\ f_{max} &= \frac{\tau_{max}}{r_D \cdot 10^{-3}} = 455N \\ v_{max} &= \frac{2\pi n_{max}}{60} \cdot r_D \cdot 10^{-3} = 18.8m/s \end{aligned} \tag{4.2}$$

All these values satisfy the constraints and the required dynamics for executing the exemplary trajectory (see Figure 4.5). In particular, the maximum cable force of 350N is reachable. Also, the nominal power given by the motor is much higher than the maximum power required by each cable during the same movement. Initially, lower-sized motors were considered, but the price difference with those chosen did not justify their use. The chosen motors have the margin for being used even for the future development of the robot. Since the maximum cable velocity is more oversized compared to the maximum wire force, a smaller drum radius could be used to increase the cable forces without increasing motor torque, and this would also expand the manipulator workspace. However, the value of 20mm was chosen according to the necessity of having a minimum internal diameter for the drum assembly on its shaft (see Figure 4.11(b)). Moreover, a smaller coiling radius would have increased the drum length by making the winch too large.

It is interesting to notice that the motor shaft moment of inertia (including a brake)

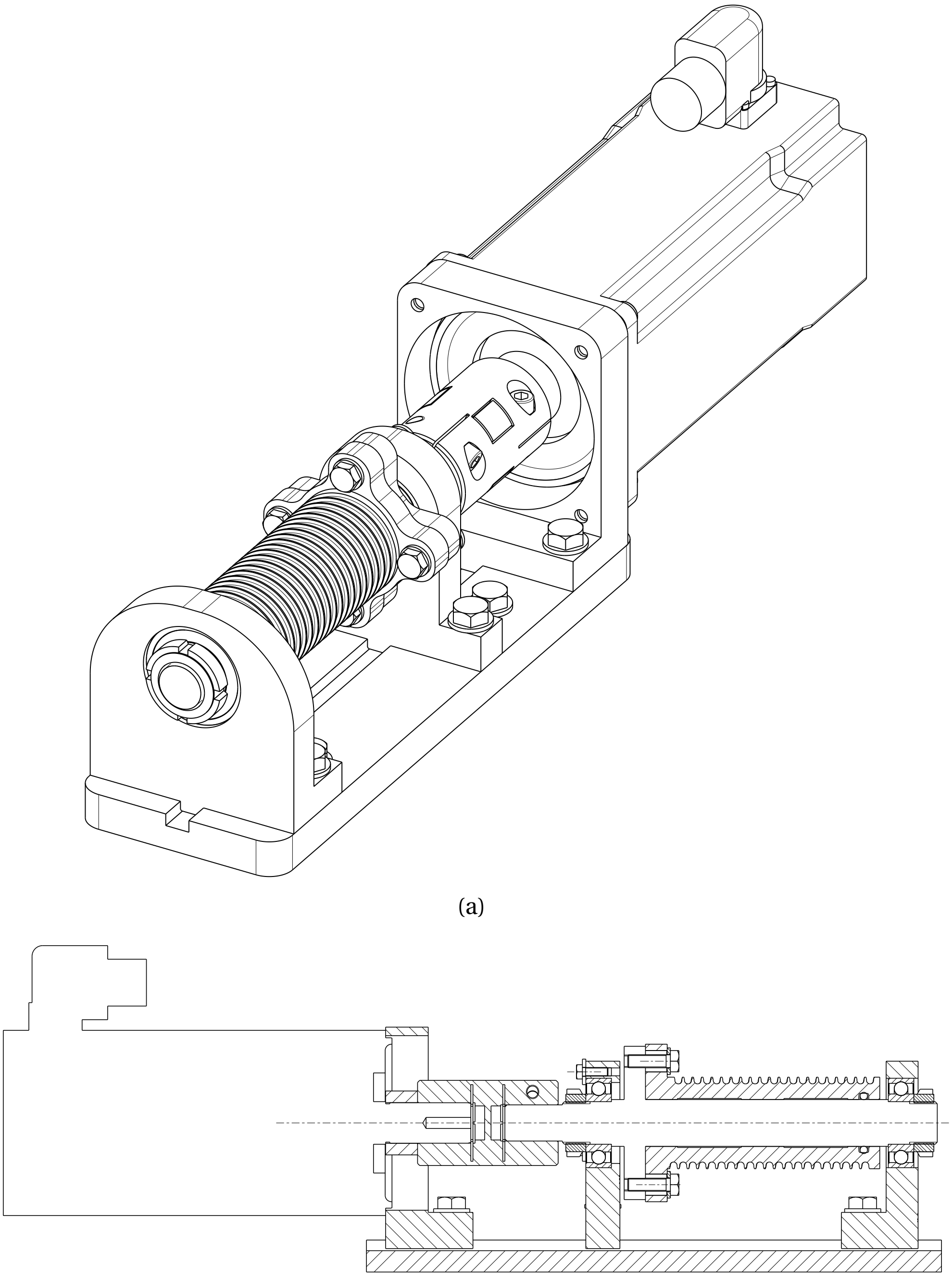

(a)

(b)

Figure 4.11: CAD model of the CORHDA winch.

is $J = 173\text{kgmm}^2$. To understand the effect of inertia in movements like the one shown in Figure 4.4, the inertial torque of the motor shaft corresponding to the maximum cable acceleration in Figure 4.5 (i.e., $a_{max} = 234\text{m/s}^2$) is:

$$\tau_{In} = \frac{a_{max}}{r_D \cdot 10^{-3}} \cdot J \cdot 10^{-6} = 2.02Nm \tag{4.3}$$

This value is almost equal to the nominal motor torque and corresponds to an equivalent force of 101N on the cable, higher than the cable tensions desired for most of the movement (see Figure 4.5). This value is increased by considering the drum inertia. For this reason, it is impossible to use other moving masses in the kinematic chain of the CORHDA (e.g., spooling helpers).

Finally, Figure 4.11 shows the mechanical components of the CORHDA winches. The motor shaft is directly connected to the drum shaft with a jaw coupling having a high-stiffness elastomer insert. The drum shaft is made of aluminum to reduce its mass and inertia. The drum is made of a photopolymer resin through stereolithography since its complex shape makes it difficult to produce it with standard machining. With this design, the inertia moment of the total moving mass connected to the motor shaft is 195.3kgmm^2, a value similar to that of the motor shaft.

4.3.2 Kinematic chain between the winch and the end-effector

The use of steel cables to actuate the CORHDA was discarded due to their high mass, which is incompatible with the required dynamics. The chosen wires are LIROS D-Pro Dyneema braided ropes with a small working stretch (less than 1%) and a diameter of 3mm. The breaking load of this cable is 950kg, which is much higher than the one obtained by applying the maximum force during the robot operation. Oversizing the cable diameter in terms of breaking load is necessary for CDPRs to extend the wire life. Otherwise, the wear due to friction effects when they slip in drums and pulleys would quickly break them. The cable diameter of 3mm is compatible with the coiling radius of the drum (20mm).

To reduce cable wear and friction as much as possible, only one swivel pulley, which guides the wire from the winch to the EE, is present in the kinematic chain. This is possible thanks to the controller presented in Chapter 3, which does not exploit force sensors. Otherwise, load cells should be mounted in the kinematic chain by adding more pulleys. The scheme of each wire kinematic chain is shown in Figure 4.10. The radius of the swivel pulley was chosen according to the cable diameter so as not to make the wire curvature on the pulley too high. All moving parts are designed in aluminum to reduce their mass, except for the counterweight mounted on the back of the pulley to keep it balanced. The CORHDA swivel pulley CAD model is shown in Figure 4.12.

As mentioned in Section 4.3.1, a winch architecture with a fixed drum constrains the relative positioning of winches and swivel pulleys. The minimum mounting distance d_{min} in Figure 4.10 is computed according to the maximum value of the angle δ (δ_{max}) and the useful drum length s, namely:

$$d_{min} = \frac{s}{2\text{tg}(\delta_{max})} \tag{4.4}$$

For the CORHDA winches, by considering $s = 45\text{mm}$ and $\delta_{max} = 2^o$, the minimum distance $d = 1288\text{mm}$ is found. By taking into account this value, it was decided to

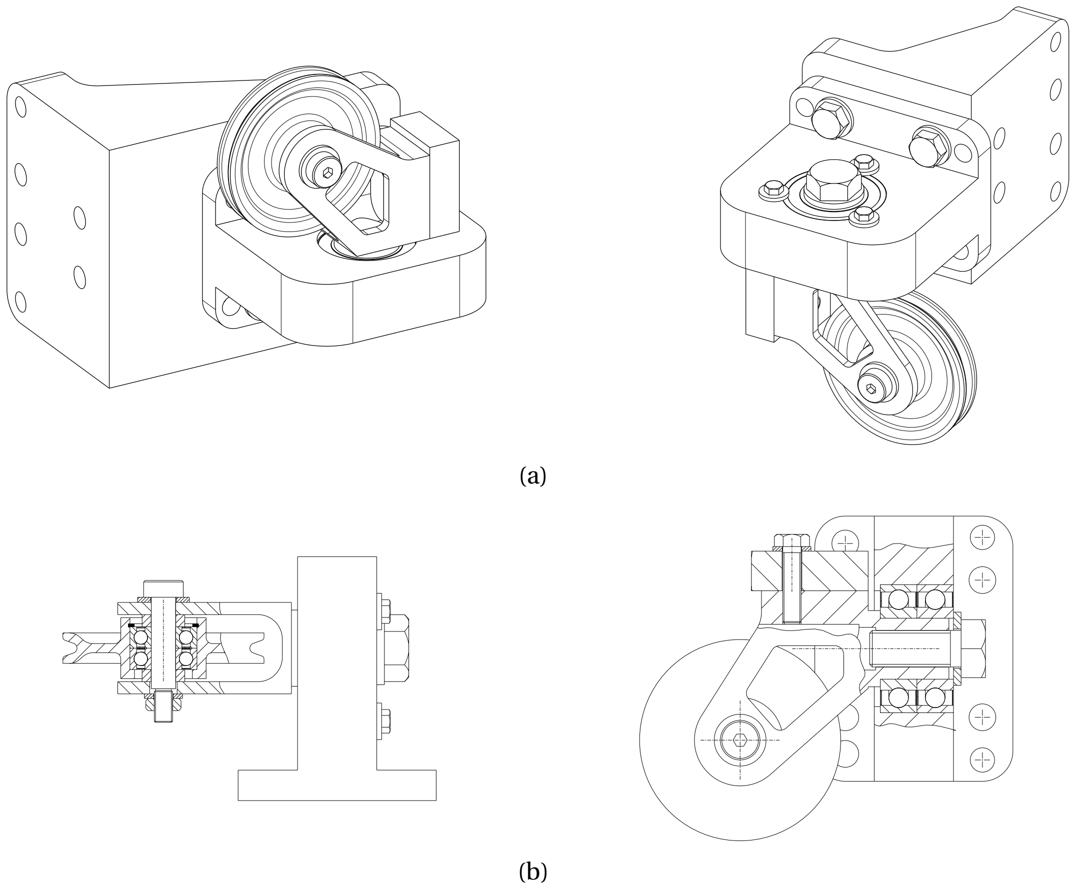

(a)

(b)

Figure 4.12: CAD model of the CORHDA swivel pulley. The possible mounting positions on the robot frame are both shown in (a).

mount the pulleys with their swivel axes parallel to the gravity direction y. This way, it is possible to exploit the vertical dimension of the CORHDA (which is a free parameter) by mounting the winches and the swivel pulleys in each vertical frame edge, as shown in Figure 4.13. This way, the lateral sides of the parallelepiped enclosing the manipulator are left free for easy access to the robot workspace. This is important for the future implementation of the CORHDA in a packaging line. If swivel axes parallel to the x or z coordinate were chosen, the cables between the drum and the pulleys would have cluttered the access to the inner part of the workspace. This mounting of the swivel pulleys justifies the position of points $A_{0,i}$, which are not aligned along the frame edges as shown in Figure 4.1.

4.3.3 End-effector mechanical design

The robot EE was designed according to the geometry introduced in Table 4.1 and shown in Figure 4.2. The gripper for the pick-and-place operations was not designed since the prototype was developed to evaluate the robot kinematics, control strategy, and winch mechanical design. On the EE shown in Figure 4.14 a component was 3D printed only to visualize the possible size of a future gripper. This part was not mounted on the EE for the tests described in Section 5.3. All trajectories assigned to the CORHDA and analyzed in Section 5.3 refer to the center O' of the MRS on the EE, not to the pick-up point P (see Figure 4.2). Figure 4.14 shows EE-1 (see Section 3.4.2) developed to obtain a mobile platform as light as possible by implementing mechanical

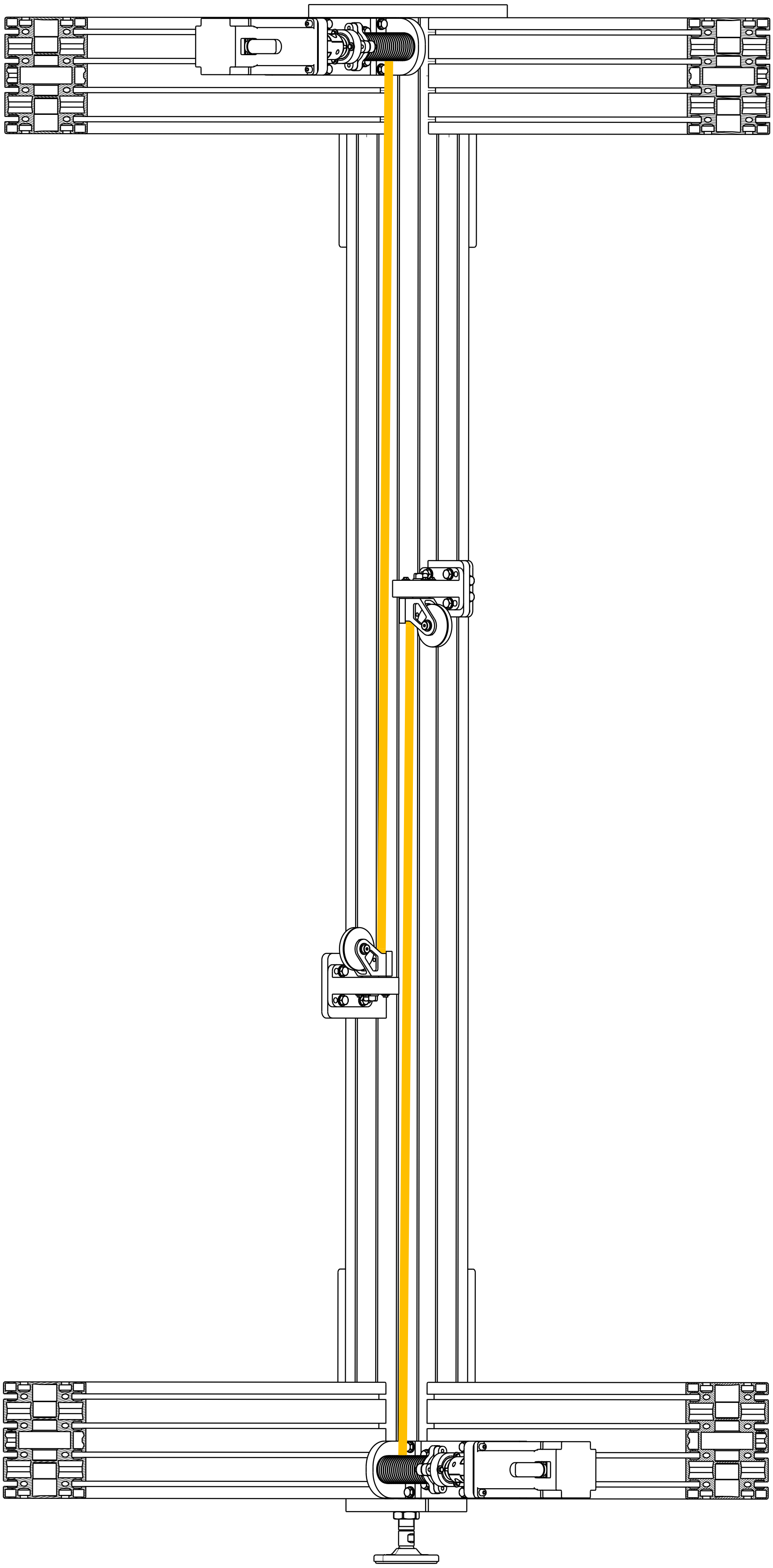

Figure 4.13: Mounting of the winches and swivel pulleys on the CORHDA frame. The cable exiting from the drum and entering the swivel pulleys is highlighted in yellow.

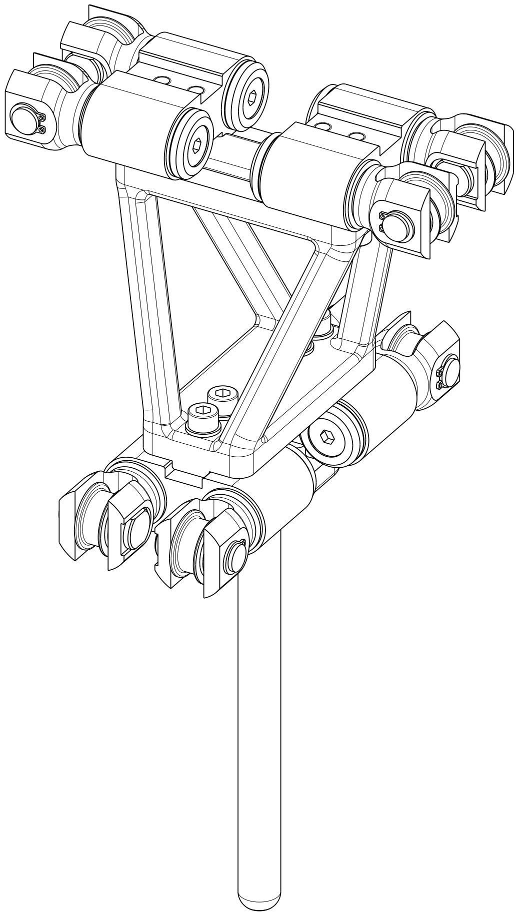

Figure 4.14: EE-1 designed for the CORHDA prototype based on the dimensions listed in Table 4.1.

solutions that can be reused for future development of the CORHDA. In particular, Figure 4.15 shows a section of the group designed for the wire attachments of two cables to the EE. Two revolute joints with perpendicular axes are used on each cable attachment. Both revolute joints are obtained through a pair of Igus Iglidur® flanged bushings. This solution reduces weight compared to classical ball bearings by guaranteeing low friction. Thanks to the platform symmetry, four groups like the one shown in Fig. 4.15 are mounted on the EE body, which was 3D-printed in Nylon 12 CF. This material combines Nylon 12 and chopped carbon fibers to achieve high flexural strength and stiffness-to-weight ratio. The mass of EE-1 (without considering the gripper) is 0.65kg. Each cable is connected to the EE by coiling it around the aluminum rings at the end of every cable attachment and fixing it by a clamp. The final CORHDA prototype is shown in Figure 4.18.

The second EE (EE-2) is shown in Figure 4.16. This platform was necessary to evaluate the hybrid control strategy introduced in Chapter 3 on the CORHDA. To do so, force sensors were mounted on each cable attachment by modifying only the aluminum ring on which the cable is coiled when EE-1 is used. A new component was produced with a threaded hole to mount the load cells (CALT DYMH-103 inline load cell with a maximum load capacity of 100kg). As explained in Section 3.1, the force sensors were directly integrated on the EE not to modify the robot kinematic chain. The wires are fixed at the other end of each load cell with the same clamps used on the EE-1. The main body of this new mobile platform was modified compared to the previous one to al-

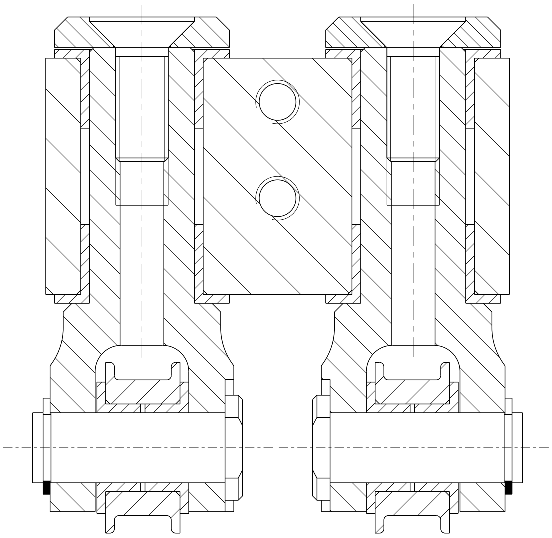

Figure 4.15: Cable attachments with revolute joints designed for the CORHDA EE.

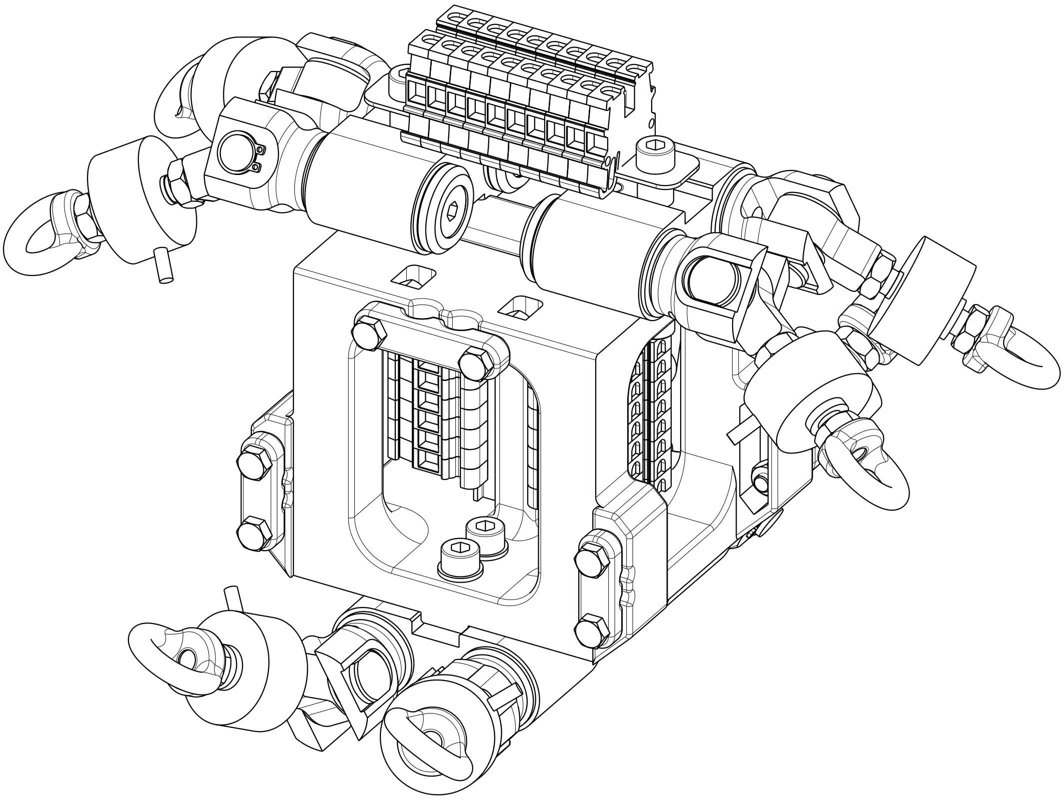

Figure 4.16: EE-2 designed for the CORHDA prototype based on the dimensions listed in Table 4.1.

low the mounting of the terminals for the connection of the load cells to the electric cable necessary to power the sensors and to transmit their output signal. The main drawbacks of the EE-2 are its higher mass (1.58kg) and its connection with the external electric cables (see Figure 4.17) that can influence the robot dynamics during fast movements.

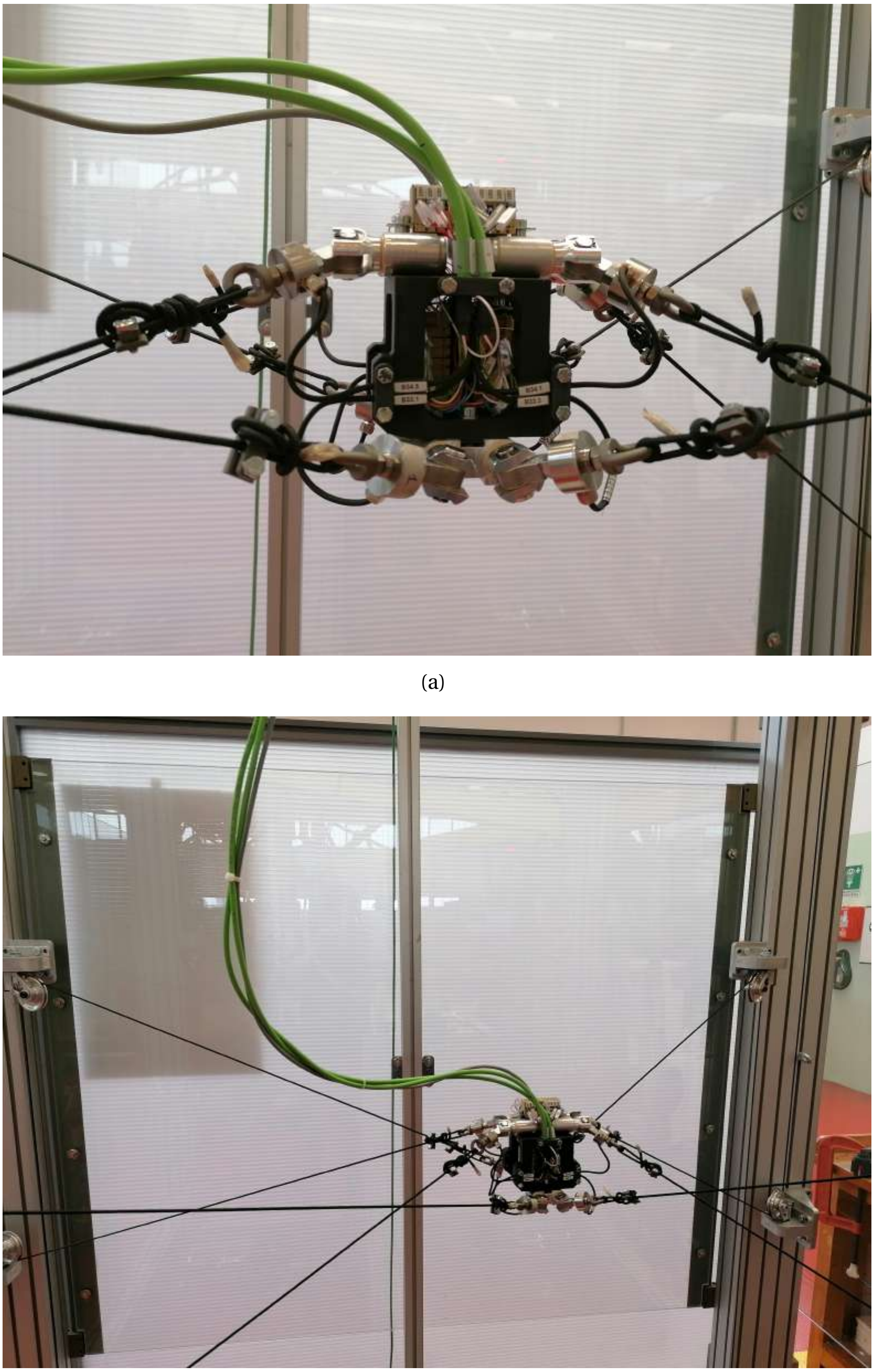

(a)

(b)

Figure 4.17: EE-2 designed for mounting the load cells on the CORHDA.

Figure 4.18: CORHDA prototype.

Chapter 5

Experimental validation

This chapter describes the experimental tests executed on the IPAnema 3 Mini and the CORHDA to validate the HC introduced in Chapter 3. For both robots, the accuracy in positioning precision and force tracking are assessed. A comparison is presented with other state-of-the-art control algorithms making use of force sensors and implemented in the IPAnema 3 Mini. In the CORHDA, since the robot is developed to work without load cells, the HC is compared with a pure inverse-kinematic controller (in which cables are position-controlled based on the results of the inverse kinetostatic model of the robot). Differently from the IPAnema 3 Mini, in the CORHDA the HC is also tested for fast movements, with linear velocities and accelerations up to 8.8m/s and 255m/s^2, respectively. This chapter also reports the experimental results obtained in a simple test bench equipped with only two cables.

Some indices are introduced to evaluate the performance in terms of cable-force tracking. Every index refers to a single wire. When a certain force f_{des} is desired in a cable, the real force f_{act} acting in it can be evaluated through the indices id_1 and id_2, which represent the mean absolute and percentage error of the real cable force with respect to the desired one, namely:

$$id_1 = \frac{\sum_{i=1}^{n_s} |f_{act,i} - f_{des,i}|}{n_s} \tag{5.1}$$

$$id_2 = \frac{\sum_{i=1}^{n_s} \frac{|f_{act,i} - f_{des,i}|}{f_{des,i}}}{n_s} \cdot 100 \tag{5.2}$$

where n_s is the number of samples collected along a certain trajectory or, in general, during a time interval. The subscript "i" refers to the i-th sampled force value. Even when a force distribution is not computed (i.e. there is not a desired force to be commanded to the cable), it is necessary to maintain the wire forces within the limits defined for the robot at hand. To evaluate if this constraint is satisfied or to quantify how much it is exceeded, the indices id_3, id_4, and id_5 are introduced. id_3 is the percentage of sampled values of the measured force that exceed the limits f_{min} or f_{max}, while id_4 and id_5 are the mean absolute value of the distance of these values from f_{min} and f_{max}, namely:

$$id_3 = \frac{n_{sMin} + n_{sMax}}{n_s} \cdot 100 \tag{5.3}$$

$$id_4 = \frac{\sum_{i=1}^{n_{sMin}} f_{min} - f_{act,i}}{n_{sMin}} \tag{5.4}$$

$$id_5 = \frac{\sum_{i=1}^{n_{sMin}} f_{act,i} - f_{max}}{n_{sMax}} \tag{5.5}$$

where n_{sMin} and n_{sMax} are, respectively, the number of sampled values where the measured force is lower than f_{min} and higher than f_{max}.

The HC introduced in Chapter 3 was developed with the idea of applying it to fast overconstrained CDPRs (like the CORHDA), for which cable forces should be maintained as low as possible (to reduce the power required to motors during fast movements). With this in mind, the criterion chosen to find the optimal FD is to minimize the minimum 2-norm of the cable tension array (see section 2.3). This way, the desired cable forces tend to be near the lower limit f_{min}. This means that errors in the actual cable forces with respect to the desired ones can let the real forces drop under the desired limit and even cause cables to become slack. On the contrary, it is uncommon for forces to overcome the higher limit. For this reason, in the following analysis, the index id_5 will not be considered, and only the values of index id_4 will be displayed to evaluate whether a cable tends to become slack.

5.1 Experimental tests on the IPAnema 3 Mini

Since the friction model introduced in Section 3.2.1 is valid only for dynamic friction, the main problem of the controllers HC-τ and HC-e is the lack of precision in predicting the forces when the robot platform is at rest. The situation is different when the load cells are used because, even if the static friction is not modeled for the correction of cable forces, the static force measures are still rather precise. However, for applications in which the robot is moving most of the time or is not required to exert specific static wrenches, it is only important to maintain cables taut to prevent them from becoming slack during motion.

Accordingly, only dynamic trajectories are tested (Figure 5.1). One triangular and one circular motion law are defined in the workspace of the robot with a FD sensitivity index $\sigma_{12} < 1.5$N (Figure 3.12(a)), whereas another pair of triangular and circular motion laws are defined in the workspace of the robot where $\sigma_{34} < 1.5$N (Figure 3.12(b)). A fifth motion law is built along a rectangular path to pass through the plane $y = 0$ so that the pair of force-controlled cables must be changed during the movement. The paths where the force-controlled cables are wires 1 and 2 are plotted in red, whereas the paths in which the force-controlled cables are 3 and 4 are plotted in blue. All trajectories are purely translational motions, and they represent the movement of the center O' of the MRS ($O' - x'y'z'$). Though different platform velocities were tested, in all motion laws shown in this thesis, for the sake of comparison, the EE reaches a velocity of 4 m/min after the first acceleration from a static position.

The force limits defined for the robot are f_{min} = 5 N and f_{max} = 35 N. To keep some margin with respect to force oscillations and imprecision in the robot geometry or wrench estimation, a minimum tension equal to 8 N is considered for the computation of the FD. The wrench exerted on the EE is simply due to its weight and inertia, computed from the platform mass (0.25kg).

The forces plotted in Figures 5.2–5.10 are the ones measured by the built-in load cells corrected with the dynamic friction model described by the coefficients in the third and fourth rows of Table 3.3.

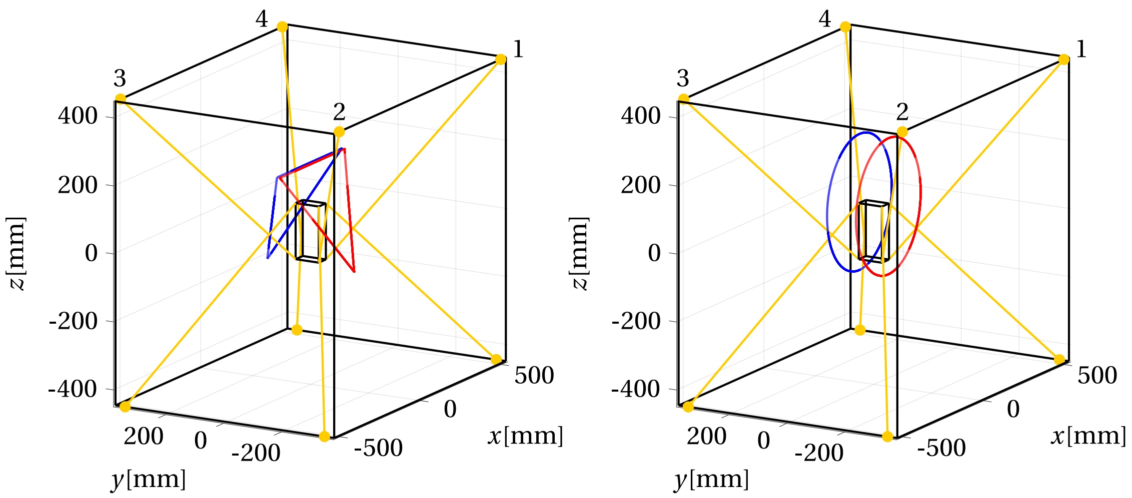

(a) Triangular trajectories (b) Circular trajectories

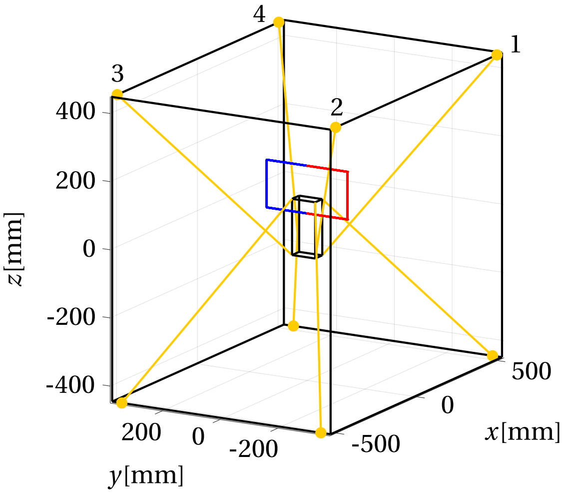

(c) Rectangular trajectory

Figure 5.1: Robot trajectories executed during the experimental tests on the IPAnema 3 Mini. The paths where the force-controlled cables are wires $1,2$ are plotted in red, whereas the ones in which the force-controlled cables are wires $3,4$ are plotted in blue.

5.1.1 Comparison between the Hybrid Control Strategies

Figures 5.2 and 5.3 show the evolution in time of forces in the force-controlled cables for the triangular (Figure 5.2) and circular (Figure 5.3) red trajectories in Figure 5.1. When the controller HC-f (Figure 3.13(a)) is used, the measured forces (solid lines) track the theoretical ones (dashed lines) computed by the FD algorithm very well. To evaluate the force-tracking accuracy, it is possible to analyze the results in Tables 5.1 and 5.2. For both trajectories, the forces on the force-controlled cables have absolute average errors of a few tenths of Newton (id_1), which correspond to less than 2% of the desired tension (id_2). The results obtained with the controllers HC-τ (Figure 3.13(b)) and HC-e (Figure 3.13(c)) are similar: in both cases, the actual forces are noisy compared to the theoretical ones, but the evolution in time of the tensions is approximately followed. The higher force fluctuations produce absolute average errors near 1N (id_1) for both controllers, corresponding to average errors in force tracking less than 8% of the desired force (id_2). Similar behaviors are also observed for different trajec-

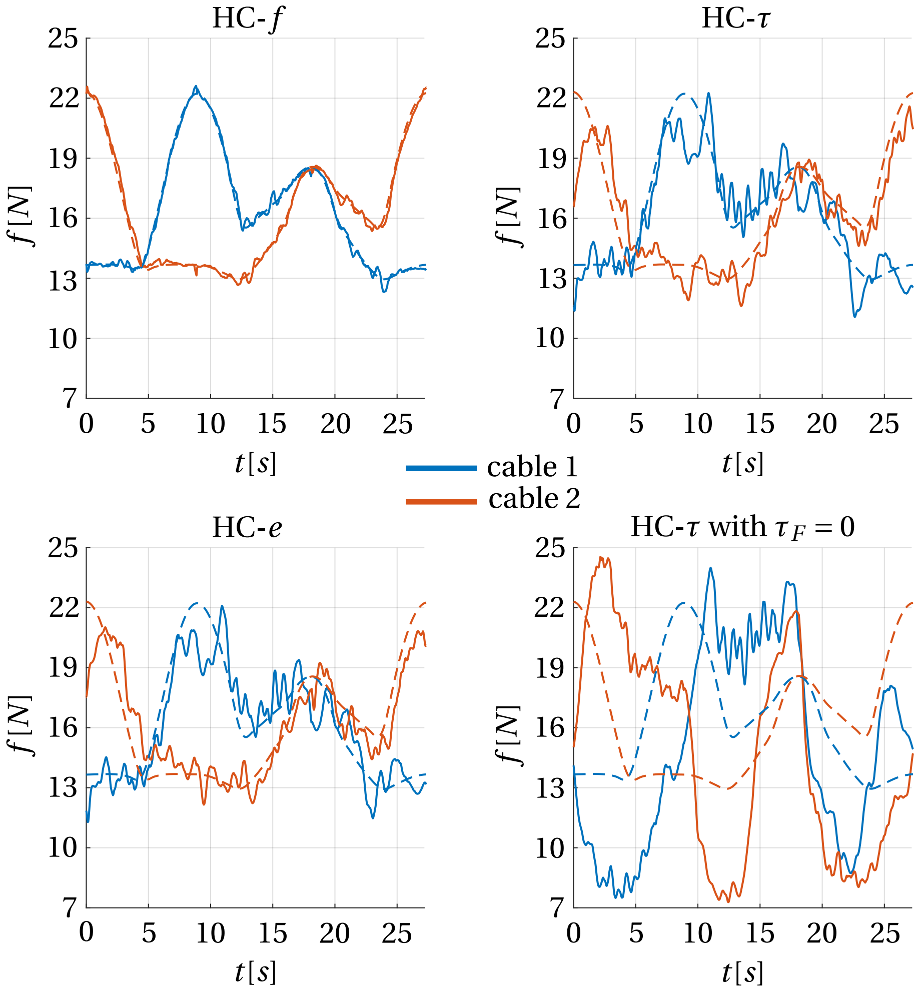

Figure 5.2: Desired (dashed lines) and measured (solid lines) tensions of the force-controlled cables for the red triangular trajectory in Figure 5.1(a) with different controllers: HC-f, HC-τ, HC-e, and HC-τ without the friction torque model.

Controller		HC-f	HC-τ	HC-e	HC-τ with $\tau_F = 0$
cable 1	id_1 [N]	0.1	0.9	1.0	4.2
cable 2		0.2	0.9	0.9	5.2
cable 1	id_2 [%]	0.9	5.4	5.7	26.1
cable 2		1.1	5.6	5.7	32.6

Table 5.1: Indices for the evaluation of the force tracking during the tests shown in Figure 5.2.

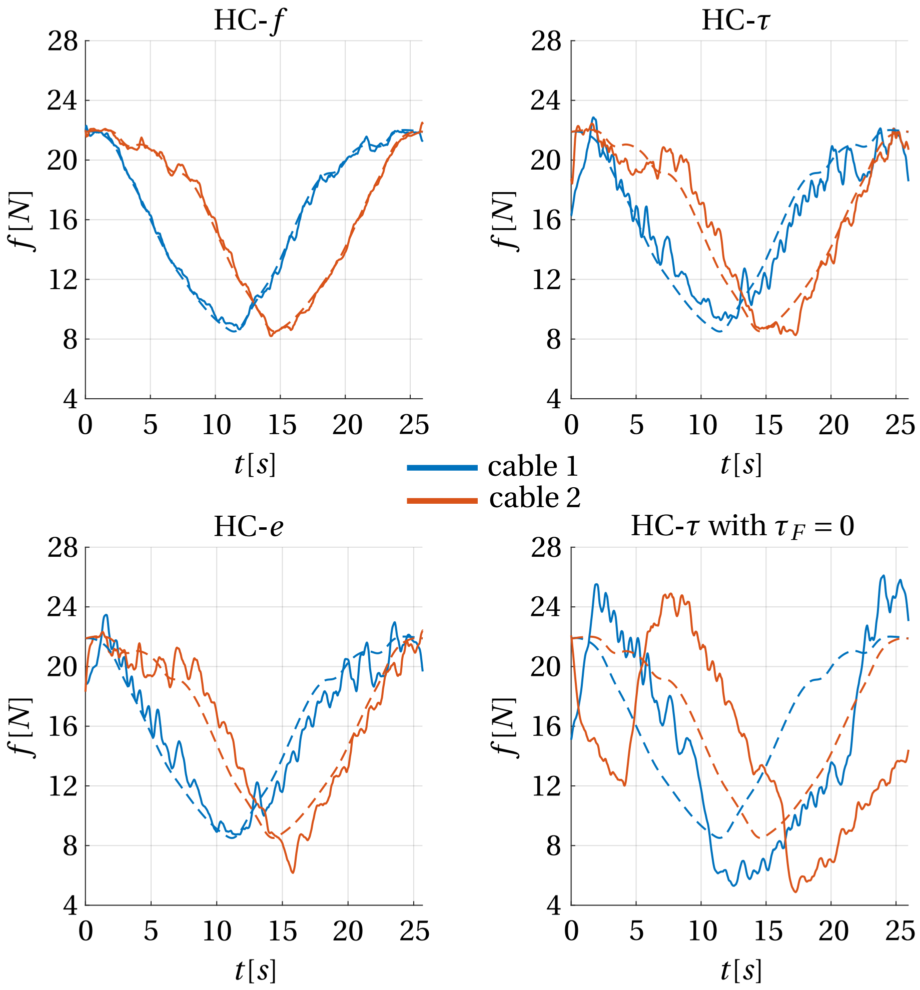

Figure 5.3: Desired (dashed lines) and measured (solid lines) tensions of the force-controlled cables for the red circular trajectory in Figure 5.1(b) with different controllers: HC-f, HC-τ, HC-e, and HC-τ without the friction torque model.

Controller		HC-f	HC-τ	HC-e	HC-τ with $\tau_F = 0$
cable 1	id_1 [N]	0.2	1.2	1.0	4.6
cable 2		0.2	0.9	1.1	6.0
cable 1	id_2 [%]	1.6	7.7	6.7	30.1
cable 2		1.4	6.3	7.9	38.4

Table 5.2: Indices for the evaluation of the force tracking during the tests shown in Figure 5.3.

tories (e.g., for the blue ones in Figure 5.1). In particular, the similarity between the forces generated by the HC-τ controller and the HC-e controller suggests that there is no practical difference in applying one controller rather than the other for the motion laws studied in this work. However, these results are obtained using a filtered motor torque and the raw value of the motor FE in the feedback loop. As mentioned in Section 3.3, filtering the torque should be a problem for faster movements, and, in this case, the HC-e controller should provide an advantage.

The last plots of Figures 5.2 and 5.3 show the effect of setting $\tau_F = 0$ in Eq. (3.1), namely, neglecting the friction model in the HC-τ controller. It is clear from the results in Tables 5.1 and 5.2 that force tracking becomes considerably worse with average errors on the actual forces between 26% and 39% of the desired tensions. Moreover, in this case, one or more tensions in the position-controlled cables go below the desired minimum value (5N), which is unacceptable. Similar results are obtained if friction is neglected in the HC-e controller, which confirms the necessity to model friction in the kinematic chains.

5.1.2 Comparison between the Hybrid Controllers and Other Controllers

To evaluate the performance of the HC method, it is compared with other controllers along different trajectories. The legend shown in Table 5.3 is used to identify different tests. The first number represents the controller used during the execution of the motion law. The controller HC-e is compared with HC-f, with the nullspace control (NC) presented in [128] (which was already developed and tested on the IPAnema 3 Mini) and with a pure inverse kinematic controller (IKC). The latter is the only method besides HC-e that does not exploit force sensors (the IKC is a pure position controller based on robot inverse kinematics, without any action on cable tensions). The second number in Table 5.3 identifies the trajectory among those shown in Figure 5.1.

In evaluating the controllers performances, the evolution in time of cable forces, the precision, and the repeatability of the robot are considered. For the estimation of the robot accuracy and repeatability, the position of a marker mounted on the EE is measured with a Leica AT960 laser tracker, which guarantees an absolute accuracy of $\pm\left(15\,\mu\text{m} + 6\,\frac{\mu\text{m}}{\text{m}}\right)$. The experimental setup configuration is the same used in [128], so we can estimate an accuracy of $\pm 33\,\mu$m, while the sampling rate of the measurements is 1000 Hz.

Table 5.3: Legend for the identification of the results shown in Figures 5.4-5.8 and Tables 5.9 and 5.10.

Test $i\,j$				
***i*:**	**Controller**	***j*:**	**Trajectory Shape**	**Force-Controlled Cables**
1:	IKC	1:	Triangular	1,2
2:	HC-e	2:	Circular	1,2
3:	HC-f	3:	Triangular	3,4
4:	NC	4:	Circular	3,4
		5:	Rectangular	

5.1.2.1 Evaluation of cable forces

Figures 5.4–5.8 represent the evolution in time of cable forces, while the values of the performance indices introduced in Eqs. (5.1)–(5.4) are listed in Tables 5.4–5.8. During the tests $1j$ ($j = 1,\ldots,5$) executed with the IKC, there is no control over cable tensions. The inverse kinematics of the manipulator is solved without the computation of any FD. Since no desired forces exist, indices id_1 and id_2 are not computed. Only the force limits defined by $f_{min} = 5\text{N}$ and $f_{max} = 35\text{N}$ are considered to evaluate the controller performances. For all trajectories, there is at least one cable force smaller than the minimum tension for large parts of the movements. Moreover, in tests 13 and 14, the force on cable 8 exceeds the maximum limit. For example, in test 11, on cable 7, there is a force lower than 5N ($id_3 = 100\%$) for the whole motion, and this force is on average 2.1N (id_4) less than f_{min}. In test 14, the force on cable 5 is on average 3.7N lower than f_{min} for 53% of the motion duration, while in test 15, the force on cable 7 is on average 3.8N lower than f_{min} for 61.6% of the motion time. Without any control on cable tensions, it is impossible to guarantee they remain within the given limits.

On the contrary, with the same hardware (that does not exploit the load cells for control aims), the controller HC-e allows the cable forces to be maintained within the predefined limits for most of the movement. During tests $2j$ ($j = 1,\ldots,5$), one or two cable tensions slightly drop under the lower limit. The forces that drop under f_{min} exceed the limit at the most for 0.7N (on average), and only in test 25 this condition lasts for more than 26% of the motion duration. So, with the same hardware as the IKC, the performance obtained with the HC-e controller is significantly better. Similar results are obtained when the HC-f controller is applied, even if it exploits load cells. In tests $3j$ ($j = 1,...,5$), the most relevant difference compared to tests $2j$ is that the better tracking of tensions in force-controlled cables produces less noisy forces. However, for the same motion law, the time lapses when tensions drop under 5N are approximately the same for both the HC-f and HC-e controllers. This consideration is confirmed by comparing the indices id_3 and id_4 for the trajectories $2j$ and $3j$. For example, in test 22 (HC-e controller), only the force on cable 7 drops under f_{min} for 25.6% of the motion duration. The same cable tension drops under the limit also in test 23 (HC-f controller); the difference is that the time interval for which the tension is lower than f_{min} is 14.6% of the motion duration. Even the mean value of the tension dropping below the limit is similar in the two cases (0.5N for the HC-e and 0.3 for the HC-f). The force tracking with HC-e and HC-f controllers can be analyzed in more detail. The values of id_1 and id_2 were already described for the force-controlled cables in tests 21/31 and 22/32 (the indices are the same listed in Tables 5.1 and 5.2): as emphasized in Section 5.1.1 for other motions, the tension tracking in the force-controlled cables is better when load cells are used. The maximum difference is visible in tests 24 and 34, where the average error on the wire tensions on cables 3 and 4 is 7.2% and 10% when the HC-e controller is used, while it is only 1.7% for both wires when the force sensors are exploited. However, as expected, the main errors between the theoretical forces computed through the FD algorithm and the real ones are in the position-controlled cables. In these wires, the errors in the real forces with respect to the desired ones often reach values near 20% for both HC-f and HC-e controller, and the difference between the two control strategies is typically between 1 and 3 percentage points (few tenths of Newtons by analyzing id_2 instead of id_3). This means that even if the force tracking by exploiting load cells is better on the force-controlled wires, the average errors of tensions in the length-controlled cables are similar in the two cases, making the overall improvement in the force tracking obtained with force sensors almost negligible. The simplification of the robot hardware brought about by the HC-e controller justifies the small drop in performance.

When the NC controller is applied, in tests $4j$ ($j = 1,\ldots,5$), the forces do not follow theoretical values computed through a FD algorithm (id_1 and id_2 are not evaluated). The controller maintains the tensions as close as possible to the mean value $\overline{f} = 12$N and corrects them when they become lower than $f'_{min} = 7$ N. The results are forces slightly smaller during the movement, but their oscillations are more similar to the ones obtained with the HC-e than those with the HC-f. In this case, the lower limit $f_{min} = 5$ N is almost always respected during the motion: the force dropping under f_{min}, both in terms of time (id_3) and average mean force under the limit (id_4), is slightly better to the one obtained with the HC-e controller, but, as said for the HC-f control strategy, the small drops in performance is justified by the hardware simplification.

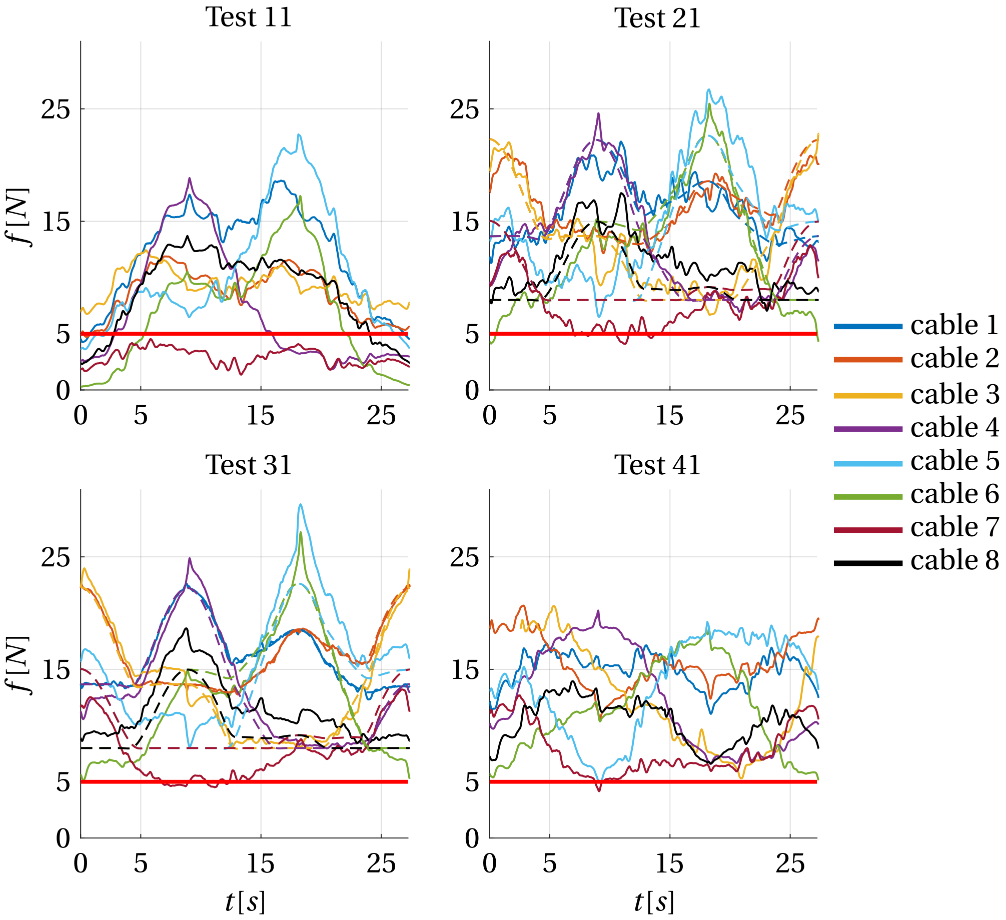

Figure 5.4: Desired (dashed lines) and measured (solid lines) cable forces during the execution of the red triangular trajectory in Figure 5.1(a) with different controllers (see Table 5.3). f_{min} = 5 N and f_{max} = 35 N are the desired bounds of cable tensions (red horizontal lines).

Test		11	21	31	41		11	21	31	41
cable 1	id_1 [N]		1	0.1		id_2 [%]		5.7	0.9	
cable 2			0.9	0.2				5.7	1.1	
cable 3			1.1	0.8				9.6	6.4	
cable 4			0.9	0.9				6.8	6.8	
cable 5			1.1	1.1				9.5	9.5	
cable 6			2.1	2.3				17.3	19.2	
cable 7			1.9	2				21.2	22.2	
cable 8			1.8	1.9				19.2	20.2	
cable 1	id_3 [%]	4.4	0	0	0	id_4 [N]	0.4	0	0	0
cable 2		2.4	0	0	0		0.2	0	0	0
cable 3		0	0	0	0		0	0	0	0
cable 4		52.2	0	0	0		1.9	0	0	0
cable 5		39.1	2.4	0	0		3.1	0.6	0	0
cable 6		11.6	0	0	0.1		0.6	0	0	0.002
cable 7		100	11.1	13.6	2.3		2.1	0.3	0.3	0.4
cable 8		22.1	0	0	0		1.5	0	0	0

Table 5.4: Values of indices in Eqs. (5.1)–(5.4) for the test analyzed in Figure 5.4. The force-controlled cables are highlighted in bold.

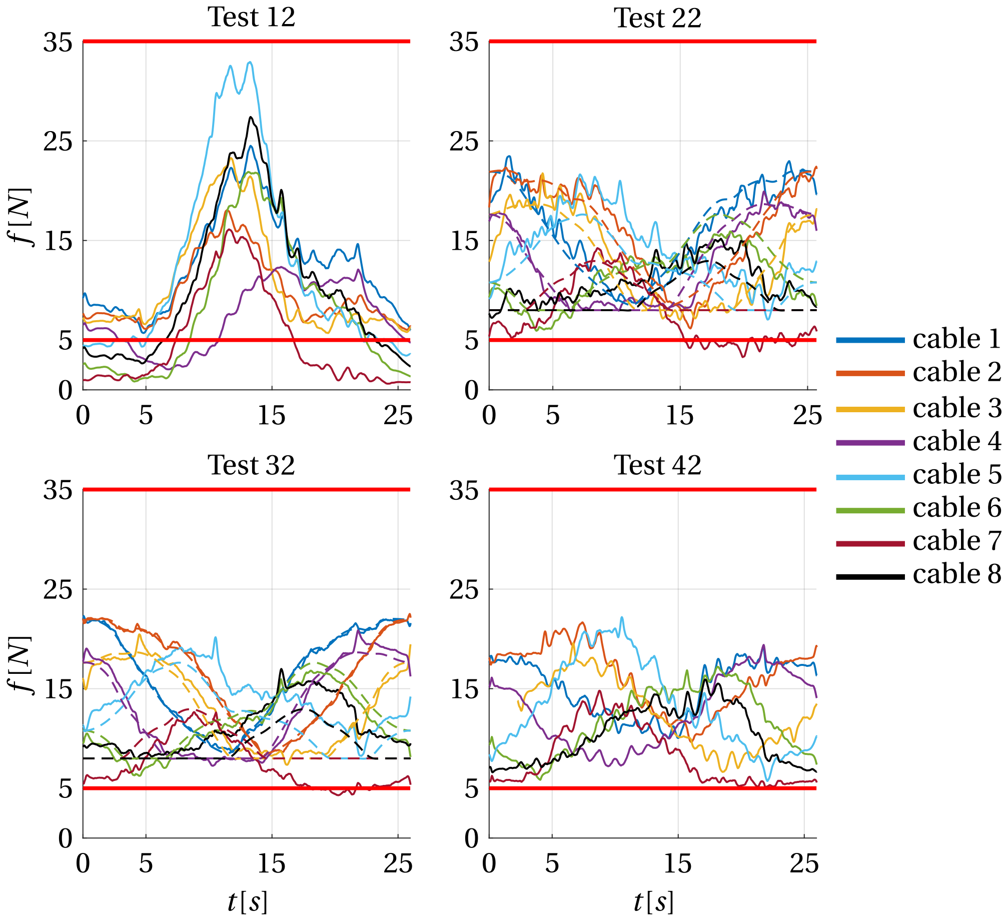

Figure 5.5: Desired (dashed lines) and measured (solid lines) cable forces during the execution of the red circular trajectory in Figure 5.1(b) with different controllers (see Table 5.3). $f_{min} = 5$ N and $f_{max} = 35$ N are the desired bounds of cable tensions (red horizontal lines).

Test		12	22	32	42		12	22	32	42
cable 1	id_1 [N]		1	0.2		id_2 [%]		6.7	1.6	
cable 2			1.1	0.2				7.9	1.4	
cable 3			1.1	0.8				8.9	6.9	
cable 4			0.8	0.6				6.7	4.4	
cable 5			1.3	0.9				10.3	7.7	
cable 6			2.1	2.1				17.6	18.8	
cable 7			2.1	1.9				24.3	22.3	
cable 8			1.7	1.9				18.6	20.1	
cable 1	id_3 [%]	0	0	0	0	id_4 [N]	0	0	0	0
cable 2		0	0	0	0		0	0	0	0
cable 3		0	0	0	0		0	0	0	0
cable 4		29.7	0	0	0		1.7	0	0	0
cable 5		46.3	0	0	0		2.9	0	0	0
cable 6		25.3	0	0	0		0.5	0	0	0
cable 7		64	25.6	14.6	0		3.3	0.5	0.3	0
cable 8		35.9	0	0	0		1.4	0	0	0

Table 5.5: Values of indices in Eqs. (5.1)–(5.4) for the test analyzed in Figure 5.5. The force-controlled cables are highlighted in bold.

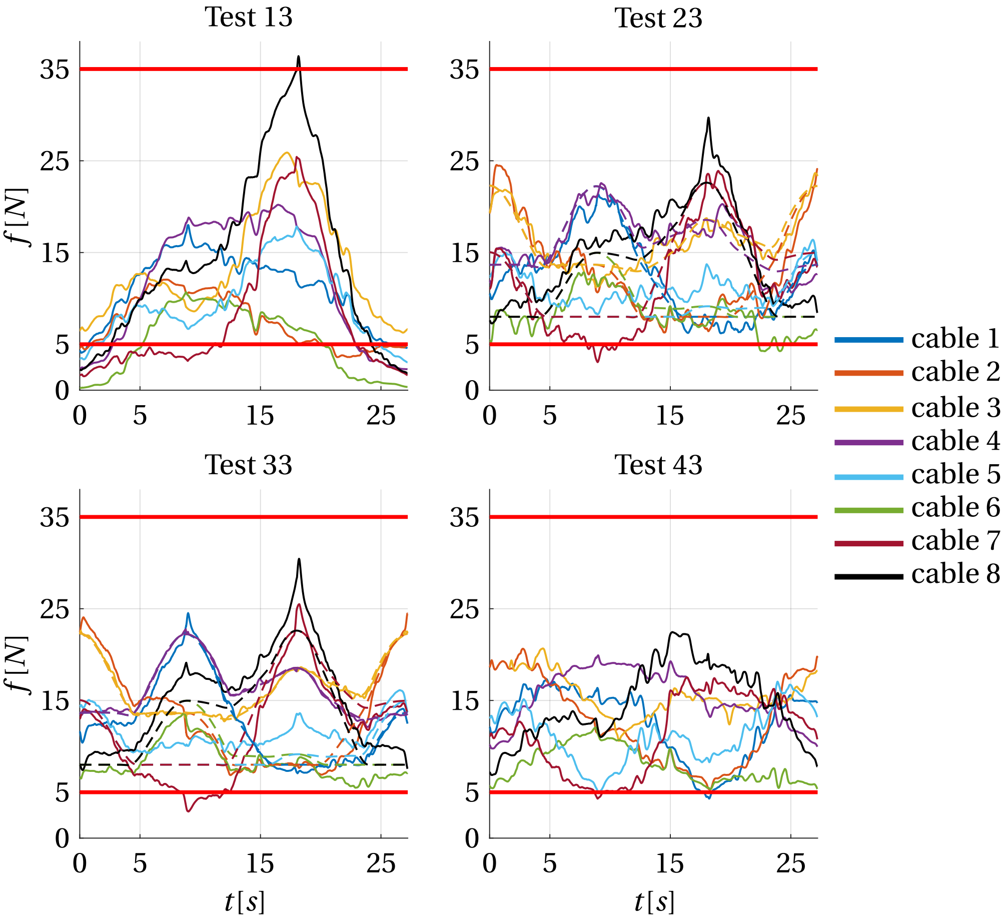

Figure 5.6: Desired (dashed lines) and measured (solid lines) cable forces during the execution of the blue triangular trajectory in Figure 5.1(a) with different controllers (see Table 5.3). f_{min} = 5 N and f_{max} = 35 N are the desired bounds of cable tensions (red horizontal lines).

Test		13	23	33	43		13	23	33	43
cable 1	id_1 [N]		1	0.7		id_2 [%]		8.2	5.1	
cable 2			1.4	1				10.6	8.2	
cable 3			0.9	0.2				5.9	1.2	
cable 4			1.3	0.2				8.3	1.2	
cable 5			1.5	1.3				16.4	13.7	
cable 6			1.7	1.9				19.7	21.7	
cable 7			2	1.9				18.1	17.5	
cable 8			1.9	2.1				15.3	16.3	
cable 1	id_3 [%]	7.6	0	0	3.1	id_4 [N]	0.4	0	0	0.3
cable 2		30.2	0	0	0		0.6	0	0	0
cable 3		0	0	0	0		0	0	0	0
cable 4		26	0	0	0		1.9	0	0	0
cable 5		44.8	5.8	0	0		3.3	0.6	0	0
cable 6		14.7	0	0	0.3		1	0	0	0.02
cable 7		58.6	9.6	13.1	2.5		1.6	0.6	0.8	0.4
cable 8		21.5	0	0	0		1.7	0	0	0

Table 5.6: Values of indices in Eqs. (5.1)–(5.4) for the test analyzed in Figure 5.6. The force-controlled cables are highlighted in bold.

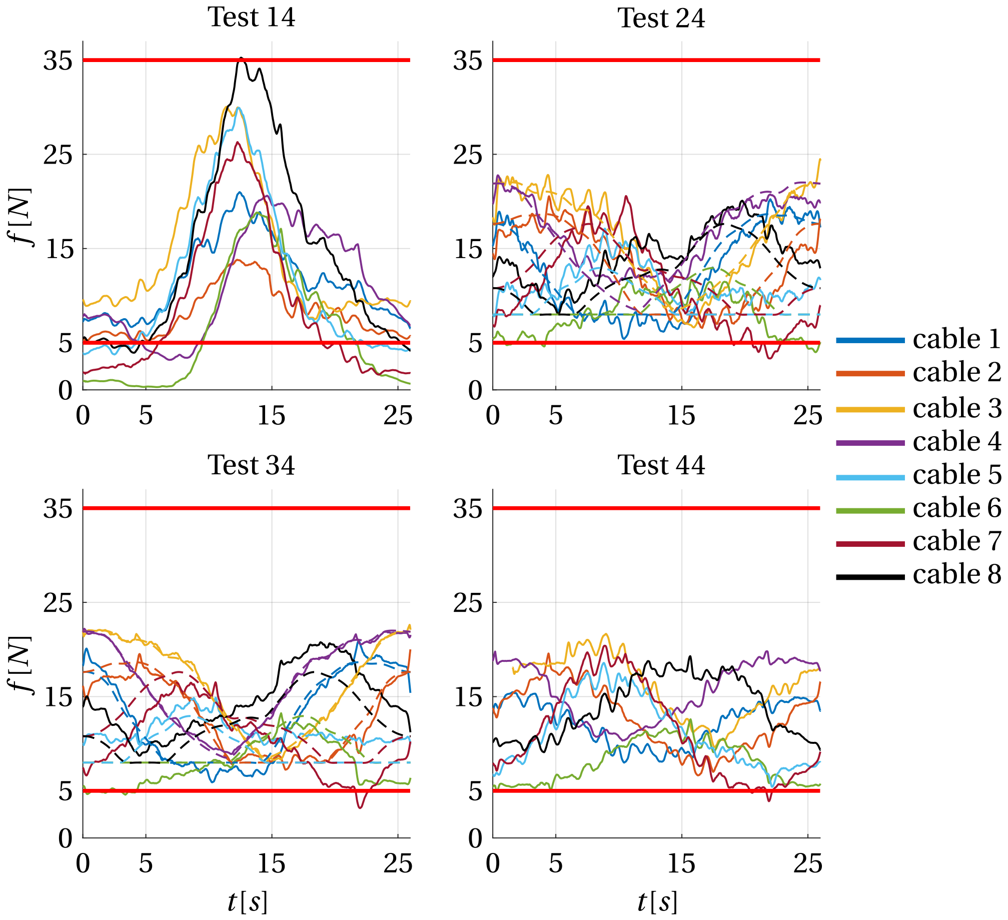

Figure 5.7: Desired (dashed lines) and measured (solid lines) cable forces during the execution of the blue circular trajectory in Figure 5.1(b) with different controllers (see Table 5.3). $f_{min} = 5$ N and $f_{max} = 35$ N are the desired bounds of cable tensions (red horizontal lines).

Test		14	24	34	44		14	24	34	44
cable 1	id_1 [N]		1	0.8		id_2 [%]		9	6.7	
cable 2			1.5	0.7				13.1	5.6	
cable 3			1	0.2				7.2	1.7	
cable 4			1.3	0.2				10	1.7	
cable 5			1.9	1.5				21.8	17.6	
cable 6			2	2.1				22.4	24.4	
cable 7			2.5	2.1				23.3	19.5	
cable 8			2	2.3				17.8	19.4	
cable 1	id_3 [%]	0	0	0	0	id_4 [N]	0	0	0	0
cable 2		0	0	0	0		0	0	0	0
cable 3		0	0	0	0		0	0	0	0
cable 4		17.8	0	0	0		1.2	0	0	0
cable 5		53	9.2	10.7	0.3		3.7	0.4	0.2	0.03
cable 6		31.2	0	0	0		0.6	0	0	0
cable 7		50.1	10.7	4	3.1		2.2	0.7	1	0.4
cable 8		14	0	0	0		0.5	0	0	0

Table 5.7: Values of indices in Eqs. (5.1)–(5.4) for the test analyzed in Figure 5.7. The force-controlled cables are highlighted in bold.

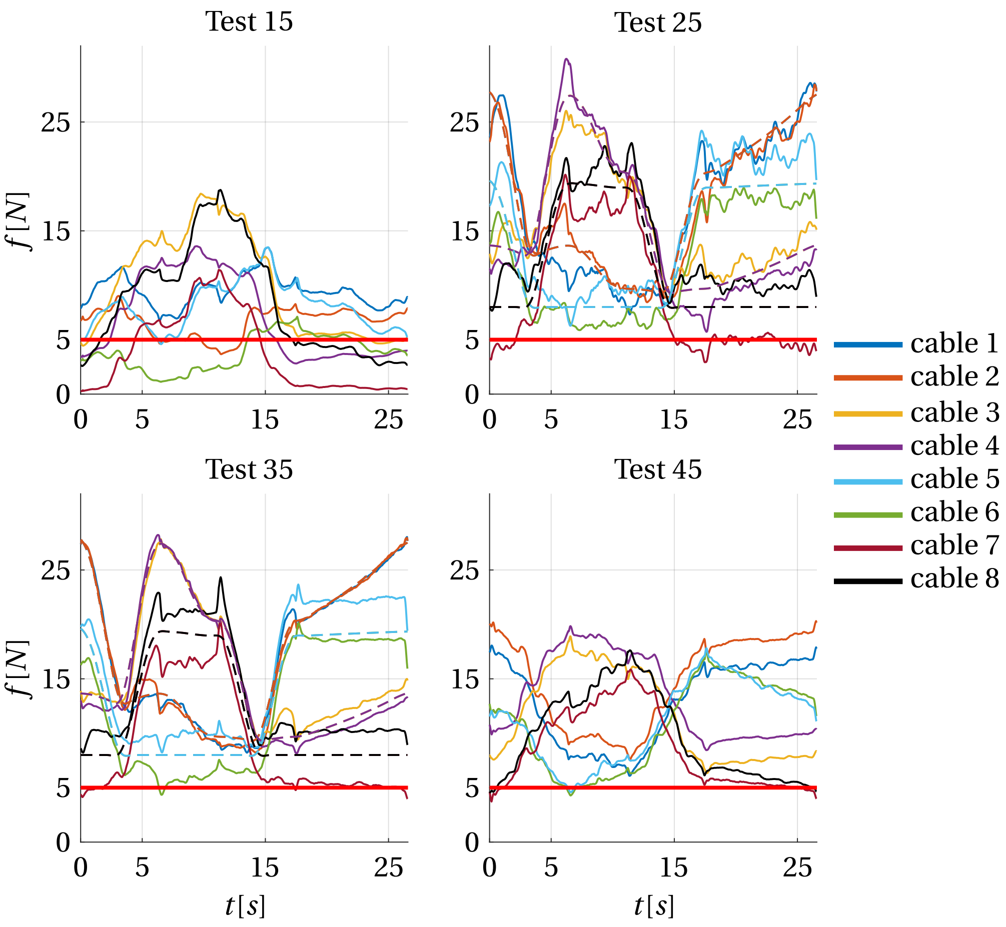

Figure 5.8: Desired (dashed lines) and measured (solid lines) cable forces during the execution of the rectangular trajectory in Figure 5.1(c) with different controllers (see Table 5.3). $f_{min} = 5$ N and $f_{max} = 35$ N are the desired bounds of cable tensions (red horizontal lines).

Test		15	25	35	45		15	25	35	45
cable 1	id_1 [N]		1.2	0.4		id_2 [%]		7.4	3	
cable 2			1.1	0.5				7.1	4	
cable 3			1.2	0.6				9	5.2	
cable 4			1.2	0.6				9.1	4.4	
cable 5			1.4	1.2				11.6	12.5	
cable 6			2.2	2.2				16.6	17.6	
cable 7			2.5	2.4				27.7	25	
cable 8			2	2				21.1	20	
cable 1	id_3 [%]	0	0	0	0	id_4 [N]	0	0	0	0
cable 2		19.9	0	0	0		0.6	0	0	0
cable 3		13.4	0	0	0		0.2	0	0	0
cable 4		49.1	0	0	0		1.4	0	0	0
cable 5		66.7	0	1.9	3.6		2.1	0	0.4	0.3
cable 6		2.5	0	0	2		0.2	0	0	0.3
cable 7		61.6	37.4	10	10.1		3.8	0.6	0.3	0.3
cable 8		41.4	0	0	2.9		1.2	0	0	0.3

Table 5.8: Values of indices in Eqs. (5.1)–(5.4) for the test analyzed in Figure 5.8. The force-controlled cables are highlighted in bold.

5.1.2.2 Evaluation of robot precision and repeatability

Table 5.9 shows the results in terms of accuracy obtained during the same tests shown in Figures 5.4–5.8. The values in the table represent the absolute error (expressed as a Cartesian distance) in the position of the marker between the set trajectory and the executed one. The maximum and mean errors over an entire motion law measure the accuracy. The results are always similar for tests $1j$, $2j$, $3j$, and $4j$, with an error in the positioning of the marker that has a maximum value between 2.6 mm and 5.5 mm and a mean value between 1.7 mm and 3.2 mm. The differences in using different controllers are in the order of tenths of a millimeter. They vary for different motion laws so that we can consider all controllers equivalent in terms of accuracy. Note that when the robot is controlled by the IKC, one or more cables can become slack, and this significantly degrades the achieved accuracy with respect to that reported in Table 5.9.

Test 51 is the last in Table 5.9 that needs to be analyzed. Here, the triangular red trajectory of Figure 5.1(a) is executed, but the controller is different from the others previously described. The control scheme shown in Figure 3.13(c) is applied to all cables (i.e., all cables are force-controlled without using load cells). Better force tracking than with HC-e is achieved in all cables, as we can see in Figure 5.9. In fact, the mean errors of the actual cable forces are always equal to or less than 10% of the desired ones (id_2 in Table 5.11). The same index is almost always higher in the position-controlled cables when the HC-e controller is applied (see Tables 5.4–5.8). However, applying force control in all cables results in poor manipulator accuracy, with a maximum position error of 23.85 mm, as shown in Table 5.9.

Finally, the repeatability ζ of the robot is evaluated by executing the triangular tra-

Table 5.9: Robot accuracy with several controllers applied to different trajectories. The errors in the positioning of the marker are evaluated for a given test through the maximum (ϵ_{max}) and mean ($\overline{\epsilon}$) value over an entire motion law.

Test	ϵ_{max} [mm]	$\overline{\epsilon}$ [mm]	Test	ϵ_{max} [mm]	$\overline{\epsilon}$ [mm]
11	3.48	2.59	31	3.78	2.73
12	3.46	1.85	32	3.36	2.30
13	4.32	2.65	33	3.78	2.34
14	4.13	2.31	34	3.71	2.56
15	3.92	2.44	35	3.77	1.97
21	3.68	2.70	41	3.10	2.22
22	3.76	2.40	42	3.49	1.74
23	3.85	2.44	43	3.04	2.01
24	4.02	2.61	44	2.66	1.72
25	3.68	2.04	45	5.53	3.24
			51	23.85	8.03

Table 5.10: Repeatability in mm over 15 consecutive trajectories.

Test	ζ_{max} [mm]	$\overline{\zeta}$ [mm]	Test	ζ_{max} [mm]	$\overline{\zeta}$ [mm]
11	0.152	0.047	31	0.143	0.044
21	0.151	0.051	41	0.076	0.033

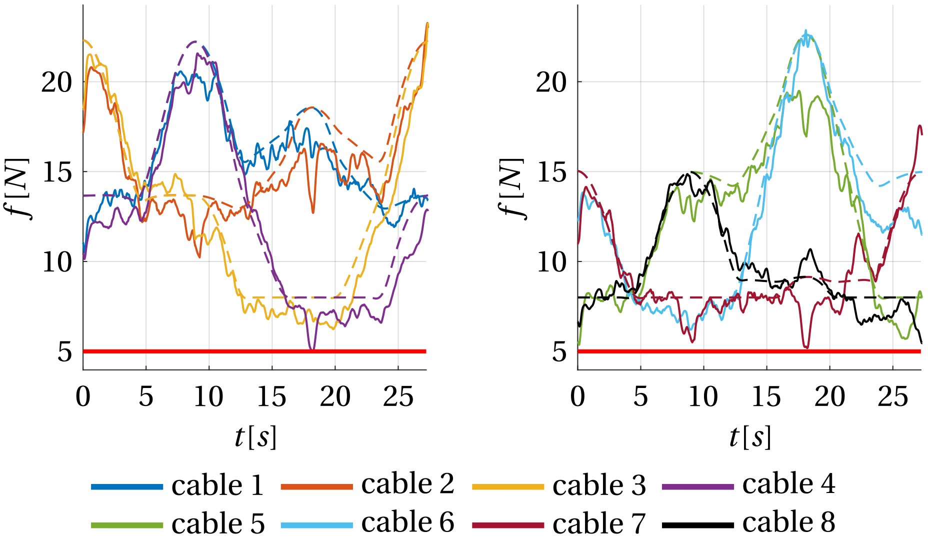

Figure 5.9: Evolution in time of the cable forces in test 51.

	id_1 [N]	id_2 [%]	id_3 [%]	id_4 [N]
cable 1	0.8	4.9	0	0
cable 2	1.3	7.9	0	0
cable 3	1.2	9.6	0	0
cable 4	1.2	10	0.3	0.02
cable 5	1.2	8.4	0	0
cable 6	1.1	8.3	0	0
cable 7	0.8	8.3	0	0
cable 8	0.6	6.5	0	0

Table 5.11: Values of indices in Eqs. (5.1)–(5.4) for the test 51 in Figure 5.9.

jectory for force-controlled cables 1,2 with the different controllers (tests 11, 21, 31, 41). The repeatability is measured by computing the standard deviation of the errors in Table 5.9 over 15 consecutive executions of the same motion law. Table 5.10 lists the maximum and mean values. The controller does not seem to have a significant influence on the repeatability of the manipulator, even if a slightly better repeatability is obtained with the NC controller.

5.1.3 Effect of Changing the Pair of Force-Controlled Cables

Some tests were conducted to analyze the effect of changing the pair of force-controlled cables during the execution of a trajectory. For this purpose, the rectangular motion law in Figure 5.1(c) is considered. The change in the force-controlled cables is managed as described in Section 3.4.1 through the value of the scaling factor h in Eq. (3.9). While cables 5, 6, 7, and 8 are always position-controlled, the scheme shown in Figure 3.13(c) is applied to all the first four cables. When the pair of force-controlled cables is switched, the value of h goes from 0 to 1 in the cables in which the force control is activated and vice versa in the cables in which the force control is deactivated. Figure 5.10 analyzes the effect of increasing δ in the time evolution of forces and position error. The areas in light blue represent the parts of the trajectory in which the force-controlled cables are 1 and 2, while the areas in yellow are the ones in which the

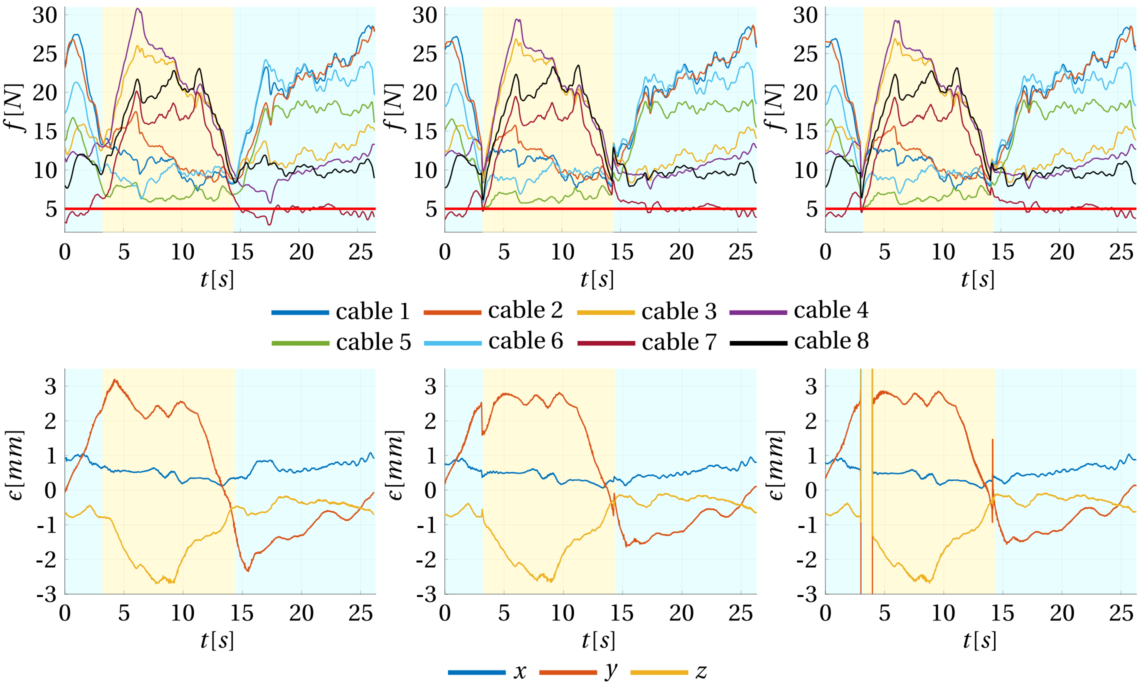

Figure 5.10: The plots show the evolution in time of cable forces (plots in the first row) and position error (plots in the second row) when force-controlled cables are changed for increasing values of δ. The areas in light blue represent the parts of the trajectory in which the force-controlled cables are 1 and 2, while the areas in yellow are the ones in which the force-controlled cables are 3 and 4.

force-controlled cables are 3 and 4. The controller used for these tests is always HC-e.

When $\delta = 0.0005$, the change is very smooth and slow, with a smooth behavior in the forces and the position error as well. The more rapid the change in the value of h (δ higher), the more the Δl applied to the length of the i-th cable is similar to a step. The time necessary for changing the force-controlled cables can be computed from Eq. (3.9) by considering that α must reach (or exceed) $\pi/2$ starting from zero with an increment equal to δ every millisecond (the cycle time of the PLC program). When $\delta = 0.0005$, the change happens in 3142 ms; when $\delta = 0.02$, it takes 79 ms; finally, when $\delta = 0.5$, the change is almost a step since it takes only 4 ms. For $\delta = 0.02$ or $\delta = 0.5$, even though forces quickly drop during the change, they do not become smaller than 5 N; however, the command given to the motor produces a sudden change in the position of the platform that is visible in the plots of the errors ϵ (difference between the set EE position and the executed one). Values of δ between 0.0005 and 0.02 seem to be appropriate for the executed tests.

5.2 Experimental tests on the test bench with two winches

Before implementing the HC on the CORHDA, some tests were executed on a test bench with two opposite cables connected to an EE. CORHDA winches actuate the two wires, so the friction and FE models of their kinematic chains are the ones respectively described in Sections 3.2.2 and 3.3.2. One of the two cables is force-controlled by the HC-e controller, while the other is position-controlled. The situation is shown in Figure 5.11. Two different end-effectors (see Figure 5.12) were mounted on the test bench to execute different movements. The first one, in Figure 5.12(b), is, in practice, a load cell on which two attachments for cables are mounted. The force sensor is a Laumas SA load cell with a maximum capacity of 60kg. This is necessary to measure the real force acting on the EE during the tested movement. However, the electric cable necessary to power the sensor and transmit its output signal did not allow us to execute the fastest movements we wanted to try. For this reason, another EE with the same cable attachments and the same dimensions of the Laumas load cell was designed for the execution of the movements with the higher dynamics, see Figure 5.12(a).

The two control schemes applied to the winches are shown in Figure 3.15, namely the same that will be used in the complete robot. As mentioned in Section 3.4.2, the PID_{HL} was tuned with the Ziegler-Nichols method, and, in this situation, a constant value $K_i = 200$ was chosen for the controller PID_{HL}.

Different movements in the gravity direction were performed. In particular, motions with a displacement of 1m executed in 0.5s, 1s, 2s, and 4s were analyzed. During these motions, three different profiles were commanded to the force-controlled cable: a constant force equal to 50N, a constant force equal to 150N, and an oscillating force between 50N and 150N. To measure the real force acting on the cable (f_{act}) with the EE shown in Figure 5.12(b), it is necessary to compensate for the effect of the load cell weight and inertia, which are both proportional to the EE mass m_{EE}. To do so, it is assumed that the force measured by the force sensor (f_{meas}) is applied exactly in the middle of the EE. This way, it is possible to study the equilibrium of the lower half part of the EE to find the actual force on the force-controlled cable (the lower one, as shown in Figure 5.11). By considering the acceleration of the EE with its own sign (i.e., positive in the positive motion direction and negative in the opposite one), and the gravity acceleration g always positive, the equilibrium of the EE is shown in Figure 5.13 (where

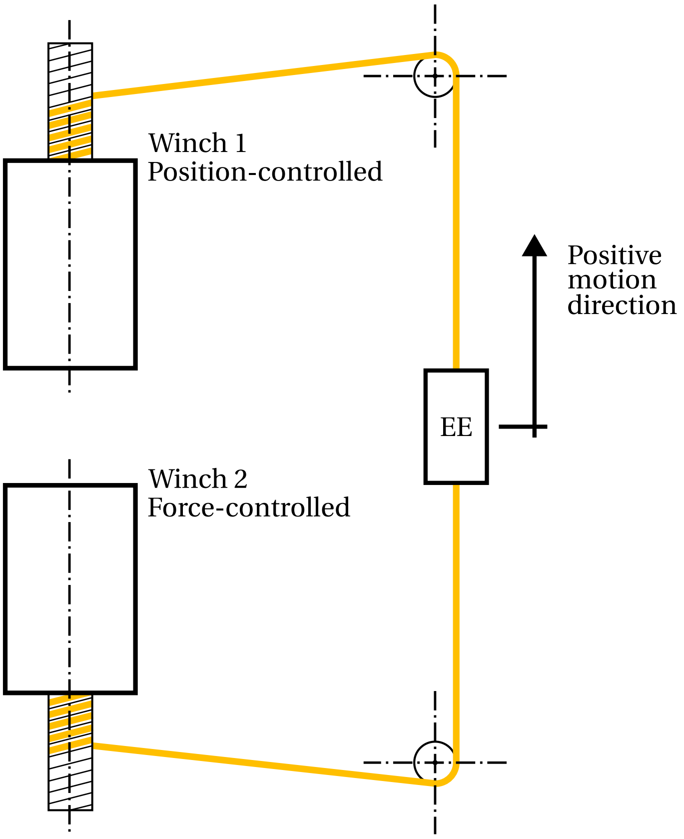

Figure 5.11: Scheme of the test bench built with two CORHDA winches.

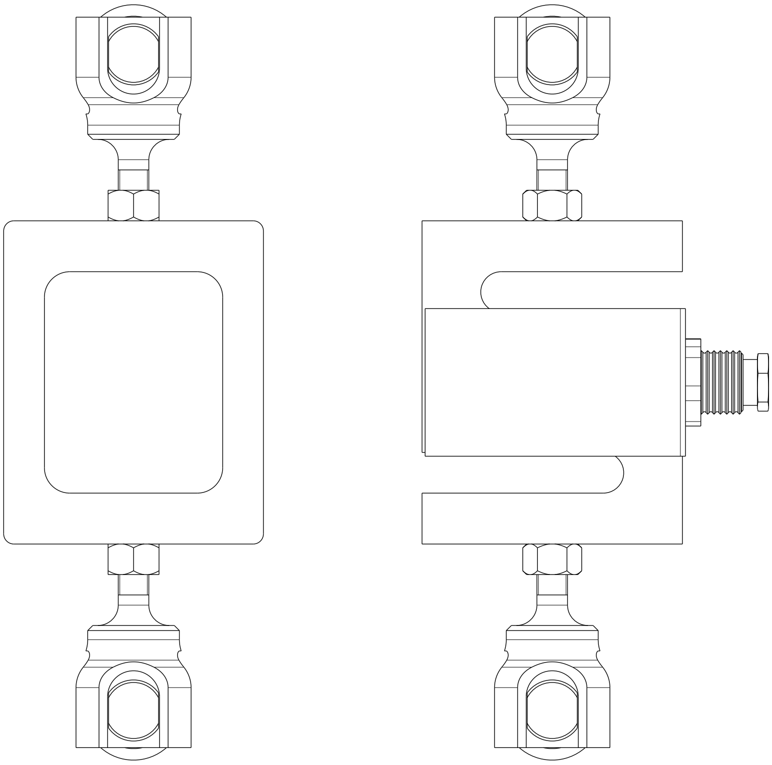

(a) (b)

Figure 5.12: End-effectors of the two cables test bench.

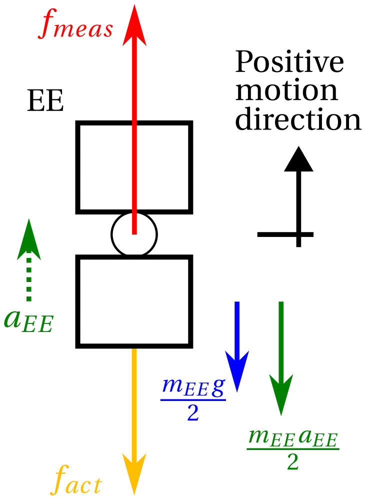

Figure 5.13: Equilibrium of the EE of the test bench with two cables to compute the force on the cable (f_{act}) from the one measured by the load cell ($f_{actMeas}$). Here, the acceleration of the EE a_{EE} is supposed to be in the positive motion direction.

a positive acceleration of the EE is considered). From these considerations, the force acting on the cable can be computed as:

$$f_{act} = f_{meas} - \frac{m_{EE}g}{2} - \frac{m_{EE}a_{EE}}{2} \tag{5.6}$$

The trajectories during which a constant force (50N or 150N) is commanded to the force-controlled wire are first analyzed. In this situation, the influence of the friction model on the HC method is also studied. To do so, for each movement, the complete force control of the lower cable with the scheme shown in Figure 3.15(a) and the simplified version that does not consider frictions in the kinematic chain (i.e., $\tau_F = 0$) are applied. Both a movement in the positive motion direction and another in the negative one (i.e. direction of the gravity) are considered, and the measured cable forces are plotted in Figure 5.14 after the compensation of the EE mass shown in Eq. (5.6). The left column displays the results when the desired cable tension (f_{des}) is 50N, while the right one shows the results when this tension is 150N. In each graph, the evolution in time of the actual force during the movement in the positive motion direction is plotted for both cases in which the friction model is considered in the control scheme (f_{actUp}) or not (f'_{actUp}). The same is done for the movement in the negative motion direction (the actual forces are respectively f_{actDw} and f'_{actDw} depending on the friction model being used or not).

The indices id_1 and id_2 are computed for all tests to evaluate force tracking, and the values are listed in Tables 5.12 and 5.13. As expected from the previous experience on the IPAnema 3 MIni, the actual forces are noisy. However, the average force tracking is very good when the friction model is considered, with a maximum mean absolute error on the tension of the force-controlled wire equal to 2.6N (id_1 for f_{actDw} in the motion law with duration 0.5s when $f_{des} = 50$N). This corresponds also to the maximum mean percentage error, which is 5.2% (id_2 in the same test). During the tests done on the IPAnema 3 Mini, similar or worse results were obtained: the values of id_2 for the force-controlled cables in Tables 5.4–5.8 were almost always higher.

By analyzing the results when the friction force model is not considered in the controller, one can observe that the absolute mean error of the actual forces (id_1) is similar for both desired forces (50N or 150N). This means that the average percentage error when a higher force is commanded to the cable is lower. In fact, mean errors lower than 5% of the desired forces arise when the commanded force is 150N (see Table 5.13). Even for lower forces, the value of id_2 is always under 14%, which is a good result if compared to the ones obtained on the IPAnema 3 Mini, where the maximum average percentage error of the actual cable force reaches the value of 38% of the desired tension (see Figures 5.2, 5.3 and Tables 5.1, 5.2). The acquired data shows that not considering the friction model when estimating motor torque has different effects in different motion directions. This is due to the shape of the friction torque, which is modeled in Figure 3.9. The friction torque is negative for the positive motion direction of the EE (which corresponds to the positive axis of the velocity in Figure 3.9). If its contribution is not considered, the torque generated by the motor on the winch connected to the force-controlled cable is higher than the one that should be commanded to the wire, generating a higher force. The result is that f'_{actUp} is always higher than f_{actUp}. In the negative motion direction, the effect of the friction torque is the opposite, resulting in a f'_{actDw}, which is always lower than f_{actDw}.

Compared to the tests executed on the IPAnema 3 Mini, the ones described here involve movements with higher velocities and accelerations. The maximum velocity the

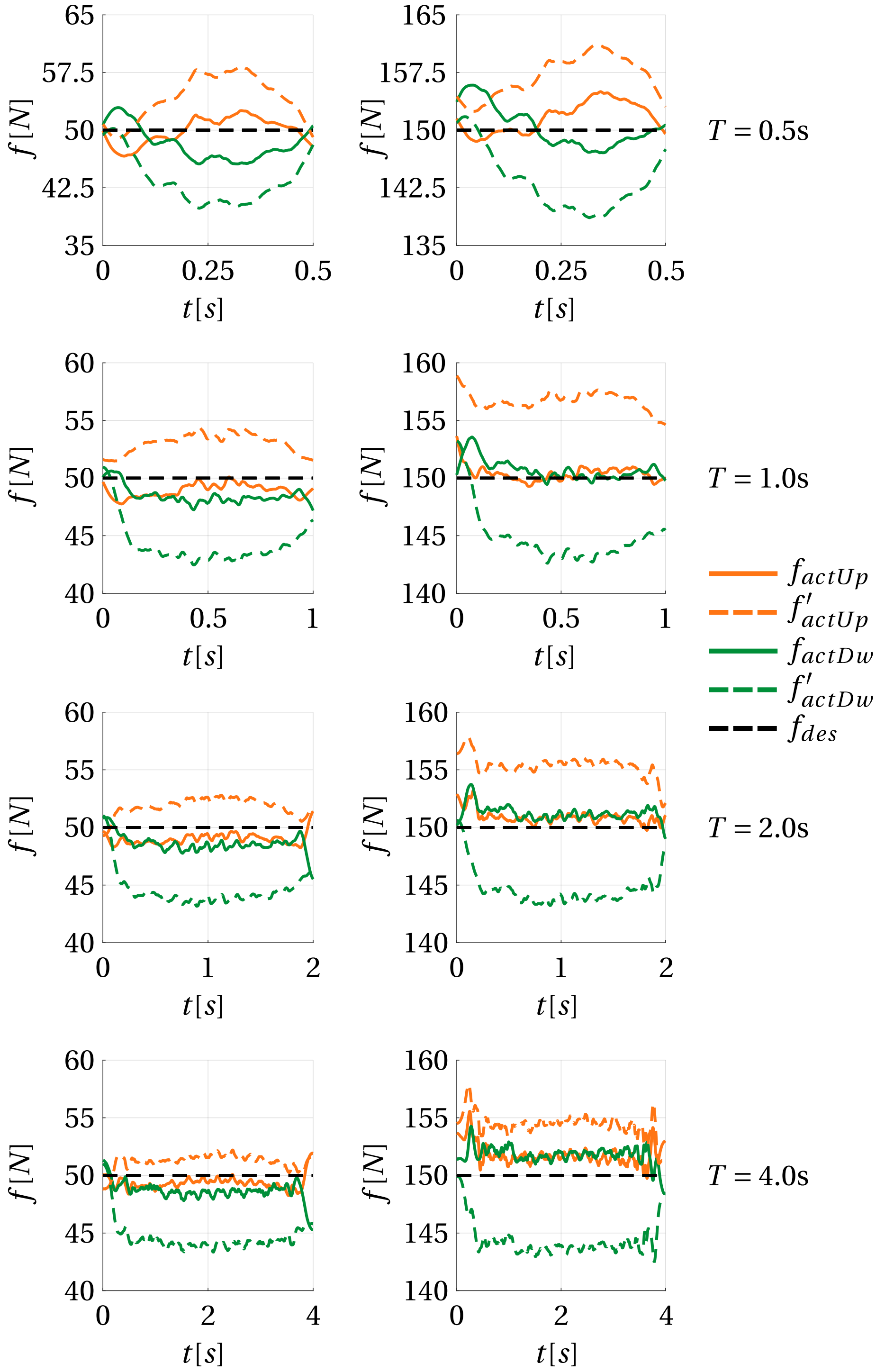

Figure 5.14: Force tracking during the experiments on the test bench with two cables when a constant force is commanded to the force-controlled cable. The desired force is 50N for the plots in the left column and 150N for the plots in the right column.

Duration		$T = 0.5$s	$T = 1$s	$T = 2$s	$T = 4$s
f_{actUp}	id_1 [N]	1.5	1.1	1.0	0.8
f'_{actUp}		4.4	3.1	1.9	1.3
f_{actDw}		2.6	1.6	1.5	1.4
f'_{actDw}		6.7	5.8	5.5	5.4
f_{actUp}	id_2 [%]	3.0	2.2	2.1	1.5
f'_{actUp}		8.8	6.1	3.7	2.6
f_{actDw}		5.2	3.2	3.0	2.8
f'_{actDw}		13.4	11.7	11.0	10.9

Table 5.12: Indices in Eqs. (5.1)–(5.2) for tests in Figure 5.14 when $f_{des} = 50$N.

Duration		$T = 0.5$s	$T = 1$s	$T = 2$s	$T = 4$s
f_{actUp}	id_1 [N]	2.1	0.5	0.9	1.8
f'_{actUp}		7.1	6.7	5.4	4.4
f_{actDw}		2.2	0.8	1.3	1.8
f'_{actDw}		7.1	5.5	5.4	5.6
f_{actUp}	id_2 [%]	1.4	0.4	0.6	1.2
f'_{actUp}		4.7	4.5	3.6	2.9
f_{actDw}		1.5	0.5	0.8	1.2
f'_{actDw}		4.7	3.6	3.6	3.8

Table 5.13: Indices in Eqs. (5.1)–(5.2) for tests in Figure 5.14 when $f_{des} = 150$N.

IPAnema 3 Mini reached during the tests described in Section 5.1 is 0.1m/s (in Cartesian space). On the contrary, during the movements executed for the tests shown in Figure 5.14, the following maximum velocities and accelerations are reached based on the motion duration T:

- if $T = 4$s, $v_{max} = 0.45$m/s and $a_{max} = 0.31$m/s^2;
- if $T = 2$s, $v_{max} = 0.9$m/s and $a_{max} = 1.24$m/s^2;
- if $T = 1$s, $v_{max} = 1.8$m/s and $a_{max} = 4.9$m/s^2;
- if $T = 0.5$s, $v_{max} = 3.6$m/s and $a_{max} = 19.8$m/s^2.

From the results obtained in terms of force tracking, the controller seems to be applicable with good performance even when high cable velocities and accelerations are required. This was an open issue after the tests executed on the IPAnema 3 Mini.

The lower effects of friction in the CORHDA kinematic chain, if compared with those of the IPAnema winches, demonstrate the effectiveness of the CORHDA design. Since both robots do not use gear reducers, the main difference is the number of pulleys between the drum and the EE: five in the IPAnema 3 Mini and only one in the CORHDA (see Figures 3.3 and 3.6). This was possible because it was decided not to mount force sensors in the CORHDA. In fact, if load cells were added to the robot, they should probably have been integrated with a pulley mechanism (see Figure 3.2(c)) since mounting them on the EE (Figure 3.2(a)) or in the winches (Figure 3.2(b)) would have reduced the maximum dynamics of the robot. The low impact of friction in the

CORHDA kinematic chain also justifies the simplifications applied to estimate the friction torque model of the robot (see Section 3.2.2).

The tests executed with a force that changes linearly between 50 and 150 N are now analyzed. The rate of change of the desired force is $\dot{f}_{des} = 25N/s$. Figure 5.15 shows the corresponding results in force tracking. Every millisecond, the desired force is incremented according to $\dot{f}_{des}$ until it reaches 150N. After that, the force is decreased at the same rate until it reaches 50N. The oscillatory behavior of f_{des} is continuous over time, i.e., the same rate of force change is applied when the EE is at rest and during the trajectories. Many movements of the EE in the positive and negative direction are executed with a break between two consecutive motions. Since the linear change in the commanded tension is independent of the EE motion, in the tests shown in Figure 5.15, different force profiles are shown in different tests (even if $\dot{f}_{des}$ is always the same). The results are analyzed to evaluate the controller capability to track desired forces that change over time, even for faster motions with respect to ones tested on the IPAnema 3

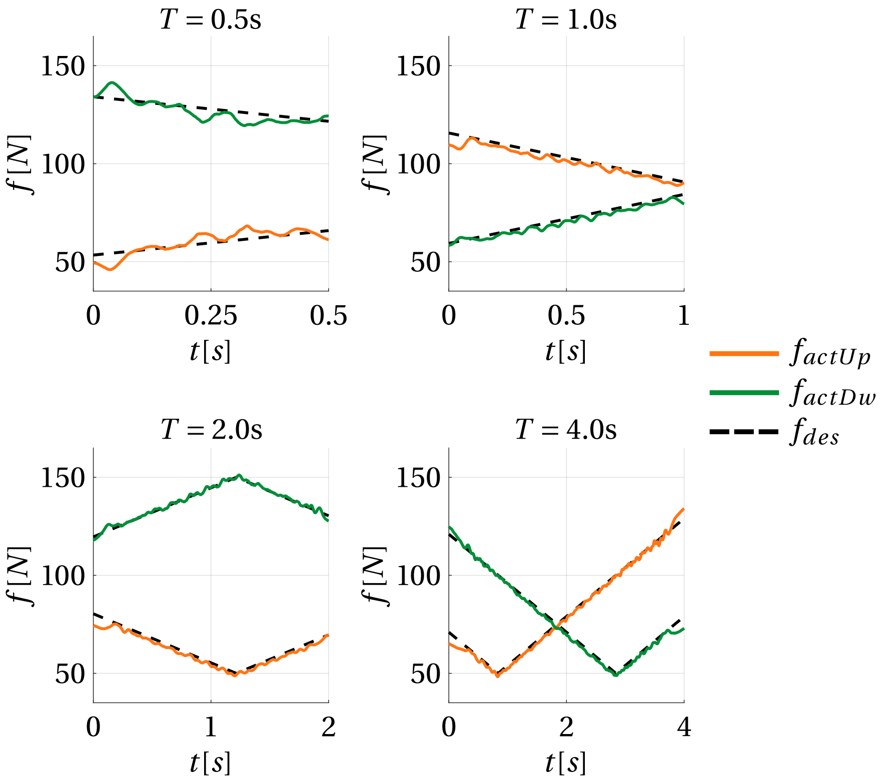

Figure 5.15: Force tracking during the experiments on the test bench with two cables when a linear force between 50N and 150N is commanded to the force-controlled cable. The rate of change of f_{des} is the same in all the tests, namely $\dot{f}_{des} = 25N/s$

Duration		$T = 0.5$s	$T = 1$s	$T = 2$s	$T = 4$s
f_{actUp}	id_1 [N]	2.6	2.1	1.6	1.4
f_{actDw}		2.8	1.6	0.7	1.5
f_{actUp}	id_2 [%]	4.4	2.0	2.5	1.8
f_{actDw}		2.2	2.2	0.5	2.0

Table 5.14: Values of indices in Eqs. (5.1)–(5.2) for the test analyzed in Figure 5.15 when a linear force with a rate of change $\dot{f}_{des} = 25N/s$ is commanded to the force-controlled cable.

Mini. Here, only the complete controller, which uses the friction torque model, is used. The performance indices computed in this case are listed in Table 5.14. The average error of the measured forces is always lower than 3N, and the average percentage error is always lower than 5%. These results are similar to those shown in Tables 5.12 and 5.13 for the trajectories during which f_{des} is constant (only the data when the friction torque model is used are taken into account even for the constant forces). Figure 5.15 shows that the real force is noisier for faster movements. As one can expect, these motions are the most critical. However, even in these cases, the controller behaves well, and the values of the indices id_1 and id id_2 confirm this claim.

The evolution in time of the cable forces found through a FD algorithm when the inverse kinetostatics of a CDPR is solved depends, above all, on the pose of the EE. This is especially true if the mass of the EE is low (as in the case of the CORHDA) since the effect of the inertia wrenches is small. It follows that the faster the trajectory of the EE, the higher the rate of change of the desired forces. An example is shown in Figure 4.5. Desired forces with rates of change $\dot{f}_{des} = 120\text{N/s}$ and $\dot{f}_{des} = 300\text{N/s}$ were also experimented during the execution of the trajectory with duration $T = 0.5\text{s}$. The results are shown in Figure 5.16 (here, the minimum and maximum forces reached during the force oscillations are respectively 20N e 140N). From the analysis of the charts and the performance indices in Table 5.15, one can see that, even in this case, the results are similar to those obtained with constant forces (Figure 5.14 and Tables 5.12 and 5.13) and with linear forces with lower rates of change (Figure 5.15 and Table 5.14). In particular, the maximum average error of the actual force is only 5.1% of the corresponding desired force (id_2 during the motion in the positive direction when $\dot{f}_{des} = 300\text{N/s}$).

For all results shown so far, the EE of the test bench made with the load cell was

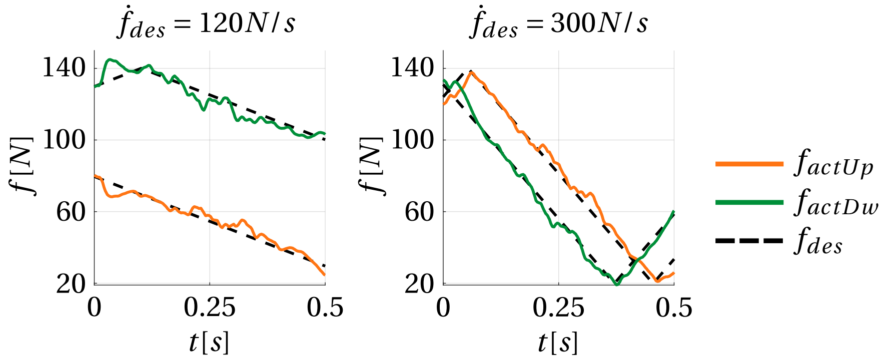

Figure 5.16: Force tracking during the experiments on the test bench with two cables when a linear force between 20N and 140N is commanded to the force-controlled cable. The rate of change of f_{des} is $\dot{f}_{des} = 120\text{N/s}$ for the tests shown on the left chart and $\dot{f}_{des} = 300\text{N/s}$ for the tests represented on the right chart.

		$\dot{f}_{des} = 120\text{N/s}$	$\dot{f}_{des} = 300\text{N/s}$
f_{actUp}	id_1 [N]	2.4	1.6
f_{actDw}		3.3	1.2
f_{actUp}	id_2 [%]	4.8	5.1
f_{actDw}		2.7	1.4

Table 5.15: Values of indices in Eqs. (5.1)–(5.2) for the test analyzed in Figure 5.15 when a linear force with a rate of change $\dot{f}_{des} = 120\text{N/s}$ or $\dot{f}_{des} = 300\text{N/s}$ is commanded to the force-controlled cable.

used (see Figure 5.12(b)). Since it is difficult to execute movements with higher cable velocities and accelerations with the force sensor mounted on the EE due to the electric cable necessary to power it and transmit its output signal, the last results that will be shown are obtained by mounting the EE without the load cell on the test bench (see Figure 5.12(a)). Two motion laws with a displacement of 1.5m executed respectively in 0.3s and 0.2s are analyzed when a constant tension equal to 100N is commanded to the force-controlled cable. During the movement with duration $T = 0.3s$, a maximum velocity and acceleration equal to 9m/s and 82.5m/s^2 are reached, while when the motion with duration $T = 0.2s$ is executed, the maximum velocity and acceleration are 13.5m/s and 186m/s^2. Since measuring the actual force on the wire is impossible, the desired and the actual motor torque are saved and analyzed. They are shown for both movements in the positive (τ_{actUp}) and negative (τ_{actDw}) motion direction in Figure 5.17. The fact that the actual motor torque reproduces the desired one (except for some oscillations) means that the high-level PID of the HC-e controller works well by generating the desired FE on the motor. This is true also when very high accelerations (which influence the inertial torque acting on the drum) and velocities (which influence the friction torque model) are involved. The faster the motion, the noisier the behavior of the torque and (probably) the force on the cable. However, the results shown in Figure 5.17 demonstrate that the controller works well even when speed changes and motion inversion are so rapid that they influence the motor torque more than the force required on the cable. The applicability of the HC-e controller, even when movements with these dynamics are involved, is also justified by the visual analysis of the motion itself since the wires do not become visibly slack while the EE executes the trajectory. Moreover, the results discussed in this section demonstrate that the effect of friction torque is limited in the CORHDA winches. This means that if the inertial torque on

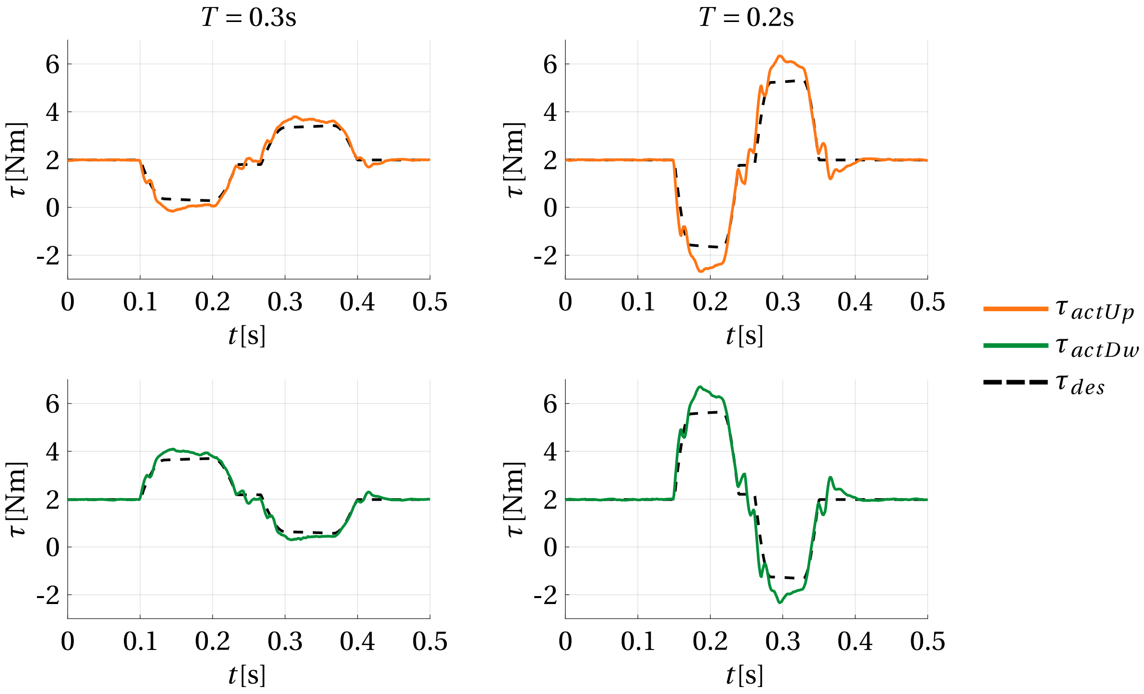

Figure 5.17: Desired and actual motor torques during two trajectories with a displacement of 1.5m executed respectively in 0.3s (charts on the left) and 0.2s (charts on the right) when a constant tension equal to 100N is commanded to the force-controlled cable.

the motor shaft is correctly estimated, the assumption of having a small error in the force commanded to the cable if the actual motor torque is similar to the desired one is acceptable.

One can observe that the HC-*e* controller introduced in Section 3.4.2 is effectively applicable for velocities and accelerations that are higher than those experimented in the IPAnema 3 Mini (see Section 5.1). The tests shown in this Section were a fundamental step in tuning the controller before its use on the complete robot. The obtained results justify the implementation of the HC in the CORHDA, which will be analyzed in the next section.

5.3 Experimental tests on the CORHDA

5.3.1 Evaluation of cable forces

The tests executed on the CORHDA to evaluate the performance of the HC-*e* controller in terms of force tracking are similar to those performed on the IPAnema 3 Mini. The pair of cables to be force-controlled is chosen according to the workspace characterization introduced in Section 3.4.2 (see Figure 3.14) in all tests. In particular, five different paths were chosen to verify the controller performance in different situations. Every designed path is tested for different dynamics. This means the EE reaches a different maximum velocity and acceleration during different executions of the same path. This way, the influence of the motion dynamics on the HC introduced in Chapter 3 is analyzed, and the possibility of using the HC-*e* controller on the CORHDA for its future application to the fast bin-picking task will be demonstrated. Every tested trajectory is identified according to the nomenclature introduced in Table 5.16.

Three rectilinear trajectories and an elliptical one with the orientation of the EE described by the rotation matrix $\mathbf{R} = \mathbf{I}_3$ are defined (i.e., paths 1 to 4). The first rectilinear path (path 1, see Figure 5.19) is completely inside the volume of the workspace in which force-controlling cables 7 and 8 guarantees to have a FD sensitivity index always lower than 2N (see Figure 3.14(b)). Similarly, the second rectilinear path (path 2, see Figure 5.29) is inside the part of the workspace in which the FD sensitivity index is lower than 2N if wires 5 and 6 are force-controlled (see Figure 3.14(a)). The force-controlled cables are assigned during these two movements. The third rectilinear path (path 3, see Figure 5.37) and the elliptical one (path 4, see Figure 5.43) cross the border between the two volumes of the workspace represented in Figure 3.14. In these cases, the online change of the force-controlled cables (between pairs 5,6 and 7,8) is tested. The last path tested (path 5, see Figure 5.51) is rectilinear as the first three ones, but, during this movement, the orientation of the EE is changed by making the Euler angles ϵ_x and ϵ_z oscillate around zero with an amplitude respectively equal to $0.25 rad$ and $0.15 rad$. In particular $\epsilon_x = -0.25 rad$, and $\epsilon_z = -0.15 rad$ in the first point of the path while $\epsilon_x = 0.25 rad$, and $\epsilon_z = 0.15 rad$ in the last point of the path. In this case, the workspace characterization represented in Figure 3.14 is no longer strictly valid since the orientation of the EE is different from the one considered to compute the FD sensitivity index. However, since the path shown in Figure 5.51 is completely inside the volume shown in Figure 3.14(a), cables 5 and 6 are still chosen to be force-controlled even in Tests 51–54. The obtained results in these last tests will demonstrate the possibility of choosing the pair of controlled cables according to the workspace characterization visualized in Figure 3.14 even when the platform orientation differs from the one used to compute the volumes shown in the figure.

For all rectilinear motion laws, the EE started its trajectory at one of the two extreme points, and back-and-fort motions were executed. The EE executed two complete revolutions for elliptical trajectories. The EE in the middle point of each test is returned to its original position after one complete movement cycle. Then, the same cycle is repeated, and at the end of the motion, the EE returns again to its initial pose.

The actual forces measured by the force sensors mounted on the EE-2 were recorded for every trajectory with two different controllers. Since the CORHDA was developed with the idea of not mounting load cells in its kinematic chain, it is impossible to control cable tensions with feedback values from the force sensors, and the latter are exploited only to verify the effectiveness of the HC strategy. For this reason, the HC-e controller will be compared only to the IKC, which is the only one among the ones already experimented on the IPAnema 3 Mini (see Section 5.1) that does not use force sensors. In each test, the indices in Eqs. (5.1)–(5.4) are computed for every cable to evaluate the performances of the two implemented controllers. The results are listed in Tables 5.18–5.37. Differently from what was done on the IPAnema 3 MIni, indices id_1 and id_2 are also computed when the IKC is applied. This is because considering the wires elastic model in the resolution of the inverse kinetostatic problem of the CORHDA allows (in theory) the application of the desired FD to the robot cables even

Table 5.16: Legend for identifying the tests done on the CORHDA to evaluate the performance of the HC-e controller. Figures 5.19–5.58 and Tables 5.18–5.37 refer to this legend.

Path	**Force-Controlled Cables**	**Test**	$\mathbf{v_{max}}[m/s]$	$\mathbf{a_{max}}[m/s^2]$
1: Rectilinear pure translation	7,8	Test 11	0.8	2.1
		Test 12	2.4	19.0
		Test 13	4.4	64.0
		Test 14	5.6	104.0
		Test 15	6.4	136.6
2: Rectilinear pure translation	5,6	Test 21	0.8	2.1
		Test 22	2.4	19.0
		Test 23	4.4	64.0
		Test 24	5.6	104.0
3: Rectilinear pure translation	5,6 and 7,8	Test 31	0.6	1.2
		Test 32	2.2	16.1
		Test 33	4.2	58.7
4: Elliptical pure translation	5,6 and 7,8	Test 41	0.3	0.3
		Test 42	1.6	8.2
		Test 43	3.2	33.0
		Test 44	4.4	64.5
5: Rectilinear rototranslation	5,6	Test 51	0.4	0.6
		Test 52	2.2	14.6
		Test 53	4.4	59.0
		Test 54	5.8	95.0

without any kind of force control (see Section 3.1).

The force limits defined for the robot are $f_{min} = 20$ N and $f_{max} = 350$ N. By following the procedure already adopted on the IPAnema 3 Mini, to keep some margin with respect to force oscillations and imprecision in the robot geometry or wrench estimation, a minimum tension $f'_{min} = 30$N is considered for the computation of the FD.

Paths 1 (Tests 11–15) and 2 (Tests 21–24) are symmetric with respect to the same plane the workspace volumes shown in Figure 3.14 are symmetric to. This means that the behavior of the controller is the same if applied in the same conditions with different force-controlled cables: by executing movements in the volume shown in Figure 3.14(b) by force-controlling cables 7,8 or movements in the volume shown in Figure 3.14(a) by force-controlling cables 5,6 the obtained results are indeed similar. In this situation, the average percentage error of the actual cable forces compared to the desired ones is always less than 10% for movements that involve EE velocity and accelerations approximately up to 4.5m/s and 65m/s^2. This is also valid for some motions with higher dynamics (for Test 24, the values of id_2 on cables 5 and 6 are 7.7% and 9%). In other cases (Tests 14 and 15), by reaching higher velocities and accelerations, the precision in tracking the desired cable tensions of force-controlled cables slightly drops: the maximum average percentage error is in cable 7 during Test 15, where $id_2 = 17\%$. In general, the error in the actual cable forces compared to the desired ones is similar to that obtained in the IPAnema 3 Mini (see Section 5.1.2.1), but it is higher than the one gained during the tests on the two-cable test bench (see Section 5.2), where id_2 was always less than 6%. This drop in the controller precision is justified by higher system complexity, higher dynamics tested, and higher modeling errors. In particular, it is impossible to model the dynamics of the electric cable necessary to power the force sensors mounted on the EE (see Figure 4.17). This is the main reason for not executing tests with higher motion dynamics with EE-2 mounted on the CORHDA. In fact, the risk of breaking the electric cables and the load cells increases when the movements become faster, and the results obtained are highly influenced by the experimental setup itself, which makes the tests useless. For example, a different real FD can arise from a different external wrench on the EE due to the electric cable dynamics. This way, the lack of precision of cable forces in the length-controlled cables could be due not to the controller itself but to a different FD (unpredictable) from the theoretical one. Moreover, the higher mass of EE-2 compared to the one of EE-1 does not allow it to reach the accelerations for which it was originally developed the robot (see Section 4.1). It was empirically noticed that the maximum accelerations possible with EE-2 are approximately between $140 m/s^2$ and 150m/s^2. Only Test 15 involves velocities and accelerations higher than 6m/s and 110m/s^2. For faster movements, see Section 5.3.3. As expected, the highest values of id_2 (38.5% for cable 6) and id_1 (12.9N for cable 2) arise in this situation. A similar average percentage error is also obtained in Test 24 even if slightly lower dynamics are involved, and, in this case, the tracking of the desired tensions in the force-controlled cables is good, with an average percentage error of forces in cables 5 and 6 lower than 10%. This suggests that even velocities and accelerations in the order of 4.5m/s and 65m/s^2 can affect the obtained results due to modeling imprecisions. However, the HC-e controller allows cable force tracking, which is much better than the one obtained with the IKC, where the average percentage errors are always much higher by reaching values up to 50% (Test 11 on cable 5, Test 23 and 24 on cable 7).

The errors of the real cable forces compared to the desired ones produce tensions that often drop under the desired lower limit (f_{min} = 20N) with IKC. For example, in Tests 15, 21, 22, 23, and 24, one force is always lower than f_{min} for more than the 60% of time (value of id_3), and, in general, in all trajectories there are at least two cable tensions that drop under the limit. On the contrary, when the HC-*e* controller is applied for slow motions, the wire forces are always higher than the given limit. For higher motion dynamics, when tensions drop under f_{min}, the time for which they stay under the limit is appreciably shorter compared to the case using the IKC. The worst case is for cable 5 in Test 15, where the force is lower than 20N for 30.6% of the time. Moreover, the average difference between the actual forces under the lower limit and the limit itself is sensibly less when the HC-*e* controller is used (see values of id_4). For example, in Test 23, when the IKC is used, the force on cable 7 drops under 20N for 51.2% of the time, and the average force value is 12.4N lower than f_{min}.

Tests 31–33 analyze the influence of changing the pair of force-controlled cables. The change is commanded in 60ms by choosing δ = 0.053 in Eq. (3.9). This value was tuned through experimental tests based on the previous experience acquired on the IPAnema 3 Mini. From the analysis of the data in Tables 5.27–5.29, we can notice that

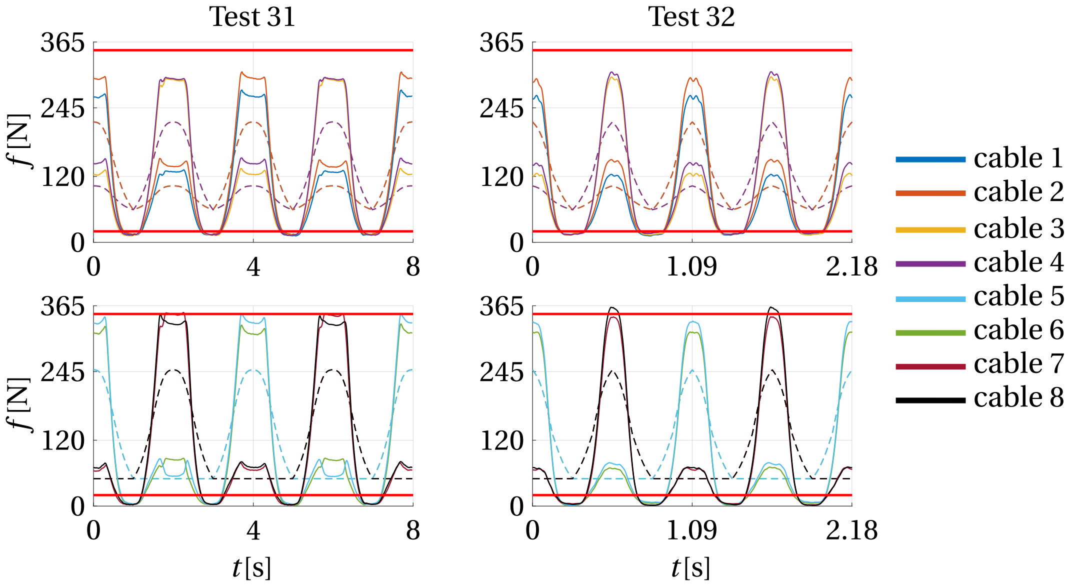

Figure 5.18: Cable forces obtained by the execution of Tests 31 (left column) and 32 (right column) with the IKC when the lower force limit for the computation of the FD is $f_{min} = 50$N.

	id_1 [N]		id_2 [%]		id_3 [%]		id_4 [N]	
Test	31	32	31	32	31	32	31	32
cable 1	41.8	41.6	42.7	46.5	23.9	32.5	5.2	4.9
cable 2	49.8	47.2	47	49.3	21.1	28.3	4.1	3.4
cable 3	46.4	44.8	44.8	47.6	23.9	31	5.4	4.4
cable 4	50.4	47.5	48	49.3	22.4	28.5	5.3	3.4
cable 5	47.4	44	55.9	54.5	31.6	40.3	13.3	12.7
cable 6	47.6	46.2	49.2	55.7	29	37.3	12.5	11.9
cable 7	49.8	46.5	53.5	55.6	35	39.6	13.4	13.2
cable 8	48.8	48.6	53.1	56.4	29.2	44.9	13.2	13.5

Table 5.17: Values of indices in Eqs. (5.1)–(5.5) for the forces shown in Figure 5.18.

the change of the pair of cables to be force-controlled does not influence the controller performances. In particular, the tracking of the desired wire tensions is optimal during tests 31 and 32, where average errors always lower than 11% arise, even on the length-controlled cables. Slightly higher errors (up to 19.3%) can be seen in Test 33. These errors are aligned with the ones obtained in Tests 11–24. The difference is that the errors are approximately spread on all wires, while when the force-controlled cables are assigned, errors on them are usually smaller. The higher force-tracking inaccuracies in Test 33 compared to Tests 31 and 32 produce forces under the limit for almost all cables. However, the time for which the forces stay under f_{min} is always very low (id_3 is always under 5%), and the average value of the drop under the limit is small (id_4 is always lower than 1.4N). Beyond the controller performance itself, its comparison with the IKC, in this case, is very interesting. In fact, the performance indices are always high for Tests 31–33 when the IKC is applied. Especially during tests 31 and 32, cables from 5 to 8 become visibly slack, influencing the pose of the EE. For example, during Test 31, the tensions on these cables drop under f_{min} for 40% – 50% of time, and the average value of force under the limit is for all wires between 13.8N and 14.8N lower than f_{min}. When the cables become visible slack, the force measured by the load cells is almost zero (see Figure 5.38). To verify if it is possible to avoid this problem with the IKC, some tests with a higher lower limit for the computation of the optimal FD (f'_{min} = 50N instead of 30N) were executed. The results are shown in Figure 5.18 and in Table 5.17. The minimum force shown in the charts and used to compute the indices is still $f_{min} = 20N$. In this case, the behavior of the EE is even worse than the previous one since the wires still become slack at the same point of the trajectory, and cable forces also overcome the higher limit (f_{max} = 350N) when the EE is near the workspace border. This proves that even by increasing f_{min}, it is impossible to guarantee that the tensions stay within the given limits without any control over them.

Tests 41–44 are executed on an elliptical path. Even in this case, we obtain much better results with the HC-*e* controller. With IKC for any motion law, many cable forces drop below the lower limit for more than 30% of time. In particular, during Test 41, cable 8 becomes almost slack: its value of id_4 is 13.2N, which is similar to the ones obtained in Test 31. Here, the change of the force-controlled cables has a more marked effect, especially when the switch is from cables 5,6 to 7,8. In this case, for the slowest trajectory (Test 41), there is a clear and sudden jump of the force on wire 7, which produces a small step during the EE motion (similar to what happened on the IPAnema 3 Mini, see Figure 5.10). For faster movements, this unwanted behavior is less present. In Test 44, it is, in practice, invisible. This suggests that a smoother switch of the force-controlled cable pair is more effective when executing slow movements. The result of this smoother change could be an error in the cable forces with a longer duration, but its effect on the overall is negligible, as it happened on the IPAnema 3 Mini (Figure 5.1.3). Smooth changes of the pair of force-controlled cables are, instead, not necessarily suitable for faster motions.

Tests 51–54 involve a rectilinear path and changes in the platform orientation. As described at the beginning of this Section, the pair of cables to be force-controlled is still chosen according to the workspace characterization introduced in Figure 3.14. Even if it is not guaranteed that cables 5,6 are still the best to be force-controlled, the obtained results are similar to those of Tests 11–24. In particular, for slower motions, the HC-*e* controller is capable of maintaining the wire tensions over the lower limit for all the time (id_3 is always zero in Test 51), while for faster movements, some cable forces go below f_{min}. However, even for the faster trajectory (Test 54), the worst case is represented by cable 7, which is taut with less than 20N only for 13.6% of the time. Even when velocities and accelerations approximately up to 6m/s and 100m/s^2 are reached, the force tracking is still good with a maximum average percentage error lower than 14% in the force-controlled cables, and lower than 36% in the length-controlled wires (see values of id_2 for Test 54). In any case, the results gained with the HC-e controller are better than the ones obtained with the IKC, demonstrating the effectiveness of the HC-e controller even when the pair of force-controlled cables is chosen according to a simplified model.

Especially from Tests 31–33 and 41–44, a general behavior can be inferred: the behavior of the HC-e controller tends to get worse for higher velocities and accelerations. However, the same is not true for the IKC. In fact, in many situations, the more marked difference between the IKC and the HC-e controller is visible for slower motions. This is interesting and unexpected. The reason is probably related to the higher complexity of the HC-e controller, which is influenced by the errors in the models used to describe and control the manipulator. This problem is more visible when fast movements are involved also because the effect of the electric cables used to power the load cells is not considered in the mathematical description of the robot dynamics. Also, higher errors in the estimations of the external wrench acting on the EE arise. Moreover, the work of the high-level PID (see Figure 3.15(a)) is more difficult since the desired FE has a higher rate of change, making it more difficult to design a controller capable of following it. Differently, the IKC can never be precise in applying the correct cable forces, so it is less influenced by the higher model inaccuracies. However, this does not mean that the use of IKC is motivated since there is no test in which the IKC is better than the HC-e controller; on the contrary, there are situations in which the IKC is not suitable to properly control the CDPR due to its impossibility of guaranteeing to maintain the cables taut (Test 31, 32, 41).

The analysis introduced in this Section shows that the HC-e controller developed in Chapter 3 is suitable for the CORHDA to control the cable forces in such a way as to guarantee to maintain cables taut without the need for direct force feedback. The controller works very well for slower movements by assuring that the wire forces are always higher than the given limits. For faster movements, the results are less accurate, but the time for which the forces drop below the predefined limit and the average value of the drop itself below f_{min} are always lower than the ones obtained by applying the IKC, which is the only other analyzed controller that does not exploit force sensors.

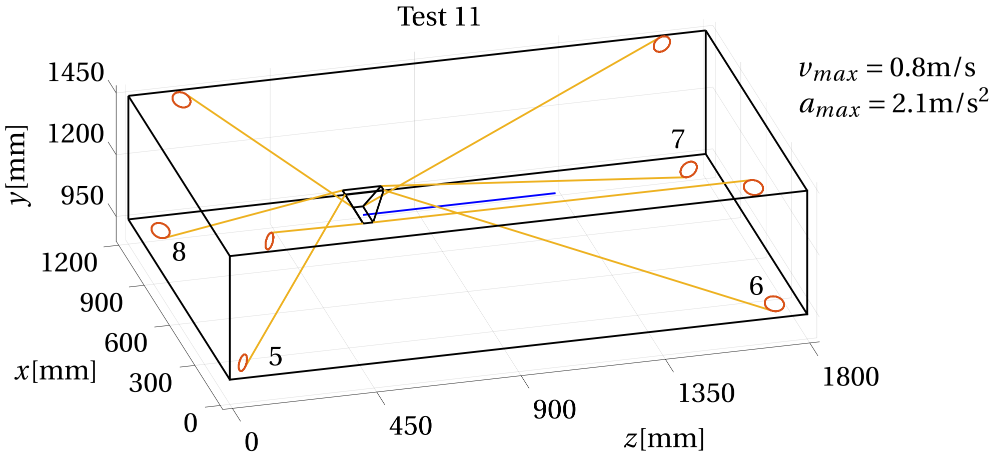

Figure 5.19: Trajectory executed during Test 11 (see Table 5.16).

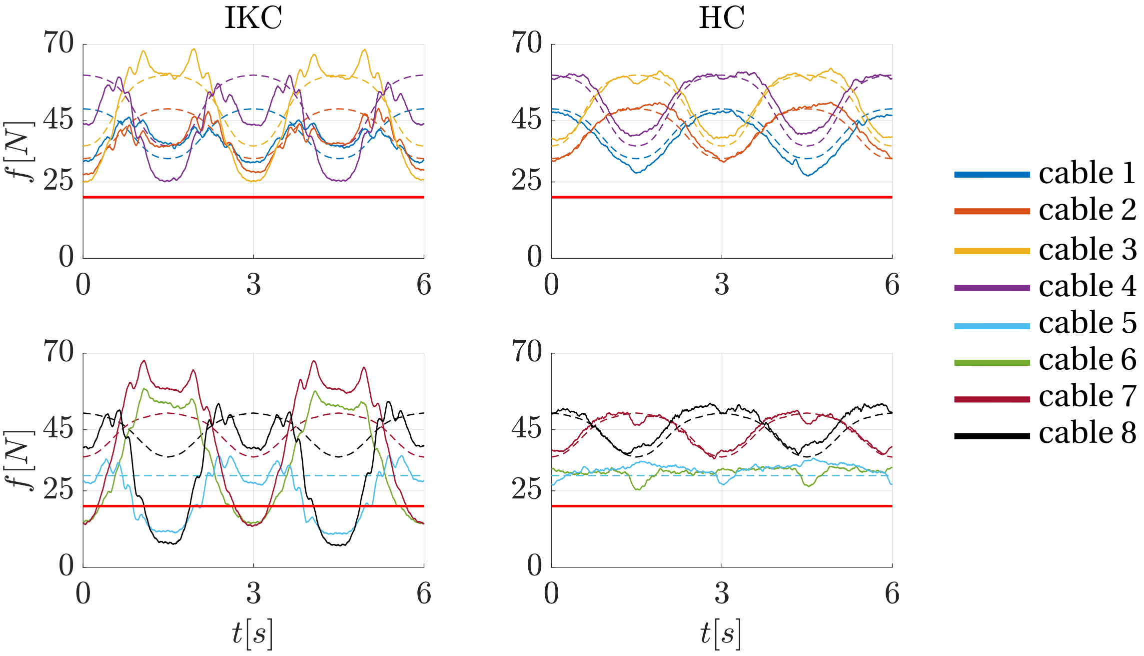

Figure 5.20: Desired (dashed lines) and measured (solid lines) cable forces during the execution of the trajectory in Figure 5.19 with IKC (left column) or HC-*e* (right column). f_{min} = 20 N and f_{max} = 350 N are the desired bounds of the cable tensions (red horizontal lines).

	id_1 [N]		id_2 [%]		id_3 [%]		id_4 [N]	
	IK	HC	IK	HC	IK	HC	IK	HC
cable 1	7.4	2.4	17	6.1	0	0	0	0
cable 2	4.7	1.4	10.9	3.3	0	0	0	0
cable 3	5.5	1.8	12.3	3.8	0	0	0	0
cable 4	7.6	2.5	16	5.5	0	0	0	0
cable 5	15	1.7	50	5.5	24.5	0	3.7	0
cable 6	8.2	2.5	27.2	8.5	37.5	0	6.2	0
cable 7	12.1	1.1	28.7	2.6	19.4	0	4.3	0
cable 8	12.3	2.3	30.6	5.3	27	0	9.4	0

Table 5.18: Values of indices in Eqs. (5.1)–(5.4) for the forces shown in Figure 5.20. The force-controlled cables are highlighted in bold.

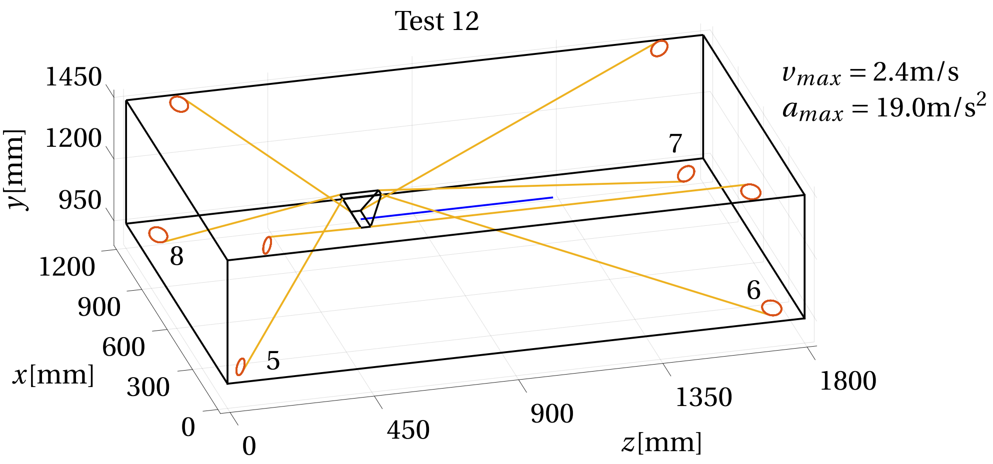

Figure 5.21: Trajectory executed during Test 12 (see Table 5.16).

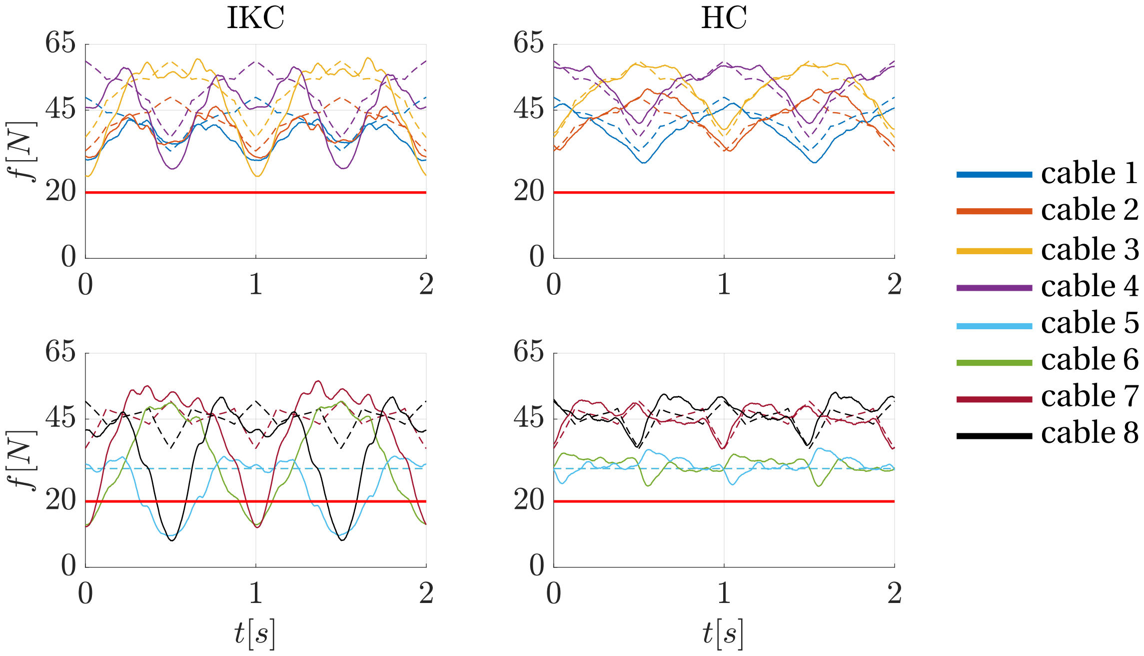

Figure 5.22: Desired (dashed lines) and measured (solid lines) cable forces during the execution of the trajectory in Figure 5.21 with IKC (left column) or HC-*e* (right column). f_{min} = 20 N and f_{max} = 350 N are the desired bounds of the cable tensions (red horizontal lines).

	id_1 [N]		id_2 [%]		id_3 [%]		id_4 [N]	
	IK	HC	IK	HC	IK	HC	IK	HC
cable 1	5.9	2.7	13	6.7	0	0	0	0
cable 2	4.3	1.9	9.7	4.5	0	0	0	0
cable 3	5.1	1.3	11	2.7	0	0	0	0
cable 4	6.3	2.1	12.8	4.5	0	0	0	0
cable 5	11.7	2	39	6.7	19.5	0	4.5	0
cable 6	7.1	1.8	23.8	6.1	32.4	0	6.3	0
cable 7	9.6	1.9	22.3	4.1	12.2	0	4.9	0
cable 8	10.8	2.6	24.9	5.7	17.3	0	7.5	0

Table 5.19: Values of indices in Eqs. (5.1)–(5.4) for the forces shown in Figure 5.22. The force-controlled cables are highlighted in bold.

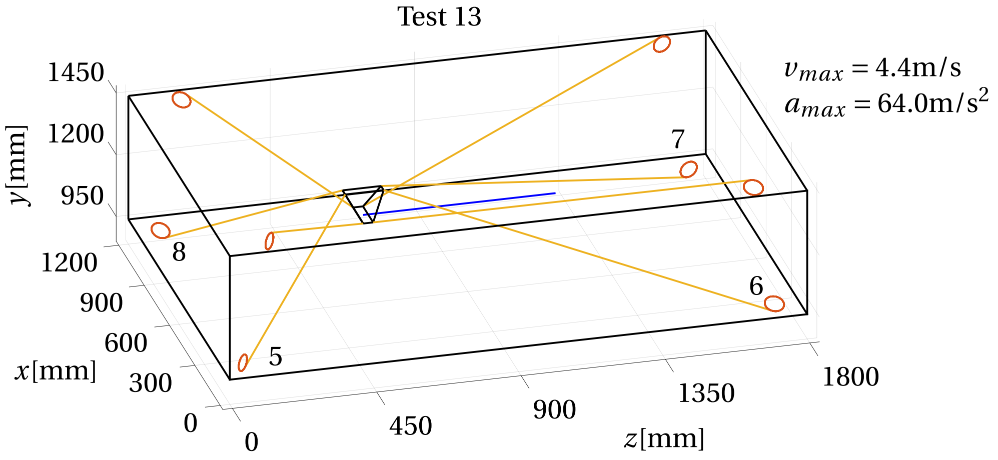

Figure 5.23: Trajectory executed during Test 13 (see Table 5.16).

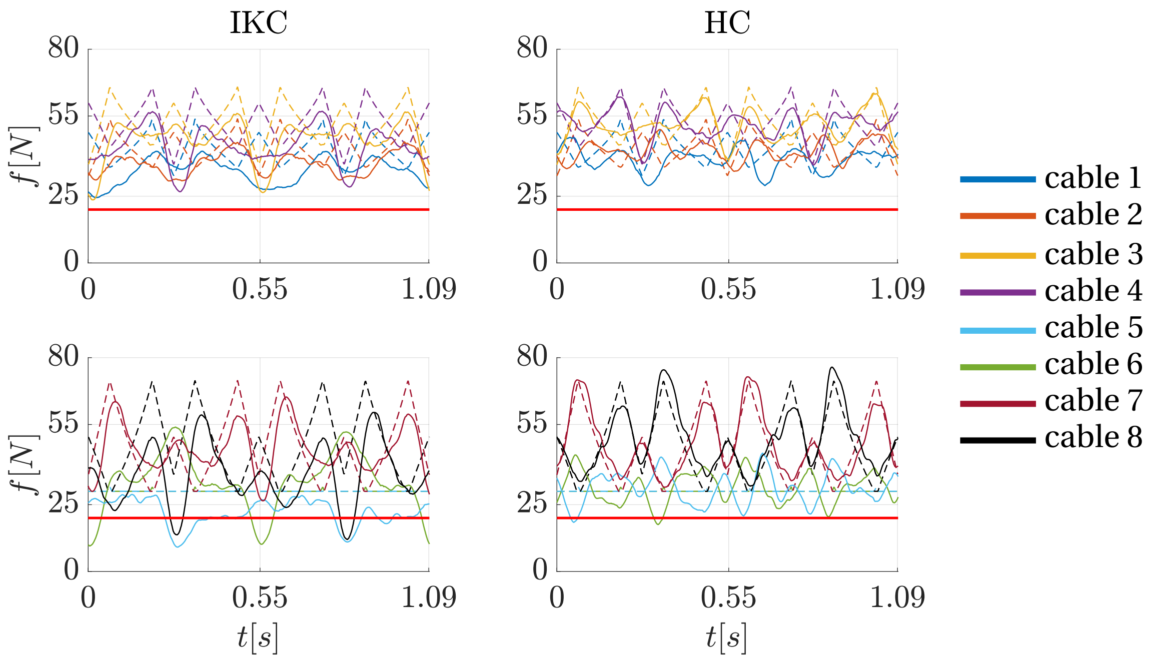

Figure 5.24: Desired (dashed lines) and measured (solid lines) cable forces during the execution of the trajectory in Figure 5.23 with IKC (left column) or HC-*e* (right column). $f_{min} = 20$ N and $f_{max} = 350$ N are the desired bounds of the cable tensions (red horizontal lines).

	id_1 [N]		id_2 [%]		id_3 [%]		id_4 [N]	
	IK	HC	IK	HC	IK	HC	IK	HC
cable 1	8.7	6.2	19.7	14	0	0	0	0
cable 2	5.9	4.1	13	9.7	0	0	0	0
cable 3	6.6	2.7	12.6	5.2	0	0	0	0
cable 4	8.9	3.5	16.7	6.6	0	0	0	0
cable 5	8.8	5.1	29.2	17.1	12.8	2.6	6.4	1.5
cable 6	7.9	5	26.3	16.6	28.5	2	4.2	1
cable 7	6.8	3.3	15.2	7.1	0	0	0	0
cable 8	11.6	3.9	24	8.4	7.7	0	5	0

Table 5.20: Values of indices in Eqs. (5.1)–(5.4) for the forces shown in Figure 5.24. The force-controlled cables are highlighted in bold.

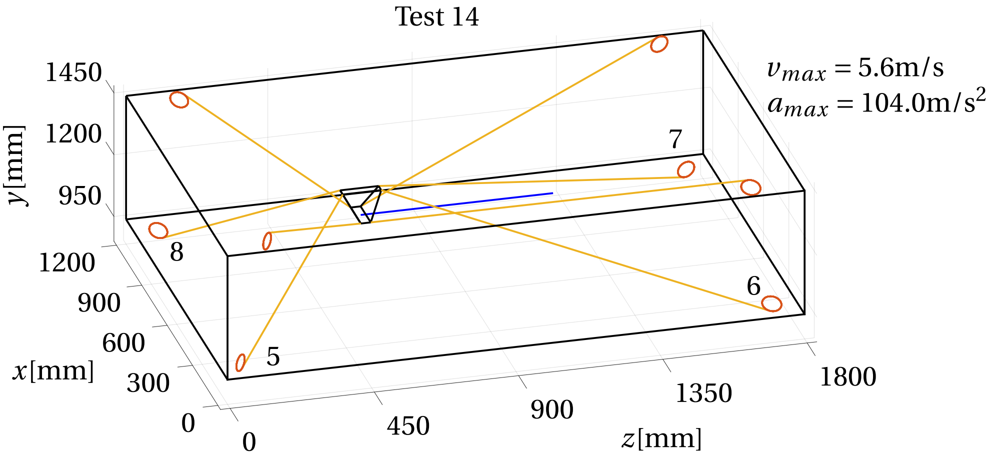

Figure 5.25: Trajectory executed during Test 14 (see Table 5.16).

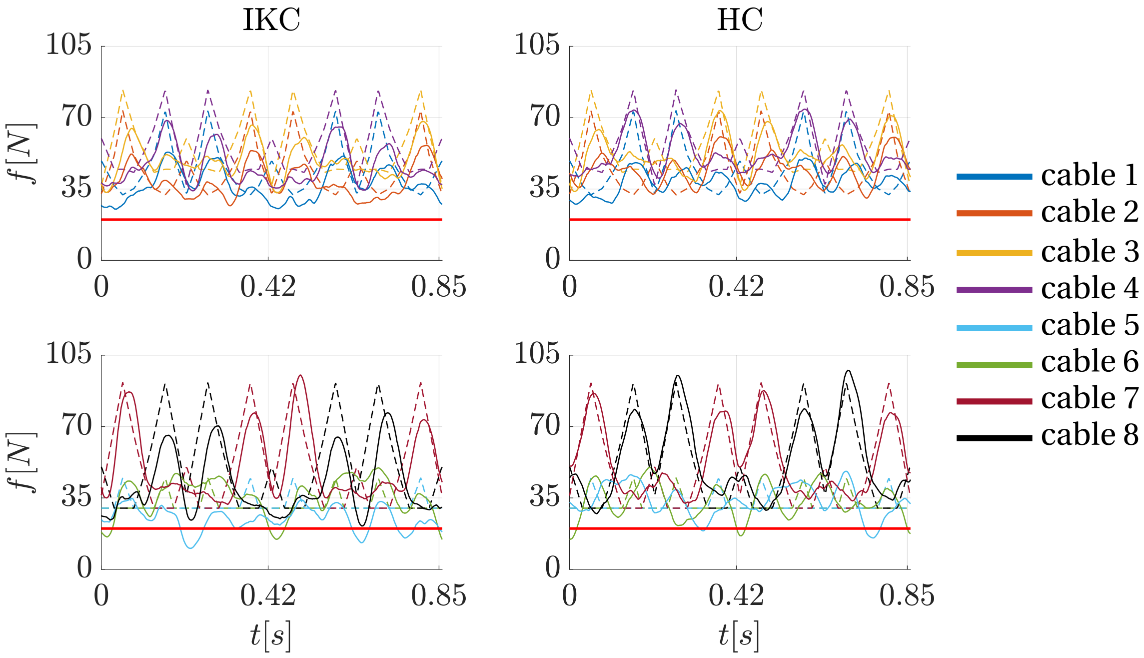

Figure 5.26: Desired (dashed lines) and measured (solid lines) cable forces during the execution of the trajectory in Figure 5.25 with IKC (left column) or HC-e (right column). $f_{min} = 20$ N and $f_{max} = 350$ N are the desired bounds of the cable tensions (red horizontal lines).

	id_1 [N]		id_2 [%]		id_3 [%]		id_4 [N]	
	IK	HC	IK	HC	IK	HC	IK	HC
cable 1	9.2	9.3	18.9	19	0	0	0	0
cable 2	8.4	9.2	17.3	21	0	0	0	0
cable 3	8	7.3	13.4	12.9	0	0	0	0
cable 4	9.5	5.5	16.1	9.9	0	0	0	0
cable 5	8	8	25.8	25.4	9.1	5.6	3.2	2.9
cable 6	7.5	8.2	23.1	25.9	18.6	6.3	4.3	2.4
cable 7	9.8	6.8	20.4	15.5	0	0	0	0
cable 8	12.4	6.1	22.5	13.3	0	0	0	0

Table 5.21: Values of indices in Eqs. (5.1)–(5.4) for the forces shown in Figure 5.26. The force-controlled cables are highlighted in bold.

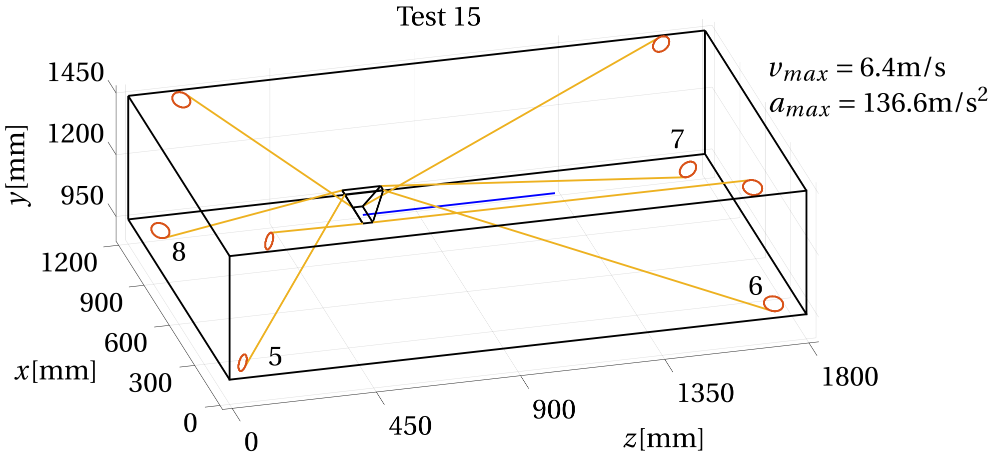

Figure 5.27: Trajectory executed during Test 15 (see Table 5.16).

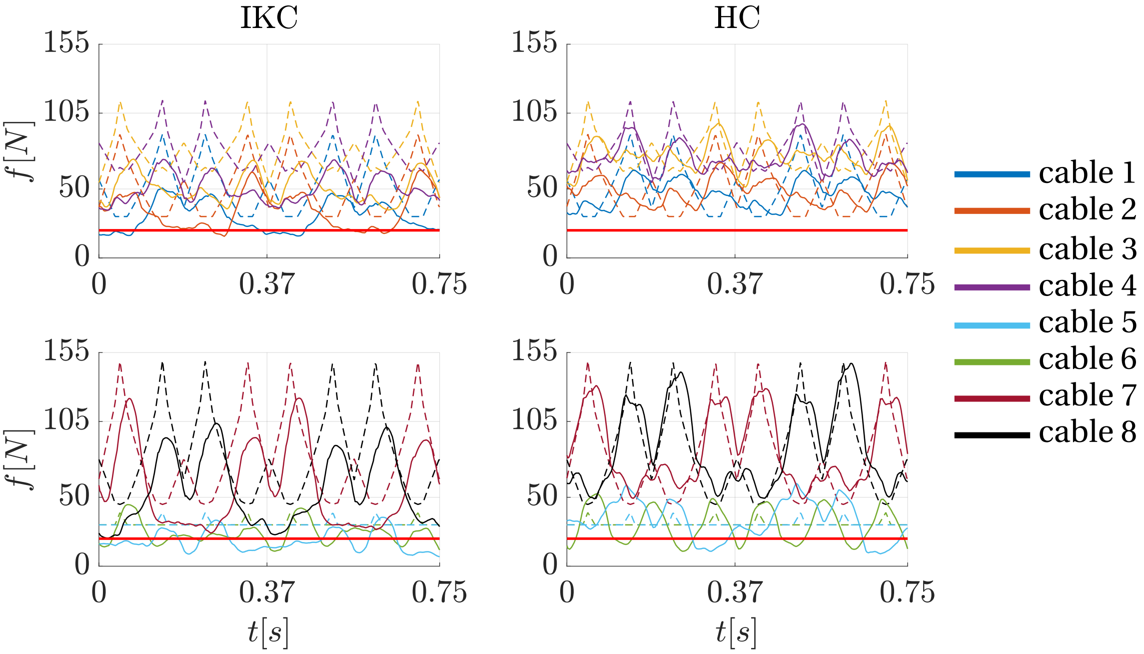

Figure 5.28: Desired (dashed lines) and measured (solid lines) cable forces during the execution of the trajectory in Figure 5.27 with IKC (left column) or HC-e (right column). $f_{min} = 20$ N and $f_{max} = 350$ N are the desired bounds of the cable tensions (red horizontal lines).

	id_1 [N]		id_2 [%]		id_3 [%]		id_4 [N]	
	IK	HC	IK	HC	IK	HC	IK	HC
cable 1	21.1	12.1	39.9	24.3	23.7	0	2.4	0
cable 2	17.5	12.9	32.9	27	12.5	0	1.7	0
cable 3	26.6	9.9	33.8	12.7	0	0	0	0
cable 4	27.4	8.2	34.9	10.2	0	0	0	0
cable 5	9	10.7	29.6	34.9	29.5	30.6	4.1	4.4
cable 6	12.8	11.9	42.3	38.5	68.6	21.3	6.1	7.1
cable 7	25.5	11.8	33.1	16.3	0	0	0	0
cable 8	26.1	11.6	32.7	15.5	0	0	0	0

Table 5.22: Values of indices in Eqs. (5.1)–(5.4) for the forces shown in Figure 5.28. The force-controlled cables are highlighted in bold.

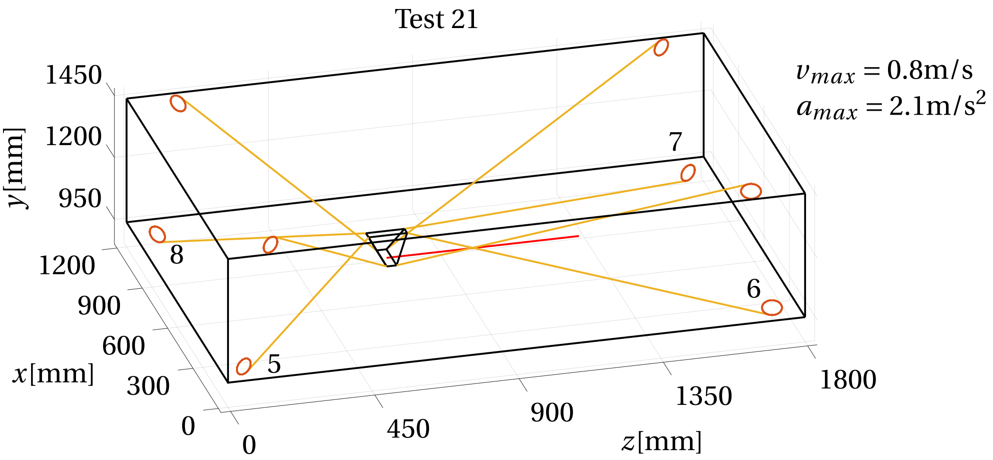

Figure 5.29: Trajectory executed during Test 21 (see Table 5.16).

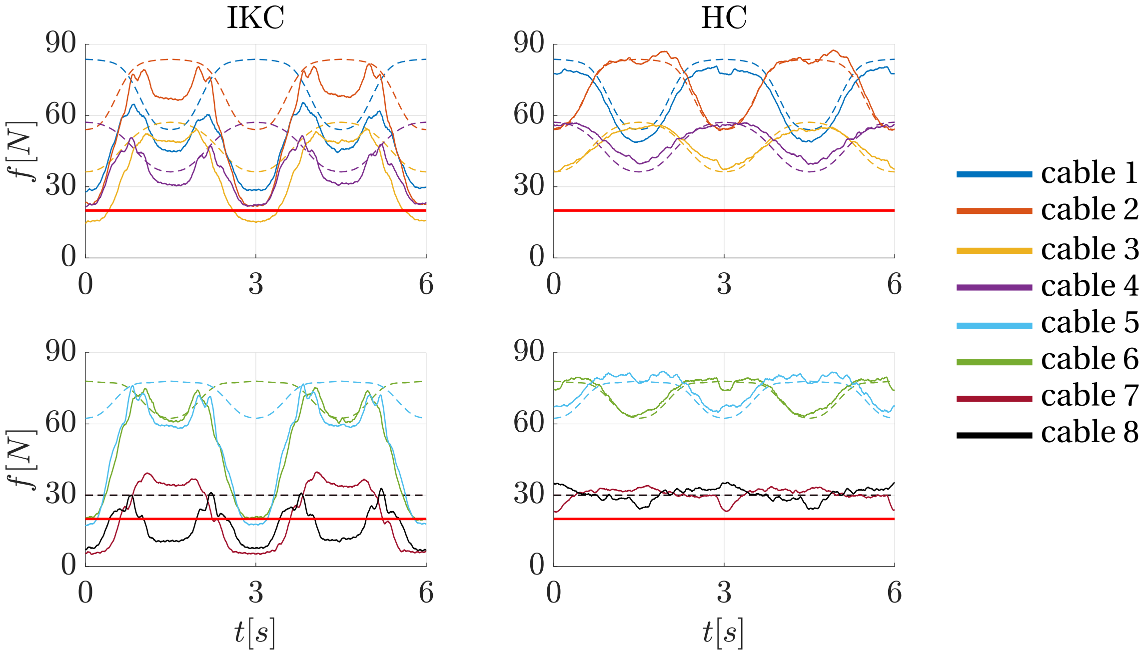

Figure 5.30: Desired (dashed lines) and measured (solid lines) cable forces during the execution of the trajectory in Figure 5.29 with IKC (left column) or HC-e (right column). f_{min} = 20 N and f_{max} = 350 N are the desired bounds of the cable tensions (red horizontal lines).

	id_1 [N]		id_2 [%]		id_3 [%]		id_4 [N]	
	IK	HC	IK	HC	IK	HC	IK	HC
cable 1	25.2	4.5	32.2	6.4	0	0	0	0
cable 2	16.8	1.4	26.1	1.8	0	0	0	0
cable 3	11.7	1.9	27.8	4.1	26.4	0	3.4	0
cable 4	13.1	2.8	24.9	6.5	0	0	0	0
cable 5	23.3	1.5	30.3	2.1	2.8	0	0.3	0
cable 6	21.9	2.9	32	4.1	14.2	0	1.8	0
cable 7	12.4	1.9	41.2	6.3	45.8	0	11	0
cable 8	13.5	2.2	44.9	7.5	61.3	0	8.3	0

Table 5.23: Values of indices in Eqs. (5.1)–(5.4) for the forces shown in Figure 5.30. The force-controlled cables are highlighted in bold.

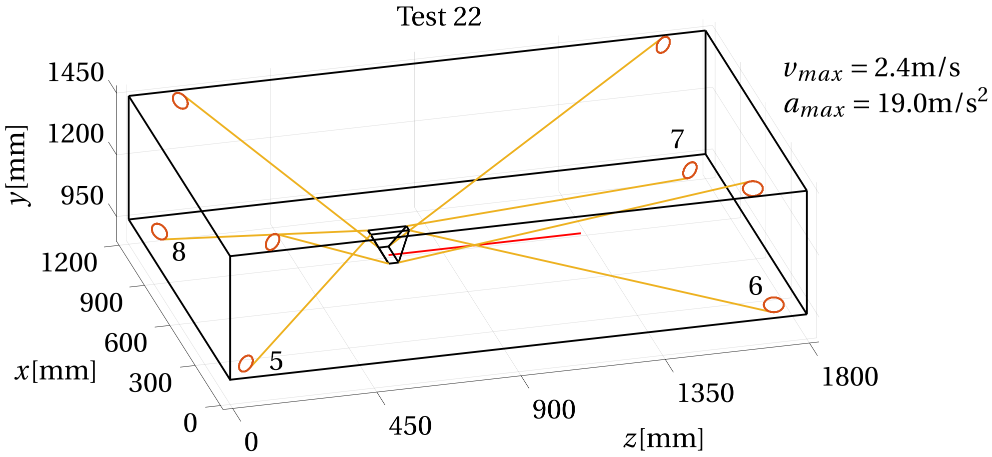

Figure 5.31: Trajectory executed during Test 22 (see Table 5.16).

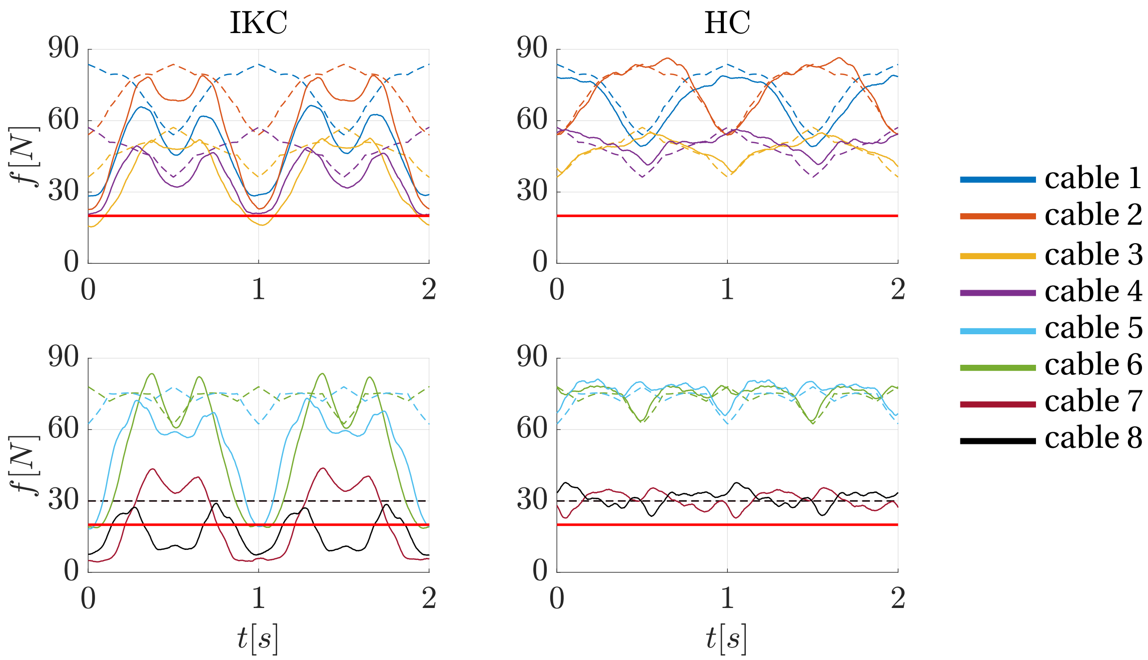

Figure 5.32: Desired (dashed lines) and measured (solid lines) cable forces during the execution of the trajectory in Figure 5.31 with IKC (left column) or HC-e (right column). $f_{min} = 20$ N and $f_{max} = 350$ N are the desired bounds of the cable tensions (red horizontal lines).

	id_1 [N]		id_2 [%]		id_3 [%]		id_4 [N]	
	IK	HC	IK	HC	IK	HC	IK	HC
cable 1	24	4.8	30.9	6.9	0	0	0	0
cable 2	15.4	1.8	23.5	2.5	0	0	0	0
cable 3	11.4	1.6	25.8	3.4	16.3	0	2.7	0
cable 4	12.7	3.1	24.8	6.9	0	0	0	0
cable 5	23.8	2	32	2.7	13.9	0	0.8	0
cable 6	20.5	3.6	28.9	5	4.9	0	0.8	0
cable 7	13.8	2.8	45.9	9.4	45.6	0	12	0
cable 8	13.7	2.8	45.7	9.3	63.6	0	8.4	0

Table 5.24: Values of indices in Eqs. (5.1)–(5.4) for the forces shown in Figure 5.32. The force-controlled cables are highlighted in bold.

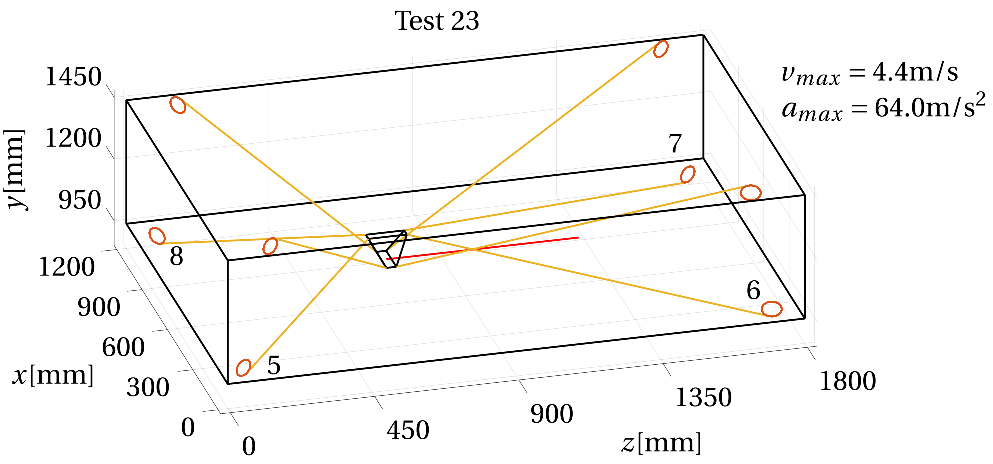

Figure 5.33: Trajectory executed during Test 23 (see Table 5.16).

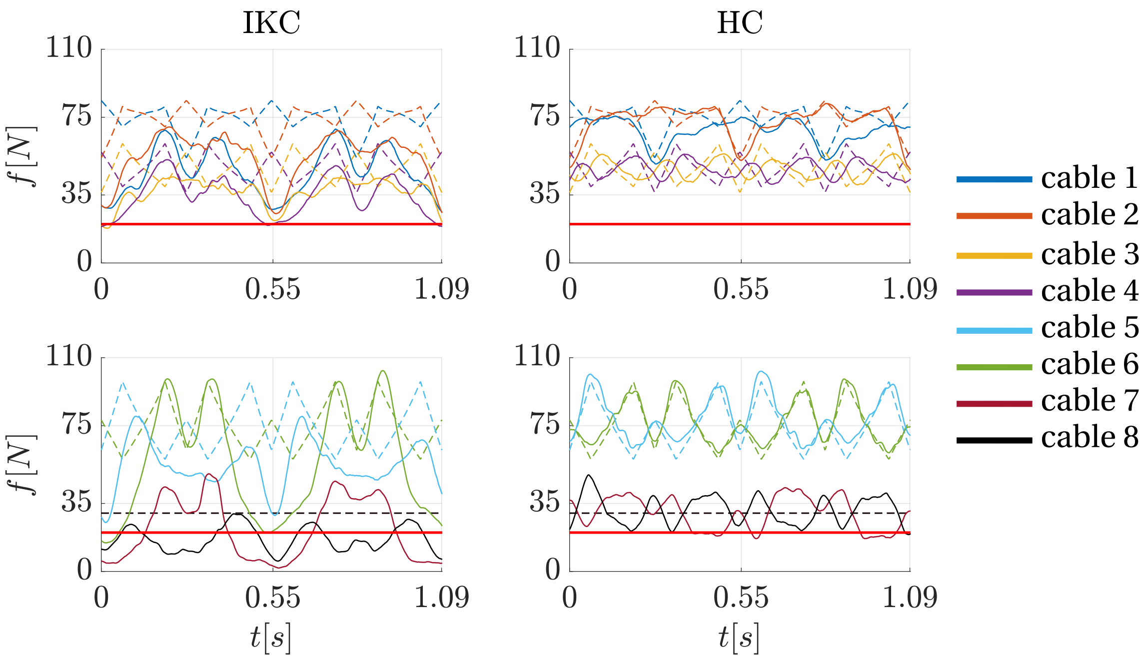

Figure 5.34: Desired (dashed lines) and measured (solid lines) cable forces during the execution of the trajectory in Figure 5.33 with IKC (left column) or HC-e (right column). $f_{min} = 20$ N and $f_{max} = 350$ N are the desired bounds of the cable tensions (red horizontal lines).

	id_1 [N]		id_2 [%]		id_3 [%]		id_4 [N]	
	IK	HC	IK	HC	IK	HC	IK	HC
cable 1	26.7	6.2	35.6	8.2	0	0	0	0
cable 2	19.2	3.2	26.5	4.5	0	0	0	0
cable 3	12.6	5	25.1	10.5	3.1	0	1.5	0
cable 4	14.7	4.7	29.9	9.6	5.7	0	0.6	0
cable 5	21.5	2.3	31	3.2	6.8	0	3.1	0
cable 6	20.2	4.3	26.5	5.9	0	0	0	0
cable 7	15.7	7.3	52.3	24.5	51.2	22.7	12.4	1.5
cable 8	13.3	6.3	44.3	21.1	66	1.6	7.2	0.8

Table 5.25: Values of indices in Eqs. (5.1)–(5.4) for the forces shown in Figure 5.34. The force-controlled cables are highlighted in bold.

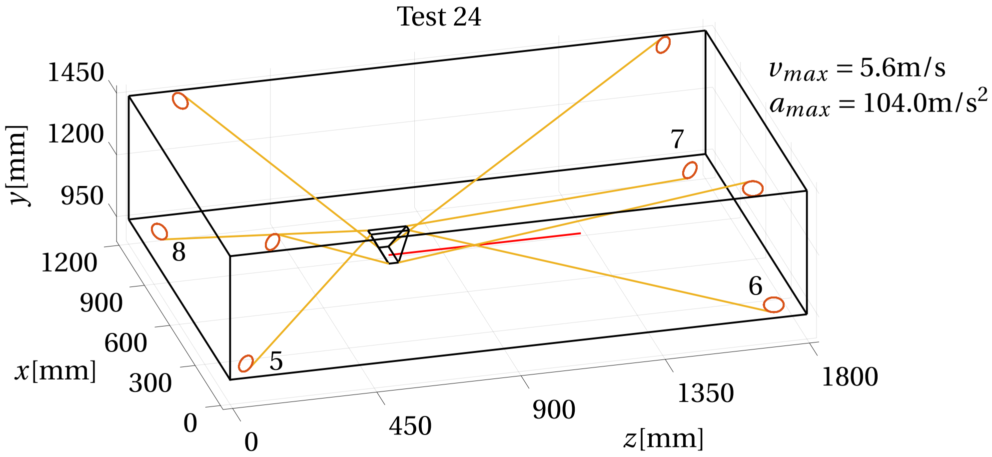

Figure 5.35: Trajectory executed during Test 24 (see Table 5.16).

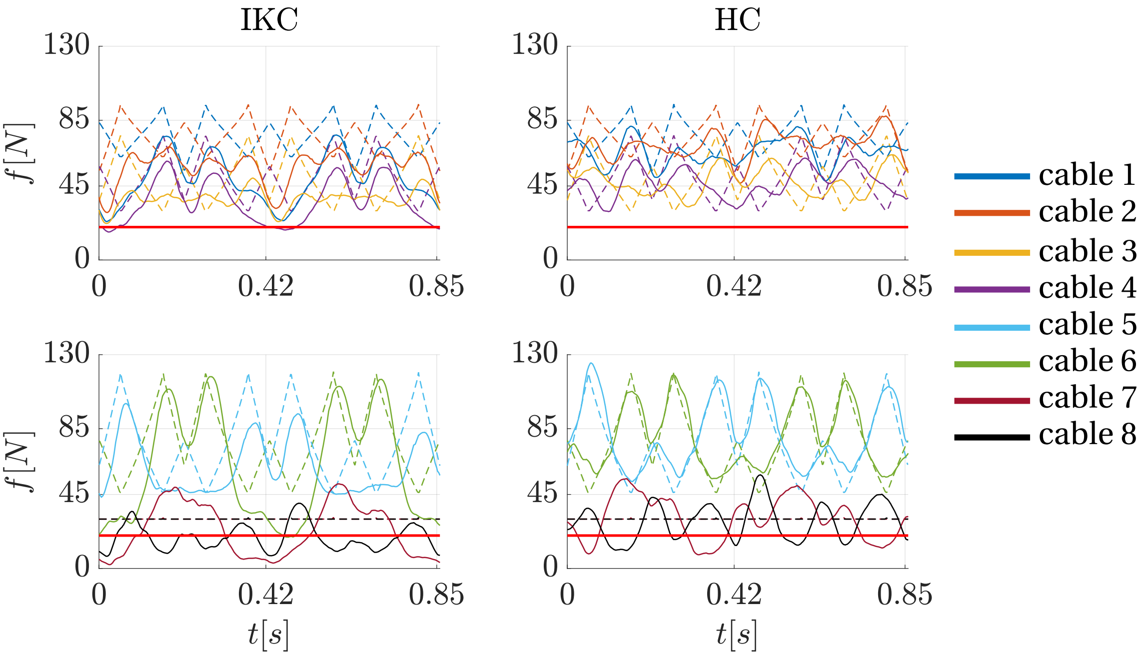

Figure 5.36: Desired (dashed lines) and measured (solid lines) cable forces during the execution of the trajectory in Figure 5.35 with IKC (left column) or HC-*e* (right column). f_{min} = 20 N and f_{max} = 350 N are the desired bounds of the cable tensions (red horizontal lines).

	id_1 [N]		id_2 [%]		id_3 [%]		id_4 [N]	
	IK	HC	IK	HC	IK	HC	IK	HC
cable 1	26	10.5	34.7	13.6	0	0	0	0
cable 2	18.9	7.6	24.6	10.1	0	0	0	0
cable 3	14.5	9.3	26.7	19.7	0	0	0	0
cable 4	14.7	9.5	29.7	19.8	14	0	1.1	0
cable 5	20.5	5.2	30.2	7.7	3.5	0	0.7	0
cable 6	15.8	6.3	19.5	9	0	0	0	0
cable 7	15.3	11.5	51	38.3	49.3	28.1	11.4	6.9
cable 8	12.4	9.5	41.2	31.8	61.4	29.1	6.6	4.4

Table 5.26: Values of indices in Eqs. (5.1)–(5.4) for the forces shown in Figure 5.36. The force-controlled cables are highlighted in bold.

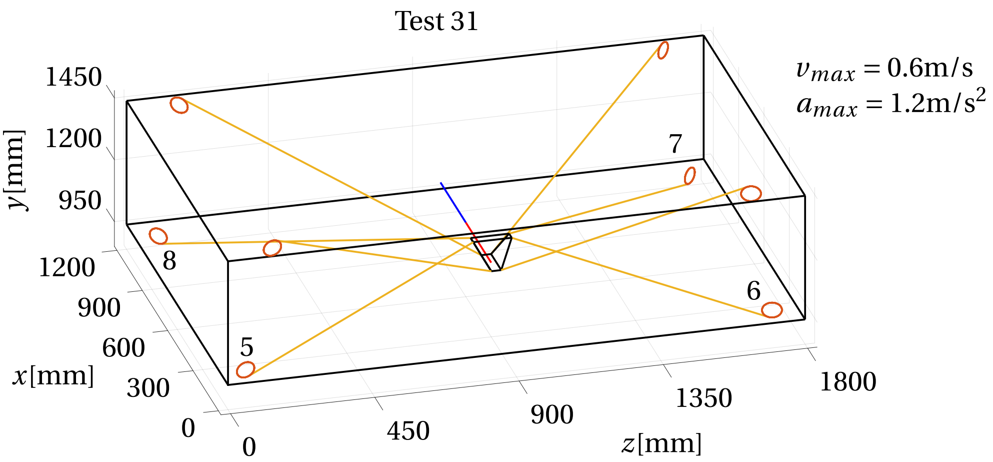

Figure 5.37: Trajectory executed during Test 31 (see Table 5.16).

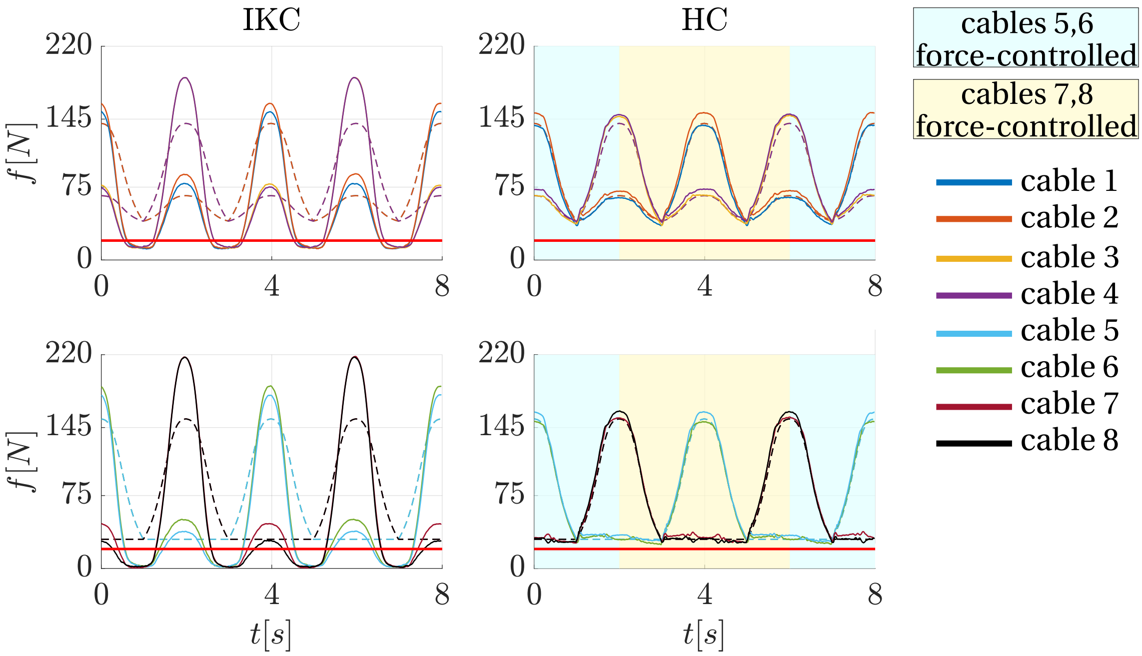

Figure 5.38: Desired (dashed lines) and measured (solid lines) cable forces during the execution of the trajectory in Figure 5.37 with IKC (left column) or HC-e (right column). $f_{min} = 20$ N and $f_{max} = 350$ N are the desired bounds of the cable tensions (red horizontal lines).

	id_1 [N]		id_2 [%]		id_3 [%]		id_4 [N]	
	IK	HC	IK	HC	IK	HC	IK	HC
cable 1	24.7	2.1	40.7	3.3	34.9	0	6.3	0
cable 2	25.8	5.4	41.8	6.9	34.3	0	5.8	0
cable 3	26.2	3.3	41	4.3	33.7	0	5.7	0
cable 4	26.1	5.4	40.7	7.2	33.8	0	5.3	0
cable 5	26.6	2.2	54.8	5.3	42.3	0	13.9	0
cable 6	25.3	3.8	50.8	7.3	46.7	0	13.8	0
cable 7	28.9	3.3	55.8	7.2	43.3	0	14.8	0
cable 8	28.7	3.5	54.7	5.6	50.6	0	13.9	0

Table 5.27: Values of indices in Eqs. (5.1)–(5.4) for the forces shown in Figure 5.38. The force-controlled cables are highlighted in bold.

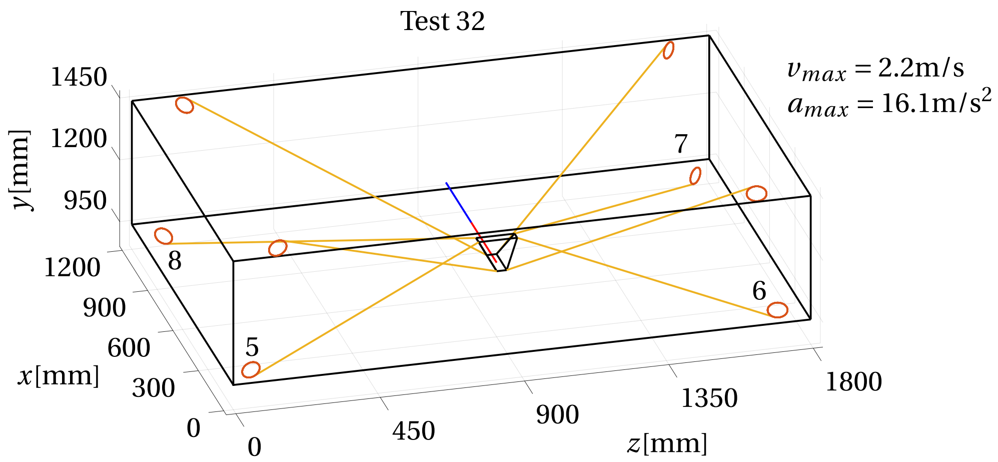

Figure 5.39: Trajectory executed during Test 32 (see Table 5.16).

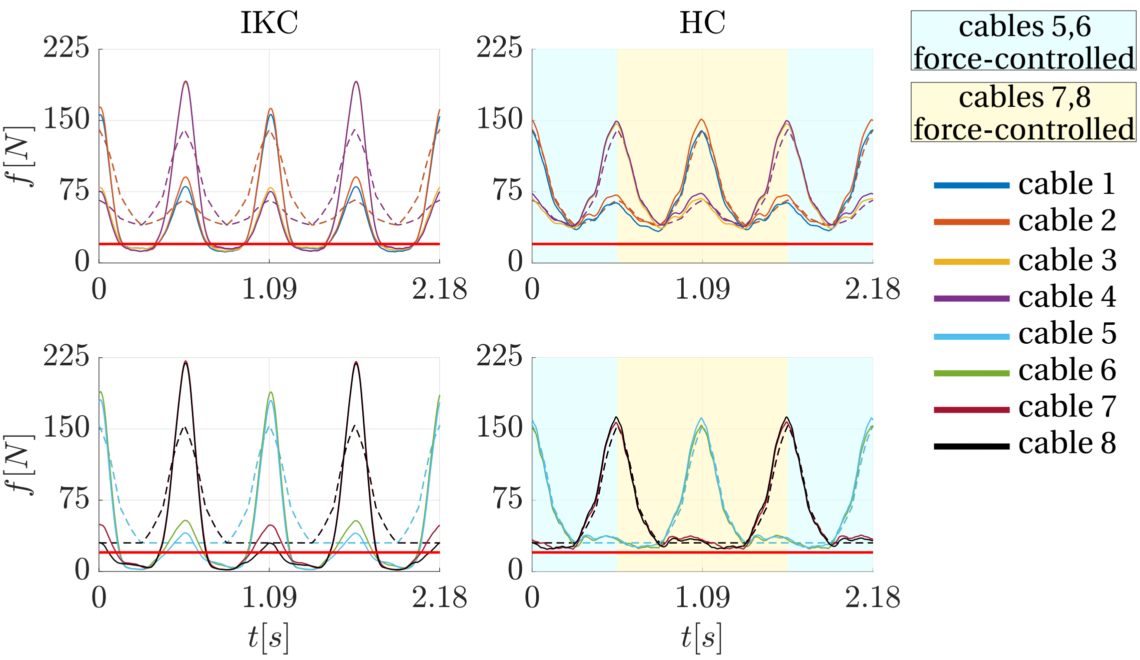

Figure 5.40: Desired (dashed lines) and measured (solid lines) cable forces during the execution of the trajectory in Figure 5.39 with IKC (left column) or HC-e (right column). f_{min} = 20 N and f_{max} = 350 N are the desired bounds of the cable tensions (red horizontal lines).

	id_1 [N]		id_2 [%]		id_3 [%]		id_4 [N]	
	IK	HC	IK	HC	IK	HC	IK	HC
cable 1	24.9	4.4	44.4	7.5	41.7	0	4.9	0
cable 2	25.5	5	44.9	7.2	40.8	0	4.6	0
cable 3	25	4.4	43.4	6.9	39.6	0	4.3	0
cable 4	25.3	4.7	44	7	40.2	0	4.4	0
cable 5	25.5	4.4	56.1	10.1	50.5	0	12.3	0
cable 6	25.2	4.8	54.5	9.9	56.7	0	12.2	0
cable 7	26.2	4.8	55.5	10.8	51	0	12.3	0
cable 8	26.8	5.4	57.3	10.6	61.4	0	12.1	0

Table 5.28: Values of indices in Eqs. (5.1)–(5.4) for the forces shown in Figure 5.40. The force-controlled cables are highlighted in bold.

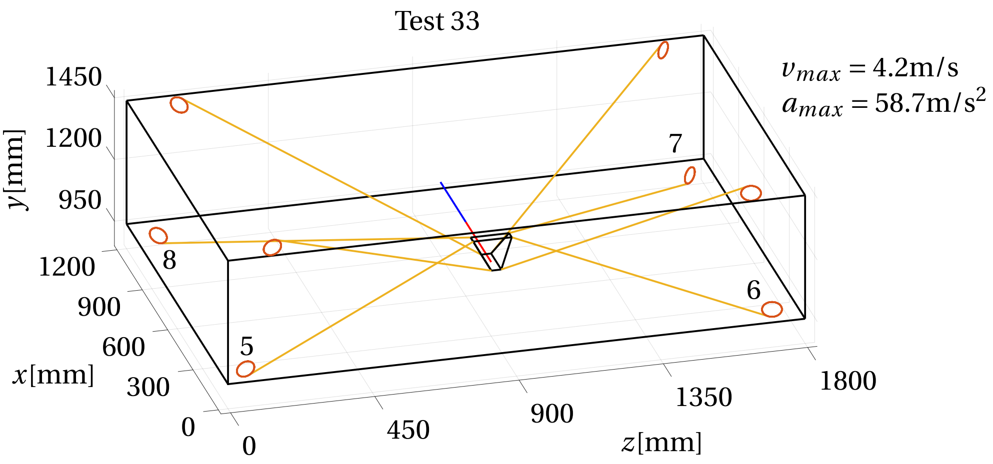

Figure 5.41: Trajectory executed during Test 33 (see Table 5.16).

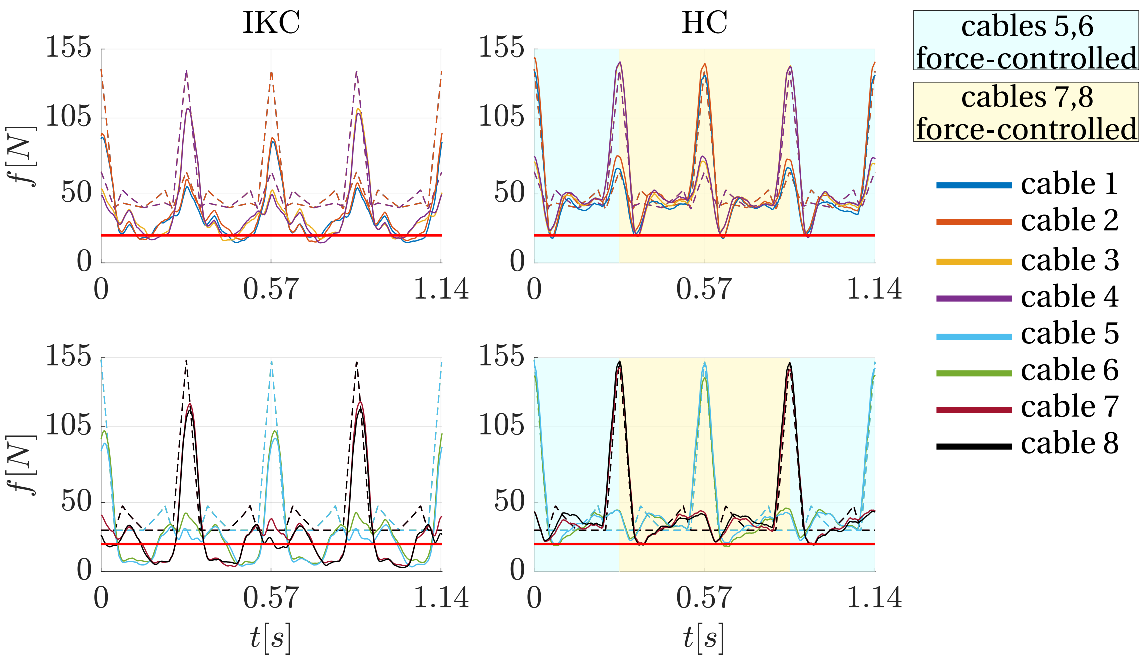

Figure 5.42: Desired (dashed lines) and measured (solid lines) cable forces during the execution of the trajectory in Figure 5.41 with IKC (left column) or HC-e (right column). f_{min} = 20 N and f_{max} = 350 N are the desired bounds of the cable tensions (red horizontal lines).

	id_1 [N]		id_2 [%]		id_3 [%]		id_4 [N]	
	IK	HC	IK	HC	IK	HC	IK	HC
cable 1	20	7	39.1	14.3	23	2.6	2.6	1.4
cable 2	18.1	8.4	35.5	16.3	19.2	1.2	2.5	1
cable 3	17.2	7.8	35	15.1	14.5	1.7	2	0.7
cable 4	17.7	8.3	36	16	16.1	1.7	2.2	0.7
cable 5	17.5	6.4	44	17.9	42.9	4.5	10.4	1.1
cable 6	18.8	6.6	46.7	17.2	44.2	0	11.6	0
cable 7	17.4	6.4	45.1	16.9	42.8	0.3	11	0.1
cable 8	18.3	7.5	48	19.3	51.5	3.5	9.8	0.4

Table 5.29: Values of indices in Eqs. (5.1)–(5.4) for the forces shown in Figure 5.42. The force-controlled cables are highlighted in bold.

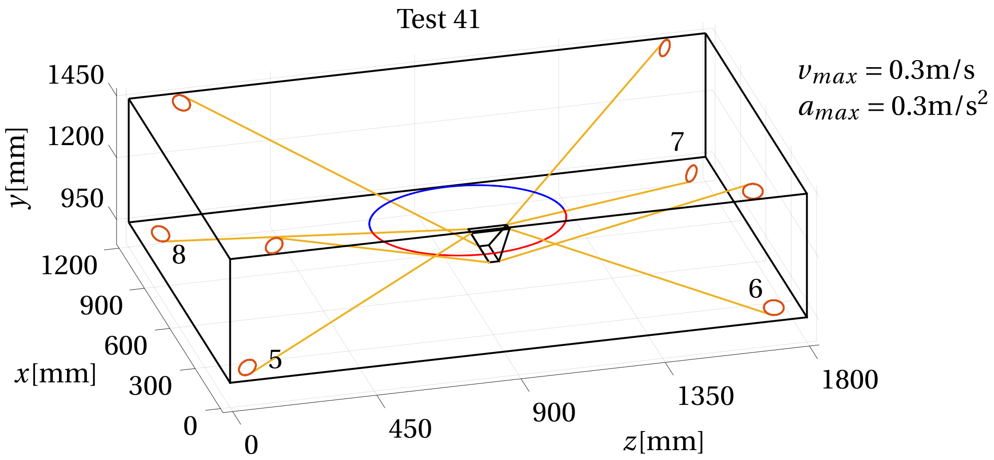

Figure 5.43: Trajectory executed during Test 41 (see Table 5.16).

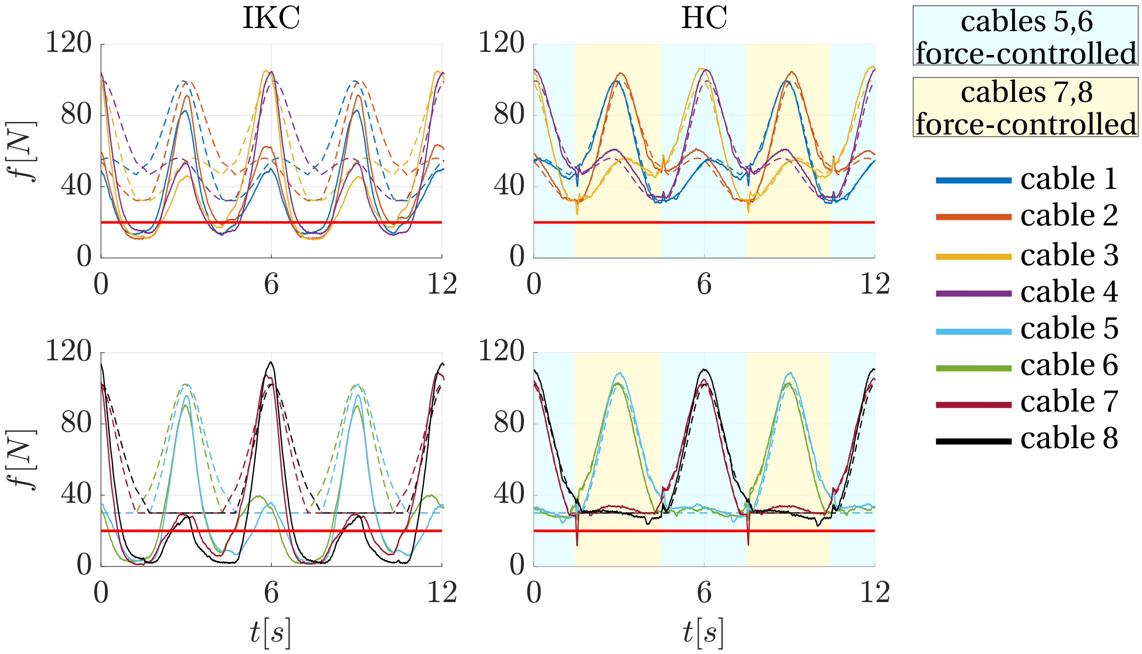

Figure 5.44: Desired (dashed lines) and measured (solid lines) cable forces during the execution of the trajectory in Figure 5.43 with IKC (left column) or HC-*e* (right column). f_{min} = 20 N and f_{max} = 350 N are the desired bounds of the cable tensions (red horizontal lines).

	id_1 [N]		id_2 [%]		id_3 [%]		id_4 [N]	
	IK	HC	IK	HC	IK	HC	IK	HC
cable 1	23	1.4	42	2.8	34.9	0	4.3	0
cable 2	20.8	2.5	40.1	4.3	26.6	0	6.2	0
cable 3	19.3	2.3	39.6	3.6	30.8	0	5.3	0
cable 4	20.6	3.1	40.1	5.7	37.9	0	4.6	0
cable 5	21.3	1.4	48.8	4	44.9	0	11.4	0
cable 6	22.3	3.1	52.1	7.1	53.7	0	11.3	0
cable 7	18.7	1.8	46.7	4.7	50.6	0.9	11.2	4.4
cable 8	22.8	3.1	57.2	6.1	59.6	0	13.2	0

Table 5.30: Values of indices in Eqs. (5.1)–(5.4) for the forces shown in Figure 5.44. The force-controlled cables are highlighted in bold.

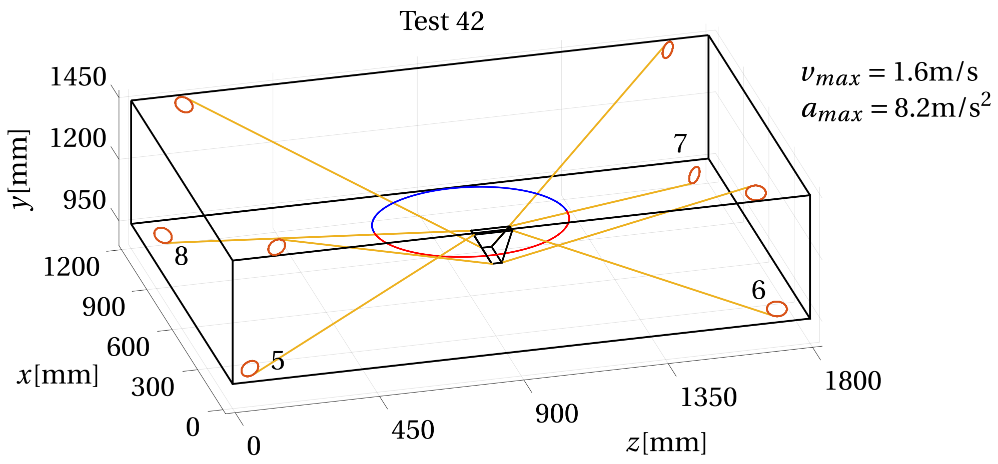

Figure 5.45: Trajectory executed during Test 42 (see Table 5.16).

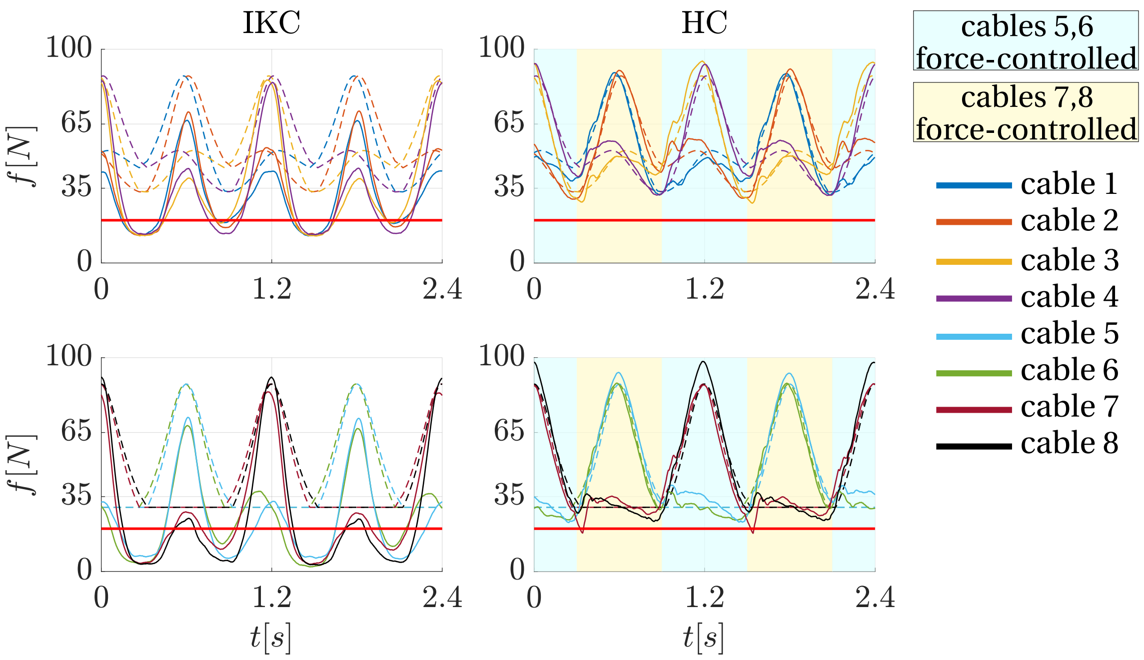

Figure 5.46: Desired (dashed lines) and measured (solid lines) cable forces during the execution of the trajectory in Figure 5.45 with IKC (left column) or HC-*e* (right column). f_{min} = 20 N and f_{max} = 350 N are the desired bounds of the cable tensions (red horizontal lines).

	id_1 [N]		id_2 [%]		id_3 [%]		id_4 [N]	
	IK	HC	IK	HC	IK	HC	IK	HC
cable 1	22.3	2.8	42.3	5.8	29.9	0	3.9	0
cable 2	20.8	3.1	41	6.4	34.1	0	4.3	0
cable 3	18.8	3.7	40	6.9	29.7	0	4.4	0
cable 4	20.3	3.4	41.9	6.4	38.3	0	4.7	0
cable 5	20.8	2.9	48.1	7.9	45.6	0	10.5	0
cable 6	21.1	4.3	50.2	11.8	54	0	9.8	0
cable 7	17.3	3.2	45.2	8.6	53	1.9	9.2	1.3
cable 8	20.3	4.7	54.5	10.9	60.4	0	11.6	0

Table 5.31: Values of indices in Eqs. (5.1)–(5.4) for the forces shown in Figure 5.46. The force-controlled cables are highlighted in bold.

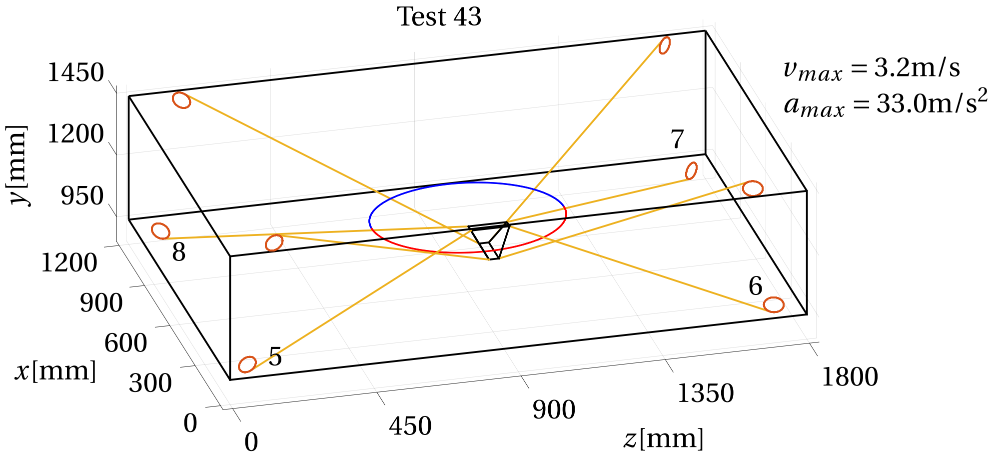

Figure 5.47: Trajectory executed during Test 43 (see Table 5.16).

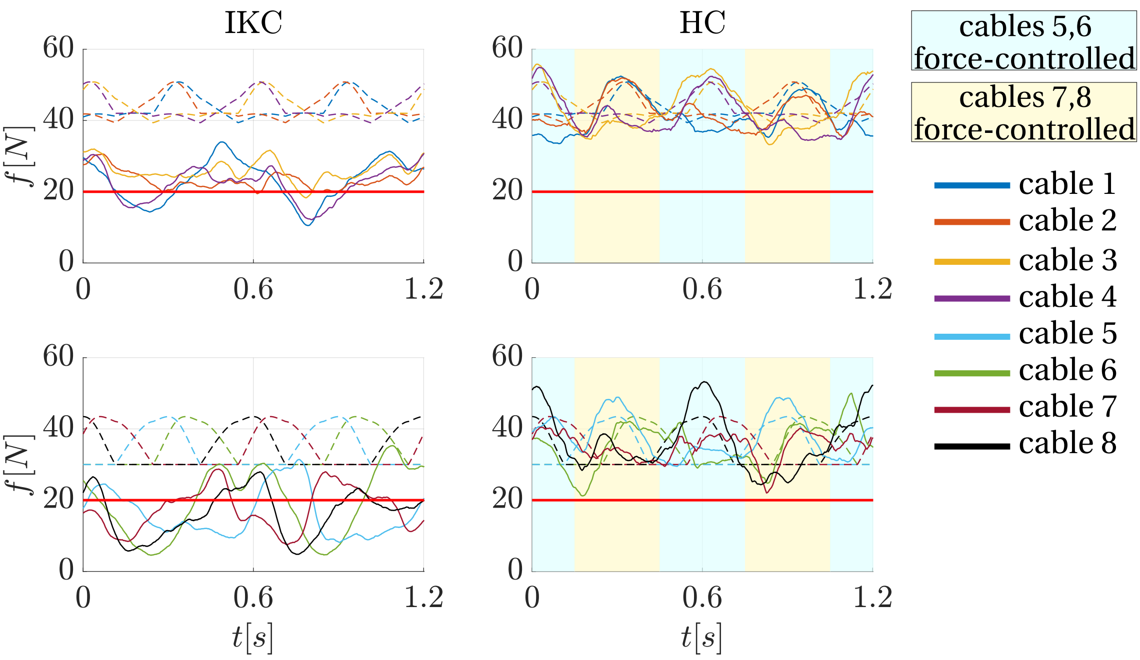

Figure 5.48: Desired (dashed lines) and measured (solid lines) cable forces during the execution of the trajectory in Figure 5.47 with IKC (left column) or HC-*e* (right column). f_{min} = 20 N and f_{max} = 350 N are the desired bounds of the cable tensions (red horizontal lines).

	id_1 [N]		id_2 [%]		id_3 [%]		id_4 [N]	
	IK	HC	IK	HC	IK	HC	IK	HC
cable 1	20.5	3.3	46.6	7.8	33.7	0	3.9	0
cable 2	20.3	2.7	46.2	6.2	4	0	0.1	0
cable 3	17.6	3.7	40.4	8.6	3.8	0	1	0
cable 4	21.4	3.3	49.1	7.6	31.9	0	3.7	0
cable 5	15.3	3.6	43.8	11.1	50.3	0	9.4	0
cable 6	18.2	4.2	51.3	12.8	73.1	0	7.4	0
cable 7	16.8	4.3	46.1	13.1	60.5	0	6.5	0
cable 8	18.1	4	53.7	11.4	68.9	0	7.2	0

Table 5.32: Values of indices in Eqs. (5.1)–(5.4) for the forces shown in Figure 5.48. The force-controlled cables are highlighted in bold.

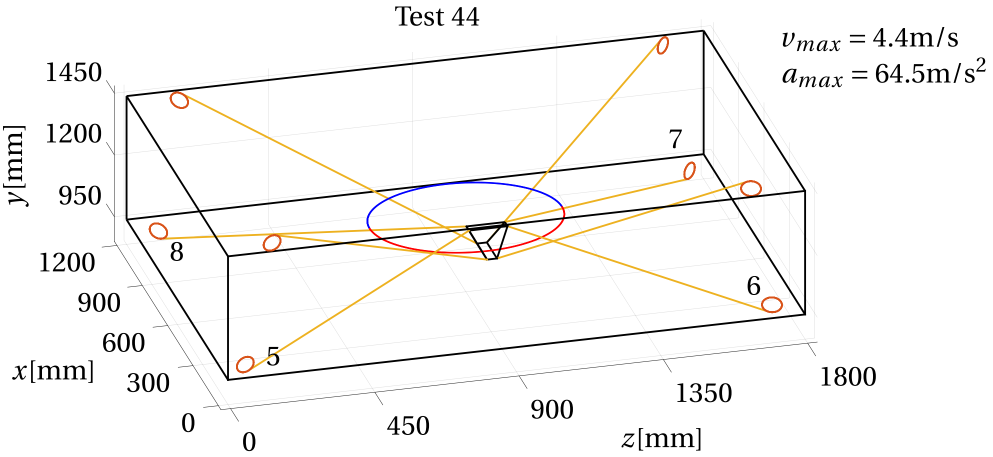

Figure 5.49: Trajectory executed during Test 44 (see Table 5.16).

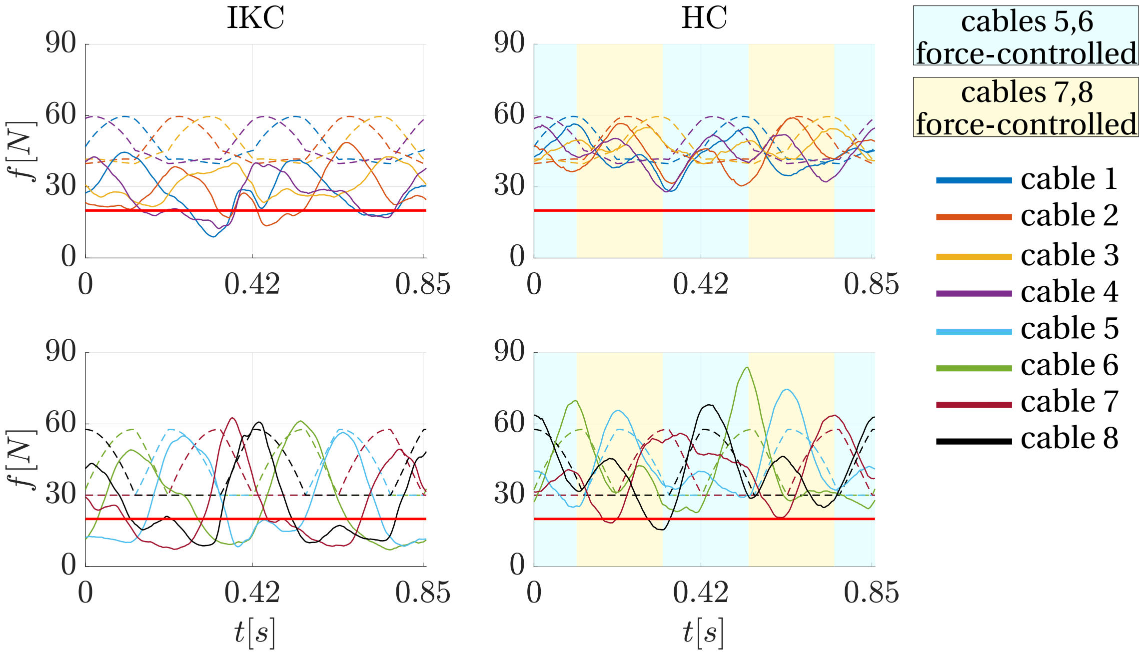

Figure 5.50: Desired (dashed lines) and measured (solid lines) cable forces during the execution of the trajectory in Figure 5.49 with IKC (left column) or HC-*e* (right column). f_{min} = 20 N and f_{max} = 350 N are the desired bounds of the cable tensions (red horizontal lines).

	id_1 [N]		id_2 [%]		id_3 [%]		id_4 [N]	
	IK	HC	IK	HC	IK	HC	IK	HC
cable 1	19.9	5	43.1	10.4	24.2	0	4.3	0
cable 2	20	5.8	43.1	12.6	17.7	0	3	0
cable 3	16.7	4.9	35.2	10.2	0	0	0	0
cable 4	21.2	7.2	45.6	15.4	33	0	3	0
cable 5	11.9	5.8	35.4	14.3	44.7	0	8.4	0
cable 6	12.2	6.4	37.1	16.8	54.2	0	6.9	0
cable 7	16	7.4	42.5	22.1	49.5	4	7.7	1.2
cable 8	13.6	7.1	39.6	20.4	54.2	6.5	6.2	3.1

Table 5.33: Values of indices in Eqs. (5.1)–(5.4) for the forces shown in Figure 5.50. The force-controlled cables are highlighted in bold.

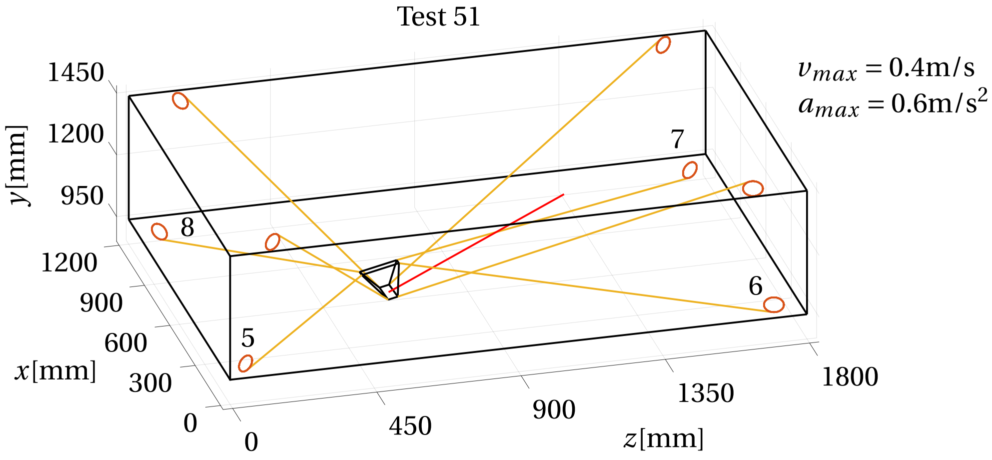

Figure 5.51: Trajectory executed during Test 51 (see Table 5.16).

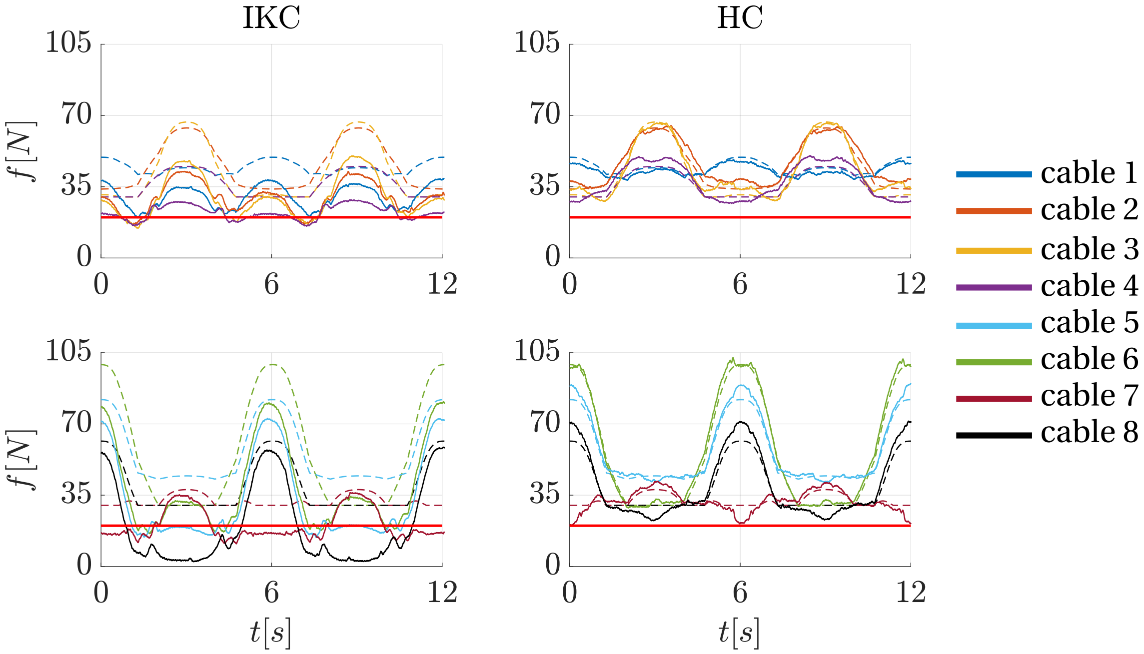

Figure 5.52: Desired (dashed lines) and measured (solid lines) cable forces during the execution of the trajectory in Figure 5.51 with IKC (left column) or HC-*e* (right column). f_{min} = 20 N and f_{max} = 350 N are the desired bounds of the cable tensions (red horizontal lines).

	id_1 [N]		id_2 [%]		id_3 [%]		id_4 [N]	
	IK	HC	IK	HC	IK	HC	IK	HC
cable 1	14.3	1.6	32.7	3.5	0.4	0	0.2	0
cable 2	15.8	2.3	33.6	5.7	12.6	0	1.7	0
cable 3	12.5	2.2	28.9	6.6	16.5	0	2.1	0
cable 4	13.7	2.9	37.5	7.9	28.5	0	1.8	0
cable 5	17.8	1.8	30.5	3.5	15.5	0	1.5	0
cable 6	23.2	2	46.4	3.4	47.3	0	2.2	0
cable 7	11.7	2.4	37.7	7.5	67.5	0	4.3	0
cable 8	19.4	3.4	58.6	8.4	67.2	0	12.8	0

Table 5.34: Values of indices in Eqs. (5.1)–(5.4) for the forces shown in Figure 5.52. The force-controlled cables are highlighted in bold.

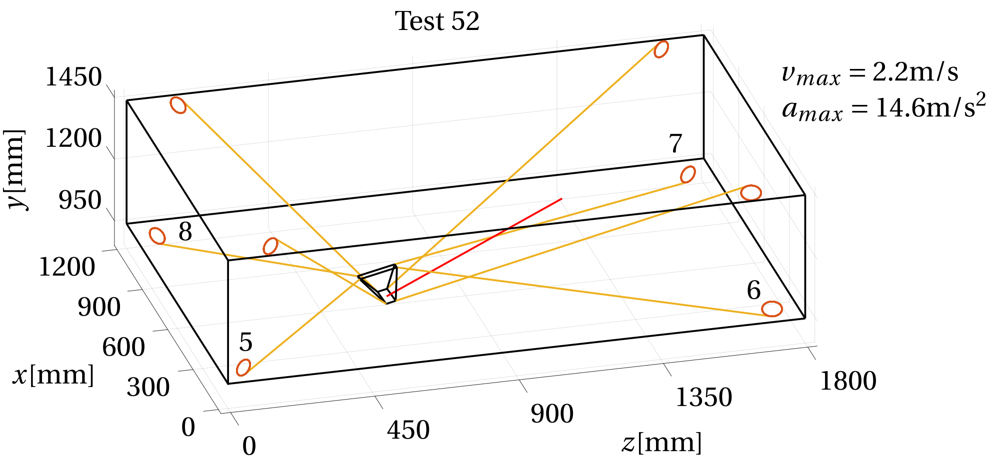

Figure 5.53: Trajectory executed during Test 52 (see Table 5.16).

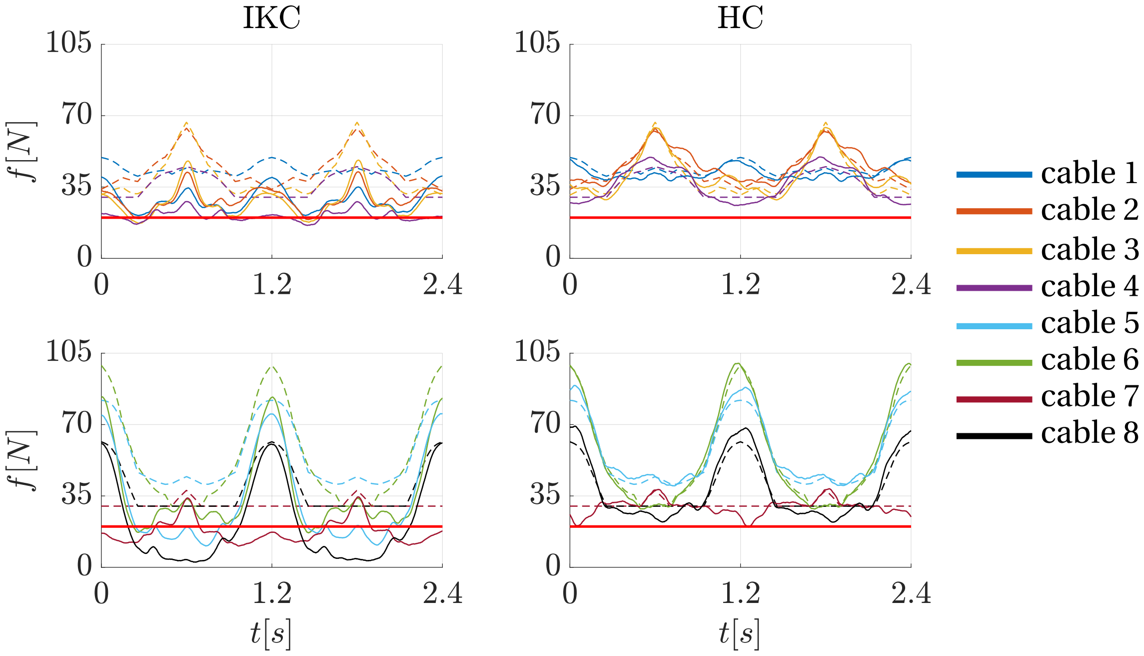

Figure 5.54: Desired (dashed lines) and measured (solid lines) cable forces during the execution of the trajectory in Figure 5.53 with IKC (left column) or HC-*e* (right column). $f_{min} = 20$ N and $f_{max} = 350$ N are the desired bounds of the cable tensions (red horizontal lines).

	id_1 [N]		id_2 [%]		id_3 [%]		id_4 [N]	
	IK	HC	IK	HC	IK	HC	IK	HC
cable 1	15.1	2.2	35.1	5	0	0	0	0
cable 2	15.5	2.6	33.1	6.3	5.5	0	0.4	0
cable 3	13.1	2.8	31.1	7.6	12.3	0	1.5	0
cable 4	14.6	2.6	40.3	7.2	39.9	0	1.3	0
cable 5	17.6	1.9	31.9	3.6	10.3	0	1.4	0
cable 6	22.8	2.7	47	4.8	45.8	0	4.2	0
cable 7	13.3	2.1	43.8	6.9	73.7	0.6	5.5	0.1
cable 8	17.7	3.6	54.8	9.4	65.3	0	12	0

Table 5.35: Values of indices in Eqs. (5.1)–(5.4) for the forces shown in Figure 5.54. The force-controlled cables are highlighted in bold.

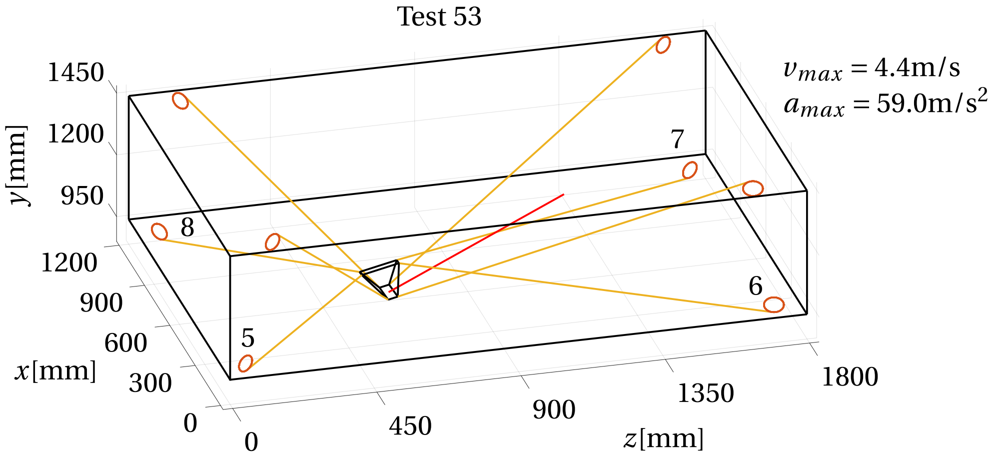

Figure 5.55: Trajectory executed during Test 53 (see Table 5.16).

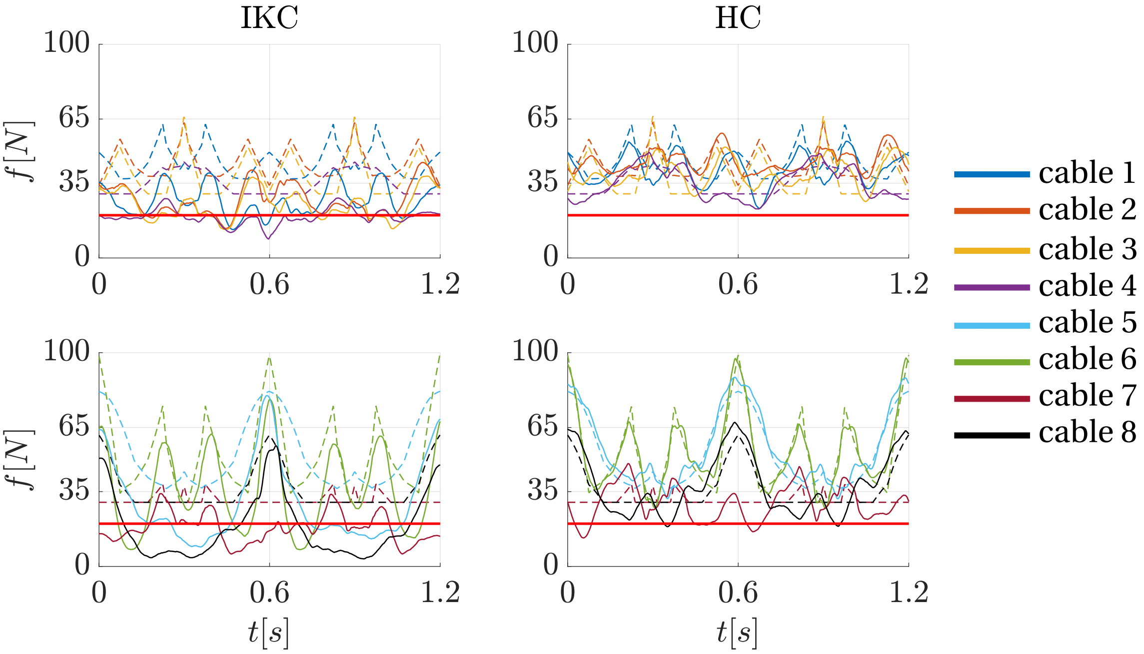

Figure 5.56: Desired (dashed lines) and measured (solid lines) cable forces during the execution of the trajectory in Figure 5.55 with IKC (left column) or HC-e (right column). f_{min} = 20 N and f_{max} = 350 N are the desired bounds of the cable tensions (red horizontal lines).

	id_1 [N]		id_2 [%]		id_3 [%]		id_4 [N]	
	IK	HC	IK	HC	IK	HC	IK	HC
cable 1	18.1	4.6	40.8	10.5	13.6	0	2.8	0
cable 2	17.2	4.7	38.6	10.8	12.6	0	2.3	0
cable 3	14.5	6.8	36.5	18	31.4	0	2.4	0
cable 4	15.8	2.7	44.5	7.7	65.1	0	2.7	0
cable 5	17.9	3.2	36	6.5	28	0	6.6	0
cable 6	23.5	3.7	48.4	7.5	44.8	0	4.7	0
cable 7	13.1	6.3	42.7	20.4	66.4	13.6	5.8	2.4
cable 8	17.9	5.9	54.9	16.9	67.1	3.5	10.5	0.8

Table 5.36: Values of indices in Eqs. (5.1)–(5.4) for the forces shown in Figure 5.56. The force-controlled cables are highlighted in bold.

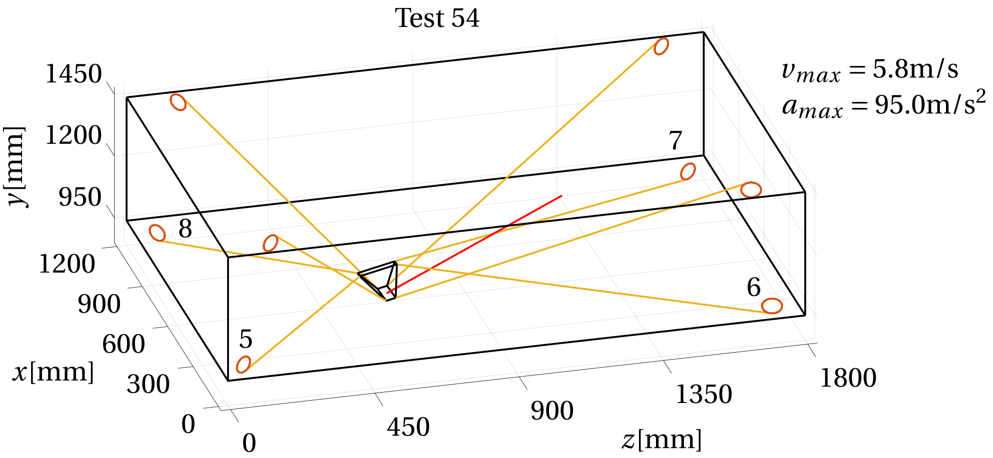

Figure 5.57: Trajectory executed during Test 54 (see Table 5.16).

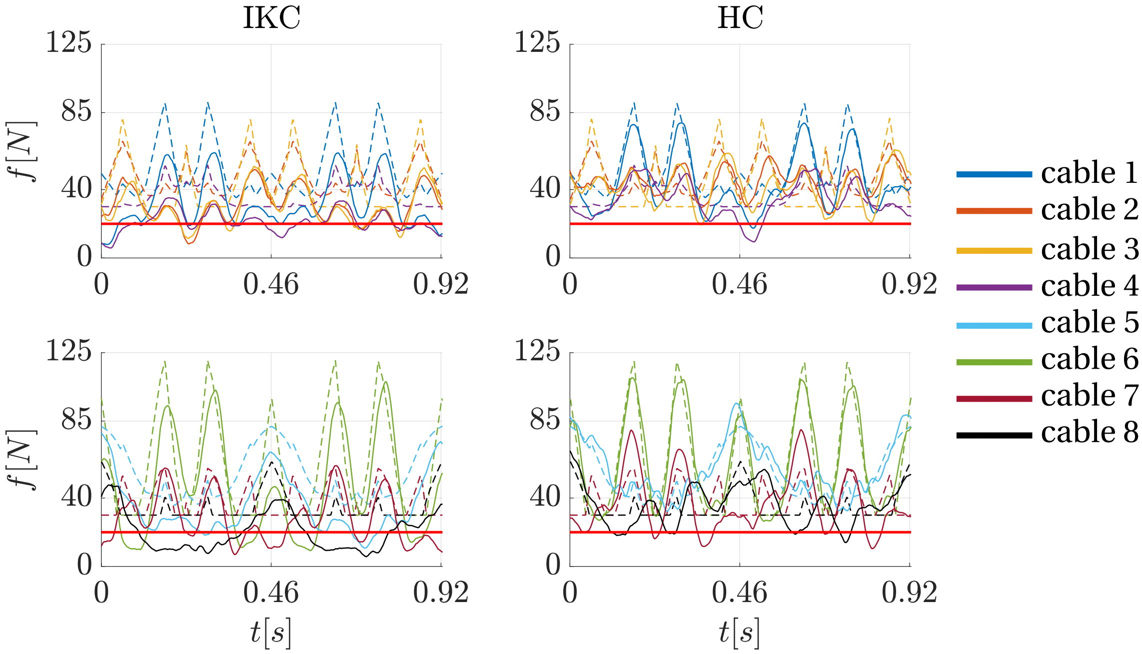

Figure 5.58: Desired (dashed lines) and measured (solid lines) cable forces during the execution of the trajectory in Figure 5.57 with IKC (left column) or HC-e (right column). $f_{min} = 20$ N and $f_{max} = 350$ N are the desired bounds of the cable tensions (red horizontal lines).

	id_1 [N]		id_2 [%]		id_3 [%]		id_4 [N]	
	IK	HC	IK	HC	IK	HC	IK	HC
cable 1	18.9	8.2	38.2	17.4	14	2.2	4.8	1.7
cable 2	16.5	9.8	34.9	20.7	13.6	0	4.6	0
cable 3	13.8	15	28.7	35.9	16.6	0.9	3.9	0.4
cable 4	15.1	5.7	41.7	15.9	44.3	7.1	3.9	6.4
cable 5	19	6.6	36.1	13.1	28.3	0	6.3	0
cable 6	19.1	6	37.7	11.9	11	0	3.9	0
cable 7	12.2	10.4	33.9	26.5	36.5	13.6	6	4.4
cable 8	15.2	8.6	44.8	25.9	54.6	12.3	8.5	1.6

Table 5.37: Values of indices in Eqs. (5.1)–(5.4) for the forces shown in Figure 5.58. The force-controlled cables are highlighted in bold.

5.3.2 Evaluation of robot precision and repeatability

The tests executed on the CORHDA to evaluate the precision and repeatability of the manipulator when the HC-*e* controller is exploited differ from those performed on the IPAnema 3 Mini. This is due to the lack of a laser tracker like the one at the Fraunhofer Institute for Manufacturing Engineering and Automation (IPA) in Stuttgart. For this reason, a different strategy to conduct the experiments was adopted.

First, an aluminum plate with many holes was designed with very strict tolerances. It was mounted in the robot workspace at a vertical position slightly under the points in which the precision of the manipulator must be measured. The tolerated holes in the plate were designed so that the measurement group shown in Figure 5.59 can be mounted in each one. The measurement group comprises a piston sliding in a body with a cylindrical bore. On the upper surface of the piston, two graduated axes are engraved. Their center is point Q in Figure 5.59(a). The reference point in the CORHDA EE is P in Figure 5.60, located below the EE bottom plane, with an offset similar to the

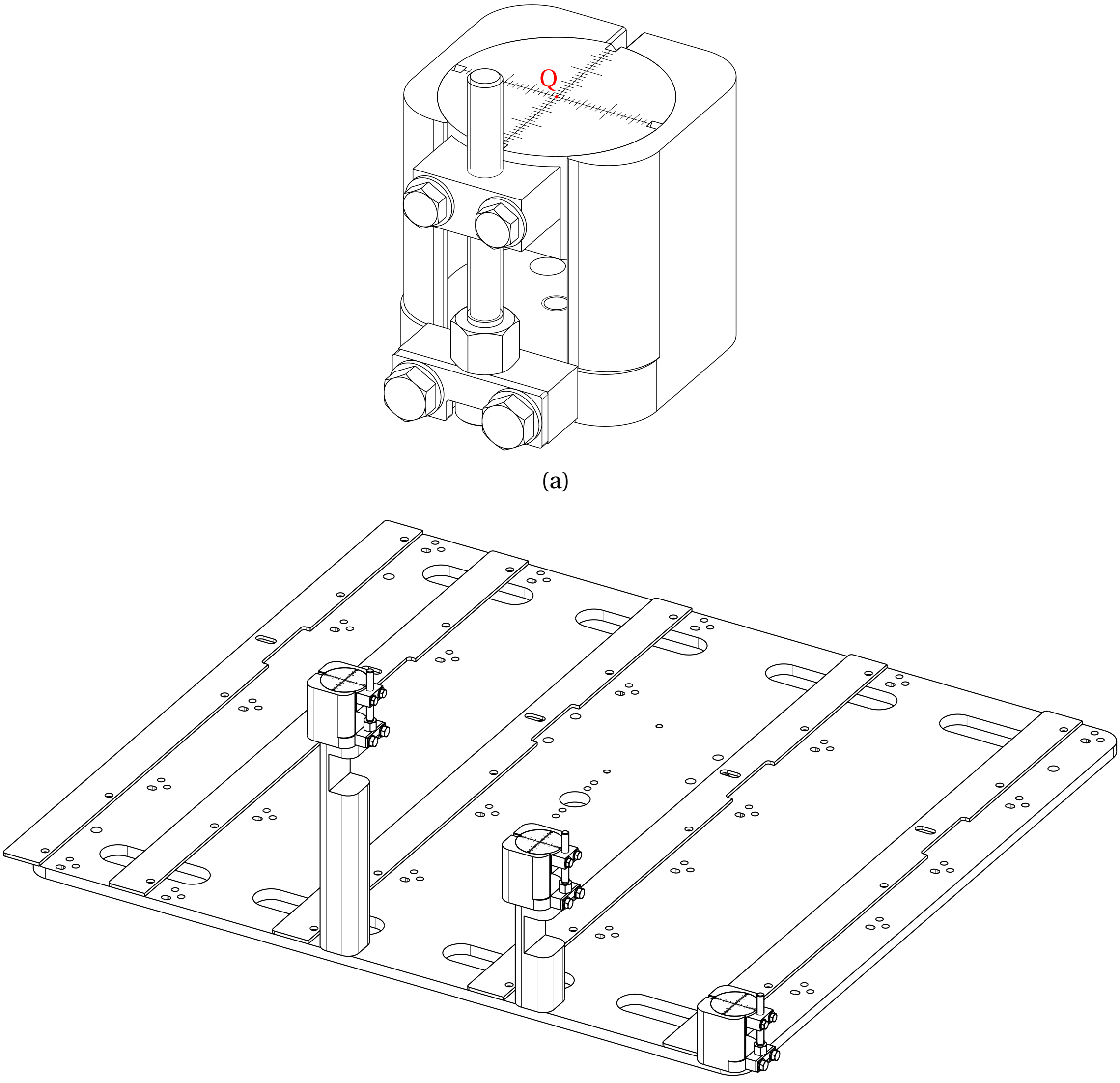

(a)

(b)

Figure 5.59: Measurement group (a), and examples of its mounting positions on the aluminum plate (b). Q is the point used to define the target pose.

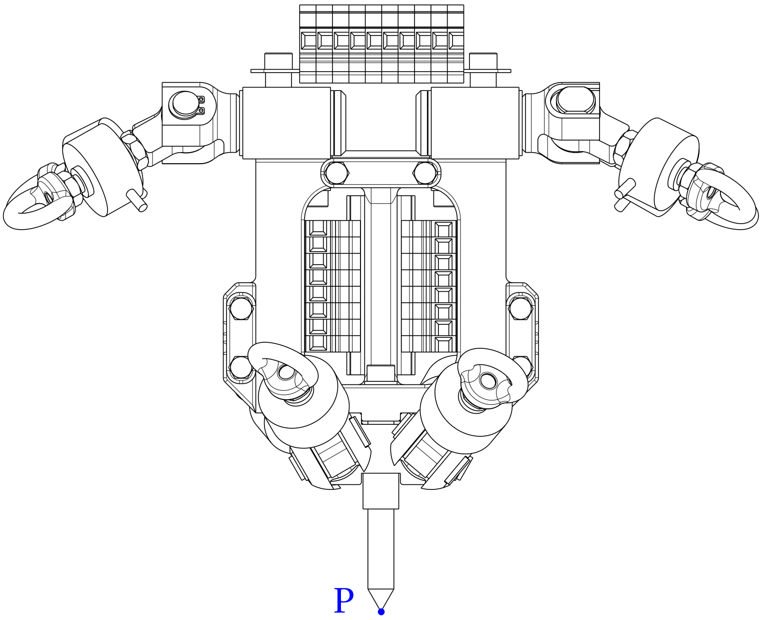

Figure 5.60: EE-2 in the configuration used for the positioning accuracy tests. P is the reference point for which positioning errors are measured.

one that will be necessary to perform the pick-an-place task in the future (see Section 4.1). EE-2 is used during these tests. At the beginning of the test, the piston upper surface is below the upper surface of its sleeve. Then, the EE is moved by commanding P to coincide with point Q with an orientation $\mathbf{R} = \mathbf{I}_3$. Then, the piston of the measurement group is moved until its upper surface comes into contact with P, as shown in Figures 5.61 and 5.62. The vertical error Δy (in the direction of gravity, i.e., y) is measured with a caliber as the distance between the piston upper surface and the sleeve upper surface. The errors in the plane xz (Δx and Δz) are the Cartesian distances between points P and Q (see Figure 5.62). An error of ±0.1mm affects the measurements in the y direction (precision of the caliber), while for the measurements in the plane, an error of ±0.25mm is considered realistic.

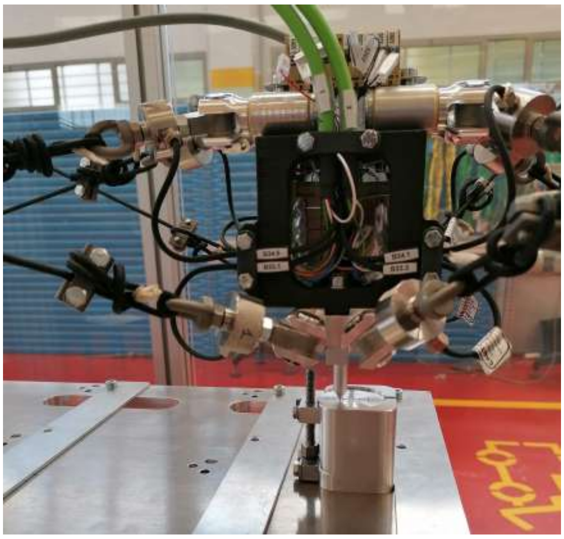

Figure 5.61: Example of a pose commanded to the EE for the measurements of the robot precision.

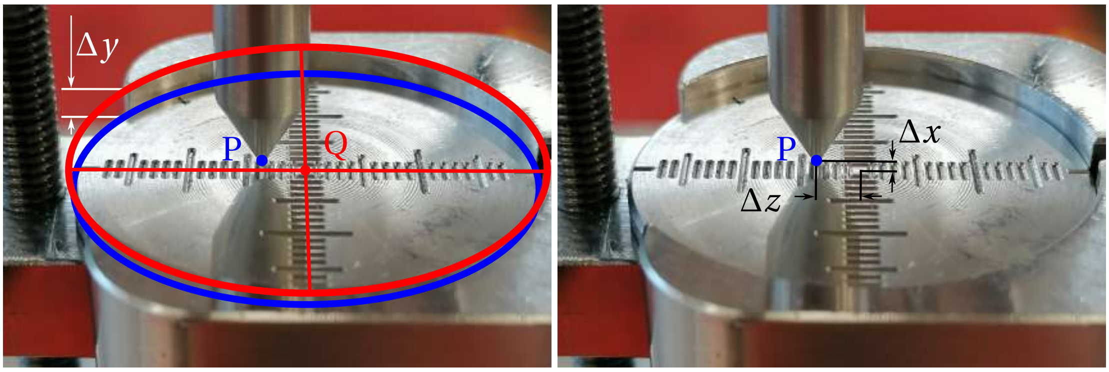

(a) Error along y axis (b) Error along x and z axes

Figure 5.62: Measurements executed for estimating the robot accuracy in every mounting position of the measurement group in the aluminum plate.

As in the tests performed on the IPAnema 3 Mini, only the positioning accuracy is measured since this is the most meaningful one for pick-and-place operations.

As shown in Figure 5.59, the measurement group can be mounted either directly on the aluminum plate or at a different height with the help of some calibrated columns. This way, three layers of reference points with the same positions in the xz plane and three different heights can be obtained. As shown in Figure 5.63, this set of 71 points is approximately spread in the task workspace shown in Figure 4.6.

The EE was brought to the target pose three consecutive times for every mounting position of the measurement group, i.e., for every point among those shown in Figure 5.63. Every time, the error ϵ in the position of point P compared to Q was measured. The repeatability is measured by computing the standard deviation ζ of the errors ϵ over the three consecutive measurements executed on each target pose. Results are shown in Table 5.38. The maximum errors along the Cartesian axes are always lower than 7mm, and the average ones are lower than 4mm. For the overall error in the po-

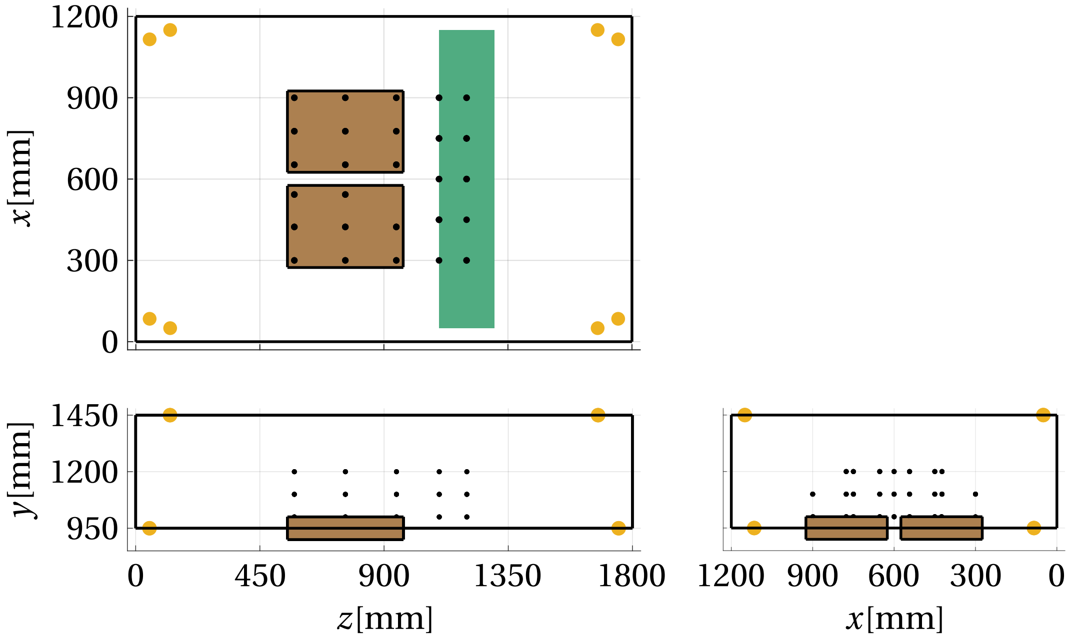

Figure 5.63: Chosen points for the evaluation of the CORHDA precision.

Table 5.38: The CORHDA accuracy with the HC-e controller is obtained by measuring the positioning errors (ϵ) of the robot in the points shown in Figure 5.63. Along all the axes, the maximum (subscript "max") and average (overline) errors are listed. The same is done for the standard deviation of the executed measurements (ζ), which is used to evaluate the robot repeatability.

Direction	x	y	z	xyz
ϵ_{max} **[mm]**	5.0	3.0	6.5	8.5
$\overline{\epsilon}$ **[mm]**	2.47	1.37	3.73	5.05
ζ_{max} **[mm]**	0.5	0.4	0.5	0.5
$\overline{\zeta}$ **[mm]**	0.26	0.12	0.25	0.36

sitioning of the robot EE, the maximum value is 8.5mm, while the average is equal to 5.05mm. These errors are higher than those obtained on the IPAnema 3 Mini. This is justified by the larger workspace of the CORHDA and by the fact that some points near its border were also considered. The same was not true on the IPAnema 3 Mini, for which the trajectories tested were all near the center of the workspace, where the cable tensions are lower and the errors due to the wire elongations are less important.

The values listed in Table 5.38 can be considered acceptable if the manipulated objects have dimensions in the order of hundreds of millimeters (e.g., 150–300mm). However, the products that the CORHDA should handle in the bin-picking cell are smaller, so a higher accuracy of the manipulator is required. To do so, it will be necessary to calibrate the robot geometrical parameters since, at the moment, the theoretical values of the robot geometry taken from its CAD model are used to solve its kinematics. These data do not consider imprecision during the manipulator construction and assembly. In general, a calibration of the geometrical parameters of a CDPR is necessary for its application in an industrial environment, and the CORHDA is no exception [154–160].

By analyzing how the positioning errors evolve in the workspace (see Figures 5.64 and 5.65), we can observe that the manipulator is more precise near the center of the workspace, as expected. This is true for the overall error (Figure 5.64), but also for the errors along the Cartesian axes (Figure 5.65). In particular, we notice that the errors along x, y, and z increase in a certain direction. For example, the error along the x

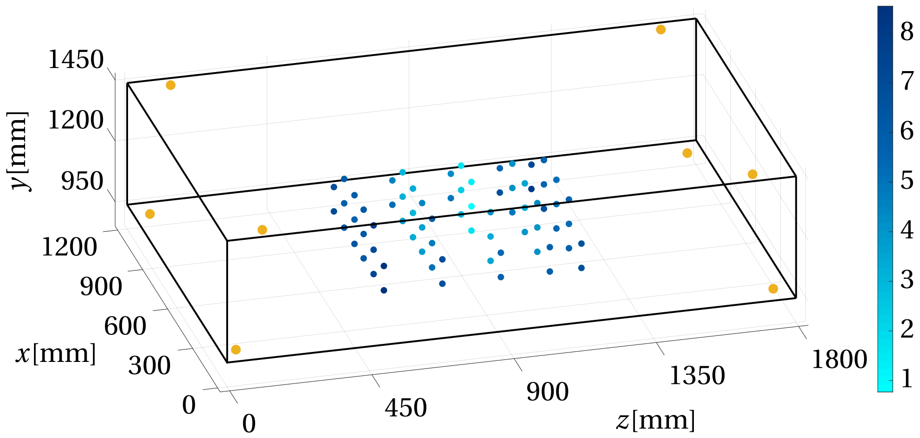

Figure 5.64: Overall error committed by the CORHDA on the set of points shown in Figure 5.63.

axis increases in the positive direction when the manipulator is moved to higher x coordinates and increases in the negative direction when the robot is moved to lower x coordinates. Similar considerations hold for the other axes. It is natural to think that this behavior is related to the already-mentioned imprecision in the geometry of the manipulator. For this reason, the idea that the robot accuracy will increase with the calibration of its geometrical parameters is justified.

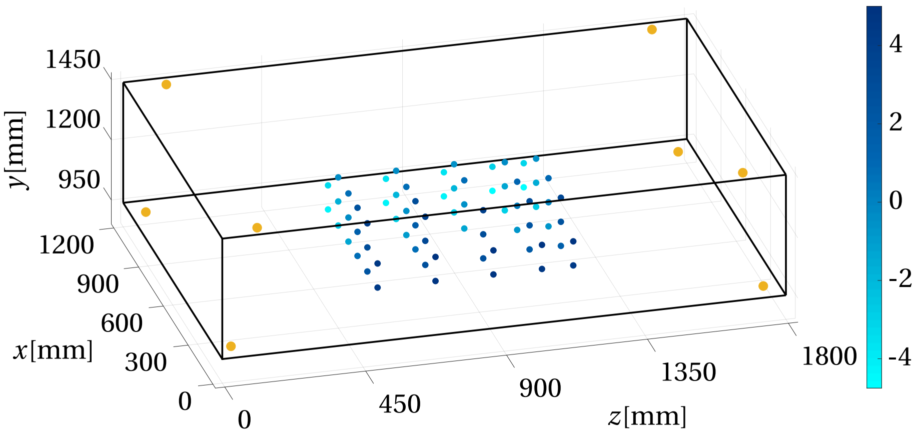

(a) Error along the x axis

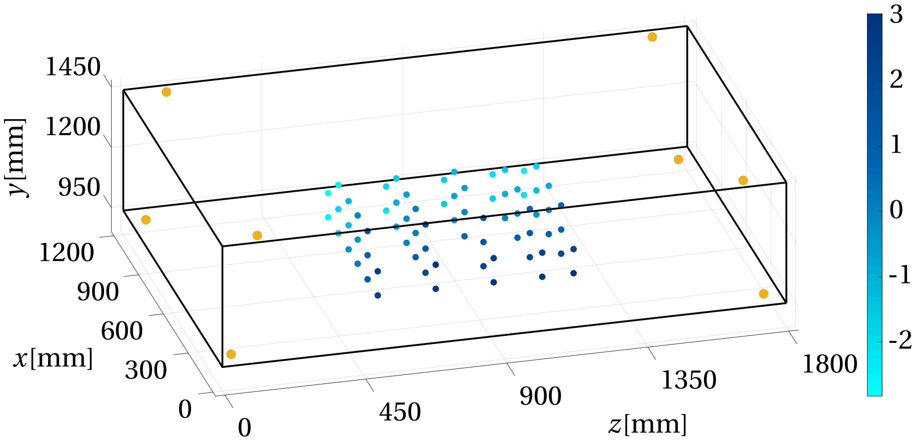

(b) Error along the y axis

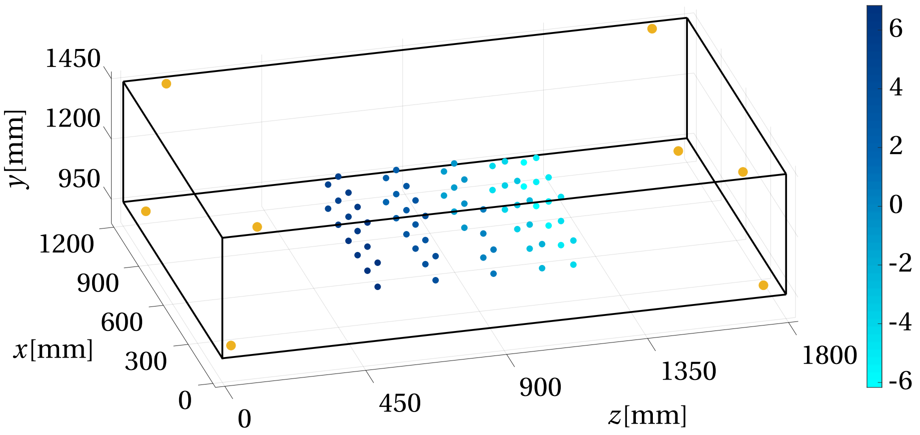

(c) Error along the z axis

Figure 5.65: Errors along the axes committed by the CORHDA on the set of points shown in Figure 5.63.

Table 5.38 also shows that the CORHDA repeatability is approximately one order of magnitude smaller than its precision, as for the IPAnema 3 Mini. However, we must observe that, during the successive measures executed for every point, the same errors were often recorded, which means that the measure differences were smaller than the precision of the measurement instruments. For this reason, values of repeatability at least equal to 0.25mm and 0.1mm were considered respectively for the measures in the plane xz and along the y axis. For pick-and-place operations, these values of repeatability are deemed to be acceptable

5.3.3 Evaluation of the robot dynamics capabilities

In Section 5.3.1, many movements involving different velocities and accelerations were tested using EE-2 mounted on the robot. The real cable forces acting on the wires were measured, but reaching the maximum velocities and accelerations for which the manipulator was originally developed was impossible. This is due to the higher mass of EE-2 compared to EE-1.

To test if the robot is actually capable of reaching the required maximum dynamics (see Section 4.1, a few tests were conducted with EE-1 mounted on the robot reaching linear velocities and accelerations up to 9m/s and 250m/s^2. In this case, it is not possible to record cable forces, so motor torques are analyzed, as done on the test bench with two cables (see Section 5.2, Figure 5.17).

To execute the experiments, a simple path similar to those used in Tests 11–24 (see Table 5.16) is considered (see Figure 5.66). The difference with the paths shown in Figures 5.19 and 5.29 is that the segment that defines the new path lies on the plane of symmetry of the volumes in Figure 3.14. In particular, the path is included in both volumes; this means that both the pair of cables 5,6 and 7,8 can be chosen to be force-controlled. It was decided to control in force wires 7 and 8.

Different trajectories with increasingly higher dynamics were tested on the aforementioned path. Velocities between 6.8m/s and 8.8m/s and accelerations between 153m/s^2 and 255m/s^2 were successfully tested

Figure 5.67 shows the desired and actual motor torques for the force-controlled cables. The tracking of the desired motor torque is similar to the one observed in the test bench with two cables (see Figure 5.17). As expected, for higher velocities and

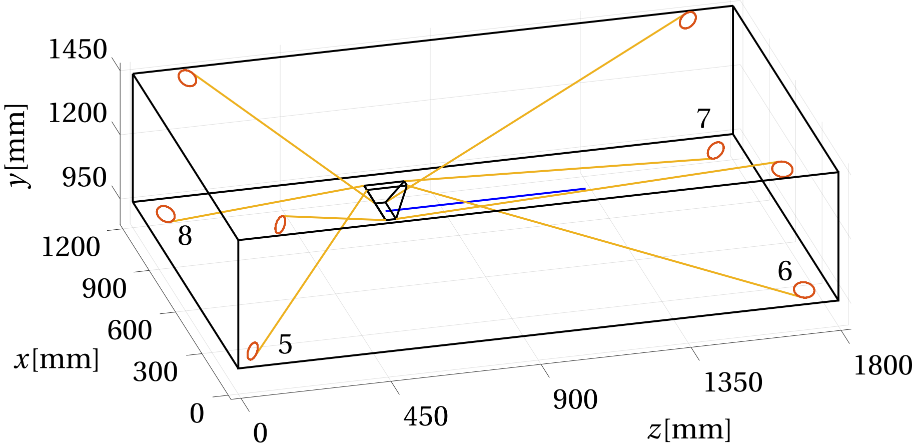

Figure 5.66: Path used to test with the CORHDA movements up to 8.8m/s and 255m/s^2. The torques obtained in these cases are shown in Figures 5.67 and 5.68.

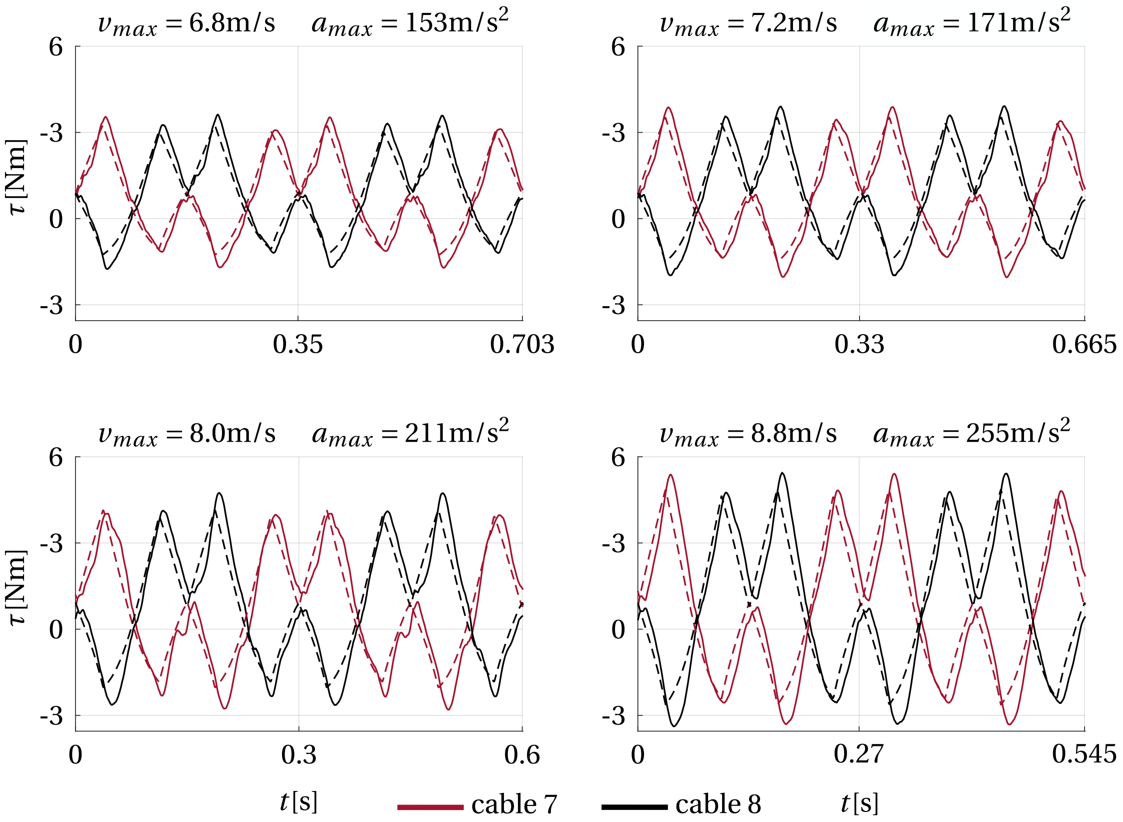

Figure 5.67: Desired (dashed lines) and real (solid lines) torques on the motors connected to the force-controlled cables when executing the path shown in Figure 5.66 with different dynamics up to 8.8m/s and 255m/s^2.

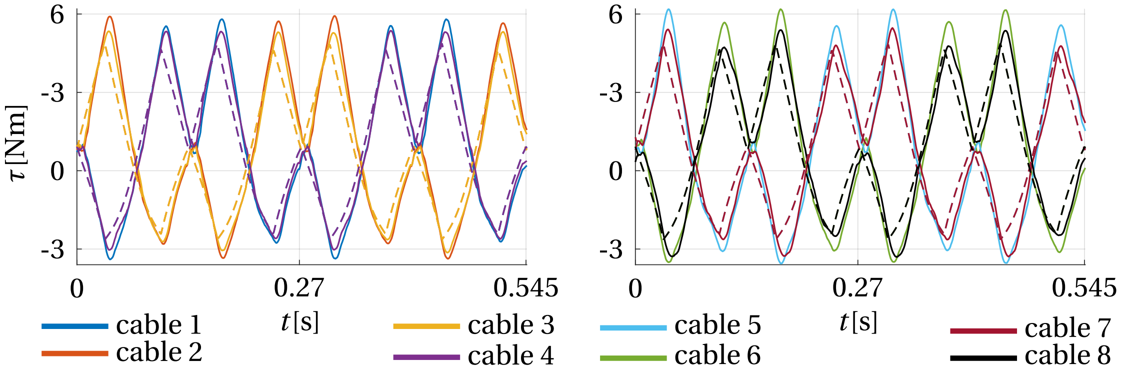

Figure 5.68: Actual torques of all the motors when the path shown in Figure 5.66 is traveled with the maximum dynamics possible ($v_{max} = 8.88$m/s and $a_{max} = 255$m/s^2).

accelerations, the torque tracking is less accurate, but the difference is rather small when passing from 6.8m/s and 153m/s^2 to 8.8m/s and 255m/s^2. Some peaks of the actual torques are higher, probably due to the necessity of using a more reactive high-level PID controller (see Figure 3.15(a)) for such rapid changes in cable forces. The desired and actual motor torques for the length-controlled cables are shown in Figure 5.68 for the fastest movement, which is the most complex case of study shown in this thesis. The results shown in Figure 5.68 are considered acceptable, and this means that the HC-*e* controller is assumed to be applicable even with EE accelerations up to 250m/s^2. The controller performance, particularly for very fast movements, can be further improved with fine-tuning of the high-level PID controller (see Section 3.4.2).

Chapter 6

Conclusions and outlooks

This thesis addressed the problem of designing a manipulator capable of executing a bin-picking task requiring high productivity (i.e., approximately 100 pieces/min) in collaboration with the company Marchesini Group S.p.a. After a preliminary analysis, a Cable-Driven Parallel Robot (CDPR) was proposed for this application. The main reason is the necessity of choosing a robot architecture with a low impact on the image acquisition by a vision system, together with the capability of the manipulator to operate with the required dynamics. The negligible dimensions of cables, if compared to rigid elements commonly used in standard industrial robots, and the parallel architecture of this class of manipulators satisfy both requirements.

6.1 Main results

First, the literature regarding CDPRs was analyzed to choose the most suitable architecture for the task at hand. Due to the velocities and accelerations required by the fast bin-picking task, an overconstrained CDPR with more cables than Degrees-Of-Freedom (DOFs) was chosen. Since the bin-picking operation requires a manipulator capable of controlling all DOFs of the End-Effector (EE), a robot with 8 actuated cables and 6 DOFs was chosen. The designed CDPR was called *CORHDA*: *Cable-driven Overconstrained Robot for Highly Dynamical Applications*.

A CDPR with swivel pulleys was chosen to minimize friction in the kinematic chain and wear of the wires. Since the architecture is overconstrained, for every EE pose, there are ∞^2 possible solutions to the inverse kinetostatic problem. Only those that guarantee that all tensions remain within given limits are acceptable. Among these, one optimal Force Distribution (FD) is computed based on the criterion of minimizing the 2-norm of the cable tension array. This choice was made to minimize the motor size.

Since no strict constraints existed on the manipulator workspace, an exemplary bin-picking task was defined for developing the CORHDA prototype. The latter dimensions were chosen based on guidelines given by Marchesini Group. The dynamics the manipulator must satisfy in terms of maximum velocity and acceleration were estimated based on the assigned task. This allowed the mechanical design of the robot winches, swivel pulleys, and EE.

Once the FD is computed for a given EE pose, it is necessary to control the manipulator to apply the correct cable tensions. Many research works are related to this topic in the literature, but all require force sensors. On the contrary, this thesis suggested to extend the Hybrid Control (HC) introduced in [125, 126] without using any force sensor (HC-e controller). The HC requires some cables to be controlled in force and the others to be controlled in length. The proposed solution was first implemented on the IPAnema 3 Mini robot at the Fraunhofer Institute for Manufacturing Engineering and Automation (IPA) in Stuttgart. The controller was then applied to the CORHDA prototype. In both cases a friction torque model of the robot kinematic chain was developed. An innovative approach to control the Following Error (FE) of the motors connected to the force-controlled cables was introduced instead of using the motor torque measurements. To do so, a model for correlating the motor torque to the FE when a pure proportional controller is used in the velocity loop at the drive level was introduced. Based on the aforementioned models, the full control schemes for the IPAnema 3 Mini and the CORHDA were developed, and an extensive experimental campaign was conducted on both robots.

The tests on the IPAnema 3 Mini involved slow motions and proved that the HC-*e* controller performance is comparable to other control methods using force sensors. As expected, the tracking of the desired tensions on the force-controlled cables obtained with the HC-*e* controller is slightly worse compared to control architectures using force sensors in the feedback loop. The maximum average percentage error is 1.7% with load cells and 10% without them. However, these errors do not greatly influence the overall FD, since the maximum average percentage error of the forces for length-controlled cables is 24.4% with load cells and 24.3% without them. These values are similar even when the online change of the pair of wires to be force-controlled is experimented. If compared with a pure inverse kinematic controller (IKC) that does not exploit force sensors, the HC-*e* controller is much better, since it guarantees that all tensions remain within the predefined limits for almost all the time, while with the IKC they often drop under the required minimum force. The HC-*e* controller performance in maintaining the wire tensions between the given limits is also similar to that of the Nullspace Control (NC) method proposed in [128]. Moreover, the HC-*e* controller did not influence the IPAnema 3 Mini precision and repeatability.

The HC-*e* controller was tested on the CORHDA prototype to evaluate its applicability in faster movements than those performed on the IPAnema 3 Mini. The results obtained were still very good. For motions involving maximum velocities and accelerations approximately up to 4.5m/s and 65m/s^2, the performances of the controller are similar to those seen on the IPAnema 3 Mini in terms of force tracking and maintaining cable forces within given limits. It is observed a slight drop in its performance for faster motions, which could also be caused by the experimental setup. However, even in this case, the results are good and much better than those gained with the IKC that uses the same hardware. In all the aforementioned tests, load cells were used not to control the robot, but to measure cable tensions for validation sake. Movements with maximum velocities and accelerations between 6.8m/s, 153m/s^2 and 8.8m/s, 255m/s^2 were experimented without load cells (the latter could not be used for these dynamics, due to hardware limitations). In this case, motor torques were recorded instead. The feasibility of these movements proved the suitability of the CORHDA prototype and the HC-*e* controller for velocities and accelerations required by the fast bin-picking task. Finally, the precision and repeatability of the CORHDA (with the HC-*e* controller) were evaluated. The robot maximum and mean positioning errors were 8.5mm and 5mm, respectively, with a maximum and mean repeatability of 0.5mm and 0.36mm. Though the CORHDA repeatability is acceptable, the robot is not yet precise enough to execute the bin-picking task. However, we expect positioning precision to be significantly increased after a suitable calibration of the geometrical parameters will be carried out.

6.2 Open Issues

The robot described in this thesis is the first prototype developed to demonstrate the applicability of an overconstrained CDPR for executing fast bin-picking tasks and for testing the HC-e controller proposed in Chapter 3. The good results obtained with this work are the starting point for the fine development of the bin-picking cell for which the robot is developed.

The EE of the manipulator will be modified to make the robot capable of executing pick-and-place operations. A sucker connected to a vacuum ejector will probably be used, so a suitable strategy to bring the compressed air to the EE will be studied. During this stage the method introduced in Section 4.2 will be used to redesign the attachment points of the EE based on the final task (i.e., the final workspace dimensions) that will be assigned to the robot.

The performance of the HC-e controller is already very good based on the data acquired during the experimental tests. However, when the final EE of the robot will be designed, a fine-tuning of the parameters of the high-level PID in the force control loop of the HC-e controller will be carried out. This could further improve the performance of the control strategy, especially for very fast movements of the EE.

Once the final geometry of the frame and the EE will be defined, a calibration of the geometric parameters of the manipulator will be performed to improve its accuracy.

Finally, the robot will be integrated with the vision system in the bin-picking cell. Based on the information coming from the vision system about the pose of the products to be taken, a suitable picking strategy and trajectory planning to satisfy the required productivity of the bin-picking cell will be defined.

Acknowledgements

Per la terza e ultima (?) volta in vita mia sono di fronte a un foglio bianco, cercando di capire come lasciare stampata tra queste pagine una parte di me che non sia strettamente legata alla fredda sfera lavorativa. Negli ultimi mesi, mi sono reso conto che queste poche righe che posso scrivere sono una semplice istantanea del periodo che sto vivendo; un frammento momentaneo del mio essere, estrapolato da una tastiera battuta a una singola mano, mentre mi trovo in casa con un gomito mezzo rotto il 10 settembre 2024. La consapevolezza che ciò che scrivo oggi, ripensando agli ultimi quattro anni, è diverso da ciò che avrei scritto un anno fa o da ciò che potrei scrivere fra dodici mesi, è, credo, l'insegnamento umano più prezioso che ho appreso.

In passato, ho percepito le esperienze che hanno fatto parte della mia crescita personale come un insieme di tasselli accumulati in modo da creare lentamente la mia persona in maniera indissolubile: dei mattoni che vengono posati in modo più o meno ordinato sulle fondamenta del mio essere. Una volta cementati, ci sono; e restano lì. Tuttavia, oggi, credo che non sia esattamente così. Mi sono reso conto in questi anni che la ricerca è fatta di piccoli passi, avanzamenti a volte infinitesimi e spesso nella direzione sbagliata, ma che complessivamente portano a *evolvere* le nostre conoscenze. A volte questa evoluzione si manifesta tramite un incremento di nozioni relative a un determinato argomento, seguendo strade già tracciate; a volte, invece, la nostra curiosità e le nostre idee ci portano a modificare preconcetti esistenti o semplicemente a fornire soluzioni alternative a quelle già note (migliori o peggiori che siano). Allo stesso modo, il muro di esperienze che costruiamo nel tempo, posando un mattone dopo l'altro sulle fondamenta della nostra identità, può crescere, ma anche essere modificato o ristrutturato.

Quando mi sono messo a studiare i robot a cavi quattro anni fa, non avrei pensato di farne funzionare uno come quello descritto in questo elaborato senza utilizzare celle di carico; invece, alla fine, il robot che abbiamo sviluppato va. Con tutti i problemi che ancora si porta dietro, essendo un prototipo. Non è nemmeno detto che sia la soluzione migliore in assoluto. Però è motivata, è fattibile e, soprattutto, funziona. Così come le mie idee sulla robotica a cavi sono cambiate, anch'io sono cambiato negli ultimi anni, andando a evolvere la mia persona e i miei preconcetti anche grazie all'opportunità che ho avuto di fare ricerca. Fare ricerca significa impiegare il proprio tempo per studiare e apprendere nuovi argomenti tramite ciò che viene trasmesso da altri. Significa scoprire cose nuove in autonomia. A volte significa poter scegliere che direzione prendere per proseguire con il proprio lavoro. Significa avere a che fare con idee diverse dalle proprie, senza dover dare per scontato che siano migliori o peggiori. Significa non sapere se quello che si sta facendo è corretto davvero o se sarà un buco nell'acqua. *Significa mettersi in discussione.* Per ultimo, fare ricerca significa anche viaggiare e incontrare ricercatori di altre parti del mondo, sapendo che il mondo, il nostro mondo, non è solo la nostra università, la nostra azienda, la nostra città o il nostro stato. C'è molto di più. Sospinto dall'euforia delle riaperture post Covid e dalle nuove prospettive che la ricerca mi ha dato, ho avuto la fortuna negli ultimi anni di poter viaggiare molto (anche da solo) sia grazie al dottorato che per scelta e possibilità personali. Così, nel viaggio, ho riscontrato alcune caratteristiche già elencate; sì, perché partire significa andare alla ricerca di qualcosa che non si conosce. Significa esplorare, scoprire. Significa incontrare ideologie e usanze diverse. Anche viaggiare significa mettersi in discussione.

Essere un ricercatore e viaggiare sono stati due fattori (probabilmente non indipendenti) che mi hanno portato a diventare quello che sono oggi, dandomi la consapevolezza che potrei non essere la persona di domani. In particolare, fare ricerca è stata quindi per me un'opportunità unica che mi ha permesso di crescere a livello personale come mai prima, dandomi un'apertura mentale che (credo) difficilmente avrei trovato tramite un percorso lavorativo più "standard" in azienda. Per questo motivo, ritengo di dover ringraziare innanzitutto chi ha reso possibile tutto ciò, ovvero Marco, Alessandro ed Eros. Senza di loro, oggi non sarei qui a scrivere queste righe al termine di un'esperienza di quattro anni che sono fiero di aver portato a termine. Mi hanno condotto in questo percorso lavorativo e senza la loro presenza nulla di tutto ciò che è in questa tesi si sarebbe mai realizzato.

Voglio ringraziare poi tutti i colleghi che ho incontrato, sia in università che in azienda, e con cui ho trascorso le giornate di questi quattro anni. Loro hanno permesso di alleggerire anche i momenti lavorativi più difficili.

Un altro ringraziamento doveroso va alla Marchesini Group e a tutte le persone (oltre a quelle già citate) che, al suo interno, hanno creduto in me, dandomi l'opportunità di portare a termine un lavoro culminato nello sviluppo di un robot che porta il mio nome a livello progettuale; un motivo di orgoglio personale per me. Senza il supporto economico e le conoscenze pregresse dell'azienda, non avrei potuto ottenere alcun risultato.

Ora è il momento dei miei amici, che devo ringraziare per la loro presenza in questi anni perché è stata per me necessaria per arrivare alla fine di questo percorso. Come dicevo prima, fare ricerca significa anche lavorare senza sapere se quello che si sta facendo funzionerà e mettersi in discussione significa, a volte, chiedersi se si è davvero in grado di fare qualcosa. Ci sono stati momenti in cui temevo di fallire e, in quei frangenti, inconsapevolmente, i miei amici sono stati la mia salvezza, il modo per staccare da ansie e stress.

Infine, non posso non ringraziare i miei genitori e mia sorella per il loro supporto costante e incondizionato che mi ha portato a essere l'uomo che sono oggi. Siete stati per me una guida e un esempio da seguire fino a questo momento e lo sarete per sempre, per quanto io possa cambiare.

* * *

For the third and final (?) time in my life, I am staring at a blank page, trying to figure out how to leave a part of myself that is not strictly related to the cold, professional world printed here. Over the past few months, I have realized that these few lines I can write are merely a snapshot of the moment I am living in, a fleeting fragment of my being, typed one-handed on a keyboard while I sit at home with a half-broken elbow on September 10, 2024. The awareness that what I am writing today, reflecting on the last four years, is different from what I would have written a year ago or what I might write in twelve months is the most valuable life lesson I have learned.

In the past, I perceived the experiences that shaped my personal growth as pieces, gradually assembling an unbreakable version of myself: bricks laid more or less neatly on the foundation of who I am. Once cemented, they remain permanently. However, today, I think that this is not quite the case. Over the past few years, I have realized that research is made up of small steps, sometimes infinitesimal and often in the wrong direction, but they lead to our knowledge *evolution*. Sometimes, this evolution is a simple increment of notions about a specific topic that follows well-worn paths; other times, our curiosity and ideas push us to modify our pre-existing assumptions or provide alternative solutions (better or worse) to those already known. Similarly, the wall of experiences we build over time, brick by brick on the foundation of our identity, can grow, but it can also be changed or restructured.

When I began studying cable-driven parallel robots four years ago, I never imagined I would get one to work, as described in this thesis, without using load cells. However, in the end, the robot we developed works despite all its issues due to its prototype nature. It is not certain that this solution is the best possible, but it is justified, feasible, and, most importantly, works. Just as my ideas about cable-driven parallel robots have changed, so have I, evolving my identity and preconceptions, partly thanks to the opportunity to be a researcher. Doing research means dedicating your time to studying and learning new topics explained by other researchers through their works. It means discovering new things on your own. Sometimes, it means having the freedom to choose your work direction. It means discovering ideas different from yours without assuming they are better or worse. It means not knowing if what you are doing is correct or if it will fail. *It means questioning yourself.* Lastly, doing research also means traveling and meeting researchers from other parts of the world, understanding that our world is not just our university, company, city, or country. There is so much more. Driven by the excitement of post-Covid reopenings and the new perspectives the academic world has given me, I have been lucky enough in recent years to travel a lot (even solo) thanks to my PhD studies and through personal choices and opportunities. I found many of the characteristics related to the research world when traveling; in fact, setting off on a journey means seeking out something unknown. It means exploring and discovering. It means encountering different ideologies and customs. Traveling means questioning yourself.

Being a researcher and traveling have been two factors (probably not independent) that have shaped me into who I am today, making me aware that I may not be the same person tomorrow. In particular, doing research has been a unique opportunity, allowing me to grow personally in a way I had never experienced before, making me probably more open-minded than in a more "standard" career in a company. For this reason, I must first and foremost thank those who made all this possible: Marco, Alessandro, and Eros. Without them, I would not be here today, writing these words at the end of a four-year journey I am proud to have completed. They guided me through this work; nothing in this thesis would have been done without their presence.

I also want to thank all the colleagues I have met at university and in the company with whom I have spent my days over the past four years. They helped me lighten even the most demanding work moments.

A special thanks is also owed to Marchesini Group and to all the people (in addition to those already mentioned) who believed in me within the company, allowing me to complete a project that culminated in the development of a robot that, on a design level, bears my name—a personal source of pride for me. Without the company financial support and pre-existing knowledge, I would not have achieved any results.

Now it is time to thank my friends, whose presence over these years has been essential for me to reach the end of this journey. As I said before, doing research also means working without knowing if what you are doing will succeed, and questioning yourself sometimes means wondering if you can achieve your goals. There were moments when I feared I would fail, and during those times, my friends, unknowingly, were my salvation, the way for me to escape anxiety and stress.

Lastly, I cannot forget to thank my parents and my sister for their constant and unconditional support, which has helped shape me into the man I am today. You have been my guides and role models up to this point, and you always will be, no matter how much I may change.

List of Author Publications

1. L. Guagliumi, A. Berti, E. Monti, and M. Carricato, “A Simple Model-Based Method for Sloshing Estimation in Liquid Transfer in Automatic Machines,” in IEEE Access, vol. 9, pp. 129347-129357, 2021, doi: 10.1109/ACCESS.2021.3113956.
2. L. Guagliumi, A. Berti, E. Monti, and M. Carricato, “Antisloshing Trajectories for High-Acceleration Motions in Automatic Machines,” in ASME. J. Dyn. Sys., Meas., Control. July 2022; 144(7): 071006, doi: https://doi.org/10.1115/1.4054224.
3. L. Guagliumi, A. Berti, E. Monti, and M. Carricato, “Design Optimization of a 6-DOF Cable-Driven Parallel Robot for Complex Pick-and-Place Tasks,” *ROMANSY 24 - Robot Design, Dynamics and Control* (A. Kecskeméthy, V. Parenti-Castelli, eds.), (Cham), pp. 283-291, Springer International Publishing, 2022, doi: https://doi.org/10.1007/978-3-031-06409-8_30.
4. L. Guagliumi, A. Berti, E. Monti, and M. Carricato, “A Software Application for Fast Liquid-Sloshing Simulation,” *IFToMM Italy 2022: Advances in Italian Mechanism Science* (V. Niola, A. Gasparetto, G. Quaglia, G. Carbone, eds.), (Cham), pp. 819–828, Springer International Publishing, 2022, doi: https://doi.org/10.1007/978-3-031-10776-4_94.
5. L. Guagliumi, A. Berti, E. Monti, M. Fabritius, C. Martin, and M. Carricato, “Force-Sensor-Free Implementation of a Hybrid Position–Force Control for Overconstrained Cable-Driven Parallel Robots,” in Robotics. 2024; 13(2):25, doi: https://doi.org/10.3390/robotics13020025.
6. F. Brasina, L. Guagliumi, R. Di Leva, and M. Carricato, “Anti-sloshing Motion Laws for One-Dimensional Piecewise Trajectories,” Rosati, G., Gasparetto, A., Ceccarelli, M. (eds) *New Trends in Mechanism and Machine Science. EuCoMeS 2024.* Mechanisms and Machine Science, vol 165. Springer, Cham. https://doi.org/10.1007/978-3-031-67295-8_18.

List of Figures

Bibliography

[1] F. Hagelskjær, T. R. Savarimuthu, N. Krüger, and A. G. Buch, “Using spatial constraints for fast set-up of precise pose estimation in an industrial setting,” in *2019 IEEE 15th International Conference on Automation Science and Engineering (CASE), Vancouver, BC, Canada*, pp. 1308–1314, 2019.

[2] S. D. Han, S. W. Feng, and J. Yu, “Toward fast and optimal robotic pick-and-place on a moving conveyor,” *IEEE Robotics and Automation Letters*, vol. 5, no. 2, pp. 446–453, 2020.

[3] F. Pierrot, C. Reynaud, and A. Fournier, “DELTA: a simple and efficient parallel robot,” *Robotica*, vol. 8, no. 2, p. 105–109, 1990.

[4] V. Nabat, M. de la O Rodriguez, O. Company, S. Krut, and F. Pierrot, “Par4: very high speed parallel robot for pick-and-place,” in *2005 IEEE/RSJ International Conference on Intelligent Robots and Systems, Edmonton, AB, Canada*, pp. 553–558, 2005.

[5] C. Stocker, M. Schmid, and G. Reinhart, “Reinforcement learning–based design of orienting devices for vibratory bowl feeders,” *The International Journal of Advanced Manufacturing Technology*, vol. 105, 12 2019.

[6] R. Matsumura, Y. Domae, W. Wan, and K. Harada, “Learning based robotic bin-picking for potentially tangled objects,” in *2019 IEEE/RSJ International Conference on Intelligent Robots and Systems (IROS), Macau, China*, pp. 7990–7997, 2019.

[7] S. Tajima, S. Wakamatsu, T. Abe, M. Tennomi, K. Morita, H. Ubata, A. Okamura, Y. Hirai, K. Morino, Y. Suzuki, T. Tsuji, K. Yamazaki, and T. Watanabe, “Robust bin-picking system using tactile sensor,” *Advanced Robotics*, vol. 34, no. 7-8, pp. 439–453, 2020.

[8] C. Martinez, H. Chen, and R. Boca, “Automated 3D vision guided bin picking process for randomly located industrial parts,” in *2015 IEEE International Conference on Industrial Technology (ICIT), Seville, Spain*, pp. 3172–3177, 2015.

[9] A. Schyja and B. Kuhlenkötter, “Realistic simulation of industrial bin-picking systems,” in *2015 6th International Conference on Automation, Robotics and Applications (ICARA), Queenstown, New Zealand, 2015*, pp. 137–142, 2015.

[10] R. T. Chin and C. R. Dyer, “Model-based recognition in robot vision,” *ACM Comput. Surv.*, vol. 18, p. 67–108, mar 1986.

[11] W. Kehl, F. Manhardt, F. Tombari, S. Ilic, and N. Navab, “Ssd-6d: Making rgb-based 3d detection and 6d pose estimation great again,” in *2017 IEEE International Conference on Computer Vision (ICCV), Venice, Italy*, pp. 1530–1538, 2017.

[12] A. Zeng, S. Song, K.-T. Yu, E. Donlon, F. R. Hogan, M. Bauza, D. Ma, O. Taylor, M. Liu, E. Romo, N. Fazeli, F. Alet, N. C. Dafle, R. Holladay, I. Morena, P. Qu Nair, D. Green, I. Taylor, W. Liu, T. Funkhouser, and A. Rodriguez, “Robotic pick-and-place of novel objects in clutter with multi-affordance grasping and cross-domain image matching,” in *2018 IEEE International Conference on Robotics and Automation (ICRA), Brisbane, Australia*, pp. 3750–3757, 2018.

[13] M. Li and K. Hashimoto, “Fast and robust pose estimation algorithm for bin picking using point pair feature,” in *2018 24th International Conference on Pattern Recognition (ICPR), Beijing, China*, pp. 1604–1609, 2018.

[14] W. Yan, Z. Xu, X. Zhou, Q. Su, S. Li, and H. Wu, “Fast object pose estimation using adaptive threshold for bin-picking,” *IEEE Access*, vol. 8, pp. 63055–63064, 2020.

[15] Z. He, W. Feng, X. Zhao, and Y. Lv, “6d pose estimation of objects: Recent technologies and challenges,” *Applied Sciences*, vol. 11, no. 1, 2021.

[16] H.-Y. Kuo, H.-R. Su, S.-H. Lai, and C.-C. Wu, “3D object detection and pose estimation from depth image for robotic bin picking,” in *2014 IEEE International Conference on Automation Science and Engineering (CASE), New Taipei, Taiwan*, pp. 1264–1269, 2014.

[17] A. Doumanoglou, R. Kouskouridas, S. Malassiotis, and T.-K. Kim, “Recovering 6D object pose and predicting next-best-view in the crowd,” in *2016 IEEE Conference on Computer Vision and Pattern Recognition (CVPR), Las Vegas, NV, USA*, pp. 3583–3592, 2016.

[18] S.-C. Liang, H.-Y. Lin, and C.-C. Chang, “Model-based 3D pose estimation for pick-and-place application,” in *2017 Fifteenth IAPR International Conference on Machine Vision Applications (MVA), Nagoya, Japan*, pp. 412–415, 2017.

[19] D. Liu, S. Arai, J. Miao, J. Kinugawa, Z. Wang, and K. Kosuge, “Point pair feature-based pose estimation with multiple edge appearance models (ppf-meam) for robotic bin picking,” *Sensors*, vol. 18, no. 8, 2018.

[20] W.-Y. Chiu, “Dual laser 3D scanner for random bin picking system,” in *2015 International Conference on Advanced Robotics and Intelligent Systems (ARIS), Taipei, Taiwan*, pp. 1–3, 2015.

[21] F. Cen, X. Zhao, W. Li, and G. Wang, “Deep feature augmentation for occluded image classification,” *Pattern Recognition*, vol. 111, p. 107737, 2021.

[22] J. Lee, T.-W. Kim, S. Kang, K. Kim, J. Kim, and J. B. Kim, “Bin picking for the objects of non-Lambertian reflectance without using an explicit object model,” in *2014 11th International Conference on Ubiquitous Robots and Ambient Intelligence (URAI), Kuala Lumpur, Malaysia*, pp. 489–493, 2014.

[23] F. Spenrath and A. Pott, "Using neural networks for heuristic grasp planning in random bin picking," in *2018 IEEE 14th International Conference on Automation Science and Engineering (CASE), Munich, Germany*, pp. 258–263, 2018.

[24] G. Du, K. Wang, S. Lian, and K. Zhao, "Vision-based robotic grasping from object localization, object pose estimation to grasp estimation for parallel grippers: a review," *Artificial Intelligence Review*, vol. 54, 03 2021.

[25] R. Xu, F.-J. Chu, and P. A. Vela, "Gknet: Grasp keypoint network for grasp candidates detection," *The International Journal of Robotics Research*, vol. 41, no. 4, pp. 361–389, 2022.

[26] J. R. Amend, E. Brown, N. Rodenberg, H. M. Jaeger, and H. Lipson, "A positive pressure universal gripper based on the jamming of granular material," *IEEE Transactions on Robotics*, vol. 28, no. 2, pp. 341–350, 2012.

[27] J. M. Krahn, F. Fabbro, and C. Menon, "A soft-touch gripper for grasping delicate objects," *IEEE/ASME Transactions on Mechatronics*, vol. 22, no. 3, pp. 1276–1286, 2017.

[28] T. Hou, X. Yang, Y. Aiyama, K. Liu, Z. Wang, T. Wang, J. Liang, and Y. Fan, "Design and experiment of a universal two-fingered hand with soft fingertips based on jamming effect," *Mechanism and Machine Theory*, vol. 133, pp. 706–719, 2019.

[29] C. Tawk, Y. Gao, R. Mutlu, and G. Alici, "Fully 3d printed monolithic soft gripper with high conformal grasping capability," in *2019 IEEE/ASME International Conference on Advanced Intelligent Mechatronics (AIM), Hong Kong, China*, pp. 1139–1144, 2019.

[30] E. Papadakis, F. Raptopoulos, M. Koskinopoulou, and M. Maniadakis, "On the use of vacuum technology for applied robotic systems," in *2020 6th International Conference on Mechatronics and Robotics Engineering (ICMRE), Barcelona, Spain*, pp. 73–77, 2020.

[31] C. Tawk, R. Mutlu, and G. Alici, "A 3d printed modular soft gripper integrated with metamaterials for conformal grasping," *Frontiers in Robotics and AI*, vol. 8, 2022.

[32] J. Mahler, M. Matl, V. Satish, M. Danielczuk, B. DeRose, S. McKinley, and K. Goldberg, "Learning ambidextrous robot grasping policies," *Science Robotics*, vol. 4, no. 26, 2019.

[33] V. Vonasek, A. Vick, and M. Saska, "Motion planning with motion primitives for industrial bin picking," in *2017 22nd IEEE International Conference on Emerging Technologies and Factory Automation (ETFA), Limassol, Cyprus*, pp. 1–4, 2017.

[34] G. Leão, C. M. Costa, A. Sousa, and G. Veiga, "Detecting and solving tube entanglement in bin picking operations," *Applied Sciences*, vol. 10, no. 7, 2020.

[35] Y. D. Patel and P. M. George, "Parallel manipulators applications — A survey," *Modern Mechanical Engineering*, vol. 2, pp. 57–64, 08 2012.

[36] A. Rosyid, B. El-Khasawneh, and A. Alazzam, “Review article: Performance measures of parallel kinematics manipulators,” *Mechanical Sciences*, vol. 11, no. 1, pp. 49–73, 2020.

[37] A. Deabs, F. Gomaa, and K. Khader, “Parallel robot - review article,” *Journal of Engineering Science and Technology Review*, vol. 14, pp. 10–27, 01 2021.

[38] V. Mattioni, *Design and control strategies of overconstrained cable-driven parallel robots.* Phd thesis, University of Bologna, Bologna, Italy, 2023.

[39] A. Pott, *Cable-driven parallel robots: theory and application.* Springer Cham, 05 2018.

[40] E. Idà, *Dynamics of underactuated cable-driven parallel robots.* Phd thesis, University of Bologna, Bologna, Italy, 2021.

[41] S. E. Landsberger, “Design and construction of a cable-controlled, parallel link manipulator,” Master’s thesis, Massachusetts Institute of Technology, Boston, USA, 1984.

[42] K. Miura, H. Furuya, and K. Suzuki, “Variable geometry truss and its application to deployable truss and space crane arm,” *Acta Astronautica*, vol. 12, no. 7, pp. 599–607, 1985.

[43] J.-P. Merlet, “Wire-driven parallel robot: open issues,” in *Romansy 19 – Robot Design, Dynamics and Control* (V. Padois, P. Bidaud, and O. Khatib, eds.), (Vienna), pp. 3–10, Springer Vienna, 2013.

[44] A. Ming and H. Toshiro, “Study on multiple degree-of-freedom positioning mechanism using wires. I: concept, design and control,” *Int. J. Jpn Soc. Eng.*, vol. 28, pp. 131–138, 01 1994.

[45] M. Carricato and J.-P. Merlet, “Stability analysis of underconstrained cable-driven parallel robots,” *IEEE Transactions on Robotics*, vol. 29, no. 1, pp. 288–296, 2013.

[46] “Spidercam.” `https://www.spidercam.tv/` [Accessed: 2023-08-09].

[47] J.-P. Merlet and D. Daney, “A portable, modular parallel wire crane for rescue operations,” in *2010 IEEE International Conference on Robotics and Automation, Anchorage, AK, USA*, pp. 2834–2839, 2010.

[48] R. Nan, D. Li, C. Jin, Q. Wang, L. Zhu, W. Zhu, H. Zhang, Y. Yue, and L. Qian, “The five-hundred-meter aperture spherical radio telescope (FAST) project,” *International Journal of Modern Physics D*, vol. 20, pp. 989–1024, jun 2011.

[49] M. Gouttefarde, J.-F. Collard, N. Riehl, and C. Baradat, “Geometry selection of a redundantly actuated cable-suspended parallel robot,” *IEEE Transactions on Robotics*, vol. 31, no. 2, pp. 501–510, 2015.

[50] G. Rosati, P. Gallina, and S. Masiero, “Design, implementation and clinical tests of a wire-based robot for neurorehabilitation,” *IEEE Transactions on Neural Systems and Rehabilitation Engineering*, vol. 15, no. 4, pp. 560–569, 2007.

[51] C. Chesher, “Robots and the moving camera in cinema, television and digital media,” in *Cultural Robotics* (J. T. Koh, B. J. Dunstan, D. Silvera-Tawil, and M. Velonaki, eds.), (Cham), pp. 98–106, Springer International Publishing, 2016.

[52] L. L. Cone, “Skycam: an aerial robotic camera system,” *Byte*, vol. 10, no. 10, pp. 122–132, 1985.

[53] G. W. Brown, “Suspension system for supporting and conveying equipment,such as a camera,” *Patent US4710819A*, 1987.

[54] J. Rodnunsky and B. Trou, “Aerial cableway and method for filming subjects in-motion,” *Patent US5224426A*, 1993.

[55] S. Tadokoro, R. Verhoeven, M. Hiller, and T. Takamori, “A portable parallel manipulator for search and rescue at large-scale urban earthquakes and an identification algorithm for the installation in unstructured environments,” in *Proceedings 1999 IEEE/RSJ International Conference on Intelligent Robots and Systems, Kyongju, Korea (South)*, vol. 2, pp. 1222–1227 vol.2, 1999.

[56] X. Tang and R. Yao, “Dimensional design on the six-cable driven parallel manipulator of FAST,” *Journal of Mechanical Design*, vol. 133, 11 2011.

[57] J. Albus, R. Bostelman, and N. Dagalakis, “The NIST SPIDER, a robot crane,” *Journalof Research of the National Institute of Standards and Technology*, vol. 97, no. 3, pp. 373–385, 1992.

[58] A. Michele, E. Idà, D. Bertin, M. Carricato, E. Mantovani, D. Bazzi, and V. Orassi, “An underactuated cable-driven parallel robot for marine automated launch and recovery operations,” in *ASME Int. Design Engineering Technical Conferences, Boston, MA, USA*, 2023.

[59] K. Iturralde, M. Feucht, D. Illner, R. Hu, W. Pan, T. Linner, T. Bock, I. Eskudero, M. Rodriguez, J. Gorrotxategi, J. Izard, J. Astudillo, J. Cavalcanti Santos, M. Gouttefarde, M. Fabritius, C. Martin, T. Henninge, S. Nornes, Y. Jacobsen, A. Pracucci, J. Cañada, J. Jimenez-Vicaria, R. Alonso, and L. Elia, “Cable-driven parallel robot for curtain wall module installation,” *Automation in Construction*, vol. 138, p. 104235, 2022.

[60] T. Bruckmann, C. Sturm, L. Fehlberg, and C. Reichert, “An energy-efficient wire-based storage and retrieval system,” in *2013 IEEE/ASME International Conference on Advanced Intelligent Mechatronics, Wollongong, NSW, Australia*, pp. 631–636, 2013.

[61] “Kite robotics.” `https://www.kiterobotics.com//` [Accessed: 2023-09-09].

[62] P. Miermeister, M. Lächele, R. Boss, C. Masone, C. Schenk, J. Tesch, M. Kerger, H. Teufel, A. Pott, and H. H. Bülthoff, “The CableRobot simulator large scale motion platform based on cable robot technology,” in *2016 IEEE/RSJ International Conference on Intelligent Robots and Systems (IROS)), Daejeon, Korea (South)*, pp. 3024–3029, 2016.

[63] I. Ben Hamida, M. A. Laribi, A. Mlika, L. Romdhane, S. Zeghloul, and G. Carbone, “Multi-objective optimal design of a cable driven parallel robot for rehabilitation tasks,” *Mechanism and Machine Theory*, vol. 156, 2021.

[64] G. Rosati, M. Andreolli, A. Biondi, and P. Gallina, “Performance of cable suspended robots for upper limb rehabilitation,” in *2007 IEEE 10th International Conference on Rehabilitation Robotics, Noordwijk, Netherlands*, pp. 385–392, 2007.

[65] C. Xie, Q. Yang, Y. Huang, S. W. Su, T. Xu, and R. Song, “A hybrid arm-hand rehabilitation robot with emg-based admittance controller,” *IEEE Transactions on Biomedical Circuits and Systems*, vol. 15, no. 6, pp. 1332–1342, 2021.

[66] D. Surdilovic and R. Bernhardt, “STRING-MAN: a new wire robot for gait rehabilitation,” in *IEEE International Conference on Robotics and Automation, 2004. Proceedings. ICRA ’04. 2004, New Orleans, LA, USA*, vol. 2, pp. 2031–2036 Vol.2, 2004.

[67] B. Liao, J. Li, S. Deng, J. Li, and G. Li, “Optimal design of a cable driven parallel robot for upper limb rehabilitations,” *Journal of Physics: Conference Series*, vol. 2365, p. 012036, nov 2022.

[68] H. Lamine, M. A. Laribi, S. Bennour, L. Romdhane, and S. Zeghloul, “Design study of a cable-based gait training machine,” *Journal of Bionic Engineering*, vol. 14, no. 2, pp. 232–244, 2017.

[69] T. Bruckmann and R. Boumann, “Simulation and optimization of automated masonry construction using cable robots,” *Advanced Engineering Informatics*, vol. 50, p. 101388, 2021.

[70] J.-B. Izard, M. Gouttefarde, C. Baradat, D. Culla, and D. Sallé, “Integration of a parallel cable-driven robot on an existing building façade,” in *Cable-Driven Parallel Robots* (T. Bruckmann and A. Pott, eds.), (Berlin, Heidelberg), pp. 149–164, Springer Berlin Heidelberg, 2013.

[71] H. Hussein, J. C. Santos, and M. Gouttefarde, “Geometric optimization of a large scale CDPR operating on a building facade,” in *2018 IEEE/RSJ International Conference on Intelligent Robots and Systems (IROS), Madrid, Spain*, pp. 5117–5124, 2018.

[72] T. Bruckmann, W. Lalo, K. Nguyen, and B. Salah, “Development of a storage retrieval machine for high racks using a wire robot,” in *Proceedings of the ASME 2012 International Design Engineering Technical Conferences and Computers and Information in Engineering Conference, Chicago, Illinois, USA*, pp. 771–780, 08 2012.

[73] C. Reichert and T. Bruckmann, “Optimization of the geometry of a cable-driven storage and retrieval system,” in *Robotics and Mechatronics* (R. (Chunhui) Yang, Y. Takeda, C. Zhang, and G. Fang, eds.), (Cham), pp. 225–237, Springer International Publishing, 07 2019.

[74] F. Zhang, W. Shang, B. Zhang, and S. Cong, “Design optimization of redundantly actuated cable-driven parallel robots for automated warehouse system,” *IEEE Access*, vol. 8, pp. 56867–56879, 2020.

[75] E. Picard, S. Caro, F. Plestan, and F. Claveau, “Stiffness oriented tension distribution algorithm for cable-driven parallel robots,” in *Advances in Robot Kinematics 2020* (J. Lenarčič and B. Siciliano, eds.), (Cham), pp. 209–217, Springer International Publishing, 2021.

[76] Z. Shao, G. Xie, Z. Zhang, and L. Wang, “Design and analysis of the cable-driven parallel robot for cleaning exterior wall of buildings,” *International Journal of Advanced Robotic Systems*, vol. 18, no. 1, 2021.

[77] V. Mattioni, E. Ida’, and M. Carricato, “Design of a planar cable-driven parallel robot for non-contact tasks,” *Applied Sciences*, vol. 11, no. 20, 2021.

[78] S. Kawamura, W. Choe, S. Tanaka, and S. Pandian, “Development of an ultrahigh speed robot FALCON using wire drive system,” in *Proceedings of 1995 IEEE International Conference on Robotics and Automation, Nagoya, Japan*, vol. 1, pp. 215–220 vol.1, 1995.

[79] S. Kawamura, H. Kino, and C. Won, “High-speed manipulation by using parallel wire-driven robots,” *Robotica*, vol. 18, no. 1, p. 13–21, 2000.

[80] A. Nasr and S. A. A. Moosavian, “Multi-criteria design of 6-DoF fully-constrained cable driven redundant parallel manipulator,” in *2015 3rd RSI International Conference on Robotics and Mechatronics (ICROM), Tehran, Iran*, pp. 001–006, 2015.

[81] R. Dekker, A. Jepour, and S. Behzadipour, “Design and testing of an ultra-high-speed cable robot,” *International Journal of Robotics & Automation*, vol. 21, 01 2006.

[82] Z. Zhang, Z. Shao, L. Wang, and A. J. Shih, “Optimal design of a high-speed pick-and-place cable-driven parallel robot,” in *Cable-Driven Parallel Robots* (C. Gosselin, P. Cardou, T. Bruckmann, and A. Pott, eds.), (Cham), pp. 340–352, Springer International Publishing, 2018.

[83] Z. Zhang, Z. Shao, and L. Wang, “Optimization and implementation of a high-speed 3-DOFs translational cable-driven parallel robot,” *Mechanism and Machine Theory*, vol. 145, p. 103693, 2020.

[84] B. Siciliano, L. Sciavicco, L. Villani, and G. Oriolo, *Robotics. Modelling, planning and control.* Springer, 2009.

[85] E. Idà, T. Bruckmann, and M. Carricato, “Rest-to-rest trajectory planning for underactuated cable-driven parallel robots,” *IEEE Transactions on Robotics*, vol. 35, no. 6, pp. 1338–1351, 2019.

[86] T. Bruckmann, A. Pott, and M. Hiller, “Calculating force distributions for redundantly actuated tendon-based stewart platforms,” in *Advances in Robot Kinematics* (J. Lennarčič and B. Roth, eds.), (Dordrecht), pp. 403–412, Springer Netherlands, 2006.

[87] M. Hassan and A. Khajepour, “Minimum-norm solution for the actuator forces in cable-based parallel manipulators based on convex optimization,” in *Proceedings 2007 IEEE International Conference on Robotics and Automation, Rome, Italy*, pp. 1498–1503, 2007.

[88] M. Hassan and A. Khajepour, “Analysis of bounded cable tensions in cable-actuated parallel manipulators,” *IEEE Transactions on Robotics*, vol. 27, no. 5, pp. 891–900, 2011.

[89] H. D. Taghirad and Y. B. Bedoustani, “An analytic-iterative redundancy resolution scheme for cable-driven redundant parallel manipulators,” *IEEE Transactions on Robotics*, vol. 27, no. 6, pp. 1137–1143, 2011.

[90] B. Ouyang and W. Shang, “Rapid optimization of tension distribution for cable-driven parallel manipulators with redundant cables,” *Chinese Journal of Mechanical Engineering*, vol. 29, 01 2016.

[91] H. Jamshidifar, A. Khajepour, B. Fidan, and M. Rushton, “Kinematically-constrained redundant cable-driven parallel robots: modeling, redundancy analysis, and stiffness optimization,” *IEEE/ASME Transactions on Mechatronics*, vol. 22, no. 2, pp. 921–930, 2017.

[92] A. F. Côté, P. Cardou, and C. Gosselin, “A tension distribution algorithm for cable-driven parallel robots operating beyond their wrench-feasible workspace,” in *2016 16th International Conference on Control, Automation and Systems (ICCAS), Gyeongju, Korea (South)*, pp. 68–73, 2016.

[93] L. Mikelsons, T. Bruckmann, M. Hiller, and D. Schramm, “A real-time capable force calculation algorithm for redundant tendon-based parallel manipulators,” in *2008 IEEE International Conference on Robotics and Automation, Pasadena, CA, USA*, pp. 3869–3874, 2008.

[94] A. Pott, T. Bruckmann, and L. Mikelsons, “Closed-form force distribution for parallel wire robots,” in *Computational Kinematics* (A. Kecskeméthy and A. Müller, eds.), (Berlin, Heidelberg), pp. 25–34, Springer Berlin Heidelberg, 2009.

[95] A. Pott, “An improved force distribution algorithm for over-constrained cable-driven parallel robots,” in *Computational Kinematics* (F. Thomas and A. Perez Gracia, eds.), (Dordrecht), pp. 139–146, Springer Netherlands, 2014.

[96] K. Müller, C. Reichert, and T. Bruckmann, “Analysis of a real-time capable cable force computation method,” in *Cable-Driven Parallel Robots* (A. Pott and T. Bruckmann, eds.), (Cham), pp. 227–238, Springer International Publishing, 2015.

[97] L. Notash, “Designing positive tension for wire-actuated parallel manipulators,” in *Advances in Mechanisms, Robotics and Design Education and Research* (V. Kumar, J. Schmiedeler, S. V. Sreenivasan, and H.-J. Su, eds.), (Heidelberg), pp. 251–263, Springer International Publishing, 2013.

[98] L. Notash, “On the solution set for positive wire tension with uncertainty in wire-actuated parallel manipulators,” *Journal of Mechanisms and Robotics*, vol. 8, 03 2016.

[99] H. Yuan, E. Courteille, and D. Deblaise, "Force distribution with pose-dependent force boundaries for redundantly actuated cable-driven parallel robots," *Journal of Mechanisms and Robotics*, vol. 8, 03 2016. 041004.

[100] M. Gouttefarde, J. Lamaury, C. Reichert, and T. Bruckmann, "A versatile tension distribution algorithm for n-DOF parallel robots driven by n+2 cables," *IEEE Transactions on Robotics*, vol. 31, no. 6, pp. 1444–1457, 2015.

[101] D. Song, L. Zhang, and F. Xue, "Configuration optimization and a tension distribution algorithm for cable-driven parallel robots," *IEEE Access*, vol. 6, pp. 33928–33940, 2018.

[102] G. Sun, Z. Liu, H. Gao, N. Li, L. Ding, and Z. Deng, "Direct method for tension feasible region calculation in multi-redundant cable-driven parallel robots using computational geometry," *Mechanism and Machine Theory*, vol. 158, p. 104225, 2021.

[103] Z. Cui, X. Tang, S. Hou, and H. Sun, "Non-iterative geometric method for cable-tension optimization of cable-driven parallel robots with 2 redundant cables," *Mechatronics*, vol. 59, pp. 49–60, 2019.

[104] E. Ottaviano and G. Castelli, "A study on the effects of cable mass and elasticity in cable-based parallel manipulators," in *ROMANSY 18 Robot Design, Dynamics and Control* (V. Parenti Castelli and W. Schiehlen, eds.), (Vienna), pp. 149–156, Springer Vienna, 2010.

[105] R. Yao, H. Li, and X. Zhang, "A modeling method of the cable driven parallel manipulator for FAST," in *Cable-Driven Parallel Robots* (T. Bruckmann and A. Pott, eds.), (Berlin, Heidelberg), pp. 423–436, Springer Berlin Heidelberg, 2013.

[106] D. Q. Nguyen, M. Gouttefarde, O. Company, and F. Pierrot, "On the simplifications of cable model in static analysis of large-dimension cable-driven parallel robots," in *2013 IEEE/RSJ International Conference on Intelligent Robots and Systems, Tokyo, Japan*, pp. 928–934, 2013.

[107] J.-P. Merlet, "Influence of parameters uncertainties on the positioning of cable-driven parallel robots," in *2019 IEEE/RSJ International Conference on Intelligent Robots and Systems (IROS), Macau, China, 2019*, pp. 6769–6774, 2019.

[108] R. Verhoeven, *Analysis of the workspace of tendon-based stewart platforms.* Phd thesis, University of Duisburg-Essen, Duisburg, Germany, 2004.

[109] J.-P. Merlet, "Kinematics of the wire-driven parallel robot MARIONET using linear actuators," in *2008 IEEE International Conference on Robotics and Automation, Pasadena, CA, USA*, pp. 3857–3862, 2008.

[110] W. Kraus, *Force control of cable-driven parallel robots.* Phd thesis, University of Stuttgart, Stuttgart, Germany, 2015.

[111] V. Schmidt and A. Pott, "Increase of position accuracy for cable-driven parallel robots using a model for elongation of plastic fiber ropes," in *New Trends in Mechanism and Machine Science* (P. Wenger and P. Flores, eds.), (Cham), pp. 335–343, Springer International Publishing, 2017.

[112] Y. B. Bedoustani, H. D. Taghirad, and M. M. Aref, "Dynamics analysis of a redundant parallel manipulator driven by elastic cables," in *2008 10th International Conference on Control, Automation, Robotics and Vision, Hanoi, Vietnam*, pp. 536–542, 2008.

[113] S.-H. Choi and K.-S. Park, "Integrated and nonlinear dynamic model of a polymer cable for low-speed cable-driven parallel robots," *Microsystem Technologies*, vol. 24, pp. 1–11, 11 2018.

[114] P. Miermeister, W. Kraus, T. Lan, and A. Pott, "An elastic cable model for cable-driven parallel robots including hysteresis effects," in *Cable-Driven Parallel Robots* (A. Pott and T. Bruckmann, eds.), (Cham), pp. 17–28, Springer International Publishing, 2015.

[115] T. Vu, D. Durville, and P. Davies, "Finite element simulation of the mechanical behavior of synthetic braided ropes and validation on a tensile test," *International Journal of Solids and Structures*, vol. 58, pp. 106–116, 2015.

[116] V. Sry, Y. Mizutani, G. Endo, Y. Suzuki, and A. Todoroki, "Estimation of the longitudinal elasticity modulus of braided synthetic fiber rope utilizing classical laminate theory with the unit N/tex," *Applied Sciences*, vol. 8, no. 7, 2018.

[117] M. Michael, C. Kern, and T. Heinze, "9 - Braiding processes for braided ropes," in *Advances in Braiding Technology* (Y. Kyosev, ed.), Woodhead Publishing Series in Textiles, pp. 225–243, Woodhead Publishing, 2016.

[118] V. Schmidt and A. Pott, "Investigating the effect of cable force on winch winding accuracy for cable-driven parallel robots," *Proceedings of the Institution of Mechanical Engineers, Part K: Journal of Multi-body Dynamics*, vol. 230, no. 3, pp. 237–241, 2016.

[119] J.-P. Merlet, *Parallel robots.* Springer Dordrecht, 2006.

[120] M. Gouttefarde and C. M. Gosselin, "On the properties and the determination of the wrench-closure workspace of planar parallel cable-driven mechanisms," in *International Design Engineering Technical Conferences and Computers and Information in Engineering Conference, Salt Lake City, Utah, USA*, pp. 337–346, 09 2004.

[121] M. Gouttefarde, J.-P. Merlet, and D. Daney, "Wrench-feasible workspace of parallel cable-driven mechanisms," in *Proceedings 2007 IEEE International Conference on Robotics and Automation, Rome, Italy*, pp. 1492–1497, 2007.

[122] S. Perreault, P. Cardou, C. M. Gosselin, and M. J.-D. Otis, "Geometric determination of the interference-free constant-orientation workspace of parallel cable-driven mechanisms," *Journal of Mechanisms and Robotics*, vol. 2, 07 2010.

[123] M. M. Aref and H. D. Taghirad, "Geometrical workspace analysis of a cable-driven redundant parallel manipulator: KNTU CDRPM," in *2008 IEEE/RSJ International Conference on Intelligent Robots and Systems, Nice, France*, pp. 1958–1963, 2008.

[124] K. Youssef and M. J.-D. Otis, "Reconfigurable fully constrained cable driven parallel mechanism for avoiding interference between cables," *Mechanism and Machine Theory*, vol. 148, p. 103781, 2020.

[125] S. Bouchard and C. Gosselin, "A simple control strategy for overconstrained parallel cable mechanisms," in *Proceedings of the 20th Canadian Congress of Applied Mechanics (CANCAM), Montreal, Quebec, Canada*, pp. 1540–1545, 2005.

[126] T. Bruckmann, L. Mikelsons, M. Hiller, and D. Schramm, "A new force calculation algorithm for tendon-based parallel manipulators," in *2007 IEEE/ASME international conference on advanced intelligent mechatronics, Zurich, Switzerland*, pp. 1–6, 2007.

[127] A. Pott, H. Mütherich, W. Kraus, V. Schmidt, P. Miermeister, and A. Verl, "IPAnema: a family of cable-driven parallel robots for industrial applications," in *Cable-Driven Parallel Robots* (T. Bruckmann and A. Pott, eds.), (Berlin, Heidelberg), pp. 119–134, Springer Berlin Heidelberg, 2013.

[128] M. Fabritius, G. Rubio-Gómez, C. Martin, J. C. Santos, W. Kraus, and A. Pott, "A nullspace-based force correction method to improve the dynamic performance of cable-driven parallel robots," *Mechanism and Machine Theory*, vol. 181, p. 105177, 2023.

[129] X. Wang, S. Ma, and Q. Lin, "Hybrid pose/tension control based on stiffness optimization of cable-driven parallel mechanism in wind tunnel test," in *2016 2nd International Conference on Control, Automation and Robotics (ICCAR), Hong Kong, China*, pp. 75–79, 2016.

[130] S. Fang, D. Franitza, M. Torlo, F. Bekes, and M. Hiller, "Motion control of a tendon-based parallel manipulator using optimal tension distribution," *IEEE/ASME Transactions on Mechatronics*, vol. 9, no. 3, pp. 561–568, 2004.

[131] J. C. Santos and M. Gouttefarde, "A simple and efficient non-model based cable tension control," in *Cable-Driven Parallel Robots* (M. Gouttefarde, T. Bruckmann, and A. Pott, eds.), (Cham), pp. 297–308, Springer International Publishing, 2021.

[132] S.-R. Oh and S. Agrawal, "Cable suspended planar robots with redundant cables: controllers with positive tensions," *IEEE Transactions on Robotics*, vol. 21, no. 3, pp. 457–465, 2005.

[133] W. Kraus, P. Miermeister, V. Schmidt, and A. Pott, "Hybrid position-force control of a cable-driven parallel robot with experimental evaluation," *Mechanical Sciences*, vol. 6, no. 2, pp. 119–125, 2015.

[134] J. Jun, X. Jin, A. Pott, S. Park, J.-O. Park, and S. Y. Ko, "Hybrid position/force control using an admittance control scheme in Cartesian space for a 3-DOF planar cable-driven parallel robot," *International Journal of Control, Automation and Systems*, vol. 14, pp. 1106–1113, 08 2016.

[135] V. Mattioni, E. Idà, and M. Carricato, "Force-distribution sensitivity to cable-tension errors: a preliminary investigation," in *Cable-Driven Parallel Robots* (M. Gouttefarde, T. Bruckmann, and A. Pott, eds.), (Cham), pp. 129–141, Springer International Publishing, 2021.

[136] V. Mattioni, E. Idà, and M. Carricato, "Force-distribution sensitivity to cable-tension errors in overconstrained cable-driven parallel robots," *Mechanism and Machine Theory*, vol. 175, p. 104940, 2022.

[137] V. Mattioni, E. Idà, M. Gouttefarde, and M. Carricato, "A practical approach for the hybrid joint-space control of overconstrained cable-driven parallel robots," in *Cable-Driven Parallel Robots* (S. Caro, A. Pott, and T. Bruckmann, eds.), (Cham), pp. 149–160, Springer Nature Switzerland, 2023.

[138] M. Otis, T. Nguyen-Dang, T. Laliberté, D. Ouellet, D. Laurendeau, and C. Gosselin, "Cable tension control and analysis of reel transparency for 6-DOF haptic foot platform on a cable-driven locomotion interface," *International Journal of Electrical, Computer and Systems Engineering*, vol. 3, pp. 16–29, 01 2009.

[139] W. Kraus, M. Kessler, and A. Pott, "Pulley friction compensation for winch-integrated cable force measurement and verification on a cable-driven parallel robot," in *2015 IEEE International Conference on Robotics and Automation (ICRA), Seattle, WA, USA*, pp. 1627–1632, 2015.

[140] J. Lamaury, M. Gouttefarde, A. Chemori, and P.-E. Hervé, "Dual-space adaptive control of redundantly actuated cable-driven parallel robots," in *2013 IEEE/RSJ International Conference on Intelligent Robots and Systems, Tokyo, Japan*, pp. 4879–4886, 2013.

[141] J. Piao, E.-S. Kim, H. Choi, C.-B. Moon, E. Choi, J.-O. Park, and C.-S. Kim, "Indirect force control of a cable-driven parallel robot: tension estimation using artificial neural network trained by force sensor measurements," *Sensors*, vol. 19, no. 11, 2019.

[142] J. Bieber, D. Bernstein, M. Schuster, K. Wauer, and M. Beitelschmidt, "Motor current based force control of simple cable-driven parallel robots," in *Cable-Driven Parallel Robots* (M. Gouttefarde, T. Bruckmann, and A. Pott, eds.), (Cham), pp. 271–283, Springer International Publishing, 2021.

[143] E. Picard, F. Plestan, E. Tahoumi, F. Claveau, and S. Caro, "Control strategies for a cable-driven parallel robot with varying payload information," *Mechatronics*, vol. 79, p. 102648, 2021.

[144] C. B. Pham, G. Yang, and S. H. Yeo, "Dynamic analysis of cable-driven parallel mechanisms," in *Proceedings, 2005 IEEE/ASME International Conference on Advanced Intelligent Mechatronics, Monterey, CA, USA*, pp. 612–617, 2005.

[145] E. Idà and V. Mattioni, "Cable-driven parallel robot actuators: state of the art and novel servo-winch concept," *Actuators*, vol. 11, no. 10, 2022.

[146] S. Wright, "Correlation and causation," *Journal of agricultural research*, vol. 20, no. 7, pp. 557–585, 1921.

[147] J. G. Ziegler and N. B. Nichols, “Optimum settings for automatic controllers,” *Journal of Fluids Engineering*, 1942.

[148] K. Kamali, A. Joubair, and I. A. Bonev, “Optimizing cable arrangement in cable-driven parallel robots to improve the range of available wrenches,” vol. Volume 5B: 42nd Mechanisms and Robotics Conference of *International Design Engineering Technical Conferences and Computers and Information in Engineering Conference, Quebec City, Quebec, Canada*, 08 2018.

[149] J. Pusey, A. Fattah, S. Agrawal, and E. Messina, “Design and workspace analysis of a 6-6 cable-suspended parallel robot,” *Mechanism and Machine Theory*, vol. 39, no. 7, pp. 761–778, 2004.

[150] B. Ouyang and W. Shang, “Wrench-feasible workspace based optimization of the fixed and moving platforms for cable-driven parallel manipulators,” *Robotics and Computer-Integrated Manufacturing*, vol. 30, no. 6, pp. 629–635, 2014.

[151] F. Ennaiem, A. Chaker, J. S. S. Arévalo, M. A. Laribi, S. Bennour, A. Mlika, L. Romdhane, and S. Zeghloul, “Sensitivity based selection of an optimal cable-driven parallel robot design for rehabilitation purposes,” *Robotics*, vol. 10, p. 7, 12 2020.

[152] A. A. Kumar, J. F. Antoine, P. Zattarin, and G. Abba, “Influence of payload and platform dimensions on the static workspace of a 4-cable driven parallel robot,” in *2nd Robotix-Academy Conference for Industrial Robotics (RACIR) 2018, Luxembourg, Luxembourg*, 6 2018.

[153] P. Miermeister, A. Pott, and A. Verl, “Dynamic modeling and hardware-in-the-loop simulation for the cable-driven parallel robot ipanema,” in *ISR 2010 (41st International Symposium on Robotics) and ROBOTIK 2010 (6th German Conference on Robotics)*, pp. 1–8, 2010.

[154] J. A. dit Sandretto, D. Daney, and M. Gouttefarde, “Calibration of a fully-constrained parallel cable-driven robot,” in *Romansy 19 – Robot Design, Dynamics and Control* (V. Padois, P. Bidaud, and O. Khatib, eds.), (Vienna), pp. 77–84, Springer Vienna, 2013.

[155] S. Qian, K. Bao, B. Zi, and N. Wang, “Kinematic calibration of a cable-driven parallel robot for 3d printing,” *Sensors*, vol. 18, no. 9, 2018.

[156] M. M. Aref and J. Mattila, “Automated calibration of planar cable-driven parallel manipulators by reinforcement learning in joint-space,” in *2018 6th RSI International Conference on Robotics and Mechatronics (IcRoM)*, pp. 172–177, 2018.

[157] F. Zhang, W. Shang, and S. Cong, “Choosing measurement configurations for kinematic calibration of cable-driven parallel robots,” in *2018 3rd International Conference on Advanced Robotics and Mechatronics (ICARM)*, pp. 397–402, 2018.

[158] N. Tremblay, K. Kamali, P. Cardou, C. Desrosiers, M. Gouttefarde, and M. J.-D. Otis, “Eye-on-hand calibration method for cable-driven parallel robots,” in *Cable-Driven Parallel Robots* (A. Pott and T. Bruckmann, eds.), (Cham), pp. 345–356, Springer International Publishing, 2019.

[159] F. Zhang, W. Shang, G. Li, and S. Cong, “Calibration of geometric parameters and error compensation of non-geometric parameters for cable-driven parallel robots,” *Mechatronics*, vol. 77, p. 102595, 2021.

[160] Z. Zhang, G. Xie, Z. Shao, and C. Gosselin, “Kinematic calibration of cable-driven parallel robots considering the pulley kinematics,” *Mechanism and Machine Theory*, vol. 169, p. 104648, 2022.